



UNIVERSITÉ DE FRIBOURG FACULTÉ DES SCIENCES
UNIVERSITÄT FREIBURG MATHEMATISCH-NATURWISSENSCHAFTLICHE FAKULTÄT

Department of Physics
University of Fribourg (Switzerland)

Laboratory based XAS measurements,
Electron-induced double K-shell
ionization of Sc, Cr and Cu
and
Chemical sensitivity of photoinduced $K^{h\beta}$
hypersatellite transitions in Cr
compounds

THESIS

presented to the Faculty of Science of the University of Fribourg (Switzerland)
in consideration for the award of the academic grade of *Doctor rerum naturalium*

by

Faisal Zeeshan

from

Pakistan

Thesis No: 2052

Editor: UniFr – UniPrint

Fribourg 2017

Accepted by the Faculty of Science of the University of Fribourg (Switzerland)
upon the recommendation of

Prof. Dr. Philipp Aebi, University of Fribourg (President of the jury),
Prof. Dr. Jean-Claude Dousse, University of Fribourg (Thesis Supervisor),
Prof. Dr. José Paulo Santos, Nova Universidade de Lisboa, Portugal (Reviewer),
Dr. hab. Joanna Hoszowska, University of Fribourg (Reviewer).

Fribourg, October 27th, 2017

Thesis supervisor



Prof. Dr. Jean-Claude Dousse

Dean



Prof. Dr. Christian Bochet

CONTENTS

Abstract	IV
-----------------	-----------

Résumé	VI
---------------	-----------

I. Introduction	1
I.1. X-ray absorption spectroscopy (XAS)	2
I.1.1. Beer-Lambert law	2
I.1.2. X-Ray absorption fine structure (XAFS) spectra	3
I.1.3. XAFS techniques	6
I.1.4. X-ray sources for XAS	8
I.2. Double 1s vacancy states produced by impact with electrons	16
I.2.1. Production of hollow K-shell atoms	16
I.2.2. Hypersatellite X-ray transitions	20
I.3. Chemical sensitivity of photoinduced $K\beta$ hypersatellite transitions in Cr compounds	22

II. Laboratory-based XAS measurements with a von Hamos curved crystal spectrometer	26
II.1. Preamble	27
II.2. Experimental setup and methodology	28
II.2.1. Von Hamos crystal spectrometer	28
II.2.2. XAS setup	32
II.2.3. Optimization of the setup parameters	35
II.3. Measurements	42
II.3.1. Samples, crystals and X-ray tubes	42
II.3.2. K-edges of Ti, Fe, Cu and Ge	45

II.3.3. L ₃ -edges of Hf, Ta and Pt	47
II.3.4. L ₁ , L ₂ and L ₃ -edges of Mo and Ag	48
II.4. Data analysis	51
II.4.1. Energy calibration	51
II.4.2. Instrumental resolution	52
II.4.3. Determination of the edge energies and absorption coefficients	53
II.5. Results and discussion	56
II.5.1. Comparison with synchrotron radiation measurements . . .	56
II.5.2. Edge energies	59
II.5.3. Absorption coefficients	62
II.6. Summary and concluding remarks	65
<hr/>	
III. Electron-induced double K-shell ionization of Sc, Cr and Cu	68
III.1. Experimental setup and measurements	69
III.1.1. Experimental setup	69
III.1.2. Attenuation factors	70
III.1.3. Measurements	71
III.2. Data analysis	75
III.2.1. Energy calibration and instrumental broadening	75
III.2.2. Fitting procedure	77
III.2.3. Intensity correction factors	85
III.3. Results and discussion	93
III.3.1. Energies	93
III.3.2. Line widths	98
III.3.3. Ratios of double-to-single K-shell ionization cross sections	100
III.4. Summary and concluding remarks	107
<hr/>	
IV. Chemical sensitivity of photoinduced K^{hβ} hypersatellite tran- sitions in Cr compounds	109
IV.1. Experiment	110
IV.1.1. Beam line setup	110
IV.1.2. Johann-type hard X-ray spectrometer	110

IV.2. Data analysis	113
IV.2.1. $K\beta$ diagram spectra	113
IV.2.2. $K^h\beta_{1,3}$ hypersatellite spectra	119
IV.3. Results and discussion	121
IV.3.1. $K\beta$ diagram and VtC transitions	121
IV.3.2. $K^h\beta_{1,3}$ hypersatellite transitions	131
IV.4. Summary and concluding remarks	139
<hr/>	
List of Figures	143
<hr/>	
List of Tables	147
<hr/>	
References	149
<hr/>	
Acknowledgements	158
<hr/>	
Curriculum vitae	159
<hr/>	
List of publications	162

ABSTRACT

The present PhD thesis includes three different projects which belong to the domain of inner-shell atomic physics and high energy resolution X-ray spectroscopy. The first project consists of a series of in-house measurements of the characteristic K and L X-ray absorption spectra (XAS) of several 3d, 4d and 5d transition metals. For this project the target chamber of the von Hamos curved crystal spectrometer of Fribourg was slightly modified to allow the operation of the spectrometer in the so-called direct geometry. As compared to the standard von Hamos setup, in this geometry the target is replaced by the anode of an X-ray tube. The XAS spectra are then measured by inserting the absorber of interest either in front of the spectrometer slit or in front of the CCD detector. In order to optimize the experimental setup, the effect of the sample thickness on the experimental edge energies and the influences of the chosen crystal and X-ray tube voltage on the shapes of the spectra were carefully investigated and compared to XAS measurements performed with synchrotron radiation (SR). Precise K and/or L edge energies could be determined and compared to existing experimental and theoretical values. The magnitudes of the absorption coefficient jumps across the edges could also be determined quantitatively and compared to the values obtained from the code XCOM developed at the National Institute for Standards and Technology (NIST).

In the second project the double K-shell ionization of Sc, Cr and Cu induced by electron impact was investigated. This second project was also carried out in-house with the von Hamos curved crystal spectrometer of Fribourg operated in the direct geometry, using the anodes of Sc, Cr and Cu X-ray tubes as targets. The double K-shell ionization was studied via high energy resolution measurements of the $K\alpha_{1,2}$ diagram and $K\alpha_{1,2}^h$ hypersatellite transitions. The main experimental difficulty in this project resided in the determination of the hypersatellite-to-diagram line intensity ratios because the same X-ray tube high voltages had to be used

for the hypersatellite and diagram line measurements to get reliable ratios. The hypersatellite lines being about 10^4 times less intense than their parent diagram lines, the X-ray tubes should be operated at rather high voltages to get hypersatellite spectra with a high enough statistics but then the diagram lines could not be measured in a straightforward way, the CCD being completely saturated due to the tremendous intensity of the diagram lines. The difficulty was circumvented by measuring the diagram lines first at low voltages without and with absorbers and then at high voltages with the same absorbers. The energies and natural line widths of the hypersatellites were determined and compared to existing experimental and theoretical values. The ratios P_{KK} of the double-to-single K-shell ionization cross sections were deduced from the measured relative intensities of the hypersatellites. The results were compared to the P_{KK} values obtained by other groups with electrons, photons and via the nuclear electron capture process.

The aim of the third project was to investigate the influence of the chemical state on the $K^h\beta_{1,3}$ hypersatellite spectra of Cr induced by single-photon double K-shell ionization. For 3d transition metals and their compounds the $K\beta$ X-ray emission spectra provide useful information on the electronic structure and oxidation state. The solid- and chemical- effects on the $K\beta_{1,3}$ diagram and the $K\beta_{2,5}$ valence-to-core (VtC) transitions are well known, and numerous measurements of the $K\beta$ X-ray emission spectra of 3d transition metals have been performed using synchrotron radiation, proton, electron and heavy ion excitations. In contrast, the sensitivity of the $K^h\beta_{1,3}$ hypersatellite transitions to chemical effects has not been explored. High energy resolution data for photoinduced hypersatellite $K^h\beta_{1,3}$ transitions are scarce because of the low double K-shell photoionization cross sections and transition yields. In this third project, the $K\beta$ hypersatellite, and also the $K\beta_{1,3}$ diagram and valence-to-core (VtC) spectra of metallic Cr and Cr compounds were measured by applying the high-resolution XES spectroscopy technique using the 7-crystal Johann-type hard X-ray spectrometer at the Stanford Synchrotron Radiation Lightsource (SSRL). The chemical effects on the energies, intensities, shapes, and widths of the $K\beta$ X-ray emission lines were investigated for Cr in four nominal oxidation states: Cr (Cr^0), Cr_2O_3 (Cr^{3+}), CrO_2 (Cr^{4+}) and $\text{K}_2\text{Cr}_2\text{O}_7$ (Cr^{6+}). Chemical speciation of chromium is important because this element and its compounds are widely used in chemical industry. Further, high resolution XES data of $K\beta$ -hypersatellites are also useful for theory because they allow for a stringent comparison with atomic structure calculations.

RÉSUMÉ

Cette thèse de doctorat contient trois différents projets qui appartiennent aux domaines de la physique atomique des couches profondes et de la spectroscopie de rayons X en haute résolution.

Le premier projet concerne l'étude des spectres d'absorption (XAS) K et L de quelques éléments de transition 3d, 4d et 5d. Les mesures ont été réalisées à Fribourg avec le spectromètre à cristal von Hamos dont la chambre à cible a été modifiée pour permettre l'emploi du spectromètre dans une géométrie différente, dite géométrie directe. Dans cette géométrie, la cible est remplacée par l'anode d'un tube de rayons X et les spectres d'absorption sont mesurés en insérant l'échantillon à analyser soit devant la fente du spectromètre, soit directement devant le détecteur CCD. Afin d'optimiser l'arrangement expérimental, l'influence de l'épaisseur de l'échantillon sur la position des bords d'absorption ainsi que les effets du choix du cristal et de la haute tension du tube de rayons X sur la forme des spectres ont été soigneusement analysés et comparés à des résultats obtenus au moyen de rayonnement synchrotronique. Les énergies des bords d'absorption K et/ou L ont été déterminées avec précision et comparées aux valeurs expérimentales et théoriques existant dans la littérature. Les amplitudes des sauts du coefficient d'absorption aux bords ont pu être déterminées quantitativement et comparées aux valeurs calculées à l'aide du programme XCOM développé à NIST (National Institute for Standards and Technology).

Le deuxième projet est une étude de l'ionisation double de la couche atomique K produite par collision avec des électrons pour trois éléments de transition 3d. Ce projet a également été réalisé à Fribourg à l'aide du spectromètre von Hamos en géométrie directe en utilisant les anodes de Sc, Cr et Cu de tubes de rayons X comme cibles. Les mesures ont porté principalement sur les raies diagrammes $K\alpha_{1,2}$ et hypersatellites $K\alpha_{1,2}^h$. La difficulté expérimentale majeure de ce projet a été la détermination des rapports d'intensité entre les raies hypersatellites et les

raies diagrammes parentes. Pour obtenir des rapports fiables, il a fallu mesurer en effet les raies hypersatellites et diagrammes en utilisant la même tension anodique. Comme les raies hypersatellites sont environ 10^4 moins intenses que les raies diagrammes, une valeur relativement élevée a dû être choisie pour cette tension, ce qui a entraîné pour les raies diagrammes des taux de comptage très élevés qui saturaient le détecteur CCD. La difficulté a été résolue en mesurant les raies diagrammes tout d'abord à basse tension avec et sans absorbeurs, puis à plus haute tension avec les mêmes absorbeurs. Les énergies, largeurs naturelles et intensités relatives des hypersatellites ont été déterminées avec précision et comparées aux valeurs expérimentales et théoriques trouvées dans la littérature. Les rapports P_{KK} des sections efficaces d'ionisation K double et simple ont été ensuite déduites des intensités relatives des hypersatellites et les résultats comparés aux valeurs obtenues par d'autres groupes au moyen d'électrons, de photons ou d'isotopes produits par capture électronique nucléaire.

L'objectif du troisième projet était d'étudier l'influence de l'état chimique sur les spectres de rayons X hypersatellites $K^h\beta_{1,3}$ du Cr produits par double photoionisation de la couche K. Pour les métaux de transition 3d et leurs composés, les spectres de rayons X $K\beta$ fournissent des informations très utiles sur la structure et l'état chimique des échantillons analysés. Les effets chimiques et du corps solide sur les transitions diagrammes $K\beta_{1,3}$ et les transitions valence-coeur (VtC) $K\beta_{2,5}$ sont bien connus et de nombreuses mesures des spectres d'émission $K\beta$ ont été réalisées en utilisant du rayonnement synchrotronique, des protons, des électrons et des ions lourds. En revanche, la sensibilité aux effets chimiques des transitions hypersatellites $K^h\beta_{1,3}$ n'a pas encore été explorée. Les données de haute résolution concernant les raies hypersatellites $K^h\beta_{1,3}$ sont aussi rares parce que les sections de double photoionisation de la couche K et les probabilités de transition $K\beta$ sont faibles. Dans ce troisième projet, les raies X hypersatellites $K^h\beta_{1,3}$ ainsi que les raies diagrammes $K\beta_{1,3}$ et les raies valence-coeur $K\beta_{1,5}$ du Cr métallique et de plusieurs de ses composés ont été mesurées par la technique de la spectroscopie X d'émission (XES) en haute résolution. Les mesures ont été réalisées à la source de rayonnement synchrotronique SSRL (Stanford Synchrotron Radiation Lightsource) au moyen d'un spectromètre à cristaux multiples de type Johann. L'influence des effets chimiques sur les énergies, intensités, formes et largeurs des raies d'émission $K\beta$ et $K^h\beta$ ont été étudiés pour des échantillons de Cr dans quatre états d'oxydation différents : Cr métallique (Cr^0), Cr_2O_3 (Cr^{3+}), CrO_2 (Cr^{4+}) et

$K_2Cr_2O_7$ (Cr^{6+}). La caractérisation chimique du Cr est importante car cet élément et ses composés sont largement utilisés dans l'industrie chimique. De surcroît, des données XES de haute résolution sur l'émission X hypersatellite $K\beta$ est aussi utile pour la théorie car elles permettent de vérifier de façon rigoureuse les calculs de structure atomique.

CHAPTER I

Introduction

I.1 X-ray absorption spectroscopy (XAS)

X-rays were first discovered by Wilhelm Conrad Röntgen in 1895 [1, 2]. This important discovery which was rewarded with the Nobel Prize in Physics in 1901 opened a new era in the investigation of matter. Due to their short wavelength and high penetration power X-rays represent indeed an unique and powerful tool to study the elemental composition and the properties of matter. Among the numerous analysis methods based on X-rays, X-ray absorption spectroscopy (XAS) has developed continuously through the 20th century [3] and the recent advent of intense, monochromatic, energy tunable and micro-focused synchrotron radiation beams has given a new boost to XAS which has become nowadays a well established routine experimental technique.

I.1.1 Beer-Lambert law

Below 100 keV, the interaction of X-rays with matter is dominated by the photoelectric effect, whose cross section is significantly bigger than the elastic or coherent scattering (called also Rayleigh scattering) and inelastic or incoherent scattering (Compton scattering) cross sections. In the photoelectric effect or photoionization, the whole energy and momentum of the incoming photon are transferred to a bound atomic electron. The latter called photoelectron is removed from the atom with a certain kinetic energy. If the energy of the incoming photon is smaller than the absolute value of the binding energy of the atomic electron, the latter can be excited into an outer unfilled level (photoexcitation). In both cases the photon disappears, i.e., is absorbed by the target atom. After a very short time, in the order of 10^{-15} to 10^{-17} s depending on the atomic number and subshell of the considered element, the ionized or excited atom decays either radiatively with the emission of a characteristic X-ray line (fluorescence) or via a radiationless Auger process. In other words, the energy of the absorbed X-ray is converted into the kinetic energy of the photoelectron and/or the energy of the fluorescence X-rays or Auger electrons as shown in Fig. I.1. According to the Beer-Lambert law, if an incident X-ray beam with an intensity I_0 interacts with a sample of thickness h , the intensity $I(E)$ which is transmitted through the sample is given by:

$$I(E) = I_0 \cdot e^{-\mu(E) \cdot \rho \cdot h}, \quad (\text{I.1})$$

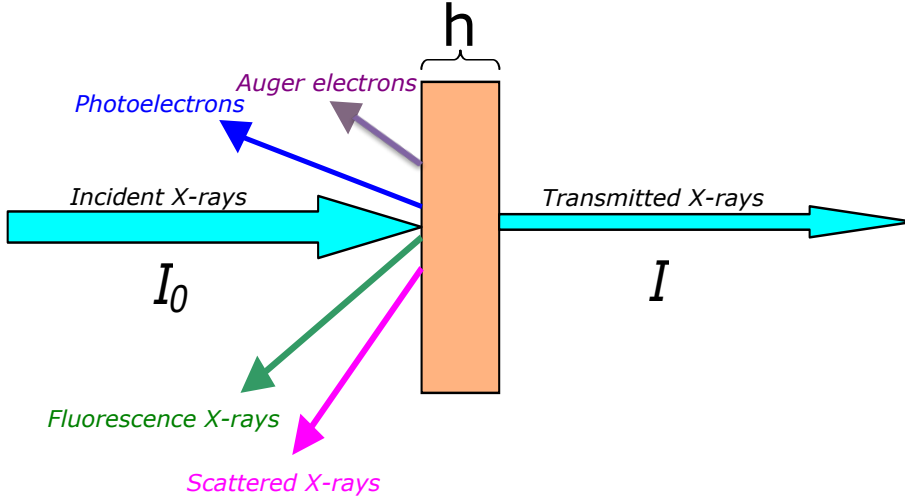


Figure I.1 – Schematic diagram representing the transmission of a collimated X-ray beam through a sample of thickness h . The indicated directions of the photoelectrons, Auger electrons and scattered and fluorescence X-rays produced in the sample as a result of the absorption of the incoming radiation are arbitrary.

where $\mu(E)$ [cm^2/g] represents the total mass absorption coefficient of the sample and ρ its density [g/cm^3]. For a collimated beam geometry as the one represented in Fig. I.1, the elastic σ_{coh} and inelastic σ_{incoh} scattering cross sections must be included in the total absorption coefficient because the scattered photons are removed from the transmitted beam even if they are not really absorbed by the sample. Thus the total absorption coefficient reads:

$$\mu(E) = \sigma_{\text{photo}}(E) + \sigma_{\text{coh}}(E) + \sigma_{\text{incoh}}(E). \quad (\text{I.2})$$

I.1.2 X-Ray absorption fine structure (XAFS) spectra

An example of an X-ray absorption fine structure spectrum, namely the one corresponding to the K-edge of Fe, is depicted in Fig. I.2. In a XAFS spectrum, the total absorption coefficient μ , or like here, the absorbance A defined by

$$A = \log_{10}[I_0(E)/I(E)] = \log_{10}[e^{\mu(E) \cdot \rho \cdot h}] \cong 0.434 \cdot \mu(E) \cdot \rho \cdot h \quad (\text{I.3})$$

is plotted as a function of the incoming radiation energy E .

The observed shape of a XAS spectrum can be explained as follows: as soon as the energy of the incoming X-ray radiation matches the absolute value of the electron binding energy of a given shell or subshell, the photoelectric effect becomes energetically possible, which leads to an abrupt increase of the total absorption

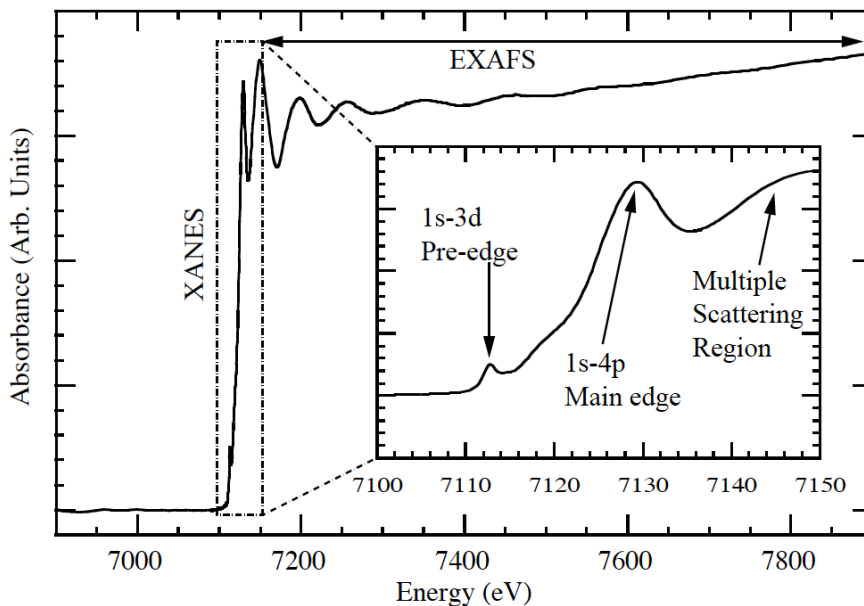


Figure I.2 – Fe K-edge XAFS spectrum showing the XANES and EXAFS regions (Source: Ref. [4]).

coefficient μ . This sudden step-like increase of μ is named absorption edge, e.g., K-absorption edge if the photoeffect takes place on a 1s electron, L₁-, L₂- or L₃-edge in the case of a 2s, 2p_{1/2} or 2p_{3/2} electron, and so on. Due to the lifetime broadenings of the initial and final states of the excited electron, the edge is characterized by a certain energy width. The width of the absorption edge is still increased by the instrumental resolution of the detector employed for the measurement. Above the edge, the absorption coefficient μ or the absorbance diminishes again gradually and exhibits usually some oscillations. Each element across the periodic table is characterized by a set of unique absorption edges which correspond to different binding energies of its electrons. The XAS technique is thus element selective. As mentioned before, if the energy of the incoming photon is smaller than the absolute value of the binding energy of the electron, the latter cannot be removed from the atom but it can be excited into an unfilled outer shell. In other words, the absorption coefficients begins to grow below the ionization threshold. The weak spectral features (pre-edge structures, see inset of Fig. I.2) observed below the main increase of the edge reflect the promotion of a core electron into an unfilled outer level lying below the Fermi level, whereas the edge itself and the peak on the top of it, the so-called "white line", as well as the secondary peaks observed close above the edge correspond to the excitation of the core electron into unoccupied bound levels lying above the Fermi level. These structures which extend typically

over an energy range of 50-100 eV are named XANES (X-ray absorption near edge structures) or NEXAFS (Near edge X-ray absorption fine structures). The characteristics of XANES features provide information about the oxidation state and spin state of the probed element.

The energy region of about 500-1000 eV above XANES is called EXAFS (Extended X-ray absorption fine structure). In this region, the energy of the incoming photon is bigger than the absolute value of the electron binding energy of the considered atomic level. As a consequence the photoelectron leaves the atom with a kinetic energy equal to that of the absorbed photon minus the binding energy (absolute value) of the initial core state. The photoelectron escaping the atom may interact with bound electrons of the surrounding non-excited atoms. Considering the wave-like nature of the photoelectron and assuming the surrounding atoms to be point-like scatterers, one can imagine that the backscattered electron wave interferes with the forward-propagating wave. The resulting interference pattern appears in the spectrum as a modulation of the measured absorption coefficient or absorbance, causing thereby the oscillation observed in the EXAFS region. The wavelength of the photoelectron is dependent on the energy and phase of the backscattered wave whose wavelength changes as a function of the energy of the incoming photon. Furthermore, the phase and amplitude of the backscattered wave depend on the type of atom causing the backscattering and on the distance of the backscattering atom from the central atom. It is thus possible to obtain information about the chemical coordination environment of the original absorbing central atom from the analysis of the EXAFS data.

The locations of absorption edges are not unambiguously defined [5] and have been variously associated in the literature with i) the first inflection point of the absorption spectrum, ii) the energy needed to produce a single core vacancy with the photoelectron "at rest at infinity" and iii) the energy needed to promote a core electron to the lowest unoccupied state. A discussion of these alternatives can be found in [6]. Note that in the alternative ii) the absorption edge energies can be determined by combining the electron binding energies of outer shells which can be measured accurately by means of photoelectron spectroscopy with the energies of emission lines involving transition electrons which originate from the same outer shells.

I.1.3 XAFS techniques

The XAFS spectrum of a sample can be measured by means of the transmission, fluorescence or electron yield method [7,8]. The corresponding experimental setups are shown in Fig. I.3.

In the transmission method [see Fig. I.3 (a)], the incident beam intensity I_0 and the transmitted beam intensity I are measured by ion chambers and the absorption coefficient $\mu_{\text{tot}}(E)$ is obtained from the Equation I.1:

$$\mu(E) = \frac{\ln\left(\frac{I_0(E)}{I(E)}\right)}{\rho \cdot h}. \quad (\text{I.4})$$

For transmission measurements, the sample must be free of pinholes and its thickness chosen so that the difference between the incident I_0 and transmitted I beam intensities is large, keeping I , however, at a reasonably high enough value. A too thick absorber leads indeed to a decrease of the overall spectral intensity, attenuation of XANES/EXAFS oscillations and to a reduction of the white line intensity resulting in an apparent shift of the absorption edge energy with the sample thickness [9,10]. As a rule of thumb, it is generally recommended to choose the absorber thickness h so that $2 < \mu \cdot \rho \cdot h < 4$. To preserve the white line shape and intensity an even smaller sample thickness given by $\mu_{\text{max}} \cdot \rho \cdot h \leq 1$, where μ_{max} represents the maximum value of the total absorption coefficient, is suggested in [11].

In the fluorescence mode [see Fig. I.3 (b)], the incident beam intensity I_0 is also measured with an ionization chamber but instead of measuring the intensity transmitted through the sample, one measures the intensity of the fluorescence X-rays from the sample. The main advantage of the fluorescence method is to permit the study of highly dilute or non-homogeneous samples which are not suitable for absorption measurements performed in the transmission mode. However, as the fluorescence X-rays can be partly absorbed in the sample, the measured intensity should be corrected for the self-absorption in the case of thick or concentrated samples. Although the fluorescence detection is the most common XAFS method in the hard X-ray regime, i.e., for XAS measurements around the K-edges of elements with $Z > 30$, it is relatively difficult to employ in the soft X-ray region because of the tiny value of the fluorescence yield factors of light elements. The fluorescence can be measured with PIN photodiodes or multichannel-plate-detectors (MCP). In this case, the method is named "total fluorescence yield" (TFY). One major drawback of the total fluorescence yield method is its low signal-to-background

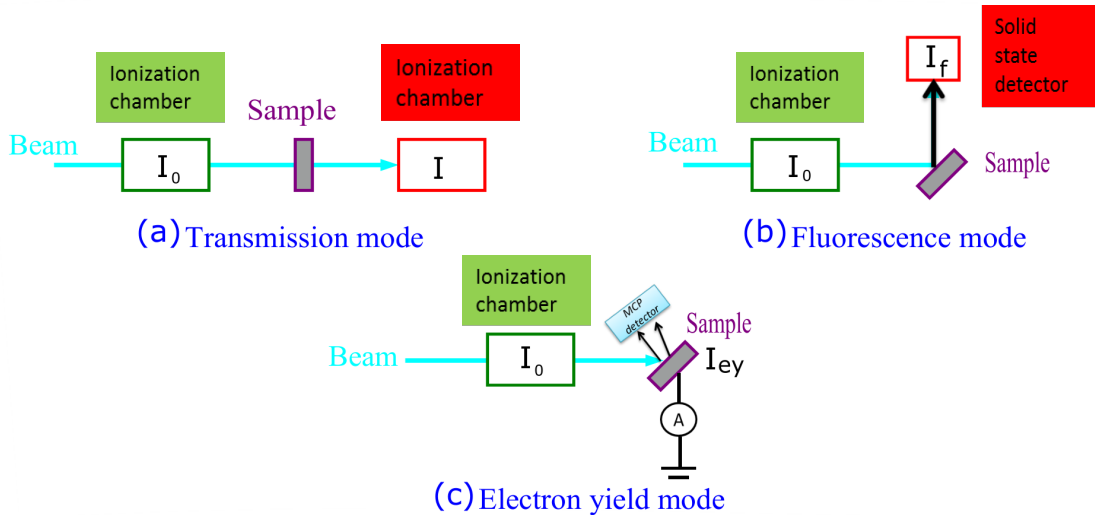


Figure I.3 – Schematic drawings of the experimental setups for XAS measurements performed by means of (a) the transmission method, (b) fluorescence method and (c) electron yield method. The drawing was reproduced from [14].

ratio. This drawback can be eliminated by using energy-dispersive detectors with a good energy resolution such as Si or Ge semi-conductor detectors. In this case, the method refers to as "partial fluorescence yield" (PFY). One of the widely used detectors in PFY XAFS measurements is the silicon drift detector (SDD) because it achieves a higher energy resolution and higher count rate as compared to conventional semi-conductor detectors and it can be used near room temperature. If the fluorescence yield is integrated over an energy interval centered on the selected fluorescence line and narrower than the natural linewidth of the latter, the method is referred to as high energy resolution XAS [12, 13]. In high energy resolution XAS, the fluorescence is measured by means of wavelength-dispersive detectors (crystal spectrometers). In the electron yield mode [see Fig. I.3 (c)], the electron emission of the sample is measured instead of the fluorescence emission, the incident beam intensity I_0 being still determined using an ionization chamber. As for the fluorescence yield mode, the total electron yield (TEY) mode and the partial electron yield (PEY) mode can be used. In the TEY mode the yield corresponding to all photoelectrons, Auger electrons and secondary electrons is measured. Secondary electrons are electrons emitted as a result of inelastic scattering processes with primary electrons. Due to the large mean free path of low energy electrons in matter, the TEY signal is dominated by electrons with kinetic energies below 10 eV. For TEY XAS in the soft X-ray region, the simplest setup consists to connect

the sample to the ground through an ammeter and to monitor the neutralization current. Alternatively, it is also possible to measure the free electrons emitted by the sample using a micro-channel-plate (MCP) detector. The partial electron yield (PEY) method consists to collect only a fraction of the electrons by using an electron energy analyser [15]. For instance, the kinetic energy of Auger electrons being characteristic for a specific radiationless transition, the Auger electron yield (AEY) can be determined by setting the analyser at this specific transition energy. As recently demonstrated, an alternative method to measure XAS spectra in the fluorescence mode is the high energy resolution off-resonant spectroscopy (HEROS) [16–19]. It is known that XAS spectra can be retrieved using the Kramers-Heisenberg formalism from high energy resolution off-resonant X-ray emission spectra. The HEROS technique combines the irradiation of the sample at a fixed incident beam energy, detuned to below the energy of the absorption edge of interest, with the detection of the sample X-ray fluorescence by means of a von Hamos-type crystal spectrometer. The main advantage of HEROS is that XAS spectra can be measured in a scanless mode of operation in very short times, allowing thus the investigation of fast chemical reactions [18, 20] or the extension of the XAS method to X-ray free electron laser (XFEL) beams [17]. In addition, HEROS was found to be insensitive to the self-absorption effect [21].

I.1.4 X-ray sources for XAS

XAS techniques have become increasingly important during the last two decades. The main reason for this expansion resides in the development all around the world of new X-ray sources, namely third-generation synchrotron radiation facilities providing monochromatic, energy tunable and micro-focused X-ray beams of very high brilliances. The XAS technique, however, has been also used and is still used with laboratory based X-ray sources such as X-ray tubes for routine measurements that do not need too sophisticated photon beams and have to be performed frequently and within short terms.

X-ray tubes

The most common laboratory based X-ray source is the X-ray tube which works according to the basic principle discovered by Röntgen to produce X-rays. However, an important improvement over the cold cathode Crookes' tube used by Röntgen

was made by Coolidge. A Coolidge-type X-ray tube consists of a sealed-off highly evacuated glass envelope containing a filament heated by an electrical current and a metallic anode called sometimes anti-cathode and made usually of Sc ($Z=21$), Cr ($Z=24$), Cu ($Z=29$), Mo ($Z=42$), Rh ($Z=45$), Ag ($Z=47$), W ($Z=74$) or Au ($Z=79$). A high voltage power source (30-450 kV) is connected across the filament and the anode to accelerate the electrons. The heating of the filament serves to increase the kinetic energy of the valence-conduction electrons present in the metallic filament until they can escape from the metal via the so-called thermionic emission. The filament is commonly surrounded by a metal cathode, which is kept at the same negative potential as the filament, and serves to focus the emitted electrons to a small area (focal spot) on the anode. For high-power X-ray tubes (electrical power of several kW), this focal spot is typically in the order of several tens of mm^2 . Anodes of X-ray tubes are cooled down by water circulation (high-power tubes) or air circulation (low-power tubes). For higher powers (20 kW or more) X-ray tubes with a water-cooled rotating anode are employed.

For X-ray applications such as X-ray imaging which need a high resolution, i.e., smaller focal spots, micro-focused X-ray tubes have been recently developed. There are two categories of such X-ray tubes, namely the solid-anode and metal-jet-anode micro-focus X-ray tubes. The solid-anode micro-focus X-ray tubes are similar to Coolidge tubes, but thanks to additional focusing electrodes a very small focal spot can be obtained on the anode, in the range 5-20 μm . However, in order to avoid melting of the anode the power density of the electron beam must be below a maximum value of 0.4-0.8 $\text{W}/\mu\text{m}$ depending on the anode material. This means that a solid-anode micro-focus source with a 10 μm electron beam focus can operate at a power in the range 4-8 W. In metal-jet-anode micro-focus X-ray tubes the solid metal anode is replaced with a thin jet of liquid metal. The advantage of the metal-jet anode is that the maximum electron beam power density is significantly increased. Values in the range 3-6 $\text{W}/\mu\text{m}$ can be reached using different materials such as Ga and Sn for the liquid jet. In this case, with a 10 μm electron beam focus a metal-jet-anode micro-focus X-ray source may operate at 30-60 W.

When a charged particle is accelerated or decelerated, it radiates electromagnetic energy. Each change of the direction or magnitude of the velocity of a charged particle results thus in some loss of its kinetic energy via the emission of photons. This process is known as the Bremsstrahlung (BS) effect. In an X-ray tube, the accelerated electrons strike the anode and are slowed down because they make

collisions with the atoms of the anode material. In each collision, part of the electron momentum is transferred to the atom, the electron slows down and, as a result of this deceleration, a Bremsstrahlung photon is emitted. The energy of the BS photon is $h\nu=K - K'$, where K and K' stand for the kinetic energy of the electron before and after the collision. An electron usually will make many collisions, and therefore emit many different photons, before it is brought to rest. As a consequence the wavelength of the photons will range from very large values corresponding to tiny energy losses up to a minimum wavelength λ_{\min} corresponding to the maximum energy loss ($K - K' = K$) if the electron loses all its energy in a single encounter. For this reason, the wavelength distribution of the BS photons is continuous and ranges from λ_{\min} to infinity (for $K - K' \rightarrow 0$), with λ_{\min} given by:

$$\lambda_{\min} = \frac{h \cdot c}{h\nu_{\max}} = \frac{h \cdot c}{K} = \frac{h \cdot c}{E_{\max}}, \quad (\text{I.5})$$

where $E_{\max} = e \cdot U$, e stands for the elementary charge and U represents the value of the high voltage at which the X-ray tube is operated.

The intensity of the BS radiation emitted by a Coolidge X-ray tube as a function of the wavelength can be deduced from the following empirical formula [22]:

$$I(\lambda) = C \cdot Z \cdot \frac{1}{\lambda^2} \cdot \left(\frac{1}{\lambda_{\min}} - \frac{1}{\lambda} \right) + B \cdot Z^2 \cdot \frac{1}{\lambda^2}, \quad (\text{I.6})$$

where Z is the atomic number of the anode element and C and B are constants with $C \gg B$. The BS intensity as a function of the energy is then given by:

$$I(E) = C \cdot Z \cdot \frac{E^2}{h^3 \cdot c^3} \cdot (E_{\max} - E) + B \cdot Z^2 \cdot \frac{E^2}{h^2 \cdot c^2}. \quad (\text{I.7})$$

The efficiency ε of the X-ray tube which is defined as the ratio of the emitted BS power to the absorbed electron power can be written approximately as [22]:

$$\varepsilon \cong 1.4 \cdot 10^{-9} [\text{V}^{-1}] \cdot Z \cdot U. \quad (\text{I.8})$$

Using Eq. I.8 one sees that for a Au anode X-ray tube operated at 90 kV, the efficiency is only about 1% so that 99% of the electron energy turns into heat energy. This explains why it is important to cool down the anode. From the same equation, one can derive the emitted BS power:

$$P_{\text{BS}} \cong 1.4 \cdot 10^{-9} [\text{V}^{-1}] \cdot Z \cdot i \cdot U^2, \quad (\text{I.9})$$

where i stands for the anode current in the X-ray tube. The emitted BS power is thus proportional to the anode current and to the squared high-voltage of the tube.

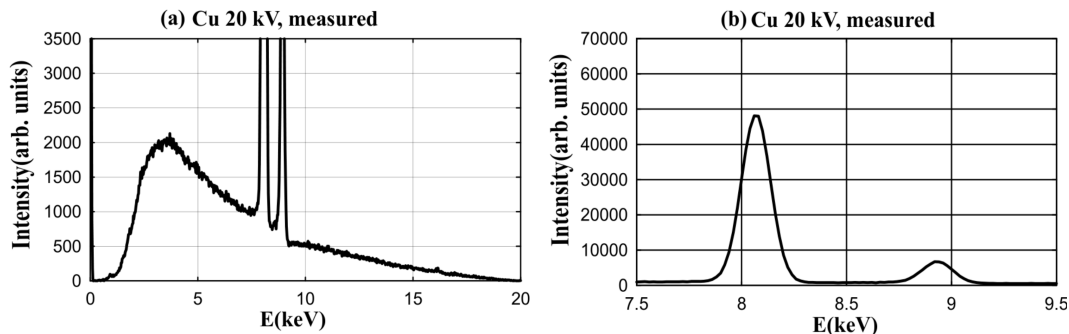


Figure I.4 – (a) Measured X-ray spectrum from a Cu anode X-ray tube operated at 20 kV. One can see the continuous Bremsstrahlung as well as the superimposed characteristic K X-ray emission. As expected the intensity of the Bremsstrahlung tends to zero at 20 keV. The cutoff below 3.5 keV is due to the absorption of low energy X-rays in the Be window of the tube. For the same reason, the characteristic L X-ray emission at about 1 keV is not observed. (b) Detailed view of the photon energy range from 7.5 to 9.5 keV with the characteristic Cu K α and K β emission lines (the Bremsstrahlung was subtracted beforehand). The two plots were taken from Ref. [23].

If the kinetic energy of the accelerated electrons is bigger than the absolute value of the electron binding energies of the core levels of the anode atoms, the latter can be ionized, which leads to the emission of sharp characteristic X-ray lines. The narrow characteristic X-ray emission is superimposed to the continuous BS emission. The BS and characteristic X-rays are emitted through a thin Be window placed usually on the side of the X-ray tube nose in front of the anode (side window X-ray tubes). Depending on the power of the X-ray tube, the thickness of the Be window ranges from 150 μm to 1 mm. For illustration, the characteristic and BS X-ray emission from a Cu anode side window Coolidge X-ray tube operated at 20 kV is shown in Fig. I.4 (a). A more detailed view of the characteristic K α and K β X-ray lines at 8.04 and 8.91 keV, respectively, is shown in Fig. I.4 (b)

Synchrotron radiation sources

The most prominent technical development that allowed XAS to become a routine experimental tool is the third-generation synchrotron radiation (SR) source. The characteristics of such a photon source match indeed perfectly the conditions required by the XAS technique, namely:

- the coverage of a wide photon energy range and the energy tunability of the beam to allow XAFS measurements at the K-, L- and M-edges of elements

across the periodic table;

- the need of monochromatic X-rays with a relative energy resolution of about 10^{-4} to permit the observation of the XANES and EXAFS fines structures;
- the need of high photon fluxes to get good statistics spectra in short times;
- the need of collimated beams to get reliable results in the transmission method or focused beams to investigate micro-size samples.

At the present time more than 75 synchrotron radiation facilities located in 23 countries are available for users [24]. The basic design of third-generation synchrotron radiation sources is depicted in Fig. I.5. The electrons produced by an electron gun are first accelerated in a linear accelerator (linac) up to an energy of several MeV and then injected into the main accelerator (booster), a synchrotron, where they acquire their final energy of several GeV. The electrons are accelerated by means of radiofrequency (RF) cavities. The latter transform also the continuous beam produced by the electron gun in a few cm-long packets or bunches of electrons. The electron bunches after reaching the final energy are injected in the storage ring where they can stay for several hours. Although the vacuum in the storage ring is high (about 10^{-10} mb), the average electron beam intensity is slowly decreasing, due to collisions between the electrons and residual gaz molecules. When the intensity reaches some fraction (e.g., 50%) of the initial intensity, the beam is dumped and new bunches are injected from the booster into the storage ring to retrieve the nominal intensity. During this operation, called refill, SR beams are not available for users. At other facilities like the Swiss Light Source (SLS), in Villigen, there is no refill, the electron beam intensity losses being compensated continuously by the injection of new electron bunches which are simply added to those already circulating.

The velocity of the electrons circulating in the storage ring is given by:

$$v = \sqrt{1 - \frac{1}{\gamma^2}} \cdot c \cong \left(1 - \frac{1}{2\gamma^2}\right) \cdot c, \quad (\text{I.10})$$

where c is the speed of light in vacuum and γ the Lorentz factor which can be written as:

$$\gamma = \frac{K + m \cdot c^2}{m \cdot c^2} \cong \frac{K}{m \cdot c^2} \cong 1957 \cdot K[\text{GeV}]. \quad (\text{I.11})$$

In the above equation, K stands for the kinetic energy of the electrons and $m \cdot c^2$ for the rest mass energy of the latter (511 keV). From the equations I.10 and

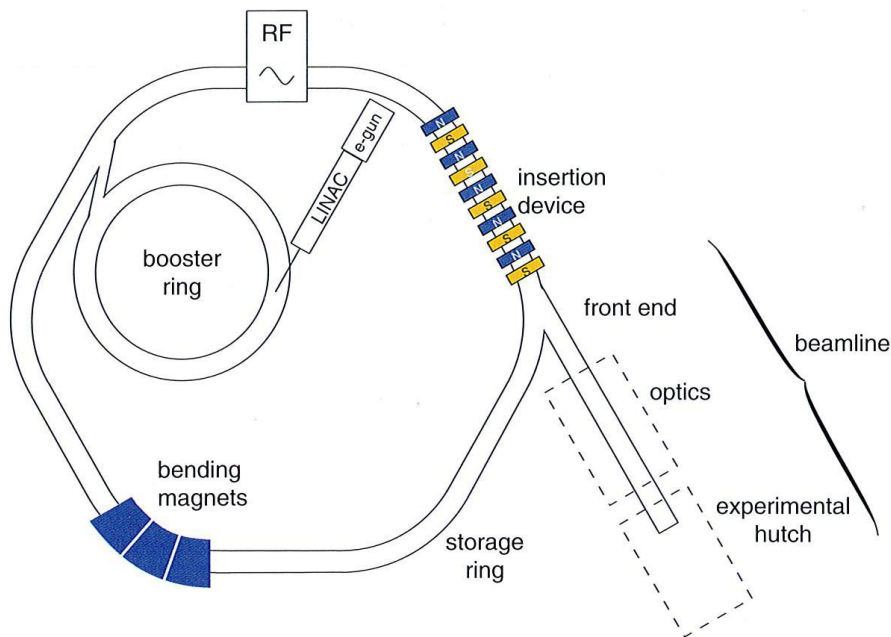


Figure I.5 – Schematic drawing of a third-generation synchrotron radiation facility showing the most important components (reproduced from Ref. [25]).

I.11 one finds that for a beam energy of 6 GeV like at the ESRF the difference $1-\beta$, where β stands for the reduced velocity v/c of the electrons, amounts only to $4 \cdot 10^{-9}$. This explains why the electrons circulating in the storage ring are said ultra-relativistic. To bend the trajectory of the electrons towards the center of the storage ring and force them to circulate in a closed orbit inside the latter, dipole bending magnets are used. Dipole magnets inducing some beam divergence, the latter is compensated with quadrupole magnets. The linear parts of the electron trajectory between two consecutive bending magnets are called straight sections. The storage ring can be operated in the multi-bunch mode (several hundreds of bunches simultaneously in the storage ring), few bunch mode (e.g., 16 bunch mode at the ESRF) or even single bunch mode.

The trajectory of the electrons traveling through the magnetic field of a bending magnet is curved due to the Lorentz force. As the electron is a charged particle and the change of its velocity direction corresponds to a centripetal acceleration, the electron deflection is accompanied by the emission of an electromagnetic radiation. The latter named synchrotron radiation (SR) is similar to the Bremsstrahlung of an X-ray tube (both types of radiation are characterized by a continuous wavelength/energy spectrum) but in the BS the radiation is predominantly due to the deceleration of the electrons, i.e., to the diminution of the magnitude of the electron velocity, whereas in the case of SR the photons are emitted as a result of the

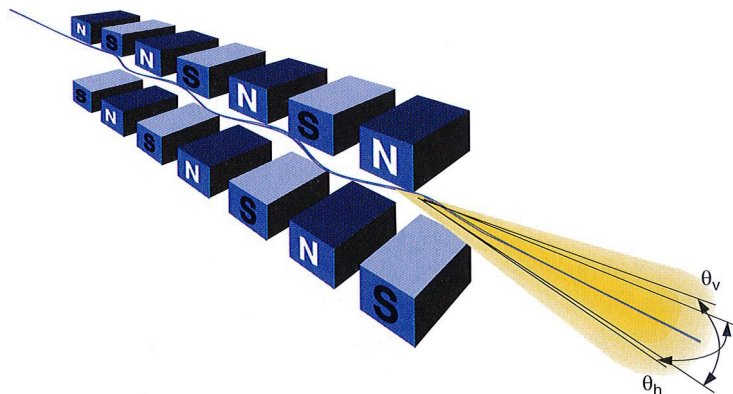


Figure I.6 – Schematic diagram of an insertion device showing the "wiggling" trajectory of the electrons. ϑ_h and ϑ_v represent the angular spreads of the radiation in the horizontal and vertical planes (reproduced from Ref. [25]).

change of the electron velocity direction, the magnitude of the velocity remaining, however, nearly the same. Another difference between BS and SR is that the angular distribution of the BS radiation is isotropic, whereas for SR, according to relativistic electrodynamics, the photons are emitted in the direction of the electron motion within a narrow cone having an angular aperture equal (in radian) to the inverse of the Lorentz factor γ [26]. This means that for 6 GeV electrons the produced SR beam has a divergence as small as $85 \mu\text{rad}$. A further difference between BS and SR, maybe the most important one, resides in the magnitude of the so-called brilliance which is 10^4 to 10^{10} times higher for SR. The brilliance gives the number of photons emitted per second by a 1 mm^2 source within a solid angle of 1 mrad^2 and an energy bandwidth of 1%. The source size is given by the cross section of the electron bunches in the center of the magnet. Furthermore, due to the bunch structure of the electrons in the storage ring, SR is emitted as about 70 ps long pulses with a repetition rate varying approximately between 1 MHz (single bunch mode) and 500 MHz (multi-bunch mode).

The brilliance of SR radiation sources can be further increased by replacing the bending magnets with wigglers or undulators. Wigglers and undulators are also called insertion devices (ID) because they are inserted in the straight sections of the storage ring. They consist of periodic arrays of magnets designed to produce a series of oscillations of the electrons around their otherwise straight trajectories (see Fig. I.6). The distance between two consecutive magnets determines the so-called ID period. The electrons whose trajectories are "wiggled" by an insertion

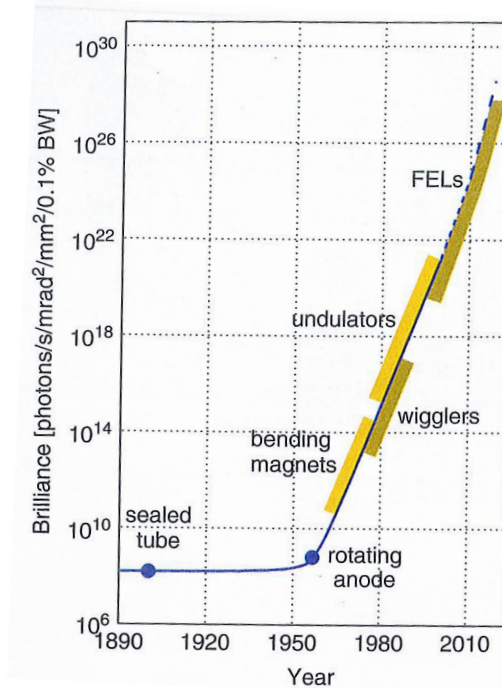


Figure I.7 – Historical graph showing the enormous increase in brilliance of X-ray sources as a function of their date of availability (reproduced from Ref. [25]).

device emit synchrotron radiation along the axis of the device. In the case of a wiggler, there is no coherence between the radiation emitted by the individual electron "wiggles" so that the total SR flux is equivalent to that of a single bending magnet multiplied by two times the number of periods of the magnet array. In the case of undulators, the radiation is emitted coherently by each electron "wiggles" so that the total flux is equivalent to that of a single bending magnet multiplied by the number of periods squared [25]. As the number of periods is always bigger than 2, undulators provide photons beams with significantly higher brilliances than wigglers (see Fig. I.7). To compensate the energy losses of the electron produced by the SR emission, one or several RF cavities are inserted in the storage ring.

The beam lines which give access to the users to the radiation produced by the bending magnets or insertion devices are positioned downstream along the axis of the SR emission. Each beam line consists of an optical hutch and an experimental hutch. The optical hutch which is connected to the storage ring via the front end shutter contains the X-ray optics elements needed to prepare the SR beam according to the specific requirements of the users: vertical and horizontal slits to define the size of the beam, mirrors to cut the radiation corresponding to upper

harmonics, crystal or multilayer monochromators to select the energy of interest and focusing elements such as Fresnel lenses or Kirkpatrick mirrors for experiments requiring micro- or nano-size beam spots. The samples, the detector systems and part of the data acquisition electronics are installed in the experimental hutch. In contrast to the optical hutch whose access is usually restricted to the sole beam line staff, the entry to the experimental hutch is authorized for users, provided that the front end shutter is closed. The computers and electronics needed to tune the SR beam (energy, position and size), adjust the position of the sample and acquire the data are located in general in a separate hutch, namely the counting room, from where the users control online the data acquisition.

As mentioned above, the pulse length of SR is in the order of 100 ps. This is too long to investigate processes with characteristic times under a picosecond such as the vibrational motion in molecules or photochemical reactions. The problem has been solved by the development of fourth-generation X-ray sources, namely the so-called X-ray free electron lasers (XFELs) that produce intense, nano-focused and coherent femtosecond X-ray pulses. XFELs have brought a revolution in the field of ultrafast time-resolved X-ray measurements. They also give access for the users to non linear X-ray processes. The first hard X-ray free electron laser source, the Linac Coherent Light Source (LCLS), which was built on the campus of the University of Stanford, is in operation since April 2009 [27]. Presently other XFEL sources are operational in Japan (SACLA/SPring-8 in Harima Science Park City) and in Italy (FERMI/Elettra in Trieste). Other ones such as the SwissFEL facility at PSI and the European XFEL at DESY (Hamburg) will be set into operation in 2017. The typical brilliances of different X-ray sources are presented for comparison in Fig. I.7.

I.2 Double 1s vacancy states produced by impact with electrons

I.2.1 Production of hollow K-shell atoms

The double K-shell ionization of neutral elements leads to the production of so-called hollow K-shell atoms, i.e., atoms with an empty K-shell while the other outer shells are occupied. The double K-shell ionization can be produced by collisions with energetic heavy ions (HI) (see, e.g., [28]), light charged particles such as α

particles (see, e.g., [29]), protons (see, e.g., [30]) and electrons (see, e.g., [31]) or by impact with photons (see, e.g., [32]). The recent advent of X-ray free electron laser (XFEL) facilities has given a new boost to the domain of hollow atoms. In this case, the extremely short (10^{-15} s) and very intense X-ray pulses allow to produce double K-shell vacancy states by the absorption of two photons in the same atom [33–37].

In collisions with charged particles, the ionization results from the Coulomb interaction between the incoming projectile and the electrons of the target atom. The ionization cross section is proportional to the squared charge of the projectile [38–40]. As the charged projectile can interact simultaneously with several bound electrons, after the collision the target atom is left in most cases in a multiply ionized state. The radiative decay of such multiply ionized atoms gives rise to complex X-ray spectra characterized by reach satellite and hypersatellite structures. For illustration the K X-ray spectrum of a Fe target bombarded by 179 MeV Ne^{9+} ions is presented in Fig. I.8.

As shown in Fig. I.8, in the case of heavy-ion bombardment the single and double K-shell ionization is accompanied by a strong additional outer-shells ionization. Whereas the L-shell satellites can be separated from their parent diagram and hypersatellite lines, provided, however, that the measurements are performed by means of high energy resolution spectroscopy, the M-shell satellites cannot be resolved because their energy shifts are smaller than the natural widths of the parent transitions. This results in energy shifts, broadenings and asymmetric shapes of the diagram and hypersatellite lines. As a consequence, if the aim of the measurements is to determine accurately the energies, line widths and relative intensities of K hypersatellites, softer collisions involving photons or light charged projectiles like electrons are preferable. In this case the photon-induced or electron-induced double K-shell ionization cross sections are several orders of magnitude smaller than those corresponding to HI-induced double K-shell ionization. However, for photons the small cross sections can be compensated by the high number of monochromatic photons delivered by synchrotron radiation facilities (about 10^{12} ph./s). The same holds for electrons for which currents up to about 100 μA (corresponding to about $6 \cdot 10^{14}$ e^-/s) can be currently obtained with standard commercial electron guns. It should be noted here that most commercial electron guns cannot be operated above about 20 kV so that only low-Z elements were investigated [31, 42]. An alternative method for studying the double K-shell ionization induced by electron

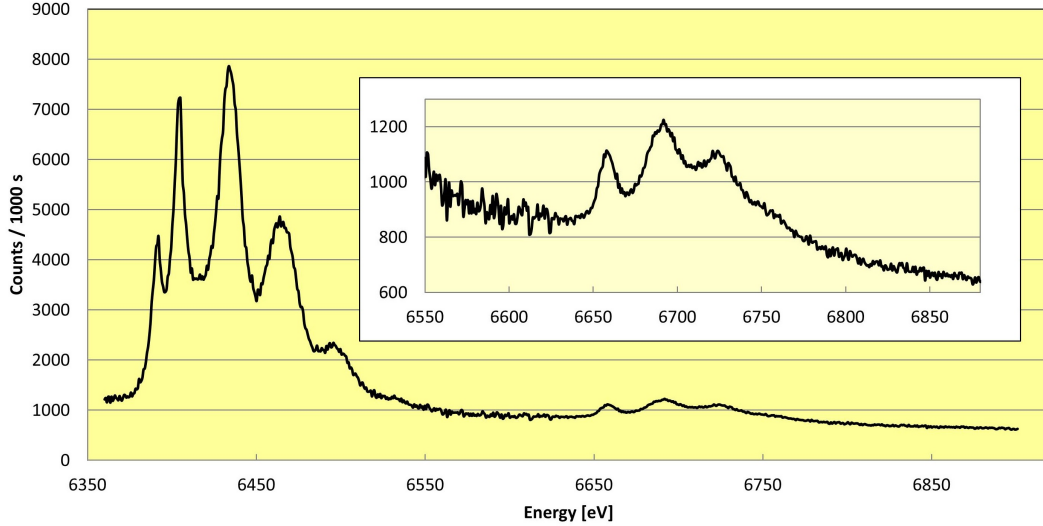


Figure I.8 – Fe $K\alpha$ X-ray spectrum induced by 179 MeV Ne^{9+} ions. The first two peaks at about 6391 and 6404 eV correspond to the $K\alpha_2$ and $K\alpha_1$ diagram lines, while the broader lines at 6432, 6461 and 6490 eV correspond to the $K\alpha_{1,2}L^{-1}$, $K\alpha_{1,2}L^{-2}$ and $K\alpha_{1,2}L^{-3}$ satellite lines, respectively, i.e., to the $K\alpha_{1,2}$ lines with one, two or three additional spectator vacancies in the L-shell. The $K^h\alpha_{1,2}L^{0,1,2}$ hypersatellite lines (at about 6661, 6693 and 6725 eV, respectively) which are represented enlarged in the inset, correspond to X-ray transitions whose initial states are characterized by two vacancies in the K-shell and zero, one and two spectator holes in the L-shell. (Taken from Ref. [41]).

impact consists to replace the electron guns by X-ray tubes that can be operated currently up to 60 kV or higher and use the anodes of the latter as sources of radiation. This permits to extend K-hypersatellite measurements induced by electron impact to heavier elements [43, 44].

A further important difference between the double K-shell ionization induced by heavy ions and photons or electrons resides in the projectile threshold energy. Due to the large mass difference between heavy ions and electrons, only a tiny part of the HI linear momentum can be indeed transferred to the bound electron so that the HI kinetic energy should be bigger to a large extent than the absolute value of the binding energy of the 1s electrons. For instance, in the above discussed $\text{Ne}^{9+} \rightarrow \text{Fe}$ collision, the projectile threshold energy for a single K-shell ionization of Fe is found to be about 1.5 MeV, which is more than 200 times bigger than the ionization energy of 1s electrons of Fe. In contrast to that, in the case of ionization induced by electron impact, the whole linear momentum of the projectile can be

transferred to the bound electron because the two collisions partners have the same mass so that the projectile threshold energy is equal to the ionization energy. The same holds for photoionization since the dominant process in this case is the photoelectric effect which becomes possible as soon as the energy of the photon becomes equal or bigger than the ionization energy.

As in the photoelectric effect a single photon interacts with a single electron and because the photon disappears after the interaction, the removal of the second electron requires another process. Actually two different mechanisms contribute to the second ionization, namely the shake [45] and the knock-out (KO) [46] processes. In the shake process, the second electron is removed due to the abrupt change of the atomic potential following the ionization of the first electron. The shaken electron can be ejected into the continuum or promoted into an unfilled outer shell. In the first case, the effect is named shake-off (SO), in the second one shake-up (SU). The SO and SU effects are quantum mechanics effects that can be explained by the overlap of the wave functions of the shaken electron in the initial and final states. To preserve the energy conservation law, the energy needed for the shake effect must be provided by the incoming photon. The shake probability can be calculated within the Sudden Approximation (SA) model [47]. Because the change of the atomic potential should be faster than the atomic relaxation time, the photoelectron must leave the target atom very quickly. This means that in a shake process the energy of the incoming photon should be significantly higher than the double ionization threshold energy. The KO mechanism is a two step process in which the first ionized electron hits a second bound electron which is then ejected from the atom. This electron-electron inelastic scattering process is also named Two-Step-One (TS1) process. The TS1 process is the dominant effect at low photon energies, whereas the shake mechanism prevails at high photon energies [32, 48].

The double ionization induced by impact with electrons can be also explained by the SO/SU and TS1 processes. In the case of electrons, however, a further mechanism, the Two-Step-Two (TS2) process, may contribute to the production of double vacancy states. In the TS2 process, the two bound electrons are ionized by the incoming electron via two consecutive inelastic scattering processes. As for photons, the SO/SU, TS1 and TS2 processes are energetically allowed only if the energy needed to ionize the second bound electron is provided by the incoming electron. In other words, the electron-induced double K-shell ionization requires

that the kinetic energy of the incoming electron should be bigger or equal to the threshold energy for the double 1s ionization.

I.2.2 Hypersatellite X-ray transitions

The radiative decay of hollow K-shell atoms leads to the emission of so-called $K\alpha$ and $K\beta$ hypersatellite X-ray lines. Hypersatellite transitions were observed for the first time by Charpak [49] in 1953 but the first theoretical study of the radiative decay of atoms with an empty K-shell is about 30 years older since this pioneering work was already carried out in 1925 by Heisenberg [50].

Transitions decaying doubly ionized atoms are shifted towards higher energies as compared to diagram transitions decaying atoms with a single vacancy. The vacancy which is not filled by the radiative transition is called spectator vacancy because the latter is not directly involved in the transition. The energy shift is due to the diminution of the electron screening originating from the spectator vacancy. This diminution of the electronic screening leads to enhanced binding energies for all atomic levels but the enhancement diminishes with the principal quantum number of the atomic level, which results into a net increase of the transition energy. Moreover, the measurements show that the energy shifts of X-ray lines emitted by doubly-ionized atoms decrease with the principal quantum number of the shell where the spectator vacancy is located. As a consequence, satellites with the spectator vacancy in the L-shell are more shifted than satellites with the spectator hole in the M-shell, which in turn are more shifted than satellites with the spectator hole in the N-shell, and so on. The strongest energy shift is thus observed when the spectator vacancy is located in the same shell as the initial vacancy. In this case the shift is much bigger than the one observed for other satellites and, for this reason, it was proposed by Briand [51] to name hypersatellites these most shifted satellites. The measurements show also that the energy shifts of X-ray satellites increase with the principal quantum number of the shell from which the transition electron originates. This explains why satellites and hypersatellites of $K\beta$ X-ray lines ($K^{-1}-M^{-1}$ transitions) are more shifted than those of $K\alpha$ X-ray lines ($K^{-1}-L^{-1}$ transitions).

The diagram $K\alpha_{1,2}$ and hypersatellite $K^h\alpha_{1,2}$ transitions are represented in Fig. I.9. The transition probabilities per electron of the $K\alpha_1$ and $K\alpha_2$ transitions are nearly the same so that, due to the fact that the $2p_{3/2}$ subshell contains 4 electrons and the $2p_{1/2}$ only 2, the $I(K\alpha_1)/I(K\alpha_2)$ intensity ratio is about 2 for all

elements throughout the periodic table. This is no more true for hypersatellite transitions because the $K^h\alpha_1$ hypersatellite which corresponds to the $^1S_0 - ^3P_1$ spin-flip transition ($\Delta S=1$) is forbidden by the E1 selection rules in the pure LS coupling. The $K^h\alpha_1$ transition is, however, allowed in the jj coupling. On the other hand, the $K^h\alpha_2$ hypersatellite which corresponds to the $^1S_0 - ^1P_1$ transition ($\Delta S=0$, i.e., no spin flip) is allowed by the E1 selection rules in both coupling schemes. Thus, for hypersatellites the $I(K^h\alpha_1)/I(K^h\alpha_2)$ intensity ratio is nearly zero for light elements, for which the LS coupling scheme prevails, while tending to the value of 2 for heavy elements which are governed by the jj coupling scheme. In the case of mid heavy elements for which the intermediate coupling scheme applies, the $I(K^h\alpha_1)/I(K^h\alpha_2)$ intensity ratio grows progressively between these two extremes as a function of the atomic number Z. Exactly the same holds for the $I(K^h\beta_1)/I(K^h\beta_3)$ yield ratio since the $K^h\beta_1$ hypersatellite corresponds again to the spin-flip transition $^1S_0 - ^3P_1$ which is forbidden by the E1 selection rules in the LS coupling scheme and thus not observable for light elements, whereas the transition corresponding to the $K^h\beta_3$ hypersatellite is allowed in both the LS and jj coupling schemes.

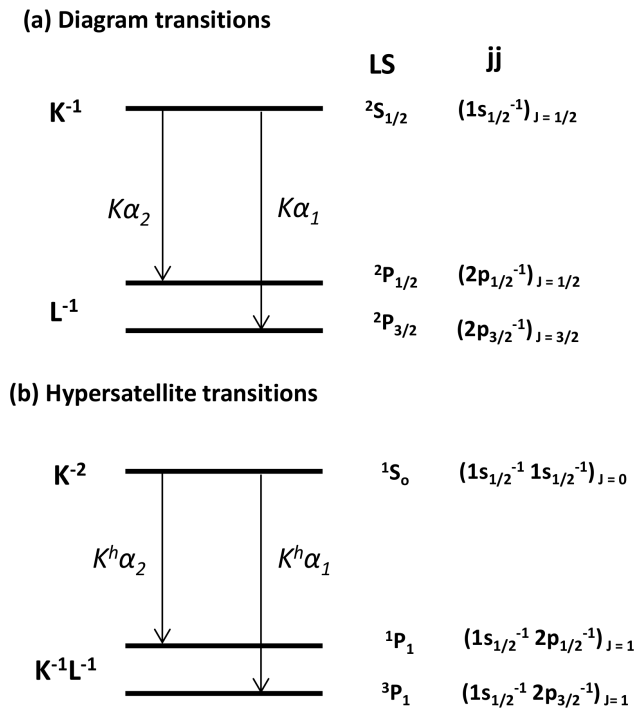


Figure I.9 – Schematic illustration of the (a) $K\alpha_1$ and $K\alpha_2$ diagram transitions and (b) $K^h\alpha_1$ and $K^h\alpha_2$ hypersatellite transitions.

Accurate measurements of hypersatellite energies represent a powerful tool to probe the goodness of atomic structure calculations. Energies of hypersatellite transitions are indeed more sensitive than diagram transitions to the Breit interaction, relativistic effects and quantum electrodynamics (QED) corrections. From the hypersatellite-to-diagram line yield ratios, the double-to-single K-shell ionization cross section ratios P_{KK} can be derived. In the case of DPI the P_{KK} ratios were investigated carefully [32] because many results from SR-based measurements are available in the literature. For electron-induced double K-shell ionization, however, P_{KK} values are scarce and only available for few light elements [31, 42, 52–54]. Furthermore, as mentioned above, the $I(\text{K}^{\text{h}}_{\alpha_1})/I(\text{K}^{\text{h}}_{\alpha_2})$ intensity ratio varies as a function of the atomic number Z from 0 to 2, allowing thus to probe the intermediacy of the coupling scheme across the periodic table [29, 44]. Finally, the natural line widths of K hypersatellite X-ray lines permit to determine the mean lifetimes of double 1s vacancy states and to compare the latter to theoretical predictions.

In the present study, the $\text{K}\alpha$ hypersatellite X-ray spectra of Sc ($Z=21$), Cr ($Z=24$) and Cu ($Z=29$) induced by electron impact were measured by means of high energy resolution spectroscopy. For the lightest element, the extremely weak $\text{K}\beta$ hypersatellite could also be measured. As for electrons the maximum ionization cross section is observed at energies that are about 2 times bigger than the ionization threshold, for each element the electron kinetic energy was chosen to be around 2 times bigger than the threshold energy for the double 1s ionization. The energy shifts of the hypersatellites with respect to their parent diagram lines and their natural line widths were determined and compared to existing experimental and theoretical data. The double-to-single-ionization cross section ratios P_{KK} were derived from the measured relative intensities of the hypersatellites and compared to other P_{KK} values found in the literature for electrons and photons.

I.3 Chemical sensitivity of photoinduced $\text{K}\beta$ hypersatellite transitions in Cr compounds

Third-generation synchrotron radiation (SR) facilities have boosted the development of high-energy resolution X-ray spectroscopic techniques, such as X-ray emission (XES), resonant inelastic X-ray scattering (RIXS), high energy resolution fluorescence detected X-ray absorption (HERFD-XAS), partial fluorescence yield (PFY) XAS and X-ray Raman spectroscopy (XRS). X-ray emission spectroscopy

of inner-core and valence-to-core (VtC) transitions in resonant and non-resonant excitation conditions is a powerful technique to probe the electronic structure and chemical state of matter [55–60]. In the soft X-ray regime XES is a popular technique because of its unique capabilities to investigate transition metal oxides and surface chemistry of adsorbates [61] [62,63]. Because of the penetrating properties of hard X-rays, hard X-ray emission has more advantages over soft X-ray emission in terms of sample environment (temperature, pressure, gas feed) allowing for *in-situ* experiments [55,64]. Over the past years numerous studies have been performed on transition metal complexes, important enzymes, geometrical compounds and catalytic systems using high-energy resolution X-ray spectroscopic techniques [57,60,64–74].

High-energy resolution and high collection efficiency are prerequisite in order to measure X-ray line energy shifts of few eV or less, as well as to evince small variations in X-ray line intensities and spectral shapes. Efficient collection of X-rays with high-energy resolution can be achieved by using curved-crystal X-ray spectrometers. For hard X-ray radiation Bragg-type perfect-crystal X-ray optics are commonly used. First Bragg-type curved-crystal spectrometer designs were presented in 1930s by Johann [75], Johansson [76], and von Hamos [77]. In the case of the Johann and Johansson geometry a point-to-point focusing scheme is realized, where both the crystal analyzer and the detector are moved, whereas the von Hamos geometry allows collecting a spectrum over a certain energy bandwidth without moving any parts. Non-dispersive or vertical focusing corresponds to the von Hamos geometry and for the dispersive or horizontal focusing to the Johann or Johansson geometries. The best focusing conditions with bent crystals were first described by DuMond and Kirkpatrick in 1930 [78]. More details on the early developments of curved-crystal spectrometers can be found in DuMond and Chap [79] and Knowles and Chap [80]. The Rowland-circle based Johann and Johansson geometries, as well as the von Hamos geometry are used today to construct curved-crystal X-ray spectrometers. Various hard X-ray spectrometers based on Bragg reflections from single or multiple perfect crystals have been developed [81,82,82–92]. Nowadays, several synchrotron facilities offer hard X-ray beam lines which are equipped with high resolution multi-crystal spectrometers [55,84,85,88,90,93–99].

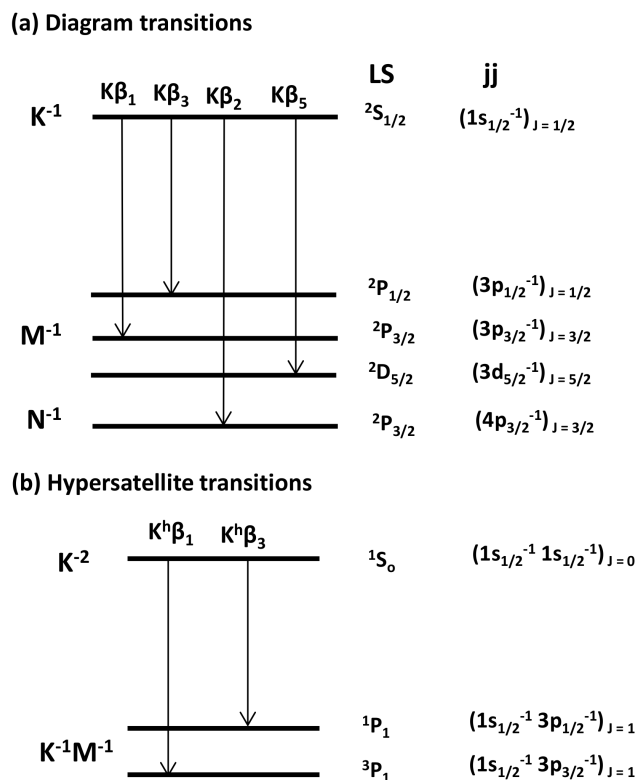


Figure I.10 – Schematic illustration for the (a) $K\beta_1$, $K\beta_3$, $K\beta_2$ and $K\beta_5$ transitions and (b) $K^h\beta_1$ - and $K^h\beta_3$ -hypersatellite transitions.

For 3d transition metals and its compounds the $K\beta$ X-ray emission spectra provide information on the electronic structure, oxidation state, ligand type and metal-ligand bond length, and spin state. A schematic of the $K\beta_1$, $K\beta_3$, $K\beta_2$ and $K\beta_5$ and the hypersatellite $K^h\beta_{1,3}$ transitions is represented in Fig. I.10. The solid- and chemical-effects on the $K\beta_{1,3}$ diagram and the $K\beta_{2,5}$ VtC transitions are well known, and numerous measurements of the $K\beta$ X-ray emission spectra of 3d transition metals have been performed using synchrotron radiation, proton, electron and heavy ion excitations to investigate the energy shifts, intensity ratios, relative positions and widths of the elements and their chemical compounds [55,57,59,100–110]. In contrast, the sensitivity of the $K^h\beta_{1,3}$ hypersatellite transitions to chemical-effects has not been explored. High energy resolution data for photoinduced hypersatellite $K^h\beta_{1,3}$ transitions are scarce because of the low double K-shell photoionization cross sections [32, 48, 111], and transition yields (*e.g.*, for Cr the intensity ratio of $K^h\beta$ to the strongest diagram transition $K\alpha$ is only about 5×10^{-5}). Hitherto, only two high-resolution measurements of the $K^h\beta_{1,3}$ hypersatellite transitions induced by photon impact have been published,

those of Diamant *et al.* [112] for elemental Fe and of Huotari *et al.* [113] for Ti metal.

The objective of this work was thus to investigate the influence of the chemical state on the $K^h\beta_{1,3}$ hypersatellite spectra of Cr induced by single-photon double K-shell ionization. The $K\beta$ -hypersatellite, and also the $K\beta_{1,3}$ diagram and VtC spectra of metallic Cr and Cr compounds were measured with the 7-crystal Johann-type hard X-ray spectrometer [92] at the Stanford Synchrotron Radiation Lightsource (SSRL) by applying the high-resolution XES spectroscopy technique. The chemical effects on the energies, intensities, shapes, and widths of $K\beta$ X-ray emission spectra were investigated for Cr in four nominal oxidation states: Cr (Cr^0), Cr_2O_3 (Cr^{3+}), CrO_2 (Cr^{4+}) and $K_2Cr_2O_7$ (Cr^{6+}). Chemical speciation of chromium is important as it is widely used in chemical industry and also because its two common oxidation states Cr^{3+} and Cr^{6+} appearing in nature are toxic, where Cr^{6+} ion is about one hundred times more toxic than Cr^{3+} [96]. The Cr^{4+} ion has also gained interest since CrO_2 was found to be a half-metallic ferromagnet [114, 115] and it has many applications in speed sensors, read sensors for magnetic disc drives, random access memories for computers and new generation of spintronic devices [116–120]. Further, high resolution XES data of $K\beta$ -hypersatellites allow for a stringent comparison with atomic structure calculations.

CHAPTER II

**Laboratory-based XAS
measurements with a von
Hamos curved crystal
spectrometer**

II.1 Preamble

X-Ray absorption fine structure spectroscopy is widely applied at synchrotron radiation sources where the bright, coherent, micro-focused, time-resolved, energy tunable and monochromatic X-ray beams are routinely used to analyze samples from different disciplines such as physics [121–124], chemistry [125, 126], environmental sciences [127], geology [128], cultural heritage [129], archeology [130] and biomedicine [131]. For external users, however, the access to such advanced research facilities is not so easy. For each experiment a proposal should be indeed submitted and if accepted the allotted beam time is only available several months after the proposal acceptance. In addition, the available beam time is usually limited to several days. It can be also noted that many XAFS applications which do not really require fine focus, high flux and time resolved X-ray beams are nevertheless performed in most cases at SR facilities because of the lack of any alternative.

However, alternative methods for XAFS measurements that do not need the full performance of SR beam lines do exist. They are provided by laboratory-based setups which offer the advantages of lower costs and better accessibility. Although such setups using conventional X-ray sources have played an important role in the early development of the XAFS technique [132–135], only sporadic in-house XAFS applications have been reported in the literature [136–146] since the advent of third-generation SR sources. More recently a laboratory-based hard X-ray monochromator for high-resolution XES and XANES measurements and a setup for single shot XANES measurements in the laboratory were developed at the University of Washington [147] and the University of Berlin [148], respectively. The possibility to use a DuMond curved crystal spectrometer as a monochromator for XAFS measurements around the K-edges of mid heavy elements such as Mo was also demonstrated [149, 150]. In the present work, we discuss an experimental setup based on a von Hamos curved crystal spectrometer and a side-window X-ray tube for laboratory-based XAFS measurements around the K-edges of elements with $11 \leq Z \leq 40$, L-edges of elements with $30 \leq Z \leq 82$ and M-edges of elements with $Z \geq 60$.

II.2 Experimental setup and methodology

The new laboratory-based setup for X-ray absorption spectroscopy measurements is based on the von Hamos curved crystal spectrometer of Fribourg [151] which was developed about 20 years ago for high-resolution XES measurements. The spectrometer can be employed for in-house projects using X-ray tubes or electron guns for the production of the sample fluorescence. Thanks to its compactness, the spectrometer can be also transported and installed at external big facilities for projects requiring synchrotron radiation or heavy-ion beams. As this Bragg-type bent crystal X-ray spectrometer represents the key part of the new XAFS setup, its working principles and main characteristics are briefly outlined in the next subsection.

II.2.1 Von Hamos crystal spectrometer

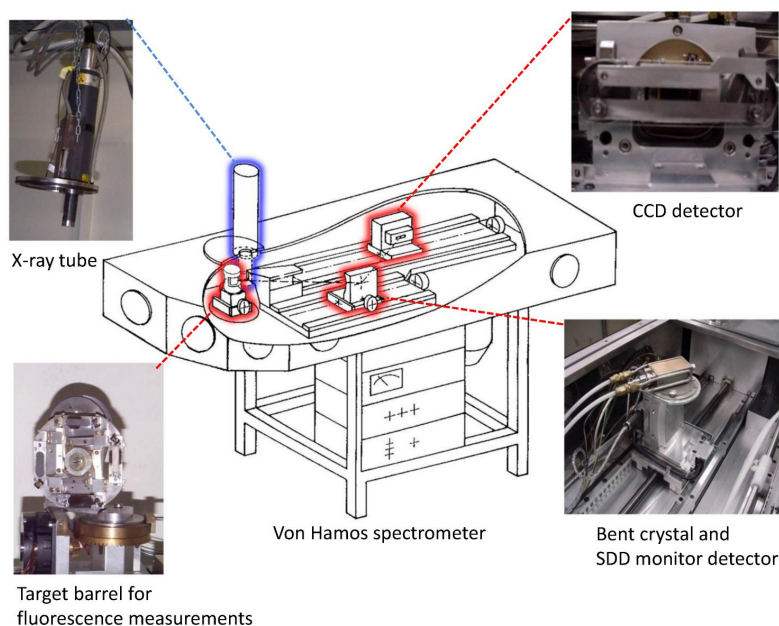


Figure II.1 – Schematic drawing of the von Hamos spectrometer. The main components are represented in the different insets.

As shown in Fig.II.1, the spectrometer consists of an effective X-ray source defined by a vertical rectangular Ta slit placed in front of the sample, a cylindrically bent crystal and a position sensitive CCD detector. The sample-slit system, crystal and detector are enclosed in a 180 cm long \times 62 cm wide \times 24.5 cm high stainless steel

vacuum chamber which can be pumped down to 10^{-6} mbar by means of a turbomolecular pump. On the top of the chamber three circular flanges give access to the sample, crystal and detector. Additional flanges are located on the side wall to connect the spectrometer under different angles to the beam line at external facilities. For in-house measurements, the X-ray tube is mounted on the flange located above the target chamber and the electron gun on the first beam port.

In the von Hamos geometry [152] the crystal is bent cylindrically around a horizontal axis parallel to the direction of dispersion and provides focusing in the vertical direction. The front surface of the detector, the slit center and the axis of curvature of the crystal are all contained in the same vertical plane. The slit-to-crystal and crystal-to-detector distances are equal. For given fixed positions of the crystal and detector, a certain angular range which is determined mainly by the extension of the CCD detector along the dispersion direction is covered by the crystal so that a certain energy range (30-300 eV depending on the Bragg angle and employed crystal) can be measured at once in a scanless mode of operation. To cover a wider energy domain, the crystal and detector are moved along their translation axis, the detector twice as much as the crystal but the position of the slit remains unchanged. The Bragg angles that can be covered with the von Hamos spectrometer of Fribourg vary between 24.4° and 61.1° . With the use of different crystals whose radius of curvature is 25.4 cm, the energy range covered by the spectrometer extends theoretically from 0.6 keV to 16.7 keV but due the low efficiency of the CCD detector at low and high photon energies, the spectrometer is normally used between 1 keV and 15 keV.

The translations of the crystal and detector (see Fig. II.2) are achieved via threaded spindles driven by remote-controlled stepping motors. For each axis, one motor step produces a displacement of 5 μm . For a given photon energy E , the distance x_c between the crystal center and the slit, measured along the dispersion axis, is given by:

$$x_c = R \cdot \cot(\vartheta), \quad (\text{II.1})$$

where R stands for the radius of curvature of the crystal and ϑ for the Bragg angle. The latter can be deduced from the Bragg law [153]:

$$\vartheta = \text{Arcsin} \left\{ \frac{12.398[\text{keV} \cdot \text{\AA}] \cdot n}{2d_{\text{hkl}}[\text{\AA}] \cdot E[\text{keV}]} \right\}, \quad (\text{II.2})$$

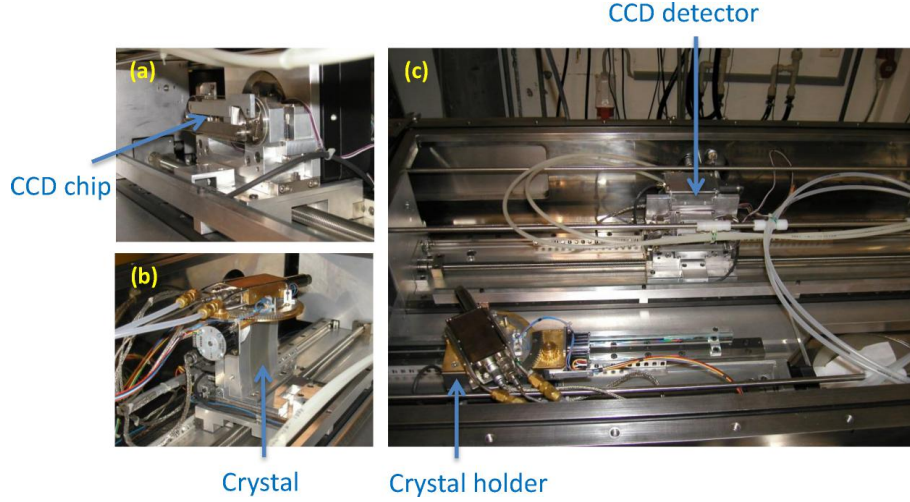


Figure II.2 – (a) CCD chip (hardly visible) and remote-controlled X-ray shutter. (b) Bent crystal and SDD detector. The latter mounted on the top of the crystal support serves to monitor the beam intensity during experiments at external facilities. (c) Top view of the interior of the vacuum chamber with the crystal and detector. The target chamber which is not visible is located on the left side hand of the photograph. The Schneeberger rails and threaded spindles used to move the detector and the crystal can be seen in a), b) and partly in c).

where n is the diffraction order and d_{hkl} the spacing of the diffraction planes (hkl) of the crystal. As in the von Hamos geometry the distances between the source and the crystal and the crystal and the detector should be equal, the distance along the dispersion axis x_d between the center of the CCD chip and the slit is similarly given by:

$$x_d = 2 \cdot R \cdot \cot(\vartheta). \quad (\text{II.3})$$

In the von Hamos slit geometry, the center of the sample should be located behind the slit on the straight line joining the slit and the crystal centers. This means that the sample position should be changed whenever the Bragg angle, i.e., the crystal position, is modified. This alignment is realized by translating the sample along the so-called TAF axis that is perpendicular to the direction of dispersion. The target carriage position is given by the following relation:

$$y_{\text{TAF}} = d \cdot \tan(\vartheta), \quad (\text{II.4})$$

where $d=2.5$ cm represents the distance along the dispersion axis between the slit and the TAF axis. The slit is mechanically coupled to the target carriage through a thin rod so that it remains automatically perpendicular to the direction defined

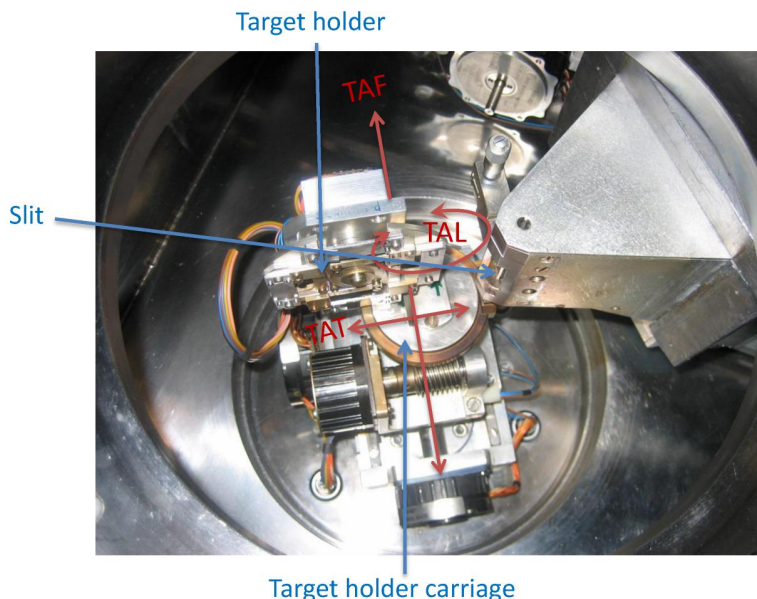


Figure II.3 – Photograph of the target chamber of the von Hamos spectrometer. The sample position can be adjusted along two translation axes (TAF and TAT) and a vertical rotation axis (TAL).

by the sample and crystal centers for any TAF position. The sample transverse position (TAT axis) and sample orientation (TAL axis) (see Fig. II.3) can also be adjusted via remote-controlled stepping motors. The target barrel allows to mount simultaneously four different samples. It is equipped with a remote-controlled stepping motor (TAB axis) which permits to select the sample to be measured. The slit width can be adjusted by means of a micrometer screw. Depending on the required instrumental resolution, the width can be varied between 0.05 and 0.5 mm.

The X-rays diffracted by the crystal are detected with a position-sensitive CCD camera. For the present XAS project, a back-illuminated CCD chip with a depletion depth of about 20 μm was employed. This camera consists of 1340 pixels (in the direction of dispersion) and 400 pixels (in the vertical direction) with a pixel size of 20 μm . The diffracted X-rays build a two-dimensional pattern on the CCD surface. Thanks to the energy resolution capability of the CCD, good pixel events can be sorted by setting appropriate charge or energy windows during the pixel reading. To avoid multiple hits on the same pixels, rather short exposure times in the order of 1 s are used. A measurement consists usually of several hundreds or thousands of images depending on the count rate. All filtered images are added and the sum is then projected onto the dispersion axis to get the one-dimensional X-ray position spectrum. The latter is then converted into an energy spectrum

via the calibration procedure (see Subsect. II.4.1).

II.2.2 XAS setup

XAS measurements are performed in the transmission mode (see Sect. I.1.3). The sample is placed either between the X-ray tube and the crystal, e.g., in front of the slit, or between the crystal and the detector, e.g., in front of the detector (see Fig.II.4). The X-ray tube is oriented so that the center of the electron beam spot on the anode, the center of the slit and the center of the crystal are aligned along the direction determined by the Bragg angle corresponding to the measured absorption edge. When the sample is placed in front of the slit, the Bremsstrahlung from the X-ray tube passes first through the sample and then the transmitted radiation is analyzed by the crystal. When the sample is placed in front of the detector, the Bremsstrahlung is first "monochromatized" by the crystal and then the fraction of the diffracted radiation which is transmitted through the absorber is detected by the CCD. Note that in both cases the transmitted intensity $I(E)$ of the Bremsstrahlung X-rays belonging to the energy range selected by the crystal is measured in a straightforward way by the CCD and there is no need to vary any element of the spectrometer (scanless measurement).

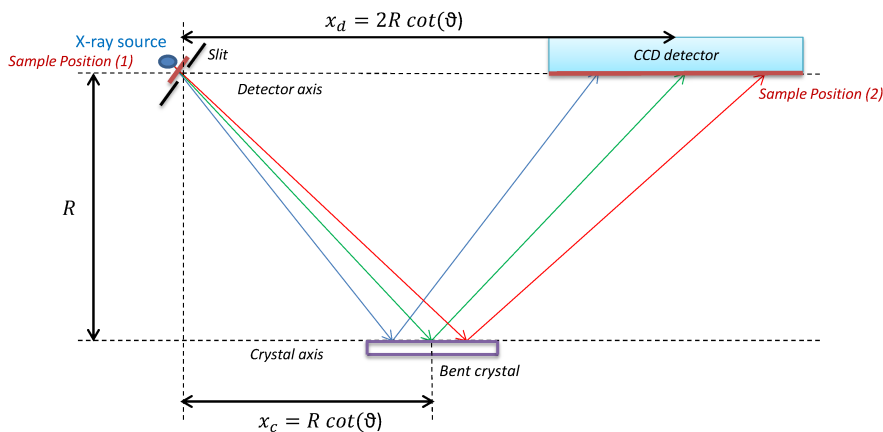


Figure II.4 – Von Hamos setup for laboratory-based XAS measurements. The sample can be placed either at position (1) (in front of the slit) or at position (2) (in front of the CCD detector). The crystal and detector positions are set according to the Bragg law

The alignment of the X-ray tube that depends on the Bragg angle is realized by rotating the flange supporting the tube by an angle φ around a vertical axis passing

through the flange center. As the tube is not coaxial with the flange, an additional rotation of the X-ray tube around its axis by an angle γ is required to align the normal to the center of the X-ray tube window on the slit-crystal direction (see Fig. II.5). The angle γ is indeed equal to zero only when the straight line joining the crystal and slit centers passes through the center of the flange. According to the schematic drawing presented in Fig. II.6, this condition is fulfilled for:

$$\vartheta = \text{Arctan} \left[\frac{b}{d} \right] = \text{Arctan} \left[\frac{2.2[\text{cm}]}{2.5[\text{cm}]} \right] = 41.3^\circ. \quad (\text{II.5})$$

For Bragg angles $\vartheta \neq 41.3^\circ$, γ reads:

$$\gamma = \text{Arcsin} \left[\frac{a \cdot \cos(\vartheta)}{c} \right], \quad (\text{II.6})$$

where $c = 4.5$ cm and the length a is given by:

$$a = d \cdot \tan(\vartheta) - b. \quad (\text{II.7})$$

From the two above equations one sees that $\gamma > 0$ (anti-clockwise rotation of the tube) for $\vartheta > 41.3^\circ$ and $\gamma < 0$ (clockwise rotation of the tube) for $\vartheta < 41.3^\circ$. Finally, as shown in Fig. II.6, the angle φ can be written as:

$$\varphi = 90^\circ + \vartheta + \gamma. \quad (\text{II.8})$$

Note that in the standard operation of the von Hamos spectrometer (XES measurements) the X-ray tube is positioned at $\varphi = \gamma = 0$.

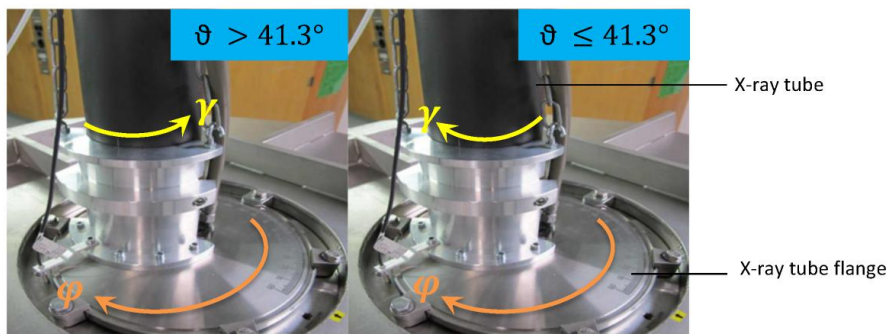


Figure II.5 – Rotary flange for the angular alignment of the X-ray tube with the angles φ and γ .

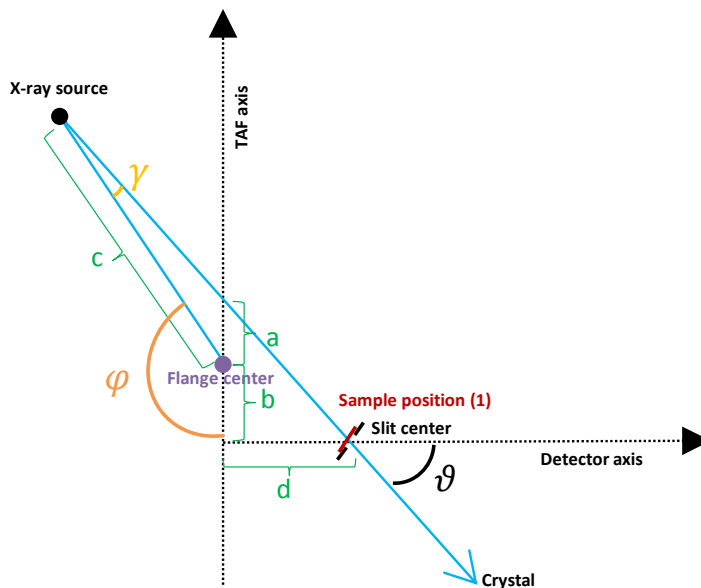


Figure II.6 – Schematic illustration of the angles φ , γ and ϑ for the case $\vartheta \geq 41.3$ deg.

The measurement of a XAS spectrum is realized in the following way: first the crystal and detector are positioned according to the Bragg angle corresponding to the absorption edge of interest using the equations II.1, II.2 and II.3. The slit is set perpendicularly to the direction defined by the Bragg angle via the stepping motor of the TAF axis (see equation II.4) and the X-ray tube is aligned according to the above mentioned procedure (see equations II.6, II.7 and II.8). The intensity $I_0(E)$ of the Bremsstrahlung corresponding to the selected energy region is measured and then the measurement is repeated, using exactly the same positions for the crystal, detector and slit as well as the same orientation, high-voltage and intensity of the X-ray tube, but this time the sample to be analysed is inserted in front of the slit or in front of the CCD detector. This second measurement provides the intensity $I(E)$. The absorption coefficient $\mu(E)$ is then calculated, using equation I.4. For illustration, the intensities $I_0(E)$ and $I(E)$ and the resulting absorption coefficient $\mu(E)$ are depicted for the K-edge of Ti in Fig. II.7. The spectra were calibrated in energy from measurements of the $K\alpha_1$ X-ray lines of Ti and V, using the values reported in Ref. [5] for the energies of these transitions.

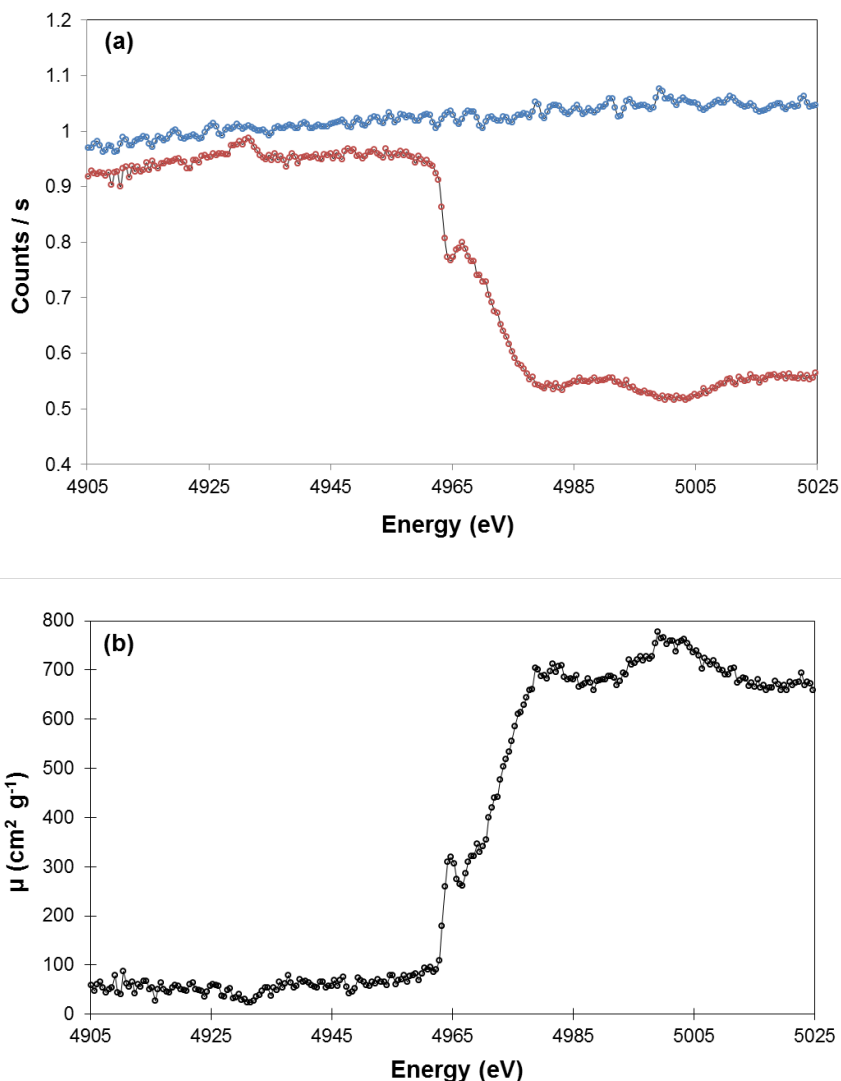


Figure II.7 – (a) Measured incident (open blue circles) and transmitted (open red circles) photon intensities around the K-edge of Ti. (b) Total absorption coefficient $\mu(E)$ deduced from (a). The sample thickness was $2.07 \mu\text{m}$ and the X-ray tube (Cr anode) was operated at $10 \text{ kV} \times 10 \text{ mA}$. The measurement was performed using a Si(220) crystal and the sample was placed in front of the slit (width of 0.2 mm).

II.2.3 Optimization of the setup parameters

In order to probe the sensitivity of the setup to different parameters and to optimize the latter, several test-measurements concerning the sample location, sample thickness, high voltage of the X-ray tube and choice of the crystal were performed. All measurements focused on the K-absorption edge of metallic Cu and they were made using a Cr X-ray tube and a slit width of 0.2 mm .

Sample location

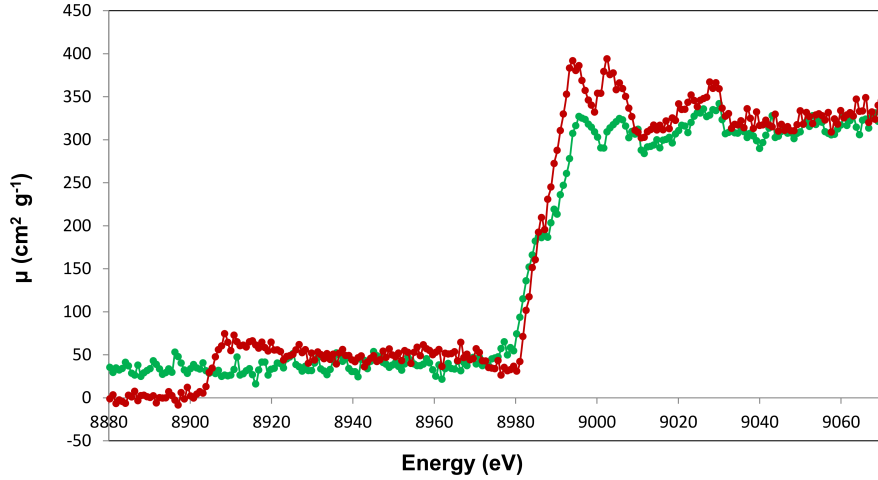


Figure II.8 – Comparison between the Cu K-edge absorption spectra measured with a 2.91 μm thick metallic foil placed in front of the slit (green curve) and in front of the CCD (red curve). Both spectra were measured with a $\text{SiO}_2(2\bar{2}3)$ crystal and the X-ray tube was operated at 15 kV \times 15 mA.

As mentioned before, the sample can be placed either in front of the slit or in front of the detector. In the latter case, the dimensions of the sample should be large enough to cover the CCD surface and the thickness should be uniform to avoid a fake modulation of the transmitted intensity. In addition, as the Bragg angle varies continuously along the dispersion axis of the CCD, the thickness h of the sample can no longer be considered as constant and has to be replaced by $h/\sin(\vartheta)$ in equation I.4. A further source of possible systematic error when the sample is placed in front of the CCD is the fluorescence produced in the right hand part of the sample which is irradiated by diffracted photons having an energy bigger than the absorption edge. As the sample is lying just in front the detector, this fluorescence is collected within a big solid angle and might not be completely eliminated by the energy window set on the CCD to sort good pixel events. This fluorescence signal increases the transmitted intensity, which leads to a too small value of the absorption coefficient. This problem is not encountered when the sample is placed in front of the slit because, in this case, the fluorescence lines are filtered by the crystal. For all these reasons, all XAS measurements discussed hereafter (see Sect. II.3) were performed with the sample in front of the slit.

To illustrate the above discussion, the XAS spectra of a 2.91 μm thick Cu foil

placed in front of the slit and in front of the CCD are presented in Fig. II.8. The variation of the sample thickness resulting from the change of the Bragg angle along the horizontal axis of the CCD was considered in the second spectrum (sample in front of the CCD). The drop of the absorption coefficient observed below 8910 eV (red curve) is due to the fact that the length of the foil in the direction of dispersion (about 24 mm) was smaller than the CCD length (27 mm). A further more important difference between the two spectra concerns the pre-edge structure which is not seen in the measurement performed with the foil in front of the CCD. The pre-edge structure is due to the resonant excitation of 1s electrons into the 3d + 4s hybridized levels. When the foil is placed in front of the CCD, the increase of $\mu(E)$ arising from this resonant excitation is canceled by a simultaneous fake diminution of the absorption coefficient due to the $K\beta_5$ fluorescence (4d-1s transition) produced in the sample. One can also see that between the edge and about 8930 eV the values of the total absorption coefficient $\mu(E)$ obtained with the foil placed in front of the CCD (red curve) are somewhat bigger, whereas above 8930 eV the two XAS spectra are again overlapping. This might indicate some local inhomogeneity of the foil thickness. On the other hand, it seems that in this case the contamination of the transmitted intensity by the foil fluorescence is negligible, the $K\alpha$ and $K\beta$ fluorescence lines from the absorber being eliminated by the energy window set on the CCD to sort good events.

Sample thickness

To probe the influence of the sample thickness, the XAS spectrum of Cu around the K-edge was measured using three foils whose thicknesses were 2.91 μm , 10.21 μm and 20.07 μm , respectively. The results are depicted in Fig. II.9. According to Ref. [11], the sample thickness should fulfill the condition $\mu \cdot \rho \cdot h \leq 1$. For the thinnest sample, this condition is satisfied ($\mu \cdot \rho \cdot h \cong 0.7$), but not for the thicker ones ($\mu \cdot \rho \cdot h \cong 2.5$ and $\mu \cdot \rho \cdot h \cong 5.0$, respectively). It is thus not surprising that the XANES oscillations are less pronounced in the spectrum corresponding to the 10.21 μm thick sample and almost invisible in the XAS spectrum measured with the 20.07 μm thick sample. Depending on the sample thickness, the XANES oscillations are indeed more or less smeared out by the effects discussed in [11]. In addition, as shown, the absorption coefficients $\mu(E)$ above the edge derived from the thicker samples' measurements are smaller by about 15% and 30%, respectively, than the one of the thinnest sample. The "hole" around 8905 eV which can be

seen in the XAS spectra of the two thicker samples is due to the $K\beta_{1,3}$ X-ray line produced in the sample and diffracted by the crystal. This fluorescence intensity increases fakeley the transmitted intensity, which results into a "negative line" in the absorption spectrum.

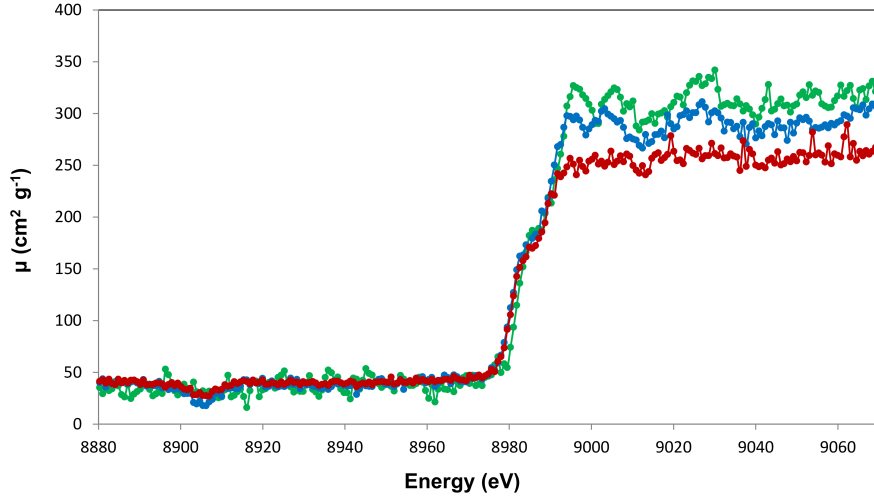


Figure II.9 – Comparison between the Cu K-edge absorption spectra measured with samples having thicknesses of 2.91 μm (green curve), 10.21 μm (blue curve) and 20.07 μm (red curve). All three spectra were measured with the sample placed in front of the slit, a high voltage of 15 kV and the $\text{SiO}_2(2\bar{2}3)$ crystal.

X-ray tube high voltage

According to equation I.9, the power of the Bremsstrahlung emitted by an X-ray tube increases quadratically with the high voltage applied to the tube. To get XAS spectra with a good statistics in reasonable acquisition times, it could seem logical to operate the X-ray tube at the highest possible voltage. However, the XAS spectrum might be then contaminated by X-rays diffracted by the crystal at higher orders and having thus energies 2 or even 3 times bigger than the measured edge energy. These "upper harmonics" X-rays, which are not fully eliminated by the energy window set on the CCD, falsify the XAS data because their absorption by the sample is smaller and not affected by the edge. To obtain reliable and precise absorption coefficients $\mu(E)$, it is therefore preferable to chose a high-voltage U so that $e \cdot U \leq 2 \cdot E_{\text{edge}}$ and to collect the data in longer acquisition times.

The high voltage effect is illustrated in Fig. II.10 showing the K-edge absorption spectra of Cu measured with the Cr X-ray tube operated at 15 kV and 45 kV,

respectively. The measurements were performed with the 2.91 μm -thick foil placed in front of the slit and the $\text{SiO}_2(2\bar{2}3)$ crystal. As shown, the absorption spectrum measured at 45 kV (red curve) does not give correct absorption coefficients. The latter are indeed found to be too small above the absorption edge as a result of the presence of intruder photons of higher energies in the measured $I_0(E)$ and $I(E)$ spectra. It can be also noted that the "negative" imprint of the $\text{K}\beta_{1,3}$ X-ray line at 8905 eV is more pronounced in the spectrum measured at 45 kV, as expected.

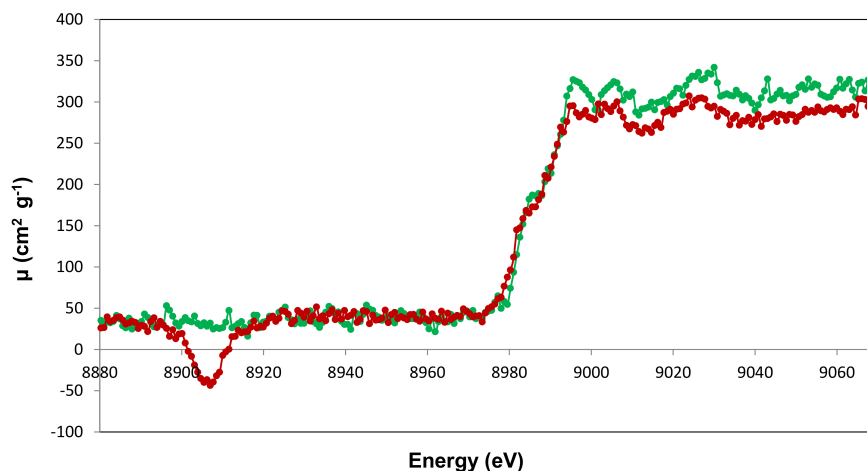


Figure II.10 – Comparison between the Cu K-edge spectra measured at 15 kV \times 15 mA (green curve) and 45 kV \times 15 mA (red curve) using a $\text{SiO}_2(2\bar{2}3)$ crystal. The 2.91 μm thick Cu foil was placed in front of the slit.

Choosing the right crystal

In order to probe the effects of the chosen crystal on the shape of the XAS spectra, the Cu K absorption edge was measured with three different crystals, namely $\text{SiO}_2(2\bar{2}3)$, $\text{Si}(333)$ and $\text{Ge}(440)$ (see Table II.2). For these measurements, the 2.91 μm thick Cu foil was placed in front of the slit and the X-ray tube was operated at 15 kV \times 15 mA. The corresponding XAS spectra are presented in Fig. II.11.

It can be seen that the absorption coefficients determined with the $\text{Si}(333)$ and $\text{Ge}(440)$ crystals differ somewhat from those obtained with the $\text{SiO}_2(2\bar{2}3)$ crystal. For $\text{Si}(333)$ the tiny differences below the edge are not significant, whereas the about 7% smaller absorption coefficients above the edge are probably due to a weak contamination of $I_0(E)$ and to a smaller extent $I(E)$ by 3 keV photons. Bremsstrahlung photons having an energy of about 3 keV are indeed also diffracted

by the crystal but in first order. Considering that the reflectivity of the Si(111) at 3 keV is about 10 times bigger than the reflectivity of the Si(333) at 9 keV (rounded value of the Cu K-edge energy), that the efficiency of the CCD is 5 times bigger at 3 keV than at 9 keV [154] and that the number of 3 keV Bremsstrahlung photons emitted by the Cr tube operated at 15 kV is about 3 times smaller than the one of 9 keV photons, the number of 3 keV photons is more than 15 times higher than the one of 9 keV photons. As a consequence, the fraction of 3 keV photons which are not eliminated by the CCD energy window or make triple hits on single CCD pixels (in this case the charge deposited on the pixels is equal to that of 9 keV photons) is not completely negligible. However, as the absorption coefficient of Cu for 3 keV photons is high, this contamination affects predominantly I_0 . This fake excess of intensity of I_0 leads to a diminution of the absorption coefficients. The calculations show that the diminution is about three times bigger above the edge than below, as observed. Note that the reflectivity of the Si(111) crystal in second order of diffraction is zero so that there is no additional contamination by 6 keV photons.

For the Ge(440) crystal, the deviations are more pronounced. Actually the absorption coefficients are too big below the edge (63 instead of 45 cm²/g) and too small above the edge (262 instead of 309 cm²/g). The explanation is similar to the one given for the Si(333) crystal but in this case the excess of intensity is due predominantly to the fluorescence of the crystal itself. The K X-rays of Ge produced by the incoming Bremsstrahlung radiation are indeed not fully eliminated by the energy window set on the CCD. This fluorescence effect is not observed with the SiO₂ and Si crystals because the average energies of the O and Si K X-ray lines (0.5 and 1.7 keV, respectively) are far apart from the K-edge of Cu (about 9 keV), whereas the energies of the Ge K X-rays (about 10 keV) are significantly closer to it.

The excess of intensity due to the fluorescence of the crystal can be estimated from the following equations derived from the relation I.4:

$$\mu(E_b) = \frac{\ln \left[\frac{I_0 - x}{I_b - x \cdot x} \right]}{\rho \cdot h} \quad (\text{II.9})$$

and

$$\mu(E_a) = \frac{\ln \left[\frac{I_0 - x}{I_a - x \cdot x} \right]}{\rho \cdot h}, \quad (\text{II.10})$$

where $\mu(E_b)$ and $\mu(E_a)$ and I_b and I_a represent the total absorption coefficients of Cu and the intensities of the transmitted beams just below and above the K-edge,

respectively, I_0 stands for the average intensity of the incoming beam and x for the contamination fraction of the latter by fluorescence photons, while χ is a constant given by:

$$\chi = e^{-\mu_{av} \cdot \rho \cdot h}, \quad (\text{II.11})$$

where μ_{av} represents the absorption coefficient of Cu averaged over the energy range of the incoming radiation. Assuming that the edge lies in the center of the energy range and that the incoming radiation is nearly constant, the parameter χ reads:

$$\chi = \frac{e^{-\mu(E_b) \cdot \rho \cdot h} + e^{-\mu(E_a) \cdot \rho \cdot h}}{2}. \quad (\text{II.12})$$

The overdetermined system of equations [II.9,II.10] can be solved by means of a least-squares-fitting method, i.e., by solving the equation:

$$\frac{d}{dx} \left\{ \left[\ln \left(\frac{I_0 - x}{I_b - \chi \cdot x} \right) - \rho \cdot h \cdot \mu_b \right]^2 + \left[\ln \left(\frac{I_0 - x}{I_a - \chi \cdot x} \right) - \rho \cdot h \cdot \mu_a \right]^2 \right\} = 0. \quad (\text{II.13})$$

Inserting in the latter equation the values $I_0=0.545 \text{ s}^{-1}$, $I_b=0.462 \text{ s}^{-1}$ and $I_a=0.275 \text{ s}^{-1}$ obtained from the Ge(440) measurements, the values $\mu(E_b)=45 \text{ cm}^2/\text{g}$ and $\mu(E_a)=309 \text{ cm}^2/\text{g}$ deduced from the XAS spectrum measured with the $\text{SiO}_2(2\bar{2}3)$ crystal and the result $\chi=0.688$ provided by Eq. II.12, a value of 0.134 s^{-1} is found for the excess intensity x . Using this result in equations II.9 and II.10, values which are consistent within the quoted errors with the $\text{SiO}_2(2\bar{2}3)$ data are retrieved for the total absorption coefficients below and above the edge, namely $\mu(E_b)=38 \text{ cm}^2/\text{g}$ and $\mu(E_a)=305 \text{ cm}^2/\text{g}$.

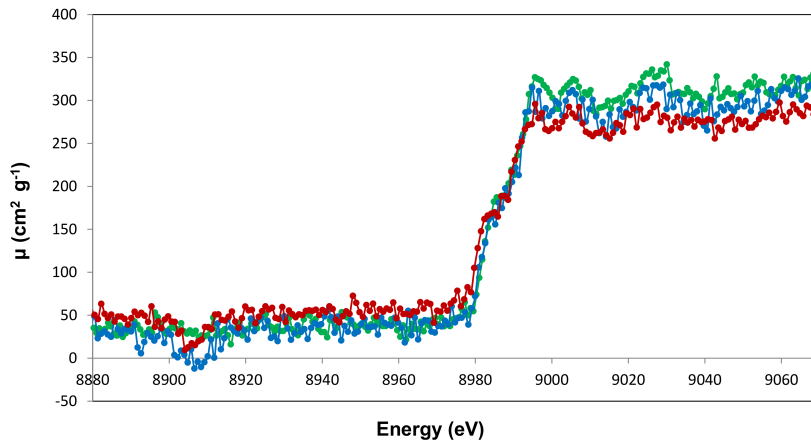


Figure II.11 – Comparison between the Cu K-edge absorption spectra measured with a $\text{SiO}_2(2\bar{2}3)$ (green curve), $\text{Si}(333)$ (blue curve) and a Ge(440) crystal (red curve).

II.3 Measurements

The present XAS setup based on the von Hamos spectrometer of Fribourg was employed to measure the absorption spectra around the K edges of Ti, Fe, Cu and Ge and around the L₃-edges of Mo, Ag, Hf, Ta and Pt. For Mo and Ag, the XAS spectra around the L₂- and L₁-edges were also measured. All measurements were performed with a slit width of 0.2 mm. More information about the employed samples, crystals and X-ray tube operational characteristics are given in the Subsect. II.3.1.

II.3.1 Samples, crystals and X-ray tubes

The samples consisted of thin metallic foils with elemental purities higher than 99.99% which were provided by Goodfellow [155]. All samples were weighted and their dimensions were measured to get accurate thicknesses in [mg/cm²]. Divided the latter by the sample density, the effective thicknesses in [μm] were obtained. In these calculations, it was assumed that the sample surface oxidation was negligible. The weights, dimensions, densities and thicknesses of the samples are listed in Table II.1. The relative uncertainty on the sample thickness was estimated to be about 2.5%. This value includes a relative uncertainty of 2% for possible thickness inhomogeneities.

Table II.1 – Weights, dimensions, densities and thicknesses of the measured samples. The notation 2.07(5) means 2.07±0.05.

Element / Edge	Mass [mg]	Area [mm ²]	Density [g/cm ³]	Thickness [μm]
Z=22, Ti / K	5.87	25.0 × 25.0	4.540	2.07(5)
Z=26, Fe / K	10.13	25.0 × 25.0	7.874	2.06(5)
Z=29, Cu / K	16.00	25.0 × 24.5	8.960	2.91(7)
Z=32, Ge / K	6.67	25.0 × 25.0	5.323	2.00(5)
Z=42, Mo / L _{1,2,3}	4.61	14.6 × 24.9	10.22	1.24(3)
Z=47, Ag / L _{1,2,3}	5.02	25.8 × 15.8	10.50	1.17(3)
Z=72, Hf / L ₃	23.40	25.0 × 24.8	13.31	2.84(7)
Z=73, Ta / L ₃	12.80	25.0 × 15.0	16.65	2.05(5)
Z=78, Pt / L ₃	4.70	16.0 × 7.0	21.45	1.96(5)

The measurements were performed with four different crystals whose specifications are given in Table II.2. The energy range covered by each crystal in first order of diffraction was determined by inserting in the Bragg law the maximum ($\approx 61.1^\circ$) and minimum ($\approx 24.4^\circ$) angles at which the von Hamos spectrometer of Fribourg can be operated. For higher diffraction orders n , the minimum and maximum energies are obtained by multiplying the values reported in Table II.2 by n .

Table II.2 – Dimensions and double interplanar spacing $2d_{hkl}$ of the crystals used in the XAS measurements. The energy range covered by each crystal in first order of diffraction is also indicated.

Crystal	Dimensions [mm ³]	$2d_{hkl}$ [Å]	Energy range [keV]
Si(111)	100×50×0.3	6.271	2.258-4.788
Ge(220)	100×50×0.3	4.000	3.539-7.505
Si(220)	100×50×0.3	3.840	3.687-7.818
SiO ₂ (2 $\bar{2}$ 3)	100×50×0.4	2.750	5.149-10.919

The specific conditions at which the K and L XAS spectra were collected are summarized in Table II.3. Note that the notation Si(333) is equivalent to Si(111) in third order of diffraction. Similarly, Si(440) and Ge(440) are equivalent to Si(220) and Ge(220) in second order of diffraction.

Table II.3 – Experimental parameters used for the measurements of the K and L-edges. The energy calibration of the spectra was carried out by measuring the reference X-ray lines listed in the fourth column.

Edge	X-ray tube (U×i)	Crystal	Calibration ^a	Acq. time [s]
Ti K	Cr (10 kV×10mA)	Si(220)	V K _{α₁} (4952.22) Cr K _{α₁} (5414.80)	I ₀ (E): 8'000 I(E): 30'000
Fe K	Cr (11 kV×11mA)	SiO ₂ (2 $\bar{2}$ 3)	Co K _{α₁} (6930.38) Ni K _{α₁} (7478.25)	I ₀ (E): 10'000 I(E): 40'000
Cu K	Cr (15 kV×15mA)	SiO ₂ (2 $\bar{2}$ 3)	Zn K _{α₁} (8638.91) Ge K _{α₁} (9886.52)	I ₀ (E): 8'000 I(E): 30'000
Ge K	Cr (20 kV×20mA)	Si(440)	Se K _{α₁} (11222.52)	I ₀ (E): 8'000 I(E): 30'000
Mo L ₃	Cu (4 kV×9 mA)	Si(111)	Cl K _{α₁} (2622.44) K K _{α₁} (3313.95)	I ₀ (E): 40'000 I(E): 60'000
Mo L ₂	Cu (4 kV×9 mA)	Si(111)	Cl K _{α₁} (2622.44) K K _{α₁} (3313.95)	I ₀ (E): 17'000 I(E): 42'200
Mo L ₁	Cu (4 kV×9 mA)	Si(111)	Cl K _{α₁} (2622.44) K K _{α₁} (3313.95)	I ₀ (E): 40'000 I(E): 60'000
Ag L ₃	Cu (6 kV×10 mA)	Si(111)	K K _{α₁} (3313.95) Sc K _{α₁} (4090.73)	I ₀ (E): 20'000 I(E): 60'000
Ag L ₂	Cu (6 kV×10 mA)	Si(111)	K K _{α₁} (3313.95) Sc K _{α₁} (4090.73)	I ₀ (E): 16'000 I(E): 40'000
Ag L ₁	Cu (6 kV×10 mA)	Si(111)	K K _{α₁} (3313.95) Sc K _{α₁} (4090.73)	I ₀ (E): 16'000 I(E): 50'000
Hf L ₃	Cu (15 kV×20 mA)	Si(333)	Zn K _{α₁} (8638.91) Ge K _{α₁} (9886.52)	I ₀ (E): 13'000 I(E): 30'000
Ta L ₃	Cr (12 kV×12 mA)	Ge(440)	Ti K _{α₁} (4510.90) ^b Ge K _{α₁} (9886.52)	I ₀ (E): 6'000 I(E): 30'000
Pt, L ₃	Cr (20 kV×25 mA)	Ge(440)	Se K _{α₁} (11222.52)	I ₀ (E): 8'000 I(E): 30'000

^aThe reference energies are given in [eV]. They were taken from Deslattes *et al.* [5].

^bMeasured in 1st order of diffraction, i.e., equivalent to 9021.80 eV in 2nd order.

II.3.2 K-edges of Ti, Fe, Cu and Ge

The K-edge XAS measurements of Ti, Fe, Cu and Ge are presented in Figs. II.12, II.13, II.14 and II.15, respectively. Present K-edge energies were determined from the first inflection points of the absorption spectra. The absorption coefficient jumps are compared to the values quoted in the NIST-XCOM database [156]. Note that the XCOM data do not take into account the processes leading to the XANES and EXAFS structures. For this reason, the XCOM plots over narrow energy domains correspond to quasi-straight lines with slightly negative slopes and sudden jumps of the absorption coefficient to bigger values at the K-edge energies. The first peaks (mid-edge shoulders) observed in the absorption spectra of Ti (at 4965 eV), Fe (at 7114 eV) and Cu (at 8983 eV) correspond to the "white lines". They are due to the large unoccupancies of 3d states in metals [157]. It can be noted that this peak does not appear in the XAS spectrum of Ge because the 3d level is filled for this element.

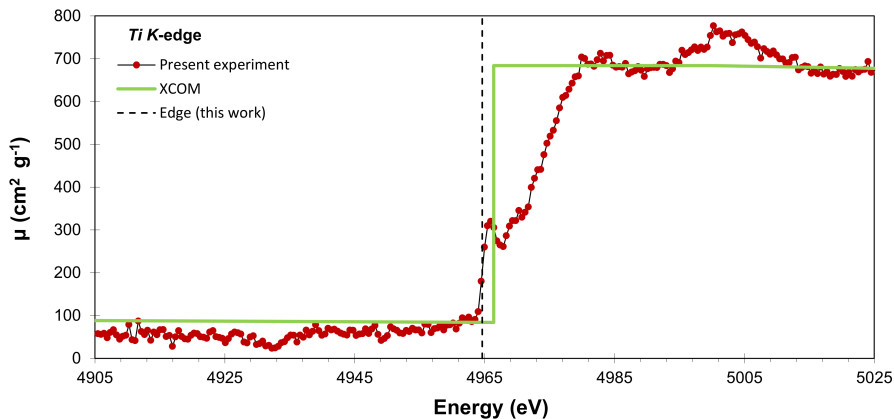


Figure II.12 – K-edge XAS spectrum of Ti. Present data are represented by the red full circles. The green solid line corresponds to the absorption coefficient $\mu(E)$ from the XCOM database [156]. The present edge energy determined from the first inflection point of the XAS curve is indicated by the vertical dashed line. The specific parameters employed for the measurement (sample thickness, crystal, voltage and current of the X-ray tube, calibration lines) are indicated in Tables II.1, II.2 and II.3.

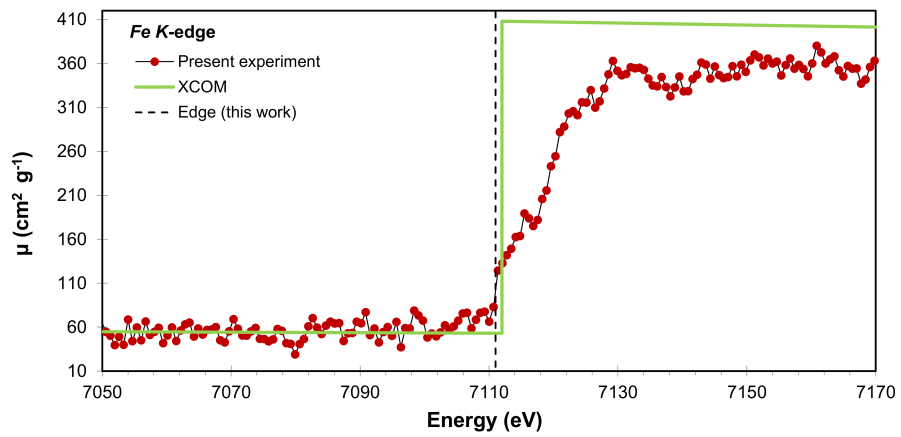


Figure II.13 – Same as Fig. II.12 but for Fe.

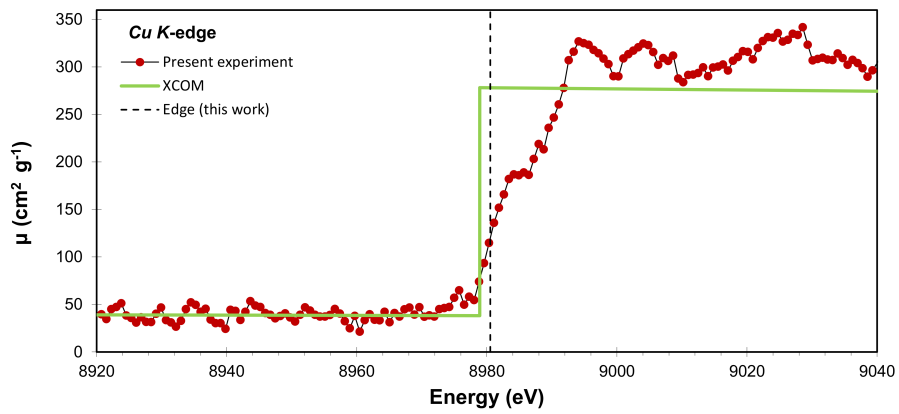


Figure II.14 – Same as Fig. II.12 but for Cu.

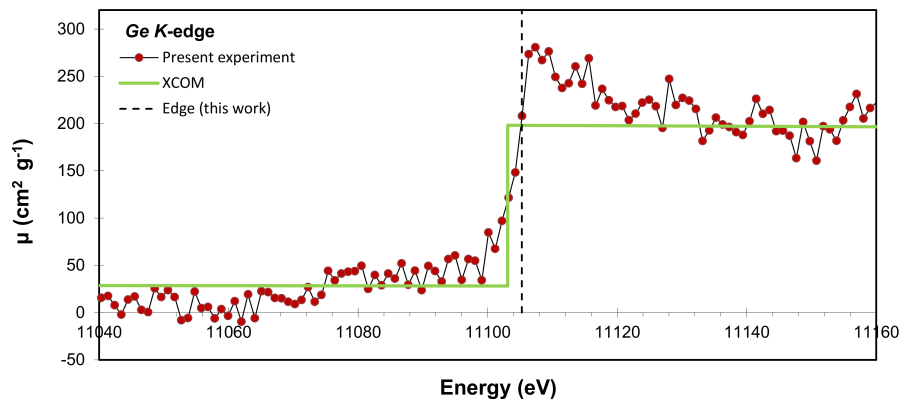


Figure II.15 – Same as Fig. II.12 but for Ge.

II.3.3 L_3 -edges of Hf, Ta and Pt

The XAS L_3 -edge spectra of Hf, Ta and Pt are presented in Figs. II.16, II.17 and II.18, respectively. As shown the L_3 -edge spectra evince strong "white lines". The latter are due to the $2p \rightarrow 5d$ dipole transitions exciting $2p$ electrons into the unfilled $5d$ level [158]. As the $2p \rightarrow nd$ excitation probability grows with the number of vacancies in the $5d$ level, the "white line" is stronger for Hf (eight $5d$ vacancies) than for Ta (seven $5d$ vacancies) and almost vanishing for Pt (a single $5d$ vacancy).

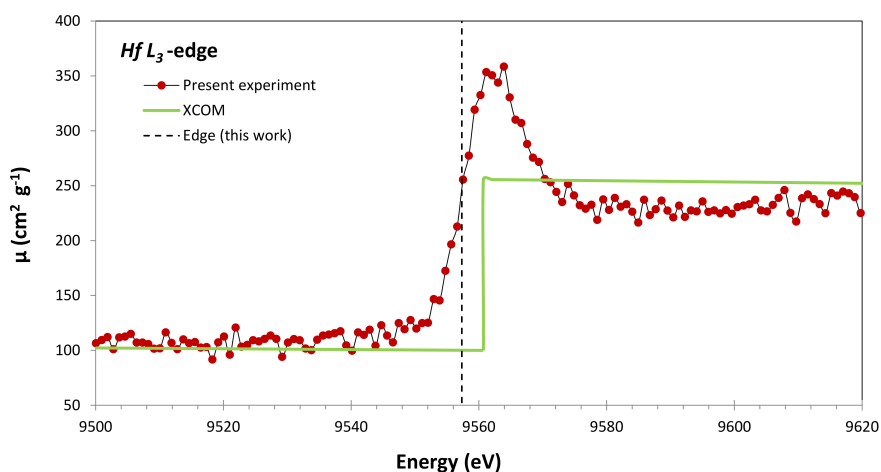


Figure II.16 – L_3 -edge XAS spectrum of Hf. Present data are represented by the red full circles. The green step-like curve corresponds to the XCOM data. The present edge energy (vertical dash line) is also indicated. The specific parameters of the setup corresponding to this measurement are given in Tables II.1, II.2 and II.3.

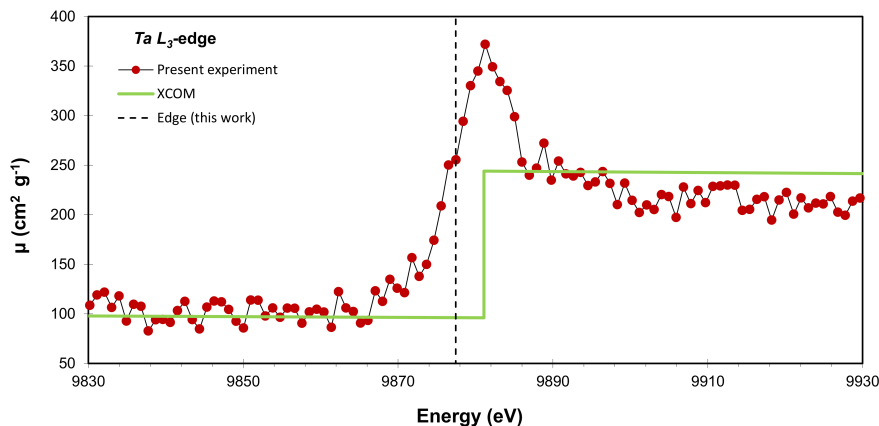


Figure II.17 – Same as Fig. II.16 but for Ta.

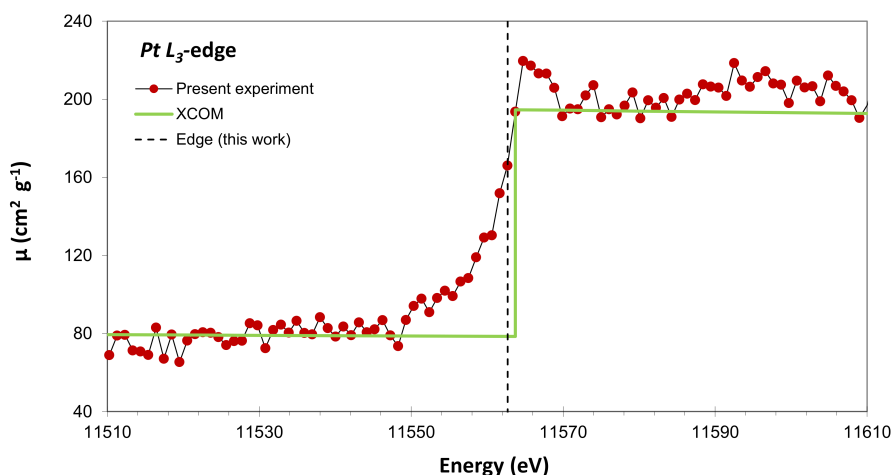


Figure II.18 – Same as Fig. II.16 but for Pt.

II.3.4 L₁, L₂ and L₃-edges of Mo and Ag

To probe the sensitivity of the experimental XAS setup, the less pronounced L₁- and L₂-edges were also measured but only for Mo and Ag. The corresponding XAS spectra are presented in Figs. II.19 and II.20. For comparison the L₃ edges of the same elements are also plotted. As shown in Fig. II.19, rather intense "white lines" are observed in the L₂ and L₃ absorption spectra of Mo but not in the L₁ one. This is due to the fact that the "white lines" correspond to the excitation of 2p electrons with an angular momentum $\ell = 1$ to the unfilled 4d ($\ell=2$) level and, to a smaller extent, the 5s ($\ell=0$) level. Such excitations are indeed allowed within the electric dipole (E1) selection rules ($\Delta\ell = \pm 1$, $\Delta j = 0, \pm 1$) [159], whereas the excitation of 3s ($\ell=0$) electrons to the 4d or 5s level is forbidden by the E1 selection rules, since in this case $\Delta\ell = 2$ or $\Delta\ell = 0$. Actually, "white lines" appear in the L_{2,3} XAS spectra of early transition metals of each transition series [160].

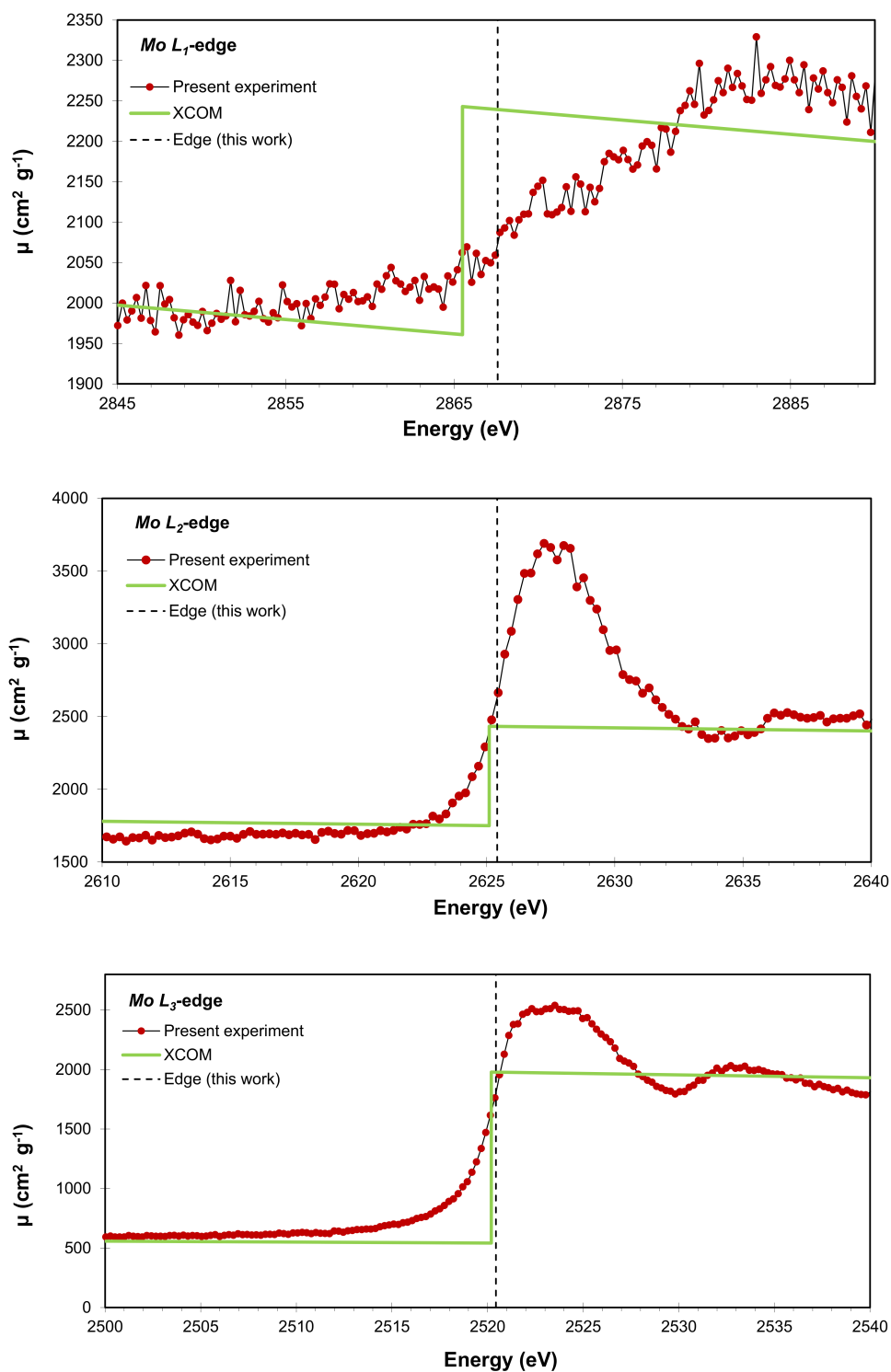


Figure II.19 – L_1 , L_2 and L_3 absorption edges of Mo (from top to bottom). Present data (red full circles) are compared to the absorption coefficient $\mu(E)$ from XCOM (green solid line). Present edge energies are represented by vertical dashed lines. The experimental parameters employed in this measurement can be found in Tables II.1, II.2 and II.3.

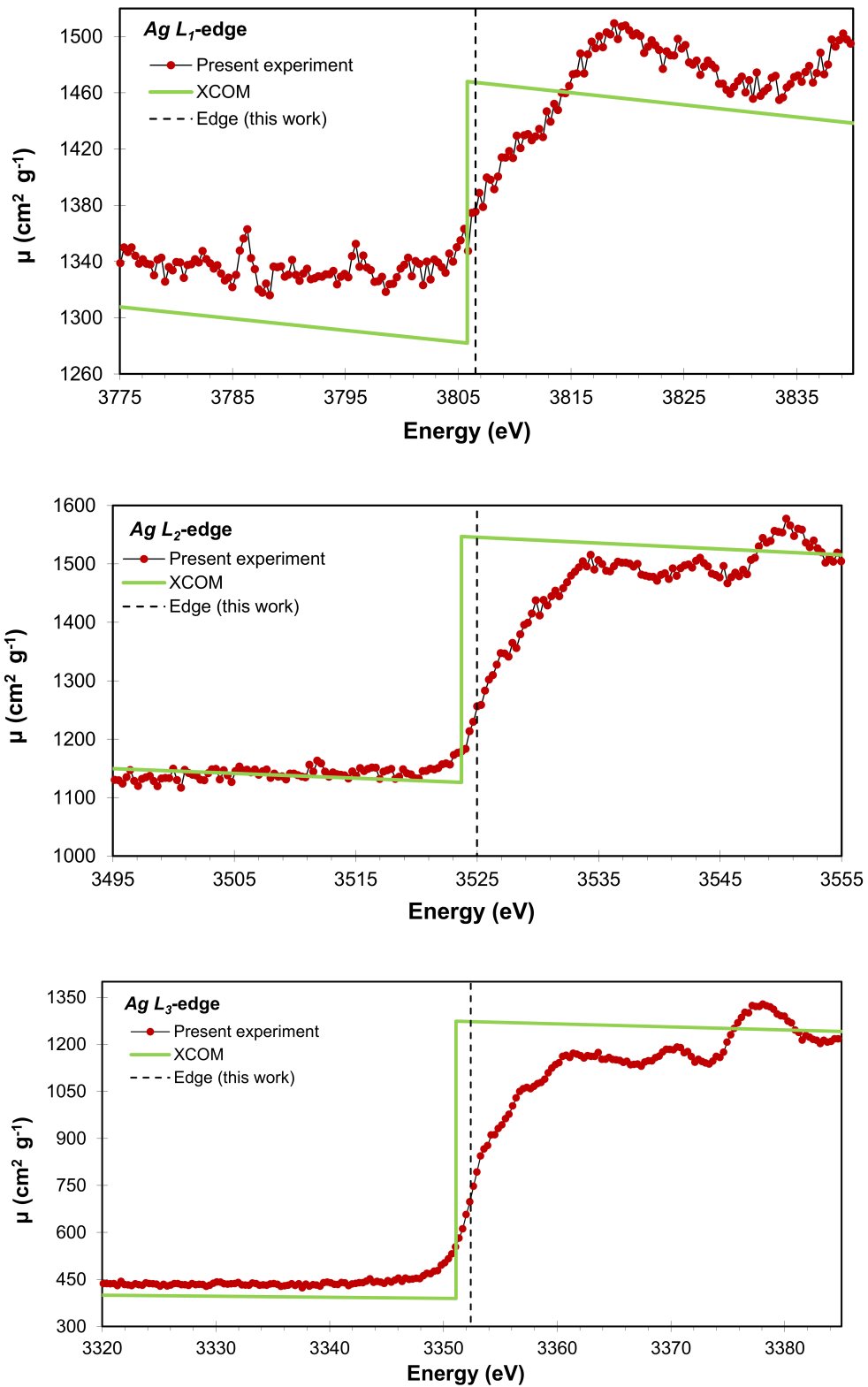


Figure II.20 – Same as Fig. II.19 but for Ag.

For Ag, the "white lines" in the L_2 and L_3 XAS spectra are hardly visible because

for this element the 4d level is filled and the 2p-5s excitation is significantly less probable than the 2p-4d one.

II.4 Data analysis

II.4.1 Energy calibration

The one-dimensional position spectrum resulting from the projection on the dispersion axis of the sum of the filtered CCD images can be converted into an energy spectrum by calculating the Bragg angle ϑ_i associated to the pixel number i of the CCD ($i= 1, \dots, 1340$) and by deriving then from this angle the corresponding energy E_i via the Bragg law. The angle ϑ_i corresponding to the pixel position x_i along the dispersion axis is given by:

$$\vartheta_i = \text{Atan} \left[\frac{2 \cdot R[\text{cm}]}{x_d + (i - 670) \cdot 20 \cdot 10^{-4}[\text{cm}]} \right], \quad (\text{II.14})$$

where R represents the distance along the direction perpendicular to the dispersion axis between the crystal surface and the front plane of the CCD camera and x_d the position of the detector center (see equation II.3) or equivalently of the pixel $i=1340/2=670$. The corresponding energy E_i can be then written as:

$$E_i[\text{keV}] = \frac{12.398[\text{keV} \cdot \text{\AA}] \cdot n}{2 \cdot d_{\text{hkl}}[\text{\AA}] \cdot \sin(\vartheta_i)}, \quad (\text{II.15})$$

where n is the diffraction order.

If the CCD front surface is located exactly in the focal plane of the crystal, the distance R entering equation II.14 coincides with the radius of curvature of the crystal. However, the value of R may slightly vary when the crystal and detector are moved along their axis because tiny deviations in the parallelism of the Schnerberger tracks cannot be a-priori excluded. The same holds for the constant d_{hkl} of the crystal occurring in equation II.15. The real value of this constant may indeed slightly differ from the known nominal value. For these reasons, the values of R and d_{hkl} are usually determined by measuring two intense $K\alpha$ X-ray lines whose energies are known accurately and whose corresponding Bragg angles are slightly smaller and bigger than the central Bragg angle of the X-ray spectrum to be calibrated. Such measurements are named energy calibration measurements because they permit to calibrate in energy the position axis of the one-dimensional X-ray

spectra via equations II.14 and II.15. However, when the Bragg angle corresponding to a reference X-ray line is very close to the central Bragg angle of the X-ray spectrum to be calibrated, the energy calibration can be performed using only this close lying reference X-ray line because in this case the energy calibration is almost insensitive to the error on the crystal radius of curvature R . For the calibration in energy of the XAS spectra presented in Sect. II.3, intense $K\alpha_1$ diagram X-ray lines of various metallic elements were used. The measurements were performed using the standard von Hamos geometry (see Sect. II.2.1). For each XAS spectrum, the employed reference X-ray lines are indicated in Table II.3.

II.4.2 Instrumental resolution

The above mentioned energy calibration measurements were also used to determine the instrumental energy resolution of the spectrometer in the energy ranges of interest. As the shape of an X-ray line is Lorentzian and the instrumental response of the spectrometer can be well reproduced by a Gauss function, and because the convolution of a Gauss function with a Lorentz function results into a so-called Voigt function, the measured reference $K\alpha_1$ X-ray lines were fitted with Voigtian profiles. The standard deviation of the Gaussian instrumental response was determined from the fits of the reference X-ray lines, the natural Lorentzian widths of the latter being kept fixed in the fits at the values deduced from the atomic level widths reported by Campbell and Papp [161].

The instrumental broadening of the von Hamos spectrometer originates mainly from the slit width, spatial resolution of the CCD detector, Darwin width and crystal mosaicity. The broadening due to the slit reads:

$$\Gamma_{\text{slit}} = \frac{w_{\text{slit}}}{2R} \cdot \cos(\vartheta) \cdot E, \quad (\text{II.16})$$

where w_{slit} represents the width of the slit, R the radius of curvature of the crystal, ϑ the Bragg angle and E the energy of the measured X-rays. Similarly the broadening resulting from the spatial resolution of the detector is given by:

$$\Gamma_{\text{CCD}} = \frac{w_{\text{pixel}}}{4R} \cdot \sin(2\vartheta) \cdot E, \quad (\text{II.17})$$

where w_{pixel} stands for the size of the CCD pixels in the direction of dispersion. From the relation II.16 one finds for instance that for the K-edge of Cu (energy $E=8980$ eV) measured with the $\text{SiO}_2(2\bar{2}3)$ crystal ($\vartheta = 30.145^\circ$), the relative broadening induced by the slit is $\Delta\Gamma_{\text{slit}}/\Delta w_{\text{slit}}=15.3$ meV/ μm . As the efficiency

of the spectrometer increases with the slit width, a width of 200 μm was chosen for all XAS measurements as a compromise between a high enough energy resolution and an acceptable luminosity. According to equation II.17, for the K-edge of Cu the detector contribution to the instrumental broadening amounts to 0.15 eV only. The 20 μm pixel resolution of the CCD detector was thus not really needed for the XAS measurements and a software binning of five adjacent pixels was performed off-line in order to obtain higher counting rates, the corresponding energy resolution remaining high enough. On the other hand, in the case of the $\text{SiO}_2(2\bar{2}3)$ crystal, the two other contributions are negligibly small. Quartz being indeed a perfect crystal, the mosaicity width can be assumed to be zero, while the Darwin width calculated from the XOP code [162] amounts to only 0.075 eV for unpolarized photons. In the case of the K-edge XAS spectrum of Cu, the experimental broadenings induced by the 200 μm slit width and the 100 μm CCD spatial resolution corresponding to a binning of 5 pixels are thus $\Gamma_{\text{slit}}=3.06$ eV and $\Gamma_{\text{CCD}}=0.77$ eV, respectively. It can be pointed out here that the FWHM energy resolution determined from the fits of the $\text{K}\alpha_1$ X-ray lines of Zn and Ge taken as references for the Cu K-edge measurement was found to be 3.82 eV at this energy, a value which is well in line with the sum of the slit and CCD instrumental broadening contributions.

II.4.3 Determination of the edge energies and absorption coefficients

Edge energies

As mentioned in Sect. I.1.2 there are several different definitions of the edge energy in the literature [5, 6]. In this work the edge energies were associated with the first inflection points of the absorption spectra. The derivative of the function $\mu(E)$ was computed numerically and then fitted with a Gaussian function. For illustration the L_3 absorption spectrum of Mo and the first derivative of the latter are presented in Fig. II.21. The maximum value of the derivative which coincides with the inflection point was determined from the energy corresponding to the centroid of the fitted Gaussian function since for symmetric functions the energy corresponding to the maximum value of the function coincides with the centroid of the latter. The errors on the edge energies quoted in this work correspond thus to the errors given by the fits for the Gaussian centroids but the errors originating

from the energy calibration measurements are included (see Table II.4). It was found that the determination of the inflection point was not really sensitive to the choice of the function employed to fit the derivative $d\mu(E)/dE$. Actually no significant differences could be evinced between the edge energies obtained from the fits of the derivatives performed with Gauss, Lorentz or Voigt functions (see the example of the Cu K-edge below).

An alternative approach was probed which consisted to interpolate the XAS spectrum in the region of the edge with a third degree polynomial:

$$\mu(E) = a_3 \cdot E^3 + a_2 \cdot E^2 + a_1 \cdot E + a_0. \quad (\text{II.18})$$

The inflection point was then determined by solving the following equation:

$$\left[\frac{d^2\mu(E)}{dE^2} \right]_{E=E_{\text{edge}}} = 6a_3 \cdot E_{\text{edge}} + 2a_2 = 0 \Rightarrow E_{\text{edge}} = -\frac{a_2}{3a_3}. \quad (\text{II.19})$$

In this case, the error on the edge energy reads:

$$\Delta E_{\text{edge}} = \pm \sqrt{\left(\frac{\partial E_{\text{edge}}}{\partial a_2} \right)^2 \cdot \Sigma_{22} + \left(\frac{\partial E_{\text{edge}}}{\partial a_3} \right)^2 \cdot \Sigma_{33} + 2 \cdot \frac{\partial E_{\text{edge}}}{\partial a_2} \cdot \frac{\partial E_{\text{edge}}}{\partial a_3} \cdot \Sigma_{23}}, \quad (\text{II.20})$$

where Σ_{22} and Σ_{33} represent the variances of the coefficients a_2 and a_3 , respectively, and Σ_{23} the covariance of the latter. After calculating the partial derivatives, Eq. II.20 becomes:

$$\Delta E_{\text{edge}} = \pm \sqrt{\frac{1}{9a_3^2} \cdot \Sigma_{22} + \frac{a_2^2}{9a_3^4} \cdot \Sigma_{33} - \frac{2a_2}{9a_3^3} \cdot \Sigma_{23}}. \quad (\text{II.21})$$

For example, for the K-edge of Cu, values of 8980.53 ± 0.44 eV, 8980.42 ± 0.42 eV and 8980.58 ± 0.39 eV were found by fitting the derivative of the XAS spectrum with a Gaussian, a Lorentzian and a Voigtian function, respectively. Note that the errors are rather large because no smoothing process was applied to the data before the numerical calculation of the derivative. For comparison, the result obtained with the third degree polynomial is 8980.56 ± 0.17 eV. In this case, the error is about three times smaller because the second derivative was calculated analytically from the polynomial interpolation of the data, which amounts to smoothing the data. However, to err on the safe side, the edge energies were determined from the fits of the first derivatives. As the choice of the fit function was found to be not critical, Gaussian functions were employed for all edges investigated in the present work.

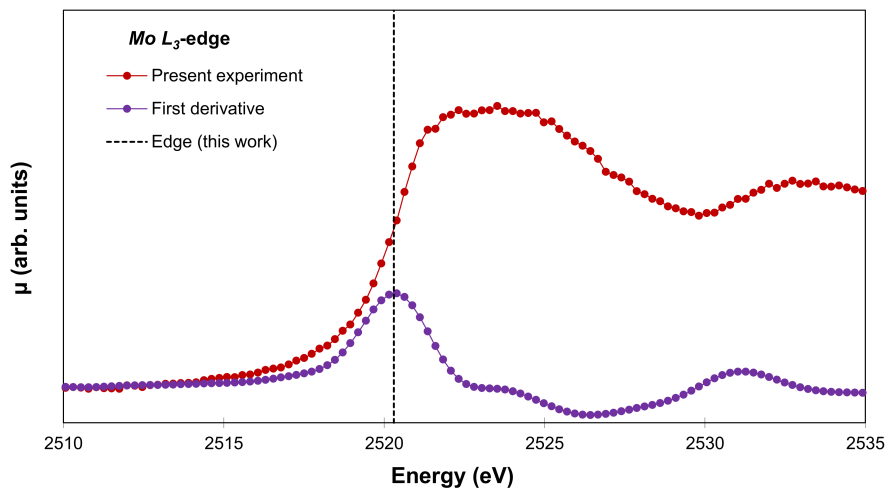


Figure II.21 – Mo L_3 -edge spectrum (red points) and its first derivative (purple points). The vertical dashed line represents the edge energy. The latter was determined from the centroid of the Gaussian used to fit the derivative in the edge region.

Absorption coefficients

The total absorption coefficients $\mu(E)$ were determined from the measured intensities of the incoming (I_0) and transmitted (I) photon beams, using the formula I.4. As in most cases the transmitted intensity $I(E)$ was significantly smaller than the incident intensity $I_0(E)$, the transmission spectra were collected using longer acquisition times than the incident spectra and all spectra were then normalized by the corresponding acquisition times to get $I_0(E)$ and $I(E)$ in counts/s. The observed variation of the incoming beam intensity I_0 with the energy reflects the energy distribution of the Bremsstrahlung emission of the X-ray tube as well as the inhomogeneous intensity of the electron beam spot on the anode of the tube. However, as the experimental setup is exactly the same in the measurements of $I_0(E)$ and $I(E)$, the same variations are observed in the spectrum $I(E)$ and the latter do not affect thus the determination of the absorption coefficient.

On the other hand, it was observed that the intensity of the X-ray tube emission may vary by a few percent between different measurements although the latter are performed with the same X-ray tube voltage and current. With our methodology the intensity spectra $I_0(E)$ and $I(E)$ being not measured simultaneously but consecutively, the absorption coefficients can be affected by this limited reproducibility of the radiation source intensity. For this reason, the latter was included in the

errors' budget of the absorption coefficients (see below).

In the XCOM tables [156], the absorption coefficients are quoted as a function of the photon energy with energy steps of 1 keV between 2 and 6 keV, 2 keV between 6 and 10 keV, 5 keV between 10 and 20 keV and 10 keV above. However, for each edge energy two values are given which correspond to the absorption coefficients just before and after the jump, i.e., to $\mu_b(E_{\text{edge}})=\mu(E_{<}^{\rightarrow}E_{\text{edge}})$ and $\mu_a(E_{\text{edge}})=\mu(E_{>}^{\rightarrow}E_{\text{edge}})$. Thus, for the comparison of the absorption coefficients obtained in the present work with the data from the XCOM database [156], linear functions were fitted to the XAS data below and above the edges, the values $\mu_b(E_{\text{edge}})$ and $\mu_a(E_{\text{edge}})$ reported in Table II.5 being obtained by calculating the values of the two linear functions for $E = E_{\text{edge}}$.

Neglecting the uncertainty on the density of the sample, the error on the absorption coefficient μ reads:

$$\Delta\mu = \pm\sqrt{\sigma_{\text{fit}}^2 + \sigma_{\text{h}}^2 + \sigma_{\text{tube}}^2}, \quad (\text{II.22})$$

where σ_{fit} represents the error from the linear fitting of the data, σ_{h} the error originating from the uncertainty on the sample thickness and σ_{tube} the error accounting for the intensity variation of the X-ray tube between the $I_0(E)$ and $I(E)$ measurements. The error σ_{h} is simply given by:

$$\sigma_{\text{h}} = \frac{\Delta h}{h} \cdot \mu, \quad (\text{II.23})$$

whereas σ_{tube} can be expressed as a function of the parameter ξ representing the variation of the X-ray tube intensity between the $I_0(E)$ and $I(E)$ measurements:

$$I(E) = \xi \cdot I_0(E) \cdot e^{-\mu(E) \cdot \rho \cdot h}, \quad (\text{II.24})$$

which leads to:

$$\sigma_{\text{tube}} = \frac{1}{\rho \cdot h} \left| \ln \left[\frac{I_0(E)}{I(E)} \right] - \ln \left[\frac{\xi \cdot I_0(E)}{I(E)} \right] \right| = \frac{1}{\rho \cdot h} \left| \ln \left[\frac{1}{\xi} \right] \right|. \quad (\text{II.25})$$

The parameter ξ was assumed to lie for all measurements within a range of 0.99 to 1.01.

II.5 Results and discussion

II.5.1 Comparison with synchrotron radiation measurements

At synchrotron radiation facilities XAS measurements are performed by scanning the energy of the beam around the absorption edge. In other words, the XAS

spectra are measured step by step but the intensities $I_0(E)$ and $I(E)$ are determined simultaneously and the acquisition time per energy step is typically in the order of 1-10 s thanks to the very high flux of monochromatic X-rays available as SR beam lines (up to 10^{12} photons/s). As a consequence, a 300 eV wide XAS spectrum can be measured in less than 1 hour, whereas about 10 hours (see Table II.3) are needed to measure the same spectrum with a laboratory-based XAS setup as the one presented in this work. Thus, XAS setups based on conventional X-ray sources cannot compete in terms of measuring times with synchrotron radiation sources but, in most cases, this is not a big disadvantage because the time constraints are not as severe at home as at external big facilities. It should be also noted that in SR-based XAS measurements the main interest resides in the determination of the edge energies and XANES oscillations and not in the values of the absorption coefficients $\mu(E)$ because in the fluorescence and electron yield XAS techniques (see Sect. I.1.3) that are most commonly used at SR facilities the coefficients $\mu(E)$ cannot be determined in a straightforward way.

Despite the above mentioned differences, XAS spectra obtained from laboratory-based measurements can be compared to those measured at SR facilities to validate the methodology and the setup used in-house. Such comparisons were done in the present work for the Cu K and Ta L₃ XAS spectra. The results are presented in Figs. II.22 and II.23, respectively.

The SR-based measurement of the Cu K-edge spectrum was performed in the fluorescence mode at the beam line SuperXAS of the Swiss Light Source (SLS). The in-house experiment was performed with a 7 μm thick foil and the X-ray tube was operated at 45 kV. This explains why this Cu XAS spectrum is less noisy than the one presented in Fig. II.14. The intensity scales of the two spectra were adjusted to get the same mean value of the absorbance before the edge. As shown, the overall shape of the two spectra is very similar although the spectrum measured at home is more noisy due to the much weaker photon flux of the conventional X-ray source as compared to the one of the SR beam. On the other hand, the mid-edge shoulder (at about 8982 eV) of the spectrum measured in Fribourg is slightly shifted towards higher energy and a little bit broader. The difference in the mid-edge shoulder width is due to the better energy resolution of the SLS measurement, whereas the energy difference of about 2 eV was assumed to originate from the bigger scatter of the in-house data.

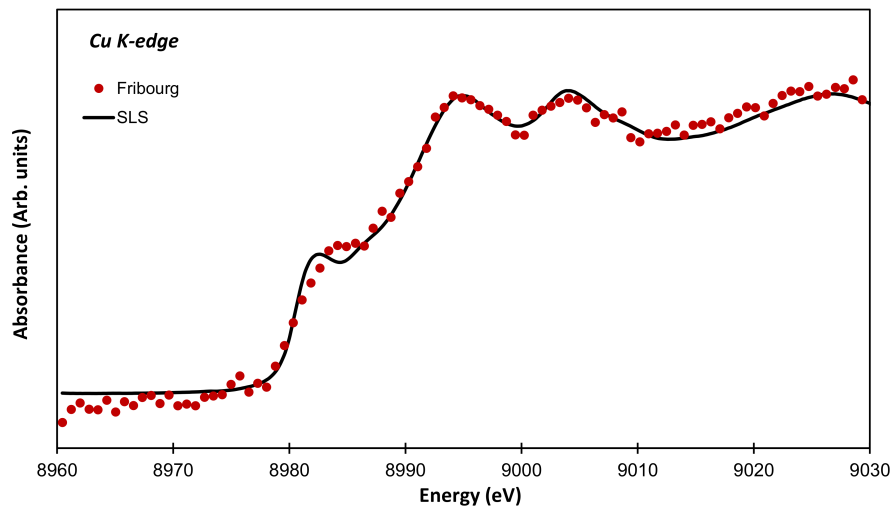


Figure II.22 – Shape comparison between the Cu K-edge absorption spectrum measured at SLS in the fluorescence mode (black solid line) and the corresponding spectrum measured in Fribourg with the laboratory-based setup (red points). The relative uncertainties of the points measured in Fribourg amount to about 10% (below the edge) and 3% (above the edge), respectively. The SLS plot was taken from [17])

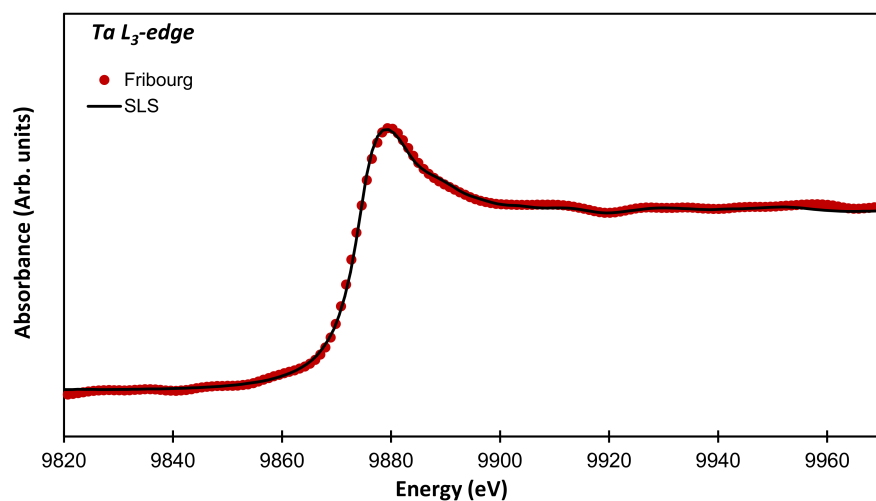


Figure II.23 – Same as Fig. II.22 but for the Ta L₃ XAS spectrum. In this case the SLS data (taken from [21]) were collected in the transmission mode and the relative uncertainties of the data of Fribourg amount to about 4% (below the edge) and 3% (above the edge), respectively.

The second comparison concerns the L₃ XAS spectrum of a 5 μm thick metallic foil of Ta. The SR-based measurement was again performed at the SuperXAS

beamline of SLS but this time in the transmission mode. The measurement of Fribourg was performed with a Ge(440) crystal and a Cr anode X-ray tube. As the aim of this measurement was to compare the shapes of the XAS spectra collected in Fribourg and SLS and not to determine the absorption coefficient, the X-ray tube was operated at a higher voltage (25 kV) to get a better statistics. In addition the data of Fribourg were smoothed off-line before calculating the absorbance. As a consequence the in-house Ta data presented in Fig. II.23 are less noisy than those shown in Fig. II.17. As it can be seen in Fig. II.23, the SLS and Fribourg Ta L_3 XAS spectra are in excellent agreement, except at about 9956 eV where a small excess of the absorbance is observed in the spectrum measured at home. The difference, however, is not significant within the uncertainty of the experimental data.

II.5.2 Edge energies

As mentioned in Sect. II.5.2, in this work the absorption edges were associated to the first inflection points of the XAS spectra and the inflection points were determined from the centroids of the Gaussian functions used to fit the first derivatives of the spectra in the edge regions. To estimate the contribution of the energy calibration measurements to the errors on the edge energies, the Cu K-edge was determined using three different combinations of references samples, namely Cu and Zn, Zn and Ge and Cu and Ge. The standard deviation of the edge energies obtained from the three calibrations was found to be 0.25 eV. This rather large value is probably due to the fact that the positions of the CCD detectors corresponding to the $K\alpha_1$ transitions of Cu and Ge are quite distant from the one employed to measure the K-edge of Cu. However, to keep the total errors on the edge energies on the safe side, an energy calibration uncertainty of 0.25 eV was assumed for all edges.

A further difficulty encountered in the energy calibration was the lack in certain cases of convenient samples for the energies of interest. For instance, for the calibration of the K-edge of Ge (at about 11103 eV) which was measured in 2nd order of diffraction with the Si(220) crystal, the $K\alpha_1$ X-ray lines of As (10544 eV) and Se (11222 eV) represented the best choice of calibration samples. However, As being highly toxic and only available in the form of lumps, we renounced to use it and decided to employ metallic foils of Cr ($E_{K\alpha_1}=5415$ eV, i.e., equivalent to 10830 eV in second order) and Mn ($E_{K\alpha_1}=5898$ eV, i.e., equivalent to 11796 eV in second

order) measured in first order of diffraction and to crosscheck the obtained edge energy using the $K\alpha_1$ transition of Se whose energy is very close to that of the Ge K-edge. It was found that the energy calibration based on the X-ray lines of Cr and Mn measured in first order was shifted by -0.79 ± 0.28 eV with respect to the calibration performed in second order with Se. The deviation could be explained by two effects, namely the refraction of the X-rays by the crystal which is different for the first and second orders of diffraction and by the penetration of the X-rays in the depth of the crystal which is higher in second order than in the first one. The calculations showed that the refraction effect produces a shift of $-0.34(24)$ eV and the depth penetration effect a smaller shift of -0.08 eV so that the total calculated shift was $-0.42(24)$ eV, a value which is just consistent within the combined error with the experimental shift of $-0.79(28)$ eV.

Table II.4 – Comparison between present edge energies and other existing experimental values. All energies are given in eV. The notation $4964.65(27/9)$ means 4964.65 ± 0.27 with an included fit error of 0.09.

Edge	Present	Kraft [124]	Bearden and Burr [163]	Bearden [164]	Other
Ti K	4964.65(27/9)	-	4966.4(6)	4964.58 (15)	4964.88(6) ^a
Fe K	7111.01 (26/8)	7110.75(2)	7112.0(1.3)	7111.28(6)	7110.86(40) ^a
Cu K	8980.53(51/44)	8980.48(2)	8978.9(6)	8980.39(48)	8980.5(1.0) ^b
Ge K	11105.29(30/17)	-	11103.1(1.0)	11103.76(74)	11103.63(55) ^b
Mo L ₁	2867.59(87/83)	-	2865.5(4)	2880.6(5.0)	2867.20(26) ^b
Mo L ₂	2625.41(26/8)	-	2625.1(4)	2627.3(8)	2625.98(33) ^b
Mo L ₃	2520.44(26/7)	-	2520.2(4)	2523.6(8)	2521.1(1.6) ^b
Ag L ₁	3806.53(50/43)	-	3805.8(4)	3807.3(2)	3807.41(34) ^b
Ag L ₂	3524.98(58/52)	-	3523.7(4)	3525.8(2)	3525.24(26) ^b
Ag L ₃	3352.40(27/9)	-	3351.1(4)	3350.96(13)	3352.58(48) ^b
Hf L ₃	9557.33(52/46)	9558.29(5)	9560.7(6)	9557.7(1.1)	9558.0(1.1) ^b
Ta L ₃	9877.45(35/25)	-	9881.1(4)	9876.7(1.2)	9878.7(2.7) ^b
Pt L ₃	11562.69(48/41)	11562.76(2)	11563.7(4)	11562.3(1.6)	11565.7(3.8) ^b

^a Sevier [165]; ^b Deslattes *et al.* [5]

The edge energies obtained in this work are presented in Table II.4 where they

are compared to experimental values reported by Kraft *et al.* [124], Bearden and Burr [163], Bearden [164], Sevier [165] and Deslattes *et al.* [5]. The values obtained by Kraft were derived from synchrotron radiation measurements and the first inflection point method and the ones reported by Bearden and Burr from photo-electron spectroscopy measurements. Values from Sevier and Deslattes were determined by adding to the energies of K and L X-ray transitions from outer levels the known energies of the latter. Regarding the edge energies reported by Bearden, no indication is provided in Ref. [164] about the employed method. On the other hand, as the values reported in [164] are given in the \AA^* scale, they were corrected by the conversion factor $\text{\AA}/\text{\AA}^*=1.0000150$ and then converted to energies using the energy-wavelength product $E \cdot \lambda = 12.398419 \text{ keV} \cdot \text{\AA}$. The second conversion factor $E \cdot \lambda$ was computed using for the Planck constant h , speed of light in vacuum c and elementary charge e the values recommended by the Committee on Data for Science and Technology (CODATA) [166]. Furthermore, the uncertainties quoted by Bearden [164] and Bearden and Burr [163] being probable errors (50% confidence limits), they were multiplied by 1.48 to obtain standard $1\text{-}\sigma$ errors (67% confidence limits). It can be mentioned here that the edge energies quoted in the XCOM database [156] (see Figs. II.12 - II.20) are those of Bearden and Burr [163].

From Table II.4, one sees that present edge energies are consistent with the data reported by Kraft *et al.* [124] for the K-edges of Fe and Cu and the L_3 edge of Pt, whereas a deviation of about 1.8σ , where σ stands for the combined error of the two measurements, is observed for the L_3 edge of Hf. The values of Kraft represent probably the most precise and reliable reference data for checking the accuracy of present values but, unfortunately Fe, Cu, Hf and Pt are the single elements common to both experiments. Regarding the deviation of the L_3 edge of Hf, it might be due to intensity variations of the X-ray tube during the $I_0(E)$ and/or $I(E)$ measurements.

The edge energies reported by Bearden and Burr [163] are all inconsistent with ours except for the L_2 - and L_3 -edges of Mo. The discrepancy cannot be explained by the different edge definitions used in our work (inflection point of lowest energy) and the one of Bearden and Burr (binding energy of the $1s$ electron) because some values from [163] are bigger than ours, some other ones smaller. Note that Bearden and Burr data are also inconsistent with those of Kraft *et al.* [124].

The comparison with Bearden's values [164] is more satisfactory since the latter are in agreement with ours for the K-edges, except in the case of Ge, and for the L_3 -

edges of Hf, Ta and Pt, whereas for the L_{1-3} -edges of Mo and Ag, discrepancies are observed. Actually, except for the L_3 -edge energy of Ag which is slightly smaller than ours, the other L-edge energies of these two elements are significantly bigger than our values. In the case of the L_1 -edge of Mo, the energy quoted by Bearden overestimates even our result by about 13 eV. We guess, however, that some problems were encountered by Bearden in this measurement because an error of ± 5 eV is reported for this edge which is much bigger than the uncertainties quoted for the other edges.

Finally, a satisfactory agreement is observed in the comparison of present values with those reported by Sevier [165] and Deslattes *et al.* [5]. As mentioned before, the latter were obtained from X-ray transition energies combined with the known binding energies of the outer levels involved in these transitions. Actually, the K-edge energies of Ti and Fe reported by Sevier are very close to our values, while the data from Deslattes are also in good agreement with the results obtained in the present work, except for the K-edge of Ge (deviation of 2.6σ), L_2 -edge of Mo (1.3σ) and L_1 -edge of Ag (1.4σ). The L_3 -edge energy of Pt quoted by Deslattes is 3.3 eV bigger than our value but nevertheless consistent with it because in this case the error quoted by Deslattes is quite big (3.8 eV). For the K-edge of Ge, the values of Bearden and Burr [163], Bearden [164] and Deslattes *et al.* [5] are consistent. The average of the three values which amounts to 11103.50(45) eV is 2.09 eV lower than the energy found in our work. Thus, our result is probably too big. The deviation might be due to the partial oxidation of the thin polycrystalline Ge film employed in our measurement because the sample which was prepared at the PTB (Physikalisch-Technische Bundesanstalt, Berlin) was exposed to the atmospheric pressure for several weeks before the measurement.

II.5.3 Absorption coefficients

The absorption coefficients determined in the present work for photon energies just below and above the edges are presented in Table II.5 where they are compared to the values from the XCOM database [156] and from the Tables of Storm and Israel [167] and Henke [168]. In the latter reference, the listed absorption coefficients do not include the coherent scattering cross sections. However, the contributions of the latter to the total absorption coefficients are quite small. For instance, in the case of the K-edge of Ti the coherent scattering cross section is about 50 times smaller than the photoionization cross section below the edge and about 400 times

Table II.5 – Comparison of the absorption coefficients μ_b (below the edge) and μ_a (above the edge) obtained in the present work with data from existing databases. All values are given in cm^2/g .

Edge	Present		XCOM [156]		Storm & Israel [167]		Henke [168]	
	μ_b	μ_a	μ_b	μ_a	μ_b	μ_a	μ_b	μ_a
Ti K	74(11)	716(22)	84	684	84	708	83	718
Fe K	55(7)	352(11)	53	408	53	414	51	412
Cu K	40(4)	309(9)	38	278	38	285	37	289
Ge K	30(12)	237(12)	28	198	28	202	27	208
Mo L ₁	1943(48)	2259(56)	1961	2243	1952	2235	-	2245
Mo L ₂	1652(41)	2518(71)	1750	2433	1758	2410	-	-
Mo L ₃	597(17)	1924(53)	542	1979	539	1940	542	-
Ag L ₁	1317(35)	1471(39)	1282	1468	1267	1457	-	1465
Ag L ₂	1132(30)	1507(40)	1126	1547	1122	1535	-	-
Ag L ₃	432(14)	1205(33)	389	1274	386	1267	385	-
Hf L ₃	101(4)	252(7)	100	256	99	262	102	-
Ta L ₃	104(4)	230(7)	96	244	95	250	93	-
Pt L ₃	78(3)	196(6)	78	195	77	197	76	-

smaller above it. Note that the incoherent scattering contribution which is still smaller (around the K-edge of Ti, $\sigma_{\text{incoh}}/\sigma_{\text{coh}} = 0.03$) is completely negligible. In addition, the values reported by Henke are only given for energies corresponding to strong K and L X-ray lines of selected elements. For this reason, the coefficients $\mu_b(E_{\text{edge}})$ and $\mu_a(E_{\text{edge}})$ listed in the last column of Table II.5 were determined from double logarithmic interpolations of the values quoted in [168] for energies below and above the edges of interest. However, as only one or even no value is reported between the L₁- and L₂-edges and between the L₂- and L₃-edges, in the case of the L-shell only the coefficients $\mu_b(E_{\text{L}_1\text{-edge}})$ and $\mu_a(E_{\text{L}_3\text{-edge}})$ could be derived.

Present absorption coefficients were determined from the equation I.4 and the corresponding errors from the equations II.22, II.23 and II.25. For small absorption coefficients and elements with a low density, the main contribution to the error originates from the uncertainty of the X-ray tube intensity, whereas for large absorption coefficients the main contribution arises from the uncertainty on the sample thickness. The contributions of the fit errors were found to be in general

small except for noisy data. For instance, in the case of Ti the contributions σ_{fit} , σ_{h} and σ_{tube} to the total error $\Delta\mu_{\text{b}}$ amount to 3.1, 1.8 and $10.6 \text{ cm}^2/\text{g}$, respectively, whereas for the L₃-edge of Ag (noisy data and big μ), the contributions to $\Delta\mu_{\text{a}}$ are $\sigma_{\text{fit}}=24 \text{ cm}^2/\text{g}$, $\sigma_{\text{h}}=46.5 \text{ cm}^2/\text{g}$ and $\sigma_{\text{tube}}= 7.9 \text{ cm}^2/\text{g}$. From Table II.5 it can be also seen that the relative errors on present absorption coefficients below the K-edges are quite big, ranging from 10% for Cu up to 40% for Ge. This can be explained by the fact that, due to the thinnesses of the employed samples and the small values of the absorption coefficients below the edges, the differences between the intensities $I(E)$ and $I_0(E)$ are quite small (see Fig. II.7), so that the relative errors on these tiny differences become large. In other words, more precise absorption coefficients below the K-edges would require the use of thicker samples but then the edge energies and XANES structures would be affected by this choice (see Sect. I.1.3).

In the Tables of Storm and Israel, it is stated that the relative uncertainties of the absorption coefficients are in the order of 10%, whereas no indication could be found about the errors affecting the values listed in [156] and [168]. However, as the values from the three databases are based on similar calculations, the same relative uncertainties of 10% were assumed for the values taken from the XCOM and Henke tables. With this assumption, one can see from the inspection of Table II.5 that all absorption coefficients determined in the present work are in agreement within the combined errors with the values reported in the three theoretical databases, except for the coefficients μ_{a} of Fe and Ge and the coefficient μ_{b} of the Ag L₃-edge which are bigger than the theoretical predictions and differ from the average values of the latter by about $1.4 \sigma_{\text{c}}$, $1.5 \sigma_{\text{c}}$ and $1.1 \sigma_{\text{c}}$, respectively, where σ_{c} stands for the combined error.

Existing experimental values for the mass absorption coefficients $\mu(E)$ are very scarce in the literature. However, some data from the Laboratoire National Henri Becquerel (LNHB, Paris) were found for the K-edges of Cu [169] and Ge [170] and the L₃-edges of Hf and Pt [170]. These recent experimental XAS data which were obtained partly at the metrology beamline of the synchrotron radiation facility SOLEIL [171] and partly with the tunable monochromatic X-ray source SOLEX [172] are reliable and very precise. To obtain the absorption coefficients $\mu_{\text{b}}(E_{\text{edge}})$ and $\mu_{\text{a}}(E_{\text{edge}})$ from the values tabulated in [169, 170], the same method as the one used for our own data was employed, namely linear spline interpolations below and above the edges. For Hf, the strong white line was excluded from the interpolation

domain. The obtained values are presented in Table II.6 where they are compared to present results. As it can be seen a quite satisfactory agreement is observed except for the coefficients μ_a of the K-edge of Ge and the L₃-edge of Pt for which our values are bigger than those of LNHB by about $2.4 \sigma_c$ and $1.6 \sigma_c$, respectively.

Table II.6 – Comparison of the absorption coefficients $\mu_b(E_{\text{edge}})$ and $\mu_a(E_{\text{edge}})$ obtained in the present work for the K-edges of Cu and Ge and the L₃-edges of Hf and Pt with experimental values from the LNHB (Laboratoire National Henri Becquerel). All values are given in cm^2/g .

Edge	Present		LNHB	
	μ_b	μ_a	μ_b	μ_a
Cu K	40(4)	309(9)	37.5(1) [169]	305.6(1.3) [169]
Ge K	30(12)	237(12)	27.8(2) [170]	207.6(7) [170]
Hf L ₃	101(4)	252(7)	97.8(2) [170]	248.4(5) [170]
Pt L ₃	78(3)	196(6)	75.1(1) [170]	186.2(3) [170]

II.6 Summary and concluding remarks

In this project a laboratory-based setup for in-house XAS measurements was developed and commissioned. The setup is based on the von Hamos bent crystal spectrometer of Fribourg and the source of radiation is an X-ray tube. The effects of parameters such as the position of the sample, the thickness of the latter, the high-voltage of the X-ray tube and the choice of the crystal were carefully investigated. The new setup was then validated by measuring the XAS spectra around the K-edges and L-edges of several solid samples. The shapes of the K-edge of Cu and L₃-edge of Ta were compared to those measured with synchrotron radiation at the SLS. The spectra were found to overlap very well in both cases. Furthermore, the edge energies and absorption coefficients below and above the K-edges of Ti, Fe, Cu and Ge, L_{1–3} edges of Mo and Ag and L₃ edges of Hf, Ta and Pt were extracted from the measurements and compared to the data from existing theoretical and experimental databases.

Present edge energies were determined from the inflection points of lowest energy. Except for the K-edge of Ge for which the energy obtained in the present work

overestimates the value found in the literature by about 1.5 eV, the so-determined edge energies were found to be in good agreement with recent and reliable values obtained with synchrotron radiation [124] and with values derived from X-ray transition energies combined with the energies of the outer levels involved in these transitions [5]. In contrast to that, most of the edge energies reported by Bearden [164] and to a smaller extent by Bearden and Burr [163] were found to be inconsistent with our values.

The absorption coefficients just before and after the edges were determined by calculating the values at the edge energies of the linear functions obtained from spline interpolations of the XAS data points measured below and above the edges. The results were compared to theoretical values from three different databases, namely the NIST XCOM [156], Storm and Israel [167] and Henke [168] databases and to recent experimental data from the LNHB [169, 170]. In both cases a quite good agreement was observed, except for Ge and Pt for which present absorption coefficients above the edge were found to slightly overestimate the literature values.

A clear advantage of the in-house setup presented in this work is its simplicity and better availability as compared to SR-based equipments. In counterpart the data taken with the laboratory-based setup are more noisy due to the significantly lower intensity of the employed X-ray source. For the same reason, the data collection times are longer than at SR facilities by one order of magnitude or more. Actually, to avoid a contamination of the XAS spectra by higher energy photons, most of present measurements were performed at low values of the X-ray tube voltage, i.e., with incoming photon intensities $I_0(E)$ in the order of 1 photon/s or less. However, thanks to the energy resolution capability of the CCD, higher energy photons can be suppressed very efficiently by applying narrow energy windows to the CCD so that probably most of the measurements presented in Sect. II.3 could have been performed at higher X-ray tube voltages (e.g., 50 kV) and thus with about 10-20 times higher incoming photon intensities.

A further weak point of the in-house setup resides in the fact that the spectra $I_0(E)$ and $I(E)$ are not measured simultaneously but sequentially. This drawback could be eliminated, however, by monitoring the X-ray tube intensity with the SDD detector placed above the crystal (see Fig. II.1) but then the sample should be placed in front of the CCD and not in front of the slit. An elegant alternative solution would consist to place again the sample in front of the CCD but to cover only the top half part of the latter (i.e., the CCD rows 201-400) with the sample

and to leave the bottom part (CCD rows 1-200) uncovered. By projecting then separately the top and bottom CCD rows onto the dispersion axis, simultaneous $I(E)$ and $I_0(E)$ spectra would be obtained. In the two latter cases, however, the sample should be at least as long as the CCD (2.68 cm), be free of pinholes and have a highly homogeneous thickness.

In conclusion, it has been proven that XAS measurements are feasible by means of the presented in-house setup and that the obtained results (XAS spectrum shapes, edge energies and absorption coefficients) are reliable. Although laboratory-based XAS setups cannot compete with SR-based ones in terms of photon beam intensities and duration of the measurements, the two techniques can be considered as complementary and both useful for academic research and industrial applications.

CHAPTER III

**Electron-induced
double K-shell ionization of
Sc, Cr and Cu**

III.1 Experimental setup and measurements

III.1.1 Experimental setup

The K hypersatellite X-ray spectra of Sc, Cr and Cu induced by electron impact were measured by means of the von Hamos spectrometer of Fribourg [151], using the same setup as the one employed for the XAS measurements (see Sect. II.2.2). For each element, the electron kinetic energy was chosen to be about 2 times bigger than the threshold energy for the double 1s ionization. As for Cr and Cu, this choice implied acceleration voltages of 26.5 and 39.6 kV, respectively, which are bigger than the maximum voltage (20 kV) at which the two electron guns available in our laboratory can be operated, 3 kW/100 kV side-window Coolidge-type X-ray tubes equipped with a Sc, Cr and Cu anode, respectively, were employed.

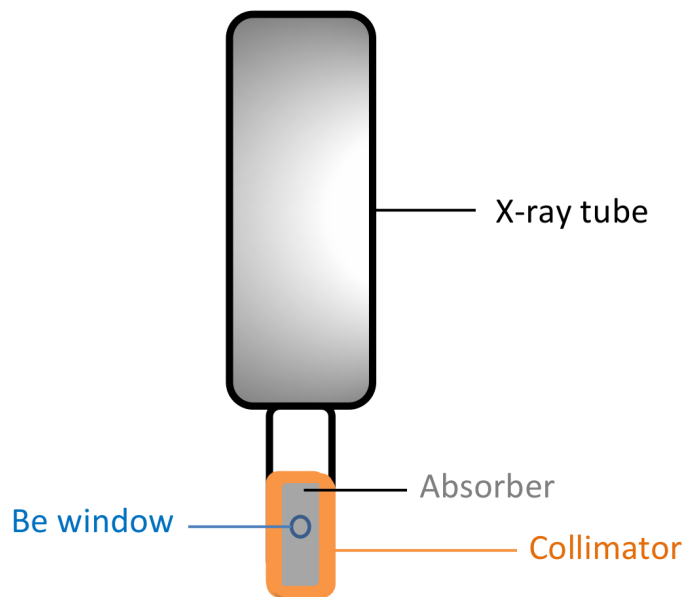


Figure III.1 – Schematic drawing showing the collimator mounted on the the X-ray tube in front of the Be window. For the measurements of the diagram lines, one or two absorbers had to be inserted between the collimator and the Be window to diminish the count rates.

To reduce the scattering of the X-rays in the spectrometer chamber, a Cu collimator with a 20 mm high \times 5 mm wide rectangular aperture was mounted on the nose of the X-ray tube in front of the Be window (see Fig. III.1). As the intensity of the radiation emitted by the X-ray tube is proportional to the electron current but

not to the high voltage employed to accelerate the electrons, the same high voltage had to be used for the measurements of the diagram and hypersatellite X-ray lines to get reliable intensity ratios. For the diagram lines, however, these high voltage values resulted in such high count rates that the CCD detector was fully saturated. The problem was solved by inserting adequate absorbers (metallic foils) between the collimator and the Be window for the diagram line measurements. The metallic absorbers were chosen so that they did not produce fluorescence lines in the energy regions corresponding to the diagram and hypersatellite transitions and their thicknesses were selected so that the count rate on the top of the $K\alpha_1$ or $K\beta_1$ line was kept below about 20 counts/s, a count rate for which the probability to observe multiple hits on the same pixel is reasonably low (a few percents).

III.1.2 Attenuation factors

The attenuation factors A of the employed absorbers were determined experimentally in separate measurements, using the following method. At first, the highest voltage U_0 and current i_0 of the X-ray tube for which the count rate measured without absorber on the top of the $K\alpha_1$ or $K\beta_1$ line was still smaller than 20 counts/s were determined. Then the attenuation factor of the absorber needed to keep the count rate of the $K\alpha_1$ or $K\beta_1$ line below the maximum value (20 counts/s) at the high voltage U and current i used for the hypersatellite measurement was estimated and the absorber or combination of absorbers (named hereafter main absorber) was chosen. The effective attenuation factor of the main absorber was then determined experimentally from the intensity ratio of the $K\alpha_{1,2}$ or $K\beta_{1,3}$ line measured at U_0 and i_0 without and with the main absorber. In some cases, however, it was found that for the $K\alpha_{1,2}$ line the attenuation factor had to be so big that the line measured with the main absorber at $U_0 \times i_0$ was too weak to be observed. In such cases, the $K\alpha_{1,2}$ intensities were also measured at the intermediate voltage U_1 ($U_0 < U_1 < U$) with the main absorber (intensity I_{abs}) and another thinner absorber (intensity I_1) as well as at the voltage U_0 with the thinner absorber (intensity I_2) and without absorber (intensity I_0). As I_0 could not be measured at the voltage U_1 (too high counting rate) like I_{abs} , the value of $I_0(U_1)$ was obtained by multiplying the measured intensity $I_0(U_0)$ by the ratio I_1/I_2 and the attenuation factor of the main absorber was determined using the following relation:

$$A = \frac{I_0}{I_{\text{abs}}} \cdot \frac{I_1}{I_2}. \quad (\text{III.1})$$

The intermediate and main absorbers (or combination of absorbers) used in the different measurements, the X-ray tube parameters $U_0 \times i_0$, $U_1 \times i_1$ and $U \times i$ as well as the corresponding attenuation factors A are presented in Table III.1. The errors on the attenuation factors originate from the errors of the fitted intensities. Furthermore, from the known thicknesses of the absorbers and the experimentally determined attenuation factors, the absorption coefficients were calculated and compared to the values given in the NIST XCOM database [156]. It was found that the relative deviations between our values and the ones from XCOM were in all cases smaller than 5% and thus consistent within the relative uncertainties reported for the NIST values.

Table III.1 – Attenuation factors of the absorbers employed to diminish the intensities of the diagram lines for the determination of the $I(K^h\alpha)/I(K\alpha)$ and $I(K^h\beta)/I(K\beta)$ yield ratios. The X-ray tube voltages and currents employed in these measurements are also given. For the $K\alpha$ measurements of Sc and Cu the intensities I_1 and I_2 (see text) were obtained using 10.6 mg/cm^2 Al and 13.7 mg/cm^2 Au absorbers, respectively.

Measurement	$U_0 \times i_0$ [kV×mA]	$U_1 \times i_1$ [kV×mA]	$U \times i$ [kV×mA]	Main absorber	Attenuation factor A
Sc $K\alpha_{1,2}$	4.5×1	6.0×2	20.0×10	16.3 mg/cm^2 Al + 3.3 mg/cm^2 Ta	4800(38)
Sc $K\beta_{1,3}$	6.5×1	-	20.0×10	18.9 mg/cm^2 Al	144(4)
Cr $K\alpha_{1,2}$	6.0×1	-	26.5×10 60.0×10	13.7 mg/cm^2 Au 13.7 mg/cm^2 Au	2462(28)
Cu $K\alpha_{1,2}$	9.0×1	32.0×1	39.6×10	38.0 mg/cm^2 Au	2528(20)

III.1.3 Measurements

In the present work the electron impact induced $K^h\alpha_{1,2}$ hypersatellite lines of Sc, Cr and Cu were measured by means of high energy resolution X-ray spectroscopy. In the case of Sc, the weaker $K^h\beta_{1,3}$ hypersatellite could also be measured. For

each sample the kinetic energy of the electron was set at a value two times bigger than the threshold energy for the double 1s ionization but for Cr additional measurements at 60 keV were also carried out. To probe the reliability of the experimental setup the Cr $K^h\alpha$ hypersatellite line was measured with three different crystals (see Table III.2).

In some hypersatellite measurements, unexpected spectral features were observed. For instance, in the Cr $K^h\alpha_{1,2}$ hypersatellite spectrum measured at $26.5 \text{ kV} \times 10 \text{ mA}$ with the Si(220) crystal (see Fig. III.2), one can see that in addition to the $K^h\alpha_2$ hypersatellite which is clearly visible at about 5650 eV, a pronounced increase of the intensity is observed on the right hand of the measured energy region. In order to elucidate the origin of this intensity enhancement, a broad scan of the energy region ranging from 5590 eV up to 6590 eV was performed. To cover this broad energy range, 18 juxtaposed and overlapping energy regions were measured successively. Before the measurement of each new region, the crystal and detector were moved along their axis by 1000 and 2000 motor steps, respectively, which corresponded to an energy shift of about 48 eV, but the alignment angles γ and φ of the X-ray tube (see Sect. II.2.2) were kept fixed for all regions at the values corresponding to the $K^h\alpha_{1,2}$ hypersatellite.

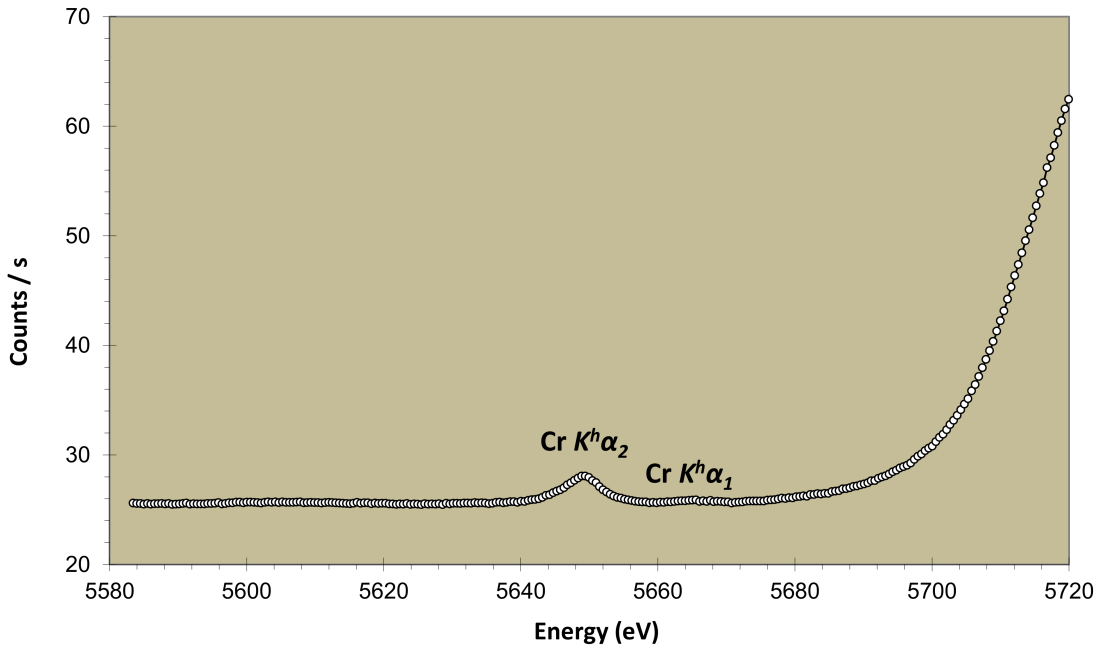


Figure III.2 – Cr $K\alpha$ hypersatellite spectrum measured at $26.5 \text{ kV} \times 10 \text{ mA}$ with the Si(220) crystal.

The obtained spectrum is presented in Fig. III.3, each energy region being depicted with a different color. From the left to the right, one can see the $K^h\alpha_2$ hypersatellite line at 5650 eV and the $K\beta_{1,3}$ and $K\beta_5$ lines at 5945 eV and 5988 eV, respectively. The abrupt decrease of the intensity on the high energy side of the $K\beta_5$ line originates from the K absorption edge of Cr at 5989 eV. The weak lines at 6390 eV and 6404 eV are the $K\alpha_2$ and $K\alpha_1$ lines of Fe which are probably due to trace impurities of this element in the Cr anode. Furthermore, as this exploratory measurement was performed without absorber, there is a hole in the center of the strong $K\beta_{1,3}$ line which indicates that the CCD was saturated, due to the too high count rate on the top of this line. From Fig. III.3, one sees also that the intensity enhancement observed in Fig. III.2, on the right of the hypersatellite line, corresponds to the left flank of an intense and broad bump centered at about 5740 eV. This line could not be identified. The same holds for the weaker structure observed at about 6300 eV. In our opinion, these two spectral features could be due to spatial inhomogeneities of the electron beam intensity on the anode (hot electron spots) or to some scattering of the X-ray tube radiation on the Cu collimator placed in front of the Be window because the energies of these structures were found to change when the X-ray tube alignment was modified.

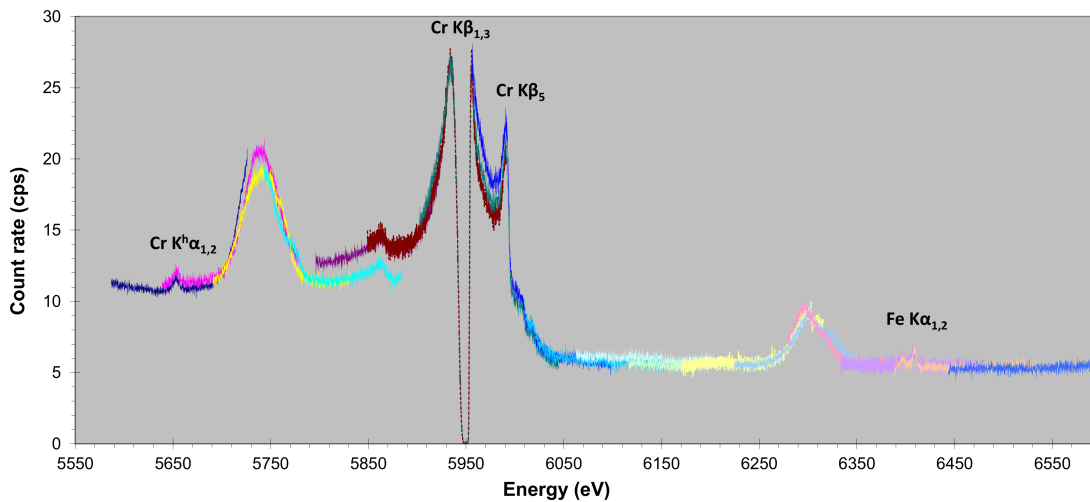


Figure III.3 – Exploratory scan of the energy region around the $K^h\alpha$ and $K\beta$ lines of Cr. The measurement was performed without absorber using the Si(220) crystal. To cover the about 1000 eV wide energy domain, 18 different positions of the crystal and detector were needed. The corresponding overlapping energy regions are presented in different colors.

The above assumption was probed by remeasuring the same energy range with another crystal, namely a HAPG(004) crystal. As in the case of the Si(220) scan, 18 partial overlapping regions were measured, each region corresponding to a given crystal and detector position. As before, the X-ray tube was operated at $26.5 \text{ kV} \times 10 \text{ mA}$ and the measurement was performed without absorber. However, as the Bragg angle corresponding to the Cr $K^h\alpha_{1,2}$ hypersatellite line is not the same for the Si(220) and HAPG(004) crystals, the alignment of the X-ray tube was different in the two measurements. The spectrum is presented in Fig. III.4. As shown, due to the different X-ray tube alignment, the intriguing spectral features observed at about 5740 and 6300 eV in the Si(220) spectrum are no more visible in the HAPG(004) spectrum but a new ghost structure is observed at about 6070 eV.

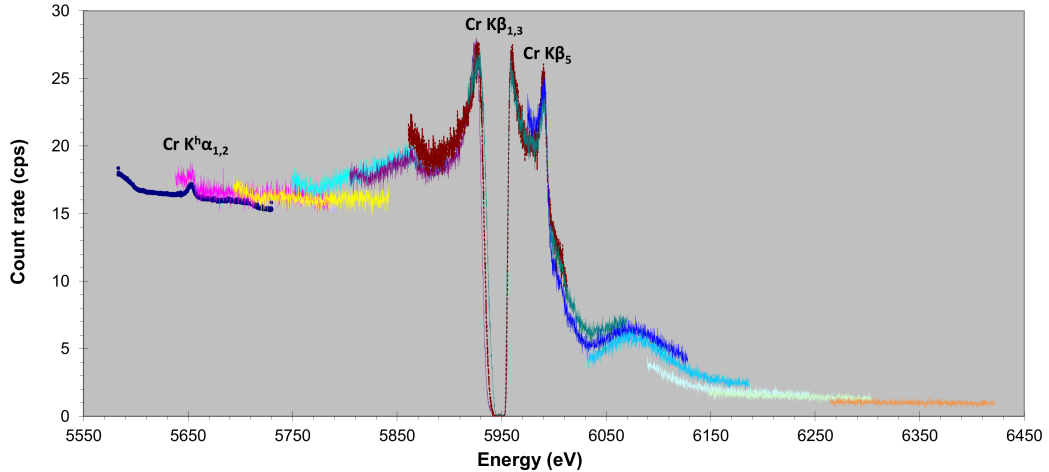


Figure III.4 – Same as Fig. III.3 but for the HAPG(004) crystal.

Similar bumps were observed in the $K^h\beta$ hypersatellite spectra of Sc, Cr and Cu. For Cr, test measurements were performed with three different crystals, namely Si(220), HAPG(004) and Ge(220). For all crystals, the strong parasitic bump was found to overlap with the $K^h\beta$ hypersatellite line. We have tried therefore to remeasure the energy regions corresponding to the $K^h\beta$ hypersatellite spectra using lower X-ray tube voltages, i.e., voltages corresponding to electron energies that were smaller than the double $1s$ ionization thresholds of the different samples. The obtained spectra were normalized to get the same background intensities outside the bumps' regions as the ones observed in the corresponding hypersatellite spectra and then subtracted from the latter. The method was found to be helpful for Sc but not for Cr and Cu so that the $K^h\beta$ hypersatellite spectrum could be measured

only for Sc.

III.2 Data analysis

III.2.1 Energy calibration and instrumental broadening

For the energy calibration of the $K^h\alpha$ hypersatellite spectra, measurements of the photoinduced $K\alpha_{1,2}$ diagram transitions of the element of interest (atomic number Z) and of the next heavier element (atomic number $Z + 1$) were performed for each target. For the $K^h\beta$ hypersatellite spectrum of Sc ($Z=21$), the $K\alpha_{1,2}$ diagram transitions of Ti ($Z=22$) and V ($Z=23$) were used. The calibration measurements were performed in the standard von Hamos geometry (see Sect. II.2.1). The energies of the reference X-ray transitions were taken from Ref. [5] and assigned to the fitted centroids of the corresponding lines. More detailed explanations about the energy calibration of X-ray spectra measured with the von Hamos spectrometer are given in Sect. II.4.1.

To crosscheck the accuracy of the energy calibration, the reference lines were also measured in the direct geometry, i.e., with the setup employed for the hypersatellite measurements, placing the reference samples in front of the X-ray tube window. The energies of the reference lines measured in the direct geometry were found to be always bigger than the energies determined in the standard geometry. The differences varied, depending on the sample, between 0.23 eV and 1.64 eV. These discrepancies could be explained by a slight displacement of the slit in the direct geometry. This displacement of a few tens of μm was produced by the nose of the X-ray tube which was coming into contact with the slit support and was then exerting a force on it when the spectrometer chamber was pumped down. This effect was accounted for by correcting the hypersatellite energies by the energy differences observed for the reference lines between the two geometries. However, as the shift of the slit depended on the X-ray tube alignment, the precision of which was limited to about 0.5 deg., an additional uncertainty of ± 0.45 eV corresponding to the standard deviation of the measured energy differences between the two geometries was included in the errors of the energy calibration.

Table III.2 – Experimental parameters used for the measurements of the $K^h\alpha_{1,2}$ and $K^h\beta_{1,3}$ hypersatellites. The reference X-ray transitions used for the energy calibration of the hypersatellite spectra are listed in the fourth column. The numbers in brackets represent the energies in [eV] of the reference transitions. The values of the instrumental broadening parameter σ corresponding to the energies of the reference transitions are given in the 5th column.

K-hypersat.	$U \times i$ [kV \times mA]	Crystal $2d_{hkl}$ [\AA]	Calibration	σ [eV]	Acq. time [s]
Sc $K^h\alpha_{1,2}$	20.0×10	LiF(200) 4.028	Sc K_{α_1} (4090.74) Ti K_{α_1} (4510.90)	0.74(4) 0.88(1)	30'000
Sc $K^h\beta_{1,3}$	20.0×10	LiF(200) 4.028	Ti K_{α_1} (4510.90) V K_{α_1} (4952.22)	0.88(1) 1.02(2)	156'000
Cr $K^h\alpha_{1,2}$	26.5×10	Si(220) 3.840	Cr K_{α_1} (5414.80) Mn K_{α_1} (5898.80)	0.85(1) 0.90(2)	30'000
Cr $K^h\alpha_{1,2}$	60.0×10	Si(220) 3.840	Cr K_{α_1} (5414.80) Mn K_{α_1} (5898.80)	0.85(1) 0.90(2)	45'000
Cr $K^h\alpha_{1,2}$	60.0×10	Ge(220) 4.000	Cr K_{α_1} (5414.80) Mn K_{α_1} (5898.80)	0.79(1) 0.93(2)	30'000
Cr $K^h\alpha_{1,2}$	60.0×10	HAPG(004) 3.354	Cr K_{α_1} (5414.80) Mn K_{α_1} (5898.80)	1.60(3) 1.77(2)	30'000
Cu $K^h\alpha_{1,2}$	39.6×10	Si(440) 1.920	Cu K_{α_1} (8047.82) Zn K_{α_1} (8638.91)	0.77(2) 0.85(1)	125'000

The above mentioned photoionization measurements were also employed to determine the instrumental energy broadening of the von Hamos spectrometer. The latter has a Gauss-like response function (see Sect. II.4.2) whose width (FWHM = $2.33 \times \sigma$, where σ^2 represents the variance of the Gaussian) varies with the photon energy. For narrow energy intervals, the variation of σ can be assumed to be linear. As the energy of the $K^h\alpha$ hypersatellite of the element Z is comprised between the energies of the parent $K\alpha$ diagram line and the $K\alpha$ diagram line of the next heavier element ($Z + 1$), the instrumental broadening σ of the spectrometer for the $K^h\alpha$ hypersatellite was determined from the linear interpolation of

the standard deviations σ obtained from the fits of the $K\alpha$ diagram lines of the reference elements Z and $(Z + 1)$. In these fits, the Lorentzian widths of the $K\alpha$ transitions were kept fixed at the values deduced from the atomic level widths reported in [161], whereas the unknown standard deviations σ were used as free fitting parameters. For the $K^h\beta$ hypersatellite of Sc, the standard deviation σ was determined from the linear interpolation of the values σ obtained from the fits of the $K\alpha$ lines of Ti and V.

The experimental parameters employed for the $K^h\alpha$ and $K^h\beta$ hypersatellite measurements are presented in Table III.2. The reference transitions used for the energy calibration of the hypersatellite spectra are presented in the fourth column with their energies (in brackets) expressed in eV. The values of the instrumental broadening parameter σ obtained from the fits of the reference transitions are listed in the fifth column. The total acquisition times employed to measure the hypersatellite spectra are indicated in the last column.

III.2.2 Fitting procedure

General points

The spectra were fitted by means of a nonlinear least squares fitting program using the software package PeakFit[®] (SYSTAT Software Inc., Richmond, USA). As the convolution of the Gauss function representing the instrumental response of the spectrometer with the Lorentz function describing the natural line shape of an X-ray transition results into a Voigt function [173], all diagram and hypersatellite lines were fitted with Voigtian profiles. The PeakFit[®] program determines first a crude linear background using a few points at the beginning and end of the spectrum and then subtracts this background from the experimental points. The residual spectrum is then fitted using a refined background which can be chosen by the user (constant, linear, quadratic, cubic, logarithmic, exponential, etc). In most cases, the energies, intensities and Lorentzian widths of the measured transitions as well as the background parameters were let free in the fitting procedure, whereas the instrumental broadening parameters σ were kept fixed at the values obtained from the fits of the reference transitions (see above). For some crystals, slight asymmetries were observed on the low energy sides of the $K\alpha_1$ and $K\alpha_2$ diagram transitions. They were accounted for by using additional Voigt profiles in the fits. For the diagram lines, despite the use of absorbers, multiple hits on the same pixel

could not be excluded *a priori*. As the intensity of the $K\alpha_1$ transition is more affected by multiple hits than the one of the two times less intense $K\alpha_2$ transition, before each measurement the $I(K\alpha_2)/I(K\alpha_1)$ yield ratios were checked and compared to the theoretical predictions of Scofield [174]. Whenever a significant disagreement was observed, the CCD images of the $K\alpha$ measurements were re-analyzed by considering pixels with double and triple hits and the corresponding one-dimensional spectra were multiplied by 2 and 3, respectively, and then added to the one-dimensional spectrum obtained from the single hit analysis.

As mentioned before the $K^h\alpha_1$ hypersatellites are very weak for light elements. For this reason, the $K^h\alpha_1$ intensities of Sc and Cr had to be kept fixed in the fits. The intensities were locked at the values obtained from the $I(K^h\alpha_1)/I(K^h\alpha_2)$ yield ratios calculated by Costa [175]. Furthermore, the same natural widths were assumed first for both hypersatellites using the option of parameters' sharing provided by the PeakFit[®] program. In the final fit, however, the Lorentzian width of the $K^h\alpha_1$ line was fixed at the value given by the first fit minus the difference between the widths of the L_2 and L_3 atomic levels.

Specific points concerning the fits of the different spectra are given hereafter.

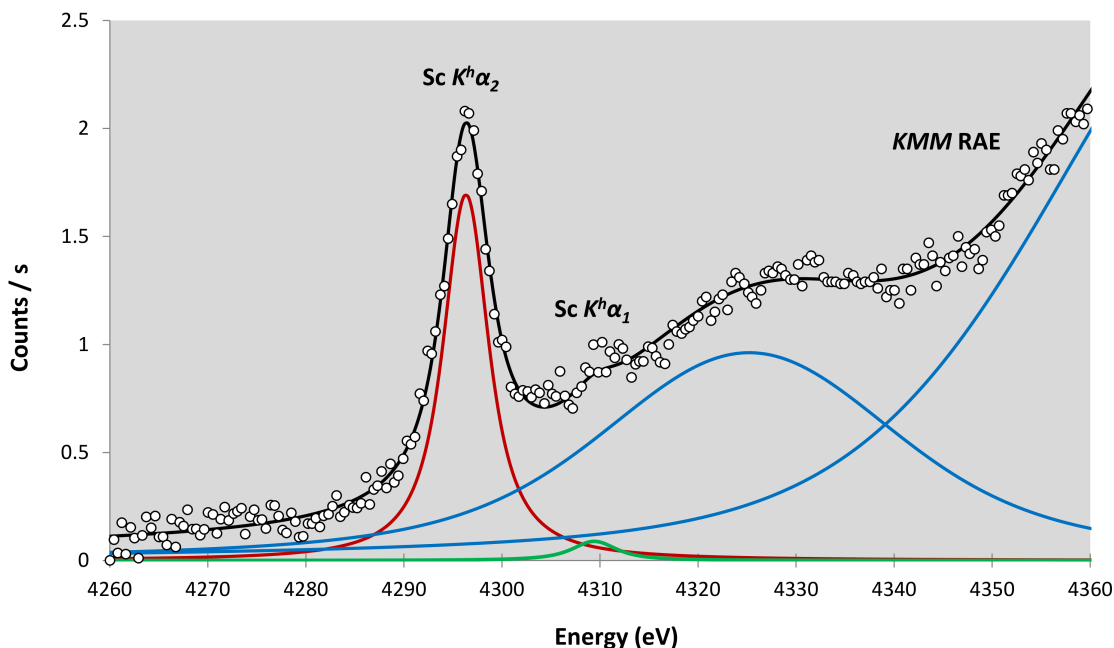
$K^h\alpha$ and $K^h\beta$ spectra of Sc


Figure III.5 – Sc $K\alpha$ hypersatellite spectrum measured at $20 \text{ kV} \times 10 \text{ mA}$ using a LiF(200) crystal. The measured spectrum is represented by the open circles and the total fit by the black solid line. The red and green curves stand for the fits of the $K^h\alpha_2$ and $K^h\alpha_1$ hypersatellites, respectively, and the blue solid lines for the Voigtians used to fit the KMM RAE structure. The fitted background was subtracted from the spectrum beforehand.

The fitted $K\alpha$ hypersatellite spectrum of Sc is presented in Fig. III.5. The background was fitted with a constant. The peak around 4296 eV corresponds to the $K^h\alpha_2$ hypersatellite and the weak bump around 4309 eV to the $K^h\alpha_1$. The latter is superimposed on the low energy tail of KMM radiative Auger transitions. Radiative Auger transitions are Auger transitions which are characterized by the simultaneous emission of an Auger electron and a photon [45, 176, 177]. More specifically, in KMM radiative Auger transitions, a M-shell electron fills the K-shell vacancy and another M-shell electron and a photon are simultaneously emitted by the atom. As the energy of the transition is shared between the electron and the photon, KMM radiative Auger structures are continuous and appear on the low energy sides of the $K\beta$ diagram lines. Since Auger transition probabilities are bigger for light elements, the radiative Auger effect (RAE) is more important for low-Z elements like Sc. Thanks to the high energy resolution of the von

Hamos spectrometer, the $K^h\alpha_2$ hypersatellite could be more or less well separated from the KMM transitions but not the $K^h\alpha_1$. The Sc $K^h\alpha_2$ hypersatellite line was fitted with one Voigtian whose energy, intensity and Lorentzian width could be let free in the fit. The $K^h\alpha_1$ hypersatellite was also fitted with one Voigtian but only the energy could be used as free fitting parameter. Regarding the KMM radiative Auger structure, the latter was fitted with two Voigtians whose energies, intensities, Lorentzian and Gaussian widths were let free in the fit.

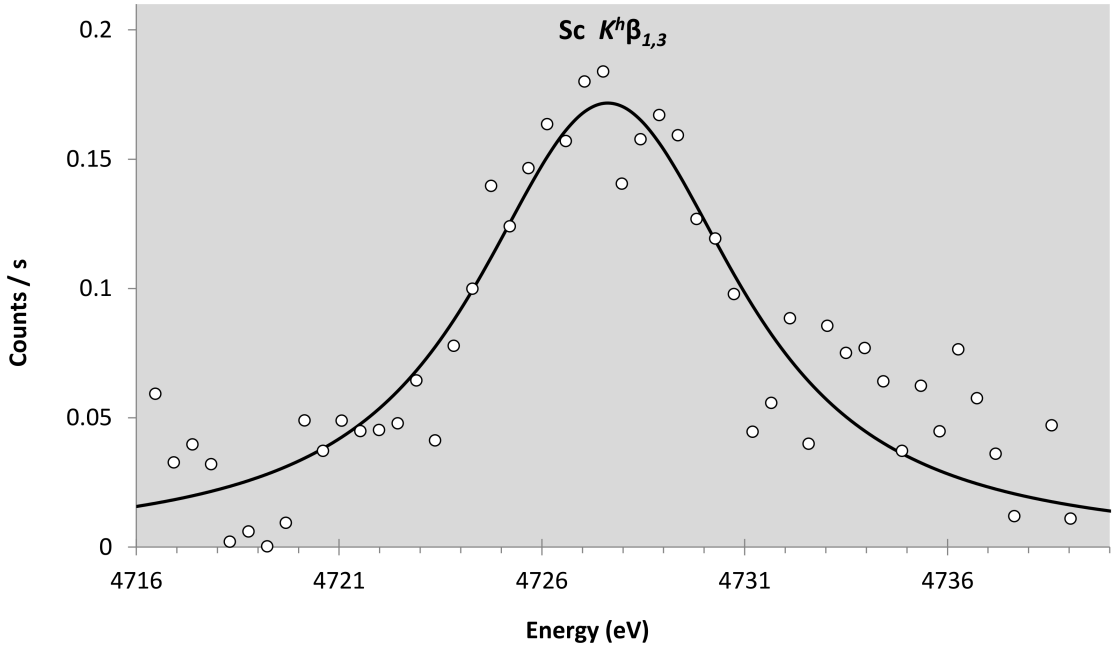


Figure III.6 – Sc $K\beta$ hypersatellite spectrum measured at $20 \text{ kV} \times 10 \text{ mA}$ using a LiF(200) crystal. The measured spectrum is represented by the open circles and the total fit by the black solid line.

The fit of the $K\beta_{1,3}$ hypersatellite spectrum of Sc is presented in Fig. III.6. As shown, the data are rather noisy due to the extremely weak intensity of the hypersatellite (about 0.16 count/s on the top of the line) and the fact that the spectrum was obtained by subtracting from the rough hypersatellite spectrum the spectrum corresponding to the same energy region but measured with the X-ray tube voltage set below the double 1s ionization threshold (see Sect. III.1.3). The $K^h\beta_{1,3}$ hypersatellite was fitted with a single Voigtian because the energy separation between the $K^h\beta_1$ and $K^h\beta_3$ components (1.4 eV according to [178]) is much smaller than the natural widths of the two components and because the intensity ratio between the forbidden $K^h\beta_1$ and allowed $K^h\beta_3$ hypersatellite transitions is only 0.047 [178].

Despite the poor statistics of the spectrum, the energy, intensity and Lorentzian width could be used as free fitting parameters but the fit errors are rather large.

$K^h\alpha$ spectra of Cr

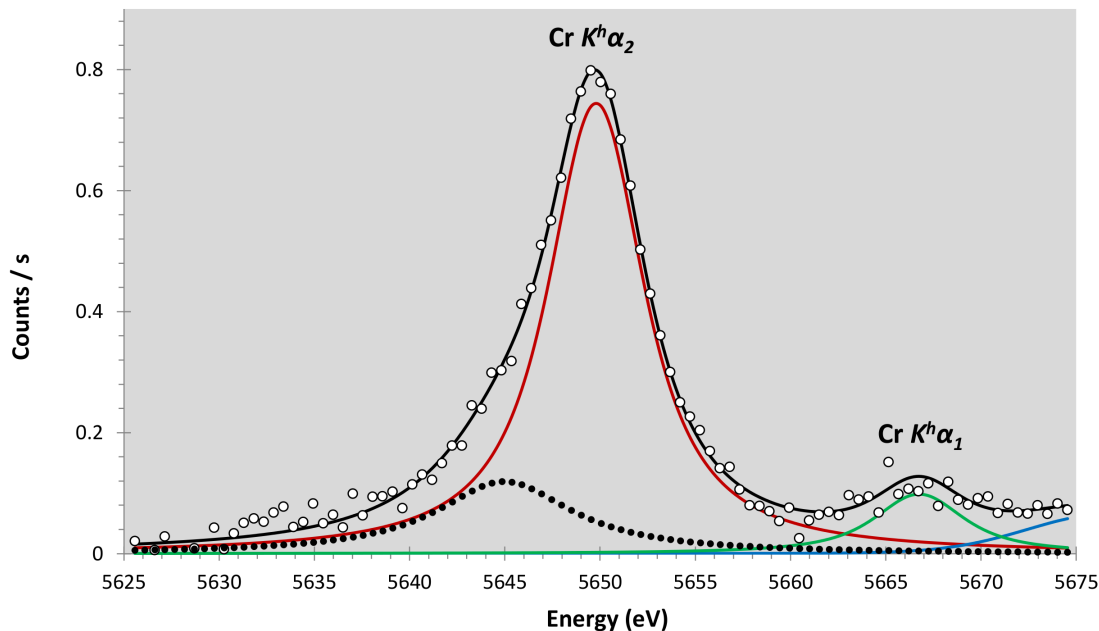


Figure III.7 – Cr $K\alpha$ hypersatellite spectrum measured at $26.5 \text{ kV} \times 10 \text{ mA}$ using a Si(200) crystal. The measured spectrum is represented by the open circles and the total fit by the black solid line. The red and green curves stand for the fits of the $K^h\alpha_2$ and $K^h\alpha_1$ hypersatellites, respectively. The black dotted line and the blue solid line represent the Voigtians used to fit the $K^h\alpha_2$ asymmetry and the residual KMM RAE intensity, respectively. The fitted background was subtracted from the spectrum beforehand.

The Cr $K\alpha$ hypersatellite spectrum was measured with a Si(220) crystal. The X-ray tube was operated first at $26.5 \text{ kV} \times 10 \text{ mA}$ and then at $60.0 \text{ kV} \times 10 \text{ mA}$. To check the reliability of the experimental setup the spectrum collected at 60 kV was re-measured with two other crystals, namely Ge(220) and HAPG(004).

The fit of the $K^h\alpha$ hypersatellite spectrum measured at 26.5 kV is depicted in Fig. III.7. The background was fitted with a linear function. The Voigtians at about 5650 eV and 5667 eV correspond to the $K^h\alpha_2$ and $K^h\alpha_1$ hypersatellites, respectively. As the $K^h\alpha_2$ line was found to evince some significant asymmetry on its low energy flank, it was fitted with two Voigtians. The energies, intensities and

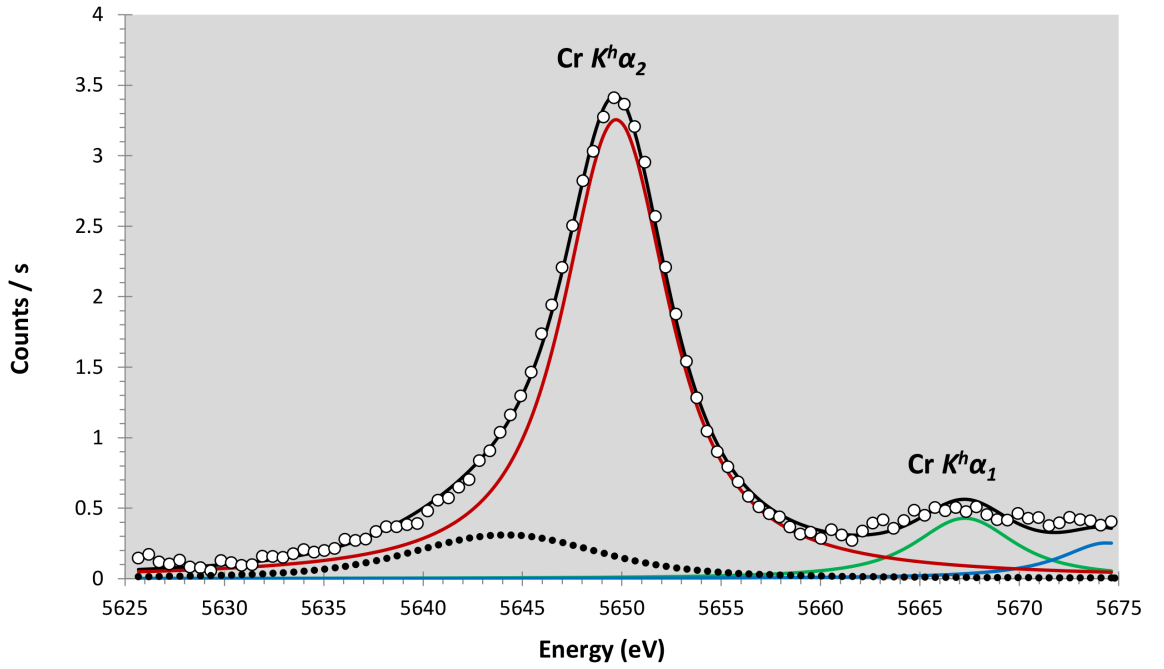


Figure III.8 – Same as Fig. III.7 but with the X-ray tube operated at 60 kV \times 10 mA

Lorentzian widths of these two Voigtians were let free in the fit. The $K^h\alpha_2$ line was fitted with one Voigtian with the energy as single free fitting parameter. As the asymmetry of the $K^h\alpha_2$ hypersatellite was found to be broader, less intense and shifted in the spectrum collected with the same crystal at 60 kV and was not observed with the HAPG(004) crystal, the asymmetry was assumed to be due to background fluctuations originating from inhomogeneities in the intensity of the electron beam spot on the X-ray tube anode. The intensity of the Voigtian used to account for the asymmetry was therefore not taken into consideration in the determination of the hypersatellite intensity. Some excess of intensity was also found on the right hand side of the spectrum. This intensity excess is probably due to KMM RAE transitions. The RAE intensity observed in the $K^h\alpha$ hypersatellite spectrum of Cr is much weaker than in the case of Sc because the energy difference between the upper edge of the KM_1M_1 RAE transitions and the $K^h\alpha_1$ hypersatellite is about 165 eV for Cr and only 66 eV for Sc [179].

The Cr $K\alpha$ hypersatellite measured with the Si(220) crystal at 60 kV \times 10 mA is shown in Fig. III.8. The spectrum was fitted as the one measured at 26.5 kV. The same spectra measured with the Ge(220) and HAPG(004) crystals are presented in Figs. III.9 and III.10, respectively. Similar fits as the one done for the spec-

trum measured with the Si(220) crystal were carried out except that no Voigtian was needed for the RAE structure, the latter being smeared out by the higher background observed in the measurements performed with these two crystals. In particular, in the spectrum measured with the Ge(220) crystal, the background was found to evince intensity increases on both ends of the $K^h\alpha$ hypersatellite region. These intensity enhancements were accounted for by adding two Voigtians (black dotted lines) to the linear fit of the background. For the measurement with the HAPG (Highly Annealed Pyrolytic Graphite) crystal, the background was more regular so that it could be well fitted with a linear function. As no asymmetry nor RAE structures were observed in the spectrum, the latter could be well fitted using only two Voigtians, one for each hypersatellite.

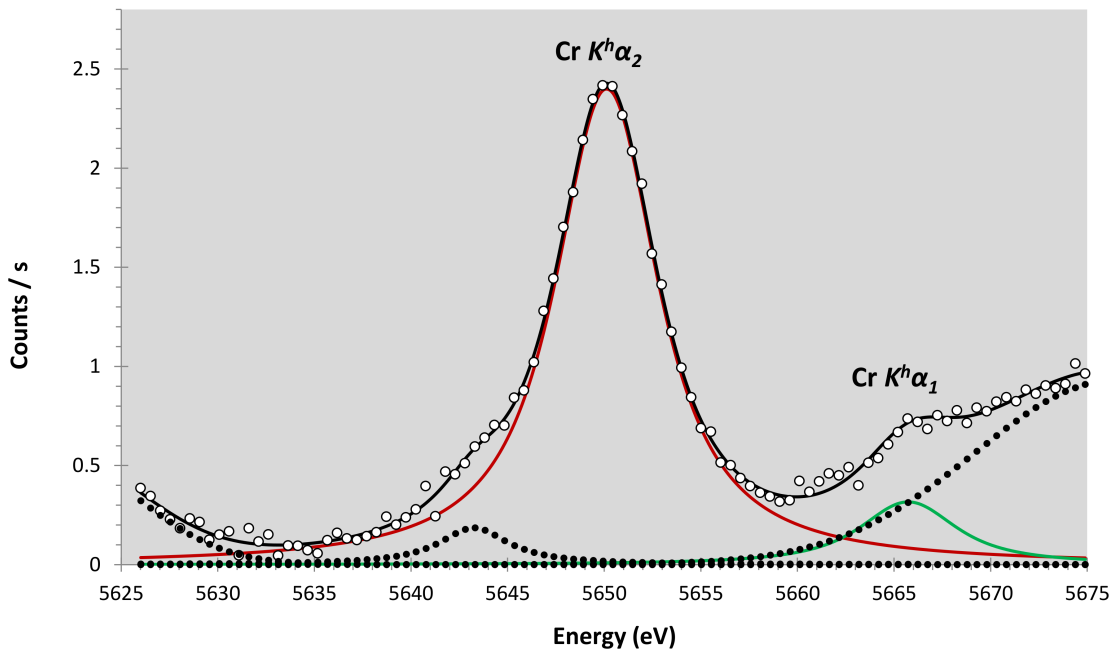


Figure III.9 – Same as Fig. III.8 but measured with a Ge(220) crystal. The black dotted lines represent the tails of the Voigtians used in the fit to account for the intensity enhancement observed with this crystal at both ends of the hypersatellite spectrum.

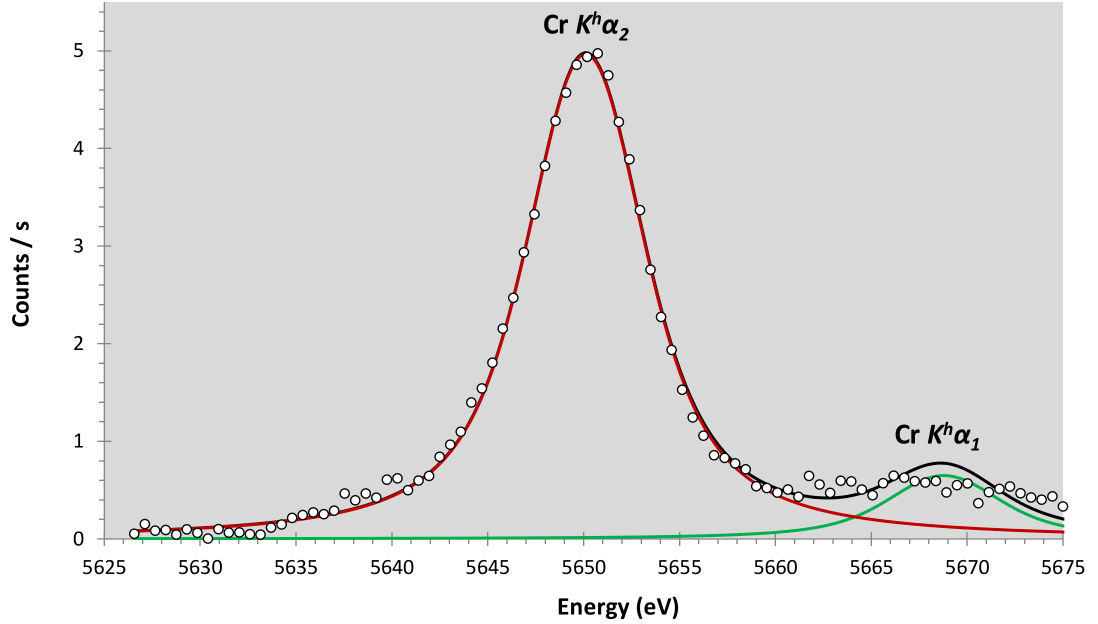


Figure III.10 – Same as Fig. III.8 but measured with a HAPG(004) crystal.

$K^h\alpha$ spectrum of Cu

The measured $K\alpha$ hypersatellite spectrum of Cu is represented in Fig. III.11. The data were collected in second order of diffraction using a Si(220) crystal. The Cu anode X-ray tube was operated at $39.6 \text{ kV} \times 10 \text{ mA}$. As shown in Fig. III.11, despite a longer acquisition time than for Sc and Cr (see Table III.2), the spectrum is rather noisy. The scatter of the experimental data originates from the statistical fluctuations of the subtracted background. The latter is mainly due to the high energy tails of the very strong $K\alpha_{1,2}$ diagram lines. Actually for the $K^h\alpha_2$ hypersatellite of Cu the peak-to-background ratio is only about 1:30, whereas the same ratio amounts to 1:6 for the Cr measurement performed at 60 kV. The hypersatellites were fitted using one Voigtian for each transition. The parameters of both Voigtians could be let free in the fit except the Lorentzian width of the $K^h\alpha_1$ component which was fixed at the width of the $K^h\alpha_2$ hypersatellite minus the difference between the L_2 and L_3 atomic level widths (0.43 eV according to Ref. [161]). When both Lorentzian widths were let free in the fit, it was indeed found that the value of the $K^h\alpha_1$ width was about two times smaller than the one of the $K^h\alpha_1$ hypersatellite, which is not physically sound. In contrast to that, the intensity of the $K^h\alpha_1$ could be let free. The $K^h\alpha_1/K^h\alpha_2$ yield ratio deduced from

the fit is $(33.3 \pm 4.6)\%$, a result well in line with the value of 32.5% predicted by the calculations of Costa *et al.* [175]. The best fit of the Cu hypersatellite spectrum was obtained when a third degree polynomial was employed for the background.

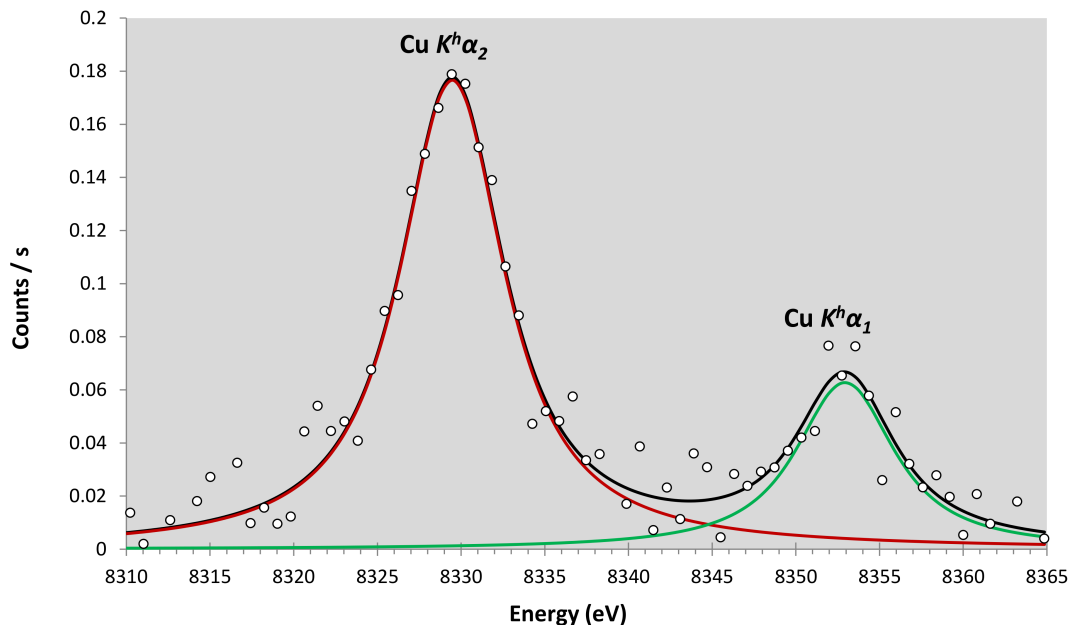


Figure III.11 – Cu $K\alpha$ hypersatellite spectrum measured at $39.6 \text{ kV} \times 10 \text{ mA}$ using a Si(440) crystal. The measured spectrum is represented by the open circles and the total fit by the black solid line. The red and green curves stand for the fits of the $K^h\alpha_2$ and $K^h\alpha_1$ hypersatellites, respectively. The fitted cubic background was subtracted from the spectrum beforehand.

III.2.3 Intensity correction factors

Solid angle

In the von Hamos geometry the solid angle of the spectrometer varies with the Bragg angle. As a consequence the hypersatellites and their parent diagram lines correspond to different solid angles and these differences should be accounted for in the determination of the hypersatellite-to-diagram yield ratios. A dedicated X-ray tracing code was developed to calculate the solid angle of the von Hamos spectrometer operated in the standard geometry (see Ref. [41]). A modified version of this code was used in the present work. The main modification needed in the code to adapt it to the present setup consisted to replace the distance between the crystal and the sample by the distance between the crystal and the the X-ray tube

anode. The latter being not vertical as the sample in the standard geometry, its orientation (see Fig. III.12) had also to be considered in the calculations.

The distance between the anode center and the crystal center is given by:

$$\ell = \frac{R}{\sin(\vartheta)} + \frac{d}{\cos(\vartheta)} + x, \quad (\text{III.2})$$

where R stands for the radius of curvature of the crystal, d is the distance between the slit and the TAF axis (see Fig. II.6), ϑ is the Bragg angle, while the length x reads:

$$x = \sqrt{a^2 + c^2 - 2a \cdot c \cdot \cos(\pi - \varphi)}. \quad (\text{III.3})$$

In the above equation, the lengths a and c and the angle φ are defined in Sect. II.2.2 and shown in Fig. II.6.

The solid angles Ω corresponding to the diagram and hypersatellite X-ray lines measured in the present project are listed in the fourth column of Table III.4. The calculations were performed using weighted average values for the energies of the $K\alpha_{1,2}$ and $K^h\alpha_{1,2}$ doublets. For the $K^h\alpha$ hypersatellite of Sc, the solid angle is bigger than the one of the corresponding diagram line although the distance ℓ is larger for the hypersatellite. This is due to the fact that the solid angle is proportional to the Darwin width [41] and for Sc the latter is bigger for the hypersatellite than for the diagram line. The Darwin widths were calculated by means of the XOP software package [162] assuming all crystals to be perfect except the HAPG one. In the latter case, the Darwin width was replaced in the calculations by the known mosaicity width of the HAPG crystal (1050 μrad).

Effective size of the radiation source

According to the manufacturer, for the employed X-ray tubes the electron beam spot on the anode is 16 mm long and 9 mm wide. As the anode makes an angle of 26 deg. with the horizontal plane, the apparent height of the source is only about 7 mm so that, as shown by the code employed for the calculation of the solid angle, the full length of the electron spot contributes to the production of the observed X-rays with the present setup. In contrast to that, only a narrow part of the electron spot width is seen by the crystal through the 0.2 mm wide slit of the spectrometer. For a point located in the center of the crystal the effective width of the radiation source is given by:

$$w_{\text{eff}} = \frac{\ell \cdot \sin(\vartheta)}{R} \cdot w_s, \quad (\text{III.4})$$

where R is the radius of curvature of the crystal, ϑ the Bragg angle, ℓ the distance between the crystal center and the anode center (see equation III.2) and w_s the width of the slit. For other points located on the crystal surface but not in the center, widths w_{eff} nearly equal to the ones given by the above equation are obtained. For all X-ray lines investigated in this project, the influence of the effective source width on the hypersatellite-to-diagram line yield ratio was found to be smaller than 1% and was thus neglected.

Crystal peak reflectivity

As the peak reflectivity R of the crystal varies as a function of the photon energy, R should also be considered for a correct determination of the hypersatellite-to-diagram line yield ratios. The peak reflectivities of the four crystals were calculated for each transition of interest with the XOP software package [162]. As K X-rays are not polarized, the average values of the peak reflectivities calculated by the XOP code for s-polarized photons (X-rays linearly polarized in the horizontal plane) and p-polarized photons (X-rays linearly polarized in the vertical plane) were used to correct the fitted intensities. The calculated average peak reflectivities R are reported in the fifth column of Table III.4. For p-polarized X-rays, the peak reflectivity tends to zero when the Bragg angle approaches 45 deg. This explains the rather big difference of the peak reflectivities corresponding to the $K\alpha$ ($\vartheta=48.8$ deg.) and $K^{\text{h}}\alpha$ ($\vartheta=44.9$ deg.) lines of Sc observed with the LiF(220) crystal.

CCD efficiency

Above the Si K-edge ($E=1839$ eV) the CCD efficiency decreases smoothly as a function of the photon energy. If one neglects the thin SiO_2 layer which deposits on the front surface of the CCD chip when the latter is exposed to air, the CCD efficiency ε can be determined from the following relation:

$$\varepsilon = 1 - \exp \left[-\mu_{\text{Si}}(E) \cdot \rho_{\text{Si}} \cdot \frac{h_{\text{Si}}}{\sin(\vartheta)} \right], \quad (\text{III.5})$$

where $\mu_{\text{Si}}(E)$ represents the total mass attenuation coefficient (without elastic scattering) of Si for the X-ray of energy E , ρ_{Si} the specific weight of Si, h_{Si} the depletion depth of the CCD chip and ϑ the Bragg angle. The back illuminated deep depleted CCD camera employed in the present experiment was fully characterized in a previous project [154]. In this former work a depletion depth $h_{\text{Si}}=15$ μm was obtained

by fitting with the above formula the experimental efficiencies of the CCD camera for a variety of X-rays ranging from 1 keV to 18 keV.

The CCD efficiencies were calculated with Eq.III.5 for the energies of the diagram and hypersatellite lines investigated in the present project, using the mass attenuation coefficients μ_{Si} reported in the XCOM database [156] and the depletion depth h_{Si} obtained in [154]. The results are presented in the sixth column of Table III.4.

Target self absorption

The correction factor accounting for the self absorption of the $K\alpha$ or $K\beta$ diagram X-rays in the anode can be written as follows:

$$\zeta_{K\alpha, K\beta} = \frac{\int_0^{h_K} \sigma_K[E_e(s)] \cdot e^{-\mu_{K\alpha, K\beta} \cdot s \cdot \text{ctg}(\alpha)} ds}{\int_0^{h_K} \sigma_K[E_e(s)] ds}, \quad (\text{III.6})$$

where $E_e(s)$ represents the kinetic energy of the electron at the depth s , σ_K the cross section of the electron-induced single K-shell ionization, α the angle made by the X-ray tube anode with respect to the horizontal plane (see Fig.III.12) and h_K the depth at which $E_e(h_K)=E_K$, E_K being the threshold energy for a single K-shell ionization.

The correction factor for the self absorption of the $K^h\alpha$ or $K^h\beta$ hypersatellites is similarly given by:

$$\zeta_{K^h\alpha, K^h\beta} = \frac{\int_0^{h_{KK}} \sigma_{KK}[E_e(s)] \cdot e^{-\mu_{K^h\alpha, K^h\beta} \cdot s \cdot \text{ctg}(\alpha)} ds}{\int_0^{h_{KK}} \sigma_{KK}[E_e(s)] ds}, \quad (\text{III.7})$$

with σ_{KK} standing for the cross section of the electron-induced double K-shell ionization and h_{KK} for the depth at which $E_e(h_{KK})=E_{KK}$, E_{KK} corresponding to the threshold energy for a double K-shell ionization.

The energy loss of the electrons in the anode can be parametrized using the following equation:

$$\frac{dE_e}{ds} = -\chi \cdot E_e^{-\nu}, \quad (\text{III.8})$$

where χ and ν are two real positive constants. The latter were determined by a linear least squares fitting of the electron stopping powers calculated with the NIST ESTAR code [180] to the function:

$$\log \left(\left| \frac{dE_e}{ds} \right| \right) = -\nu \cdot \log(E_e) + \log(\chi). \quad (\text{III.9})$$

The results obtained from the fits are presented in Table III.3. As the electron stopping powers calculated by the ESTAR code are given in $[\text{MeV} \cdot \text{cm}^2/\text{g}]$, the obtained penetration depths are expressed in $[\text{g}/\text{cm}^2]$.

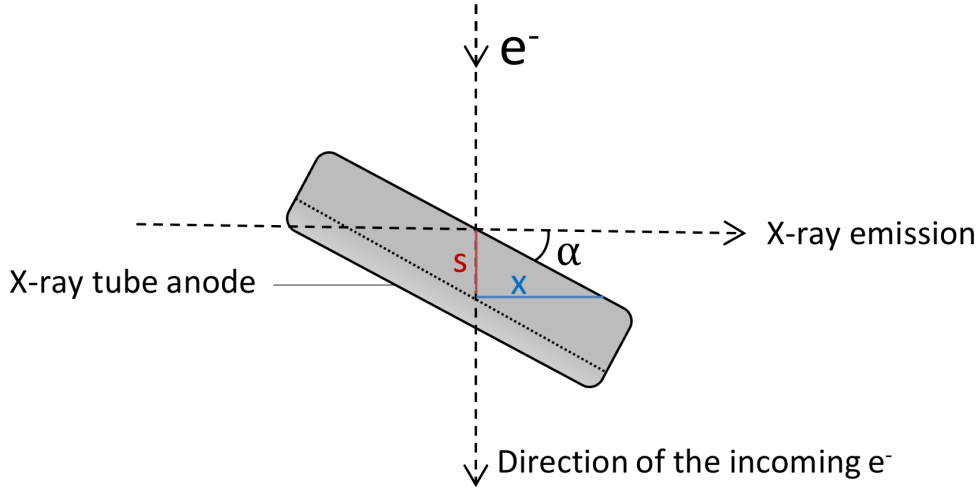


Figure III.12 – Schematic drawing of the X-ray tube anode geometry showing the penetration depth s of the incoming electrons and the distance x travelled by the X-rays to exit the anode. For the three X-ray tubes used in the present project the angle $\alpha=26$ deg.

The kinetic energy of the electrons at the depth s is obtained by integrating equation III.8:

$$E_e(s) = \left\{ [E_e(0)]^{\nu+1} - (\nu + 1) \cdot \kappa \cdot s \right\}^{\frac{1}{\nu+1}}, \quad (\text{III.10})$$

where the initial kinetic energy of the electrons $E_e(0) = e \cdot U$, U representing the high voltage of the X-ray tube. The maximum penetration depths h_K and h_{KK} can be deduced from the above equation. One finds:

$$h_{K, KK} = \frac{[E_e(0)]^{\nu+1} - [E_{K, KK}]^{\nu+1}}{(\nu + 1) \cdot \kappa}. \quad (\text{III.11})$$

The single K-shell ionization threshold energies E_K were taken from the LBNL X-ray data booklet [181], whereas the double K-shell ionization threshold energies E_{KK} were calculated from the following relation:

$$E_{KK}(Z) = 2 \cdot E_K + \varepsilon_K \cdot [E_K(Z + 1) - E_K(Z)], \quad (\text{III.12})$$

where ε_K is a constant comprised between 0 and 1 which accounts for the increase of the electronic screening resulting from the removal of the first 1s electron. The

value $\varepsilon_K=0.570$ reported in [111] for 3d transition elements was adopted. The so-determined maximum penetration depths h_K and h_{KK} are quoted in Table III.3.

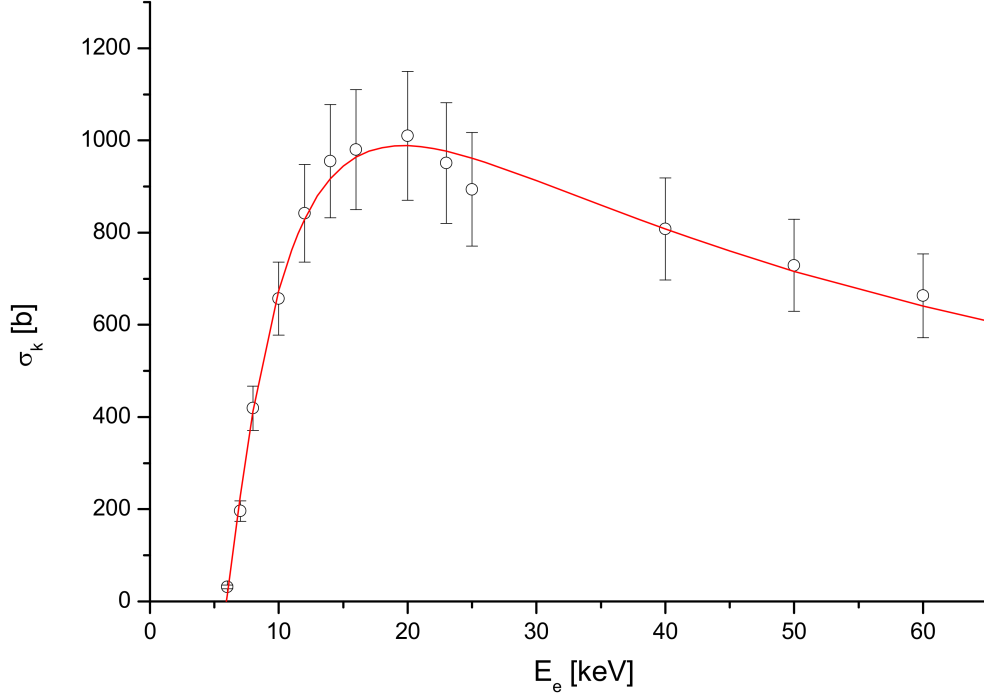


Figure III.13 – Variation of the single K-shell ionization cross section as a function of the electron energy for the case of the Cr X-ray tube operated at 60 kV. The data from Refs. [182, 183] were fitted with a Gryzinsky-like function (solid red line). For details, see text.

The single K-shell ionization cross sections $\sigma_K [E(s)]$ were determined from least squares fits of Gryzinsky-like functions to the experimental values reported by Liu *et al.* [182]. For Cr, however, the experimental cross sections reported in [182] are given only for electron energies below 25 keV and above 2 MeV so that the fitted Gryzinsky functions for the 60 kV measurements were not reliable. The difficulty was circumvented by calculating the cross sections at 40, 50 and 60 keV by means of the universal function proposed in [183]:

$$\sigma_K \cdot E_K^2 \cdot u_K = 1.32 \cdot 10^5 \cdot b_K \cdot [\ln(u_K) + \ln(c_K)], \quad (\text{III.13})$$

where u_K is a dimensionless parameter defined by $u_K=E_e/E_K$. The parameters b_K and c_K were adjusted to match Liu's data below 25 keV. For illustration, the variation of σ_K as a function of the electron energy corresponding to the Cr X-ray tube operated at 60 kV is depicted in Fig. III.13.

Unfortunately, for the double K-shell ionization cross section the same method could not be applied because, to our best knowledge, no experimental cross sections $\sigma_{KK}(E)$ are available in the literature. The problem was solved by making the following approximations in Eq. III.6:

$$\frac{\int_0^{h_K} \sigma_K[E_e(s)] \cdot e^{-\mu_{K\alpha,K\beta} \cdot s \cdot \text{ctg}(\alpha)} ds}{\int_0^{h_K} \sigma_K[E_e(s)] ds} \cong \frac{\bar{\sigma}_K \cdot \int_0^{h_K} e^{-\mu_{K\alpha,K\beta} \cdot s \cdot \text{ctg}(\alpha)} ds}{\bar{\sigma}_K \cdot h_K}, \quad (\text{III.14})$$

where $\bar{\sigma}_K$ represents the average value of the cross section σ_K for the anode layer of thickness h_K . Using the above approximation and calculating the integral, one obtains the following simpler expression for the self absorption correction factor:

$$\tilde{\zeta}_{K\alpha,K\beta} = \frac{1 - e^{-\mu_{K\alpha,K\beta} \cdot h_K \cdot \text{ctg}(\alpha)}}{\mu_{K\alpha,K\beta} \cdot h_K \cdot \text{ctg}(\alpha)}. \quad (\text{III.15})$$

For the hypersatellites, a similar expression is obtained:

$$\tilde{\zeta}_{K^h\alpha,K^h\beta} = \frac{1 - e^{-\mu_{K^h\alpha,K^h\beta} \cdot h_{KK} \cdot \text{ctg}(\alpha)}}{\mu_{K^h\alpha,K^h\beta} \cdot h_{KK} \cdot \text{ctg}(\alpha)}. \quad (\text{III.16})$$

The goodness of the above approximations was probed by comparing for the diagram lines the values obtained for the self absorption correction factors using the exact expression III.6 and the simplified one III.15. For Sc, values $\tilde{\zeta}_{K\alpha}=0.862$ and $\tilde{\zeta}_{K\beta}=0.889$ are found which are close to the exact values $\zeta_{K\alpha}=0.877$ and $\zeta_{K\beta}=0.901$. Similar negative differences of about 1.5% and 3% are found for Cr (26.5 kV measurement) and Cu, respectively, whereas for the 60 kV measurement of Cr the relative deviation is positive and somewhat bigger (5%). To summarize, the relative differences between ζ and $\tilde{\zeta}$ are smaller than 5% in all cases and the above approximations are thus quite acceptable within the 10% uncertainty assumed for the self absorption corrections. The correction factors $\tilde{\zeta}_{K\alpha,K\beta}$ and $\tilde{\zeta}_{K^h\alpha,K^h\beta}$ are listed in Table III.4. For the Sc $K^h\beta$ the correction factor is smaller than for the parent diagram line $K\beta$ because the hypersatellite lies above the K-absorption edge, which leads to a significantly bigger absorption coefficient.

Table III.3 – Parameters α and ν describing the electron energy loss, single and double K-shell ionization threshold energies E_K and E_{KK} and maximum penetration depths h_K and h_{KK} .

Anode	HV [kV]	α	ν	E_K [keV]	E_{KK} [keV]	h_K [mg/cm ²]	h_{KK} [mg/cm ²]
Sc	20.0	0.551	0.716	4.492	9.254	1.186	0.943
Cr	26.5	0.527	0.714	5.989	12.291	2.024	1.607
Cr	60.0	0.527	0.714	5.989	12.291	8.739	8.323
Cu	39.6	0.507	0.707	8.979	18.346	4.296	3.412

Table III.4 – Solid angles Ω , crystal peak reflectivities R , CCD efficiencies ϵ and self-absorption correction factors ζ for the X-ray lines of interest.

Crystal	Target	X-ray line	Ω [μ sr]	R	ϵ	ζ
LiF (200)	Sc	$K\alpha$	5.69	0.829	0.861	0.862
		$K^h\alpha$	6.67	0.584	0.837	0.901
		$K\beta$	5.37	0.680	0.817	0.889
		$K^h\beta$	4.12	0.878	0.784	0.539
Si (220)	Cr	$K\alpha$	3.49	0.799	0.682	0.840
		$K^h\alpha$	3.32	0.834	0.653	0.883
Si (220)	Cr ^a	$K\alpha$	3.49	0.799	0.682	0.506
		$K^h\alpha$	3.32	0.834	0.653	0.556
Ge (220)	Cr ^a	$K\alpha$	8.09	0.819	0.696	0.507
		$K^h\alpha$	7.73	0.851	0.668	0.556
HAPG (004)	Cr ^a	$K\alpha$	43.3	0.206	0.632	0.506
		$K^h\alpha$	43.3	0.217	0.603	0.556
Si (440)	Cu	$K\alpha$	1.14	0.850	0.240	0.803
		$K^h\alpha$	1.03	0.771	0.226	0.852

^aX-ray tube operated at 60 kV \times 10 mA

III.3 Results and discussion

III.3.1 Energies

Absolute energies

The fitted energies of the hypersatellite transitions observed in the present work are presented in Table III.5 where they are compared to other experimental and theoretical values found in the literature. Calibration errors which are included in the total uncertainties are rather large due to the energy differences between the reference lines measured in the direct and standard geometries (see 2nd paragraph of Sect. III.2.1).

In the case of Sc, the $K^h\alpha_2$ and $K^h\alpha_1$ hypersatellite energies obtained in our work are 4296.33(47) eV and 4309.42(94) eV, respectively. These results are in excellent agreement with the experimental values of 4296.31(8) eV and 4309.60(70) eV obtained with synchrotron radiation [32], whereas the theoretical predictions from [184] underestimate present values by about 2.2 and 3.2 eV, respectively. For the weak $K^h\beta$ hypersatellite, an energy of 4727.63(69) eV was found. The latter could not be compared to other values because no experimental nor theoretical value was found in the literature.

For Cr, the measurements were performed at 26.5 kV with the Si(220) crystal and at 60.0 kV with the Si(220), Ge(220) and HAPG(004) crystals. If one compares first the energies of the $K^h\alpha_2$ hypersatellites measured at 60.0 kV, one sees that the values obtained with the three crystals are consistent. The average energy is 5649.99 eV with a standard deviation of 0.19 eV which is somewhat smaller than the calculated error on the average value (0.26 eV). The average energy corresponding to the measurements performed at 60 kV is also consistent with the energy obtained at 26.5 kV (5649.79 eV), the difference (0.20 eV) being about two times smaller than the combined error (0.54 eV). The same holds for the $K^h\alpha_1$ hypersatellite for which an average energy of 5667.25(31) eV is found for the 60 kV measurements which is also consistent with the value of 5666.75(73) eV corresponding to the 26.5 kV measurement. However, the energies found at 60 kV with the three different crystals are not consistent, the average error of the three measurements being about 0.5 eV and the standard deviation 1.2 eV. In our opinion, the scatter of the 60 kV $K^h\alpha_1$ data is due to the poor intensity of this hypersatellite and the resulting high sensitivity of the line centroid to the rather hilly background observed in the

measurements performed with the Cr X-ray tube.

Table III.5 – Hypersatellite energies obtained from the fits. Present values are compared to existing experimental and theoretical results. The experimental values from other sources were obtained by irradiating the targets with synchrotron radiation (SR), Bremsstrahlung from X-ray tubes (BS), heavy-ions (HI) and electrons (e^-). All energies are quoted in [eV]. The notation 4296.33(47/12) means 4296.33 ± 0.47 with an included error from the fit of ± 0.12 .

Target/crystal	X-ray line	Present	Other sources (experimental)	Other sources (theoretical)
Sc/LiF(200)	$K^h_{\alpha_2}$	4296.33(47/12)	4296.31(8) ^a [32]	4294.16 [184]
	$K^h_{\alpha_1}$	4309.42(94/82)	4309.60 (70) ^a [32]	4306.27 [184]
	$K^h_{\beta_{1,3}}$	4727.63(69/52)	-	-
Cr/Si(220)	$K^h_{\alpha_2}$	5649.79(47/12)	5649.2(1) ^a [111]	5648.5 [111]
			5649(2) ^b [52]	5649.2 [52]
			5650(2) ^b [185]	5648.4 [187]
			5645(2) ^d [186]	5647 [184]
	$K^h_{\alpha_1}$	5666.75(73/57)	5665.1(3) ^a [111] 5666(3) ^b [185]	5662 [184] 5666.1 [52]
Cr ^e /Si(220)	$K^h_{\alpha_2}$	5649.72(46/7)		
	$K^h_{\alpha_1}$	5667.26(53/28)		
Cr ^e /Ge(220)	$K^h_{\alpha_2}$	5650.13(45/4)		
	$K^h_{\alpha_1}$	5665.73(55/31)		
Cr ^e /HAPG(004)	$K^h_{\alpha_2}$	5650.11(46/9)		
	$K^h_{\alpha_1}$	5668.78(52/27)		
Cu/Si(440)	$K^h_{\alpha_2}$	8329.46(47/14)	8329.1(1) ^a [111]	8329.3 [111]
			8331(3) ^d [186]	8330 [188]
			8329.9(2) ^c [41]	
	$K^h_{\alpha_1}$	8352.94(58/36)	8352.6(2) ^a [111]	8354 [188]
			8352(3) ^d [186]	
			8351(3) ^d [44]	
		8354.4(6) ^c [41]		

^a SR; ^bBS; ^cHI; ^d e^- ; ^eX-ray tube operated at 60 kV \times 10 mA

The most accurate and most reliable Cr $K^h\alpha_2$ energy is probably the one reported by Diamant *et al.* [111]. Our results obtained with the Si(220) crystal at 26.5 kV and 60 kV are just consistent with this value, whereas the energies determined with the Ge(220) and HAPG(004) crystals are slightly inconsistent (about 0.9 eV bigger for a combined error of 0.5 eV). For the $K^h\alpha_1$ energy, the value obtained in the present work with the Ge(220) crystal is consistent with the value quoted in [111] but the three other values are bigger by 1-3 eV. On the other hand, present $K^h\alpha_2$ and $K^h\alpha_1$ energies are well in line with the experimental results from [52,185] but the latter are characterized by bigger uncertainties (2 eV). In contrast to that, the energy reported by Salem *et al.* [186] for the $K^h\alpha_2$ hypersatellite is more than 4 eV smaller than ours, although the same experimental technique (electron bombardment) was used. Regarding theory, the predictions from [184] are 2.2 eV ($K^h\alpha_2$) and 3.1 eV ($K^h\alpha_1$) smaller than the values from Ref. [111], confirming thus the observation done for the $K^h\alpha$ hypersatellites of Sc. The average value of the other theoretical values is 5648.7 eV for the $K^h\alpha_2$, a value well in line with our results if one assumes a precision of 1 eV for these calculations. It can be noted here that the energies calculated by Aberg [189] more than 30 years ago for the $K^h\alpha_2$ (5649.2 eV) and $K^h\alpha_1$ (5666.1 eV) hypersatellites are very close to the experimental values reported by Diamant *et al.* [111].

For Cu the $K^h\alpha_2$ and $K^h\alpha_1$ hypersatellite energies found in our work are 8329.46(47) and 8352.94(58) eV, respectively. These energies are in good agreement with the experimental values [8329.1(1) and 8352.6(2) eV] obtained by Diamant *et al.* [111] with synchrotron radiation and by Salem [186] with electrons [8331(3) and 8352(3) eV]. The energy reported in [41] for the $K^h\alpha_2$ hypersatellite [8329.9(2) eV] is also well in line with our value, whereas for the $K^h\alpha_2$ hypersatellite the quoted energy [8354.4(6) eV] is 1.5 eV bigger than ours. As for Cr, theoretical predictions are well in line with present energies if uncertainties of 1 eV are assumed in the calculations.

Energy shifts

In several papers only the energy shifts of the hypersatellites with respect to their parent diagram lines are quoted. In theory, energy shifts are in general more reliable than absolute energies because they are not affected by the uncertainty related to the origin of the energy scale. We have thus also determined from our measurements the energy shifts $\Delta\alpha_2=E(K^h\alpha_2)-E(K\alpha_2)$, $\Delta\alpha_1=E(K^h\alpha_1)-E(K\alpha_1)$

and for Sc $\Delta\beta_{1,3}=E(K^h\beta_{1,3})-E(K\beta_{1,3})$. For Cr, the shifts $\Delta\alpha_2$ and $\Delta\alpha_1$ were calculated from the average values of the $K^h\alpha_2$ and $K^h\alpha_1$ energies obtained at 26.5 and 60 kV. However, for the calculation of the average $K^h\alpha_1$ energy, the measurement performed at 60 kV with the HAPG crystal was not considered, the obtained energy being obviously too big. The results are presented in Table III.6 where they are compared to experimental and theoretical data found in the literature. As for the absolute energies, the most reliable and accurate energy shifts are those obtained with synchrotron radiation by Hoszowska *et al.* for Sc [32] and by Diamant *et al.* for Cr and Cu [111]. As the shifts $\Delta\alpha_1$ are not reported in [111], they were determined from the $K^h\alpha_1$ and $K^h\alpha_2$ absolute energies quoted in [111] and the shifts $\Delta=E(K^h\alpha_2)-E(K\alpha_1)$ reported earlier by the same group [190].

As it can be seen in Table III.6, present energy shifts are consistent with all other experimental values, except in two cases. The first one concerns the shift $\Delta\alpha_2$ of Cr for which a deviation of 0.7 eV is observed between our value and the one reported in [111], whereas the combined error amounts to 0.25 eV. No explanation was found for this discrepancy. The second case concerns the shift $\Delta\alpha_1$ of Cu, the value quoted in [41] being 2.0 eV bigger than ours and the deviation 2 times bigger than the combined error. In this case, however, the value quoted in [41] which was obtained with heavy ions is obviously too big as compared to other experimental and theoretical values.

A similar good agreement is observed between present hypersatellite shifts and theoretical predictions. Actually, if one assumes an uncertainty of 1 eV for the calculations, 75% of the theoretical values agree with our shifts within the combined errors and the percentage of agreement is even 100% if the uncertainty of the calculations is increased to 2 eV.

The energies of the diagram and hypersatellite X-ray lines can be written as follows:

$$E(K\alpha_{2,1}) = E_K - E_{L_2,L_3}, \quad (\text{III.17})$$

$$E(K\beta_{3,1}) = E_K - E_{M_2,M_3}, \quad (\text{III.18})$$

$$E(K^h\alpha_{2,1}) = E_{KK} - E_{KL_2,KL_3}, \quad (\text{III.19})$$

$$E(K^h\beta_{3,1}) = E_{KK} - E_{KM_2,KM_3}, \quad (\text{III.20})$$

where E_K , E_{L_2,L_3} and E_{M_2,M_3} represent the energy of the ion with a single $1s^{-1}$, $2p_{1/2,3/2}^{-1}$ and $3p_{1/2,3/2}^{-1}$ vacancy, respectively. Similarly, E_{KK} , E_{KL_2,KL_3} and E_{KM_2,KM_3} stand for the energy of the ion with a double $1s^{-2}$, $1s^{-1}2p_{1/2,3/2}^{-1}$ and

$1s^{-1}3p_{1/2,3/2}^{-1}$ vacancy, respectively. Note that, if the origin of the energy scale corresponds to the total energy of the neutral atom, the excitation energy E_K is equal to the absolute value of the binding energy of the 1s electron in the neutral atom. The energy E_{KK} can be calculated by means of Eq. III.12. Similar approximations can be used for E_{KL_2,KL_3} and E_{KM_2,KM_3} , namely:

$$E_{KL_2,KL_3}(Z) = E_K + E_{L_2,L_3} + \varepsilon_{L_2,L_3} \cdot [E_{L_2,L_3}(Z+1) - E_{L_2,L_3}(Z)], \quad (\text{III.21})$$

$$E_{KM_2,KM_3}(Z) = E_K + E_{M_2,M_3} + \varepsilon_{M_2,M_3} \cdot [E_{M_2,M_3}(Z+1) - E_{M_2,M_3}(Z)], \quad (\text{III.22})$$

where ε_K , ε_{L_2,L_3} and ε_{M_2,M_3} are real constants comprised between 0 and 1 that account for the increase of the electronic screening of the K-, $L_{2,3}$ - or $M_{2,3}$ -subshells resulting from the vacancy in the K-shell. Using above equations, the energy shifts can be written as:

$$\Delta\alpha_2(Z) = \varepsilon_K \cdot [E_K(Z+1) - E_K(Z)] - \varepsilon_{L_2} \cdot [E_{L_2}(Z+1) - E_{L_2}(Z)], \quad (\text{III.23})$$

$$\Delta\alpha_1(Z) = \varepsilon_K \cdot [E_K(Z+1) - E_K(Z)] - \varepsilon_{L_3} \cdot [E_{L_3}(Z+1) - E_{L_3}(Z)], \quad (\text{III.24})$$

$$\Delta\beta_{1,3}(Z) = \varepsilon_K \cdot [E_K(Z+1) - E_K(Z)] - \varepsilon_{M_{2,3}} \cdot [E_{M_{2,3}}(Z+1) - E_{M_{2,3}}(Z)]. \quad (\text{III.25})$$

For 3d elements $\varepsilon_K=0.570$ [111]. As for the screening parameters ε_{L_2} and ε_{L_3} no value could be found in the literature, the latter were determined from the measured shifts $\Delta\alpha_2$ and $\Delta\alpha_1$ by means of a linear least-squares fit method which leads to the following formula [41]:

$$\varepsilon_{L_{2,3}} = \frac{\varepsilon_K \sum_Z [E_K(Z+1) - E_K(Z)] - \sum_Z \Delta\alpha_{2,1}(Z)}{\sum_Z [E_{L_{2,3}}(Z+1) - E_{L_{2,3}}(Z)]}. \quad (\text{III.26})$$

Using the electron binding energies quoted in [181] and the above mentioned value $\varepsilon_K=0.570$, one finds from Eq. III.26 $\varepsilon_{L_2}=0.998$ and $\varepsilon_{L_3}=0.937$, values which are very close to the ones found in [41] for Ca, V, Fe and Cu ($\varepsilon_{L_2}=0.995$ and $\varepsilon_{L_3}=0.935$). On the other hand, if one uses the theoretical shifts $\Delta\alpha_2$ and $\Delta\alpha_1$ reported in [175] for Sc, Ti, V, Fe, Co, Ni, Cu and Zn, one finds $\varepsilon_{L_2}=0.991$ and $\varepsilon_{L_3}=0.945$ which are also close to the results obtained from our experimental shifts. Finally, inserting the screening factors $\varepsilon_K=0.570$, $\varepsilon_{L_2}=0.998$ and $\varepsilon_{L_3}=0.937$ in Eqs III.23 and III.24 and assuming that $\varepsilon_{M_{2,3}} \cong 1$ in Eq. III.25, one obtains the shifts $\Delta\alpha_2$, $\Delta\alpha_1$ and $\Delta\beta_{1,3}$ quoted in the last column of Table III.6. As shown, the values obtained with this simple method are quite satisfactory, the average relative deviation with respect to the present experimental shifts being 0.9% only.

Table III.6 – Energy shifts $\Delta\alpha_2=E(K^h\alpha_2)-E(K\alpha_2)$, $\Delta\alpha_1=E(K^h\alpha_1)-E(K\alpha_1)$ and $\Delta\beta_{1,3}=E(K^h\beta_{1,3})-E(K\beta_{1,3})$ obtained in the present work. Experimental values from other sources as well as theoretical predictions are also quoted for comparison. Values obtained from the formulas III.23 - III.25 are presented in the last column. All energy shifts are quoted in eV.

Target	Shift	Present	Other (exp)	Other (theo)	Eqs. III.23 - III.25
Sc	$\Delta\alpha_2$	210.38(47)	210.36(8) [32]	209.29 [175]	213.7
	$\Delta\alpha_1$	218.69(94)	218.87(70) [32]	216.69 [175]	218.6
	$\Delta\beta_{1,3}$	267.19(83)	-	267.66 [178] 268.3 ^a [188]	265.9
Cr	$\Delta\alpha_2$	244.40(23) ^b	243.7(1) [111]	243.0 [111]	247.5
			243(2) [52]	243.2 [52]	
			245(2) [185]	243.15 ^c [175]	
	$\Delta\alpha_1$	251.78(35) ^d	243.5 [191]	243.4 ^c [188]	253.0
251(3) [185]	249.75 ^c [175]	249.8 ^c [188]			
Cu	$\Delta\alpha_2$	301.62(47)	301.3(1) [111]	301.93 [175]	295.2
			303(3) [44]	301.6 [111]	
			302.7(7) ^e [41]	302.2 ^f [188]	
	$\Delta\alpha_1$	305.12(58)	307.1(8) ^e [41]	305.59 [175]	304.1
	304.9(3) [111, 190]		306.0 ^f [188]		

^alinear interpolation of the shifts reported for Ca (Z=20) and Mn (Z=25)

^baverage values of the measurements performed at 26.5 kV and 60 kV

^clinear interpolation of the shifts reported for V (Z=23) and Fe (Z=26)

^dsame as ^b but the energy obtained with the HAPG crystal was not considered

^eHI experiment

^flinear interpolation of the shifts reported for Mn (Z=25) and Zn (Z=30)

III.3.2 Line widths

As mentioned in Sect. III.2.2 the Lorentzian widths of the $K^h\alpha_1$ hypersatellites had to be kept fixed in the data analysis to get reliable fits but the widths of the $K^h\alpha_2$ and, for Sc, $K^h\beta_{1,3}$ hypersatellites could be used as free fitting parameters. The obtained Lorentzian widths are presented in Table III.7 together with the few other experimental and theoretical data found in the literature. For Cr, the values

obtained at 26.5 kV with the Si(220) crystal [5.32(16) eV] and at 60 kV with the Si(220) [5.71(10) eV], Ge(220) [5.80(38) eV] and HAPG(004) [5.35(12) eV] crystals were found to be nearly consistent within the fit errors so that only the average value is given in Table III.7. For the $K^h\beta$ hypersatellite of Sc, the obtained line width has a big uncertainty due to the very poor intensity of this transition.

As the width of an X-ray transition is equal to the sum of the natural widths of the initial and final atomic states, the line width of the $K^h\alpha_2$ hypersatellite is given by:

$$\Gamma(K^h\alpha_2) = \Gamma_{KK} + \Gamma_{KL_2} \cong (2 \cdot \Gamma_K) + (\Gamma_K + \Gamma_{L_2}) = 3 \cdot \Gamma_K + \Gamma_{L_2}, \quad (\text{III.27})$$

where Γ_K and Γ_{L_2} stand for the widths of the 1s and $2p_{1/2}$ atomic levels.

In the above equation, we have assumed, as proposed by Mossé [192], that the mean lifetime of a double K-shell vacancy state is two times shorter than a single K-shell vacancy state, i.e., $\Gamma_{KK} \cong 2 \cdot \Gamma_K$. For the same reason, $\Gamma_{KL_2} \cong \Gamma_K + \Gamma_{L_2}$. For the $K^h\beta_{1,3}$ hypersatellite, one gets similarly:

$$\Gamma(K^h\beta_{1,3}) \cong 3 \cdot \Gamma_K + \Gamma_{M_{2,3}}, \quad (\text{III.28})$$

where $\Gamma_{M_{2,3}}$ stands for the natural width of the $3p_{1/2,3/2}$ atomic levels.

The widths derived from the above formulas using for the atomic level widths the values reported by Campbell and Papp [161] are presented in the last column of Table III.7. Table III.7 shows that for Cr and Cu present $K^h\alpha_2$ hypersatellite widths are in a quite satisfactory agreement with the experimental values reported in [111] and the theoretical predictions obtained in [193], whereas for Sc the present value overestimates significantly the experimental result quoted in [32] and the theoretical prediction from [193]. This discrepancy is probably due to the close lying and partly overlapping KMM RAE transitions (see Fig. III.5). Regarding the width of the $K^h\beta_{1,3}$ hypersatellite of Sc, it is difficult to make a comment because no experimental nor theoretical data was found in the literature for comparison. Nevertheless, the present value of (7.1 ± 1.1) eV looks quite reasonable since a width of 7.8 eV is reported in [113] for the $K^h\beta_{1,3}$ hypersatellite of Ti, the next higher Z element. A rapid examination of Table III.7 shows also that the widths calculated with Eqs III.27 and III.28 underestimate considerably the real widths of the hypersatellites. This is, however, a well known problem that was already pointed out in several papers (see, e.g., [32, 111]).

Table III.7 – Natural line widths in [eV] of the $K^h\alpha_2$ hypersatellites of Sc, Cr and Cu and $K^h\beta_{1,3}$ hypersatellite of Sc obtained in the present work. For Cr, the indicated value corresponds to the average of the measurements performed at 26.5 kV and 60 kV and the error to the standard deviation of the average. Other available experimental (Exp.) and theoretical (Theo.) values are also quoted for comparison as well as the widths derived from Eqs.III.27 and III.28.

Transition	Present	Other (Exp.)	Theo. [193]	Eq. III.27 - III.28
Sc $K^h\alpha_2$	4.89(13)	3.88(17) [32]	4.24 ^a	2.85
Sc $K^h\beta_{1,3}$	7.1(1.1)	-	-	3.69
Cr $K^h\alpha_2$	5.55(21)	5.7(1) [111]	5.77	3.82
Cu $K^h\alpha_2$	6.95(61)	6.99(34) [111]	7.09 ^b	5.51

^adetermined by a linear interpolation of the values quoted for Ca (Z=20) and V (Z=23)

^bdetermined by a linear interpolation of the values quoted for Co (Z=27) and Zn (Z=30)

III.3.3 Ratios of double-to-single K-shell ionization cross sections

The measured count rates of the hypersatellite X-ray lines can be written as:

$$I_{K^h\alpha,K^h\beta} = I_e \cdot \int_0^{h_{KK}} \sigma_{KK}[E_e(s)] ds \cdot n \cdot \omega_{K^h\alpha,K^h\beta} \cdot \Omega_{K^h\alpha,K^h\beta} \cdot R_{K^h\alpha,K^h\beta} \cdot \varepsilon_{K^h\alpha,K^h\beta} \cdot \tilde{\zeta}_{K^h\alpha,K^h\beta}, \quad (\text{III.29})$$

where I_e represents the number of electrons impacting the anode per second, σ_{KK} the double K-shell ionization cross section, h_{KK} the maximum penetration depth of the electrons producing a double K-shell ionization, n the number of anode atoms per unit volume, $\omega_{K^h\alpha,K^h\beta}$ the partial fluorescence yield of the considered hypersatellite line and $\Omega_{K^h\alpha,K^h\beta}$, $R_{K^h\alpha,K^h\beta}$, $\varepsilon_{K^h\alpha,K^h\beta}$ and $\tilde{\zeta}_{K^h\alpha,K^h\beta}$ the corresponding solid angle of the spectrometer, crystal peak reflectivity, CCD efficiency and self absorption correction factor, respectively. The partial fluorescence yield $\omega_{K^h\alpha,K^h\beta}$ is given by:

$$\omega_{K^h\alpha,K^h\beta} = \frac{W_{K^h\alpha,K^h\beta}}{W_{K^h\alpha} + W_{K^h\beta}} \cdot \omega_{KK}, \quad (\text{III.30})$$

where $W_{K^{h\alpha}}$ and $W_{K^{h\beta}}$ stand for the radiative transition probability of the $K^{h\alpha}$ and $K^{h\beta}$ hypersatellites and ω_{KK} for the fluorescence yield of the doubly ionized K-shell atom.

Similarly, the measured count rates of the diagram lines read:

$$\begin{aligned} I_{K\alpha,K\beta} &= \frac{1}{A} \cdot I_e \cdot \int_0^{h_K} \sigma_K[E_e(s)] ds \cdot n \cdot \omega_{K\alpha,K\beta} \cdot \Omega_{K\alpha,K\beta} \cdot R_{K\alpha,K\beta} \cdot \varepsilon_{K\alpha,K\beta} \cdot \tilde{\zeta}_{K\alpha,K\beta} \\ &= \frac{1}{A} \cdot I_e \cdot \int_0^{h_{KK}} \sigma_K[E_e(s)] ds \cdot \frac{\int_0^{h_K} \sigma_K[E_e(s)] ds}{\int_0^{h_{KK}} \sigma_K[E_e(s)] ds} \cdot n \cdot \omega_{K\alpha,K\beta} \cdot \Omega_{K\alpha,K\beta} \cdot R_{K\alpha,K\beta} \cdot \varepsilon_{K\alpha,K\beta} \cdot \tilde{\zeta}_{K\alpha,K\beta}, \end{aligned} \quad (\text{III.31})$$

where A represents the attenuation factor of the absorber used for the measurement of the considered diagram line (see Sect. III.1.2).

Note that the contribution of the bremsstrahlung to the production of the observed hypersatellite and diagram X-ray yields was assumed to be negligibly small and thus omitted in Eqs III.29 and III.31. Actually, this contribution was estimated in [53] and found to be less than 2% of the X-ray yield produced by electron impact, i.e., far below the uncertainties related to the X-ray intensities measured in the present work.

Using the definitions

$$\bar{\sigma}_K = \frac{1}{h_{KK}} \cdot \int_0^{h_{KK}} \sigma_K[E_e(s)] ds \quad (\text{III.32})$$

$$\bar{\sigma}_{KK} = \frac{1}{h_{KK}} \cdot \int_0^{h_{KK}} \sigma_{KK}[E_e(s)] ds \quad (\text{III.33})$$

$$\chi = \frac{\int_0^{h_K} \sigma_K[E_e(s)] ds}{\int_0^{h_{KK}} \sigma_K[E_e(s)] ds} \quad (\text{III.34})$$

and dividing Eq. III.29 by Eq. III.31 one finds the relative intensity of the hypersatellite line with respect to the parent diagram line:

$$\frac{I_{K^{h\alpha},K^{h\beta}}}{A \cdot I_{K\alpha,K\beta}} = \frac{\bar{\sigma}_{KK}}{\bar{\sigma}_K} \cdot \frac{1}{\chi} \cdot \frac{\omega_{K^{h\alpha},K^{h\beta}}}{\omega_{K\alpha,K\beta}} \cdot \frac{\Omega_{K^{h\alpha},K^{h\beta}}}{\Omega_{K\alpha,K\beta}} \cdot \frac{R_{K^{h\alpha},K^{h\beta}}}{R_{K\alpha,K\beta}} \cdot \frac{\varepsilon_{K^{h\alpha},K^{h\beta}}}{\varepsilon_{K\alpha,K\beta}} \cdot \frac{\tilde{\zeta}_{K^{h\alpha},K^{h\beta}}}{\tilde{\zeta}_{K\alpha,K\beta}}. \quad (\text{III.35})$$

Finally, the double-to-single K-shell ionization cross section ratio P_{KK} can be derived from Eq. III.35:

$$P_{KK} = \frac{\bar{\sigma}_{KK}}{\bar{\sigma}_K} = \left[\frac{I_{K^{h\alpha},K^{h\beta}}}{A \cdot I_{K\alpha,K\beta}} \right]_{\text{cor}} \cdot \frac{\omega_{K\alpha,K\beta}}{\omega_{K^{h\alpha},K^{h\beta}}} \cdot \chi, \quad (\text{III.36})$$

where

$$\left[\frac{I_{K^h\alpha, K^h\beta}}{A \cdot I_{K\alpha, K\beta}} \right]_{\text{cor}} = \frac{I_{K^h\alpha, K^h\beta}}{A \cdot I_{K\alpha, K\beta}} \cdot \frac{\Omega_{K\alpha, K\beta}}{\Omega_{K^h\alpha, K^h\beta}} \cdot \frac{R_{K\alpha, K\beta}}{R_{K^h\alpha, K^h\beta}} \cdot \frac{\varepsilon_{K\alpha, K\beta}}{\varepsilon_{K^h\alpha, K^h\beta}} \cdot \frac{\tilde{\zeta}_{K\alpha, K\beta}}{\tilde{\zeta}_{K^h\alpha, K^h\beta}}. \quad (\text{III.37})$$

The corrected $K^h\alpha$ and $K^h\beta$ relative intensities which were calculated with the solid angles, crystal peak reflectivities, CCD efficiencies and self absorption correction factors given in Table III.4 are presented in Tables III.8 and III.9, respectively. To show the size of the corrections, the uncorrected relative intensities are also listed. A relative uncertainty of 5% was assumed for each correction factor except for the self absorption $\tilde{\zeta}$ for which a relative uncertainty of 10% was estimated, due to the additional uncertainty related to the approximation $\tilde{\zeta} \cong \zeta$ made in the calculations (see subsection "Target self absorption" in Sect. III.2.3).

Table III.8 – Measured and corrected relative intensities of the $K\alpha$ hyper-satellites (see text)

Target/Crystal	$[I(K^h\alpha_{1,2})/[A \times I(K\alpha_{1,2})]]_{\text{fit}}$	$[I(K^h\alpha_{1,2})/[A \times I(K\alpha_{1,2})]]_{\text{cor}}$
Sc/LiF(200)	$1.14(7) \times 10^{-4}$	$1.35(20) \times 10^{-4}$
Cr/Si(220)	$0.82(7) \times 10^{-4}$	$0.87(14) \times 10^{-4}$
Cr ^a /Si(220)	$1.04(2) \times 10^{-4}$	$0.99(13) \times 10^{-4}$
Cr ^a /Ge(220)	$0.84(12) \times 10^{-4}$	$0.80(16) \times 10^{-4}$
Cr ^a /HAPG(004)	$0.70(2) \times 10^{-4}$	$0.63(8) \times 10^{-4}$
Cu/Si(440)	$0.50(4) \times 10^{-4}$	$0.62(10) \times 10^{-4}$

^aX-ray tube operated at 60 kV \times 10 mA

Table III.9 – Same as Table III.8 but for the $K\beta$ hypersatellite of Sc.

Target/Crystal	$[I(K^h\beta_{1,3})/[A \times I(K\beta_{1,3})]]_{\text{fit}}$	$[I(K^h\beta_{1,3})/[A \times I(K\beta_{1,3})]]_{\text{cor}}$
Sc/ LiF(200)	$1.08(19) \times 10^{-4}$	$1.87(41) \times 10^{-4}$

For the Cr measurements performed at 60 kV with three different crystals, the corrected intensity ratios should be the same but, as shown by Table III.8, there is a large scatter of the results. However, in view of the rather big uncertainties characterizing the three ratios, this scatter is not really surprising. Actually, the standard deviation of the three ratios is 0.15×10^{-4} , a value which is comparable to the average uncertainty of the three measurements which is equal to 0.12×10^{-4} .

The partial fluorescence yields were calculated using the fluorescence yields ω_K for singly ionized atoms from Kostroun [194] and the fluorescence yields ω_{KK} for doubly ionized atoms from Natarajan [187]. The relative intensities $I(K\alpha, K\beta)/I(K\alpha + K\beta)$ of the diagram lines were determined from the radiative emission rates quoted by Scofield [174] and the relative intensities $I(K^{h\alpha}, K^{h\beta})/I(K^{h\alpha} + K^{h\beta})$ of the hypersatellites from the rates reported for Al and Sc by Costa [178]. The correction factors χ (see Eq. III.34) for the difference in the effective thicknesses of the anode layers contributing to the production of the diagram lines and hypersatellites, respectively, were computed by integrating numerically the Gryzinsky-like functions used to reproduce the variation of σ_K as a function of the electron energy. The values obtained for all these parameters are presented in Tables III.10.

Table III.10 – Fluorescence yields ω_K and ω_{KK} for singly and doubly K-shell ionized atoms, resulting partial fluorescence yield ratios $\omega_{K^{h\alpha}, K^{h\beta}}/\omega_{K\alpha, K\beta}$ and correction factors χ accounting for the effective source thicknesses.

Target	ω_K [194]	ω_{KK} [187]	$\frac{W_{K\alpha, K\beta}}{W_{K\alpha} + W_{K\beta}}$ [174]	$\frac{W_{K^{h\alpha}}}{W_{K^{h\alpha}} + W_{K^{h\beta}}}$ [178]	$\frac{\omega_{K\alpha, K\beta}}{\omega_{K^{h\alpha}, K^{h\beta}}}$	χ
Sc ^a	0.183	0.212 ^b	0.900	0.857	0.906	1.118
Sc ^c	0.183	0.212	0.100	0.143	0.604	1.118
Cr	0.276	0.316	0.897	0.852 ^d	0.920	1.151
Cr ^e	0.276	0.316	0.897	0.852 ^d	0.920	1.035
Cu	0.448	0.478 ^f	0.892	0.848 ^d	0.986	1.126

^a $K^{h\alpha}$ hypersatellite

^blinear interpolation from the values reported for Ca (Z=20) and Ti (Z=22)

^c $K^{h\beta}$ hypersatellite

^dlinear extrapolation from the values reported for Al (Z=13) and Sc (Z=21)

^e60 kV measurement

^flinear interpolation from the values reported for Fe (Z=26) and Zn (Z=30)

Finally, inserting above values in Eq. III.36, one obtains the double-to-single ionization cross section ratios presented in Table III.11. As shown, for Sc the values obtained from the relative intensities of the $K^{h\alpha}$ and $K^{h\beta}$ hypersatellites are fully consistent. For the Cr measurements performed at 60 kV, the ratio P_{KK} was calculated from the average relative intensity (0.81×10^{-4}) of the hypersatellites measured with the three crystals using the standard deviation of the three measurements (0.15×10^{-4}) as uncertainty. One sees that the value P_{KK} obtained for

Cr at 60 kV is about 20% smaller than the one measured at 26.5 kV.

Table III.11 – Double-to-single K-shell ionization cross-section ratios P_{KK} .

Target	P_{KK}
Sc ^a	$1.37(22) \times 10^{-4}$
Sc ^b	$1.26(29) \times 10^{-4}$
Cr	$0.92(16) \times 10^{-4}$
Cr ^c	$0.77(13) \times 10^{-4}$ ^d
Cu	$0.69(12) \times 10^{-4}$

^aK α hypersatellite

^bK β hypersatellite

^cX-ray tube operated at 60 kV

^daverage value of the P_{KK} ratios obtained with the three crystals

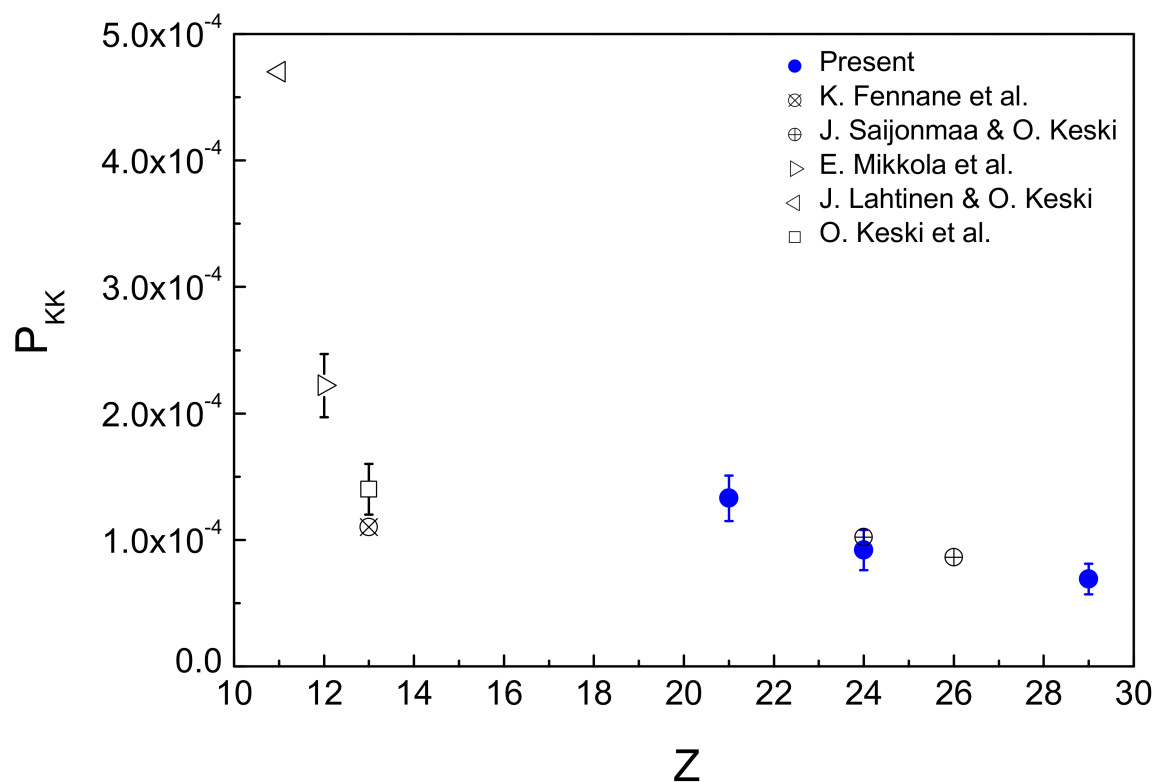


Figure III.14 – Double-to-single K-shell ionization cross-section ratios versus atomic number for electron impact. ● present results, ⊗ [31], ⊕ [53], ▷ [42], ◁ [54], □ [195]

Present P_{KK} values are compared with other available experimental data in Figs. III.14 and III.15. Fig. III.14 presents results obtained with electrons only, whereas

in Fig. III.15 results obtained from measurements performed with photons and electrons as well as data derived from nuclear electron capture (EC) are plotted. In our experiment, the dimensionless parameter $\eta = E_e/E_{KK}$ amounts to about 2.2 (see Table III.3) for Sc, Cr (26.5 kV measurement) and Cu and to about 4.9 for the 60 kV measurement of Cr. As it is more sound to compare the ratios P_{KK} of different elements for the same η , the present Cr value depicted in Figs. III.14 and III.15 corresponds to the 26.5 kV measurement. For Sc, the weighted average $[(1.33 \pm 0.18) \times 10^{-4}]$ of the P_{KK} values derived from the $K^{h\alpha}$ and $K^{h\beta}$ hypersatellites is plotted.

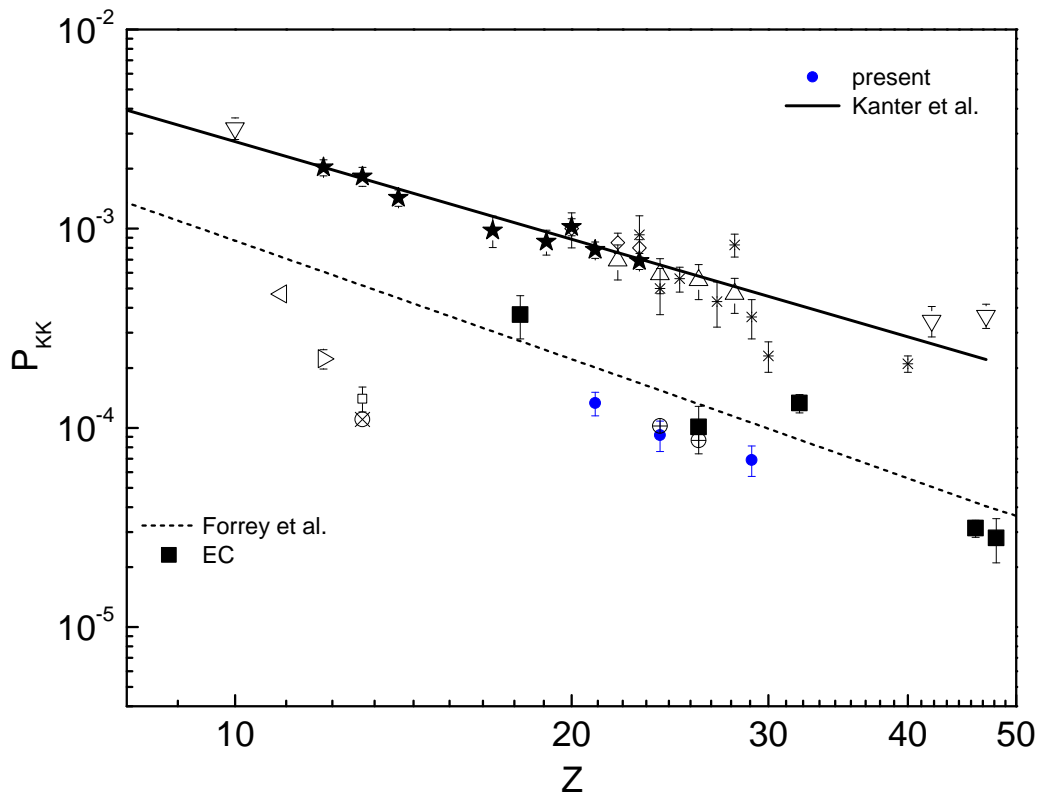


Figure III.15 – Double-to-single K-shell ionization cross-section ratios versus atomic number for electron impact, photoionization and nuclear electron capture (EC). Electron impact: ● present results, ⊕ [53], ▷ [42], ◁ [54], □ [195], ⊗ [31]. Photoionization: ◊ [196], * [113, 197], △ [185], ▽ [198], × [46, 199], ★ [32]. Nuclear electron capture: ■ [200]. Also shown are the photoabsorption asymptotic limits of Forrey *et al.* [201] (dashed line) and the power-law fit of Kanter *et al.* [198, 202] of the photoionization data (solid line).

Fig. III.14 shows that our result for Cr agrees well with the one obtained by

Saijonmaa and Rahkonen [53] for a similar excitation energy ($\eta \cong 2$). On the other hand, a power-law fit of the few electron data found in the literature for elements $11 \leq Z \leq 26$ shows a Z^{-2} dependence of P_{KK} . This is well confirmed by our results since a double logarithmic fit of the Sc, Cr and Cu P_{KK} ratios leads to a straight line whose slope is -1.999. Furthermore, the P_{KK} ratio deduced from the Cr measurements performed at 60 kV ($\eta=4.9$) is smaller by about 20% than the value obtained at 26.5 kV ($\eta=2.2$). This suggests that the maximum value of P_{KK} occurs below 60 keV.

As a result of the combined influence of the TS1 and shake processes, the double-to-single photoionization cross section ratio P_{KK} increases rapidly with the excitation energy, levels off in the so-called broad maximum region and then drops smoothly with growing energy to reach an asymptotic value corresponding to the photoabsorption shake probability. The latter can be determined via the nuclear electron capture process (EC) in which the first 1s electron is captured by the nucleus and the second one is ejected as a result of a shake process produced by the abrupt change of the nuclear Coulomb potential. Most of the photon data depicted in Fig. III.15 correspond to excitation energies belonging to the broad maximum region.

In the case of the double ionization induced by electron impact, the atomic electrons are ejected with a continuous energy distribution but most of them leave the atom with small velocities even at high excitation energies. As a consequence, the shake contribution to the double ionization is significantly smaller than for photons and the TS1 process, which tends rapidly to zero for growing energies in photoionization, still contributes to the double ionization at the asymptotic energy limit [203–205]. A further difference between photon and electron excitation resides in the fact that for electrons the direct multiple ionization is possible. In contrast to photons, an electron can indeed interact sequentially with two bound electrons producing a direct double ionization (TS2 process). Despite of that, Fig. III.15 shows that the P_{KK} values obtained in electron measurements are about 10 times lower than those obtained with photons. Fig. III.15 shows further that the electron data lie below the Forrey fit of the EC data [201], indicating that the contribution of the shake process is much smaller for electron impact than in photoionization.

III.4 Summary and concluding remarks

We have investigated the radiative decay of double K-shell vacancy states produced in solid Sc, Cr and Cu targets by impact with electrons. The K-hypersatellite X-ray transitions were measured in-house with the von Hamos curved crystal spectrometer of Fribourg operated in the direct geometry, using the Sc, Cr and Cu anodes of X-ray tubes as targets. The high voltages of the X-ray tubes were chosen so that the kinetic energy E_e of the electrons at the front surface of the anode was about 2 times higher than the threshold energy E_{KK} for the double K-shell ionization. In order to probe the evolution of the relative intensities of the hypersatellites as a function of the electron energy and check the reliability of the experimental setup, the Cr measurements were also performed at a higher voltage (60 kV) and with three different crystals.

The measured hypersatellite spectra were analysed by means of a least-squares fitting program using Voigt profiles to fit the diagram and hypersatellite lines. The major difficulties encountered in the data analysis were related to the poor peak-to-background ratios characterizing the measured hypersatellites and the bumps observed in the background as a result of intensity inhomogeneities of the electron beam spots on the X-ray tube anodes. Despite of this, the energies, line widths and relative intensities of the hypersatellite transitions could be determined from the fits.

The values obtained for the absolute energies of the hypersatellites and the energy shifts of the latter with respect to their parent diagram lines were found to be in good agreement with other available experimental values and theoretical predictions, except for the $K^h\alpha_1$ hypersatellite of Cr. In this case, the scatter of the values obtained with the three different crystals was found to be more than two times bigger than the errors of the individual measurements and the average energy about 2 eV bigger than the value obtained with synchrotron radiation.

The Lorentzian widths of the weak $K^h\alpha_1$ hypersatellites had to be kept fixed in the fits so that only the natural widths of the hypersatellites $K^h\alpha_2$ of Sc, Cr and Cu and $K^h\beta_{1,3}$ of Sc could be determined. For Cr and Cu, the obtained widths were found to be in good agreement with the ones determined at synchrotron radiation facilities and those predicted by MCDF calculations. For Sc, however, the value obtained for the $K^h\alpha_2$ hypersatellite is about 1.3 times bigger than the synchrotron radiation value and 1.2 times bigger than the theoretical prediction.

The deviation was explained by the close lying and partly overlapping KMM RAE transitions. For the width of the extremely weak $K^h\beta_{1,3}$ hypersatellite of Sc, no other experimental value nor theoretical prediction could be found but the obtained value (7.1 eV) seems to be well in line with the width of 7.8 eV reported in the literature for the next heavier element (Ti).

The main objective of the present project was to determine the double-to-single K-shell ionization cross section ratios P_{KK} and to compare the latter with other available experimental values. The P_{KK} ratios were deduced from the relative intensities of the hypersatellites corrected beforehand for the energy dependent solid angle of the von Hamos spectrometer, crystal peak reflectivity, CCD efficiency and self absorption in the target. Our results are well in line with the ratios found in the literature for 3d elements, namely Cr and Fe, that were measured at similar relative electron energies ($\eta = E_e/E_{KK} \cong 2$). A power-law fit of the few electron data found in the literature for elements $11 \leq Z \leq 26$ shows a Z^{-2} dependence of P_{KK} . This could be well confirmed by our results. A double logarithmic plot of the Sc, Cr and Cu P_{KK} ratios leads indeed to a straight line whose slope is -1.999. Furthermore, the P_{KK} ratio deduced from the Cr measurements performed at 60 kV ($\eta=4.5$) was found to be smaller by about 20% than the value found at 26.5 kV ($\eta = 2.2$). This suggests that the maximum of the $P_{KK}(E_e)$ function lies below 60 keV. Our results were also compared to other experimental ratios obtained with photons and radioactive sources decaying via the nuclear electronic capture (EC). From this comparison, it was found that present P_{KK} ratios deduced from electron impact measurements are about 10 times smaller than those obtained by photon impact, confirming thus an observation made in all former similar investigations. It was also found that the P_{KK} found in the present study like the ones obtained in other electron impact measurements lie below the EC data, indicating that the contribution of the shake process to the electron induced double K-shell ionization is negligibly small.

CHAPTER IV

**Chemical sensitivity of
photoinduced $K^{h\beta}$
hypersatellite transitions in
Cr compounds**

IV.1 Experiment

IV.1.1 Beam line setup

The experiment was performed at the Stanford Synchrotron Radiation Lightsource (SSRL) beam-line 6-2, and for the measurements of the X-ray emission spectra the seven-crystal Johann-type hard X-ray spectrometer [92] was employed. Beam-line 6-2 is equipped with two liquid nitrogen cooled Si(111)- and Si(311)-crystal monochromators, and the incident x-ray beam is provided by the 0.9 T 56-pole wiggler. The high flux and monochromaticity of the photon beam, and the wide solid angle of detection allow studying weak atomic processes even for relatively low-density samples. Rh-coated mirrors were positioned before and after the monochromators for focusing and collimation of the beam. A beam size of about 170 μm vertical and 400 μm horizontal was delivered at the sample position. The incident beam flux was typically $1\text{-}2 \times 10^{13}$ photons/s. For the measurements of the Cr $K\beta$ spectra ($K\beta_{1,3}$, $K\beta_{2,5}$, $K\beta''$) the photon beam energy was set to 6.1 keV, whereas for the $K^h\beta_{1,3}$ hypersatellites the beam energy of 13.7 keV close to the maximum of the double K-shell photoionization cross section for Cr was chosen.

IV.1.2 Johann-type hard X-ray spectrometer

The schematic of the seven-crystal Johann-type hard X-ray spectrometer [92] is depicted in Fig. IV.1 and a photograph of the experimental setup is shown in Fig. IV.2. The Johann geometry is semi-focusing in which the crystal planes are bent to a radius $2R$, where R is the radius of the Rowland circle but the crystal inner surface is not grounded. In order to reduce the geometrical effects [88], the Rowland circle was placed on a vertical plane as the vertical beam size was smaller. The analyzer crystals were spherically bent to a radius of 1 m with a projected diameter of 100 mm. All crystal modules are placed on the common plate that moves vertically with the help of stepping motors as shown in Fig. IV.2, and each crystal module can move along its normal direction so that the crystals can follow the exact Rowland circle as the spectrometer is scanned. The spectrometer captures a backscattering Bragg angular range of 88° to 74° .

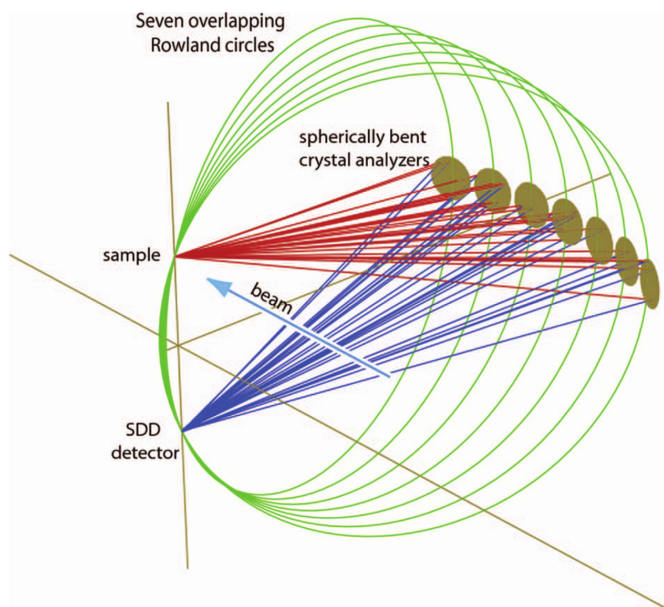


Figure IV.1 – Schematic drawing of the overlapping Rowland circles and seven spherically bent crystal analyzers (taken from Ref. [92]).

In the present experiment, five Ge(440) analyzer crystals for the Cr $K\beta$ spectra and seven Si(333) crystals for the $K^h\beta_{1,3}$ transitions were placed on intersecting Rowland circles of 1 m of diameter as shown in Fig. IV.1. The Bragg angle for the Cr $K\beta_{1,3}$ was 85.9° and for the $K^h\beta_{1,3}$ lines 82.3° . The diffracted X-rays from all crystals were recorded simultaneously with a SDD detector placed on the vertical axis. The energy resolution of the SDD at the full width at half maximum (FWHM) was about 150 eV at 5.9 keV. As the spectrometer was operated at atmospheric pressure a helium filled bag was placed between the crystal analyzers and the detector to minimize the attenuation and the diffuse scattering of X-rays. For each energy point the incident photon beam intensity was monitored with ionization chambers. The photon beam energy was calibrated using the K-edge energies of Cr and Mn as references. The energy resolution and the energy calibration of the spectrometer were determined from the elastically scattered peaks in the photon energy domain of interest. For the Cr $K\beta$ transitions the experimental resolution (FWHM) was 0.47 eV and for the $K^h\beta_{1,3}$ lines 0.49 eV. The collection time per energy point was 1 s for the $K\beta_{1,3}$, and 5 s for the VtC and $K^h\beta_{1,3}$ transitions. The samples were in form of pellets from compressed high-purity powders from Aldrich Chemical Co., Inc., Milwaukee, WI.

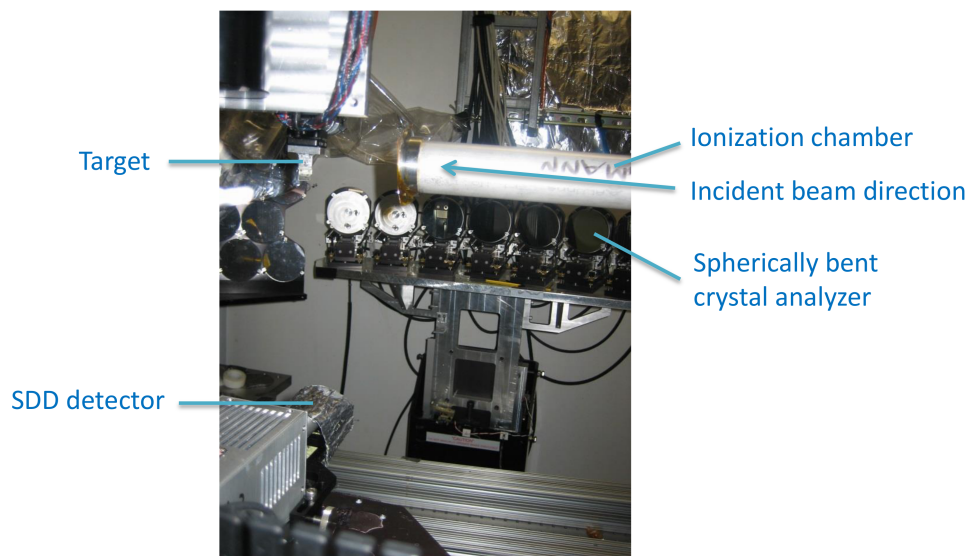


Figure IV.2 – Photograph of the experimental set-up showing the 7-crystal Johann-type hard X-ray spectrometer [92] at the beam-line 6-2 of SSRL equipped with 5 Ge(440) analyzer crystals.

IV.2 Data analysis

The spectra were fitted by means of a least squares fitting program using the software package named PeakFit[®]. Voigt functions were employed for all the fits because they correspond to the convolution of the Gaussian and Lorentzian functions [173] which represent the instrumental response of the spectrometer and the natural line shape of the transitions, respectively. Prior to fitting, each spectrum was normalized with the photon beam intensity and the total acquisition time.

IV.2.1 $K\beta$ diagram spectra

The electronic configuration of Cr in the ground state is $[Ar] 3d^5 4s^1$, with 5 unpaired electrons in the 3d shell. The $K\beta_{1,3}$ line is generated in the $3p \rightarrow 1s$ transition and is the strongest among the $K\beta$ X-ray lines. The unpaired electron in the $3p^{-1}$ state is strongly coupled with the unpaired electrons in the partially filled 3d shell. Due to the $3p3d$ exchange interaction two transitions are possible depending on the spin orientation of the unpaired electron in the $3p^{-1}$ state with respect to that of the 3d electrons. According to the dipole selection rules, if the spins are parallel the $K\beta_{1,3}$ transition line will occur and if the spins are anti-parallel then the $K\beta'$ satellite line of lower energy will originate. A shoulder on the low energy side of the main $K\beta_{1,3}$ line arises when a 3d electron flips its spin and is denoted as $K\beta_x$ [206]. The $K\beta_5$ transition is dipole forbidden in free atoms. In solids, the $K\beta_{2,5}$ line reflects the valence band and corresponds to transitions from the metal 3d or 4p states (hybridized with the ligand 2p or 3p orbitals in case of compounds) to the metal 1s state [71]. For oxide compounds, the $K\beta''$ crossover transition from the ligand 2s orbital states mixed with np -metal states to the 1s state of the central atom can be identified between the $K\beta_{1,3}$ line and the valence-to-core $K\beta_{2,5}$ transitions. The energy of the $K\beta''$ line gives information about the type of ligand that is bound to the central atom and its intensity is related to the number of ligand atoms and the distance between them and the emitting atom [207].

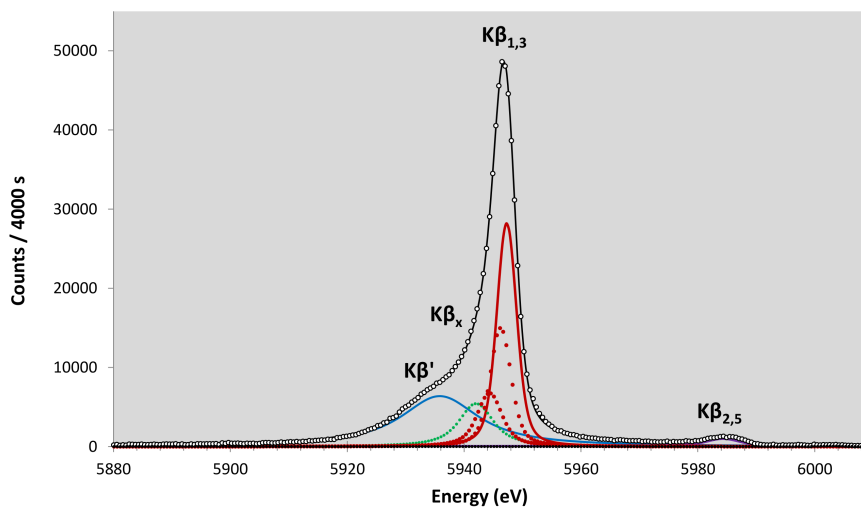


Figure IV.3 – Fit of the $K\beta_{1,3}$ spectrum of Cr metal (Cr^0) collected in-house with the von Hamos spectrometer of Fribourg [151]. Shown are the background subtracted experimental spectrum (open circles), the total fit (black curve) together with the five individual Voigt components of the fit: the red solid line and the two red dotted lines for the main $K\beta_{1,3}$ transition, the green dotted line for the $K\beta_x$ transition and the blue line for the $K\beta'$ transition.

$K\beta_{1,3}$ diagram transitions

In Figs. IV.4, IV.5, IV.6 and IV.7 we present the $K\beta_{1,3}$ X-ray emission spectra for Cr-metal (Cr^0), and Cr compounds (Cr_2O_3 , CrO_2 and $\text{K}_2\text{Cr}_2\text{O}_7$) measured at SSRL. The Cr-metal and Cr-compound spectra were all fitted with four Voigtians. Three Voigt functions were used for the $K\beta_{1,3}$ main component keeping the instrumental response function width fixed and all other parameters free. Since the limited angular range of the X-ray spectrometer does not allow for Bragg angles higher than 88 degrees, the $K\beta'$ transition could not be measured with the Ge(440) crystal. For a reliable fit of the main $K\beta_{1,3}$ line the $K\beta'$ transition should be included. The fitting parameters for the $K\beta'$ transition were therefore determined from the Cr-metal $K\beta_{1,3}$ spectrum collected in-house with the von Hamos spectrometer of Fribourg [151]. The fit of the $K\beta_{1,3}$ X-ray emission spectrum of Cr-metal is shown in Fig.IV.3. To obtain the values for the energy, width, and intensity of the $K\beta'$ line the spectrum was analyzed using the fitting parameters reported by G. Hölzer *et al.* [104]. To account for the $K\beta'$ transitions in the measured spectra of Cr-compounds, the energies, Lorentzian and Gaussian widths were

fixed, while the intensities were let free in the fit where the relative energy shifts with respect to the peak energy of $K\beta_{1,3}$ were adopted from [107].

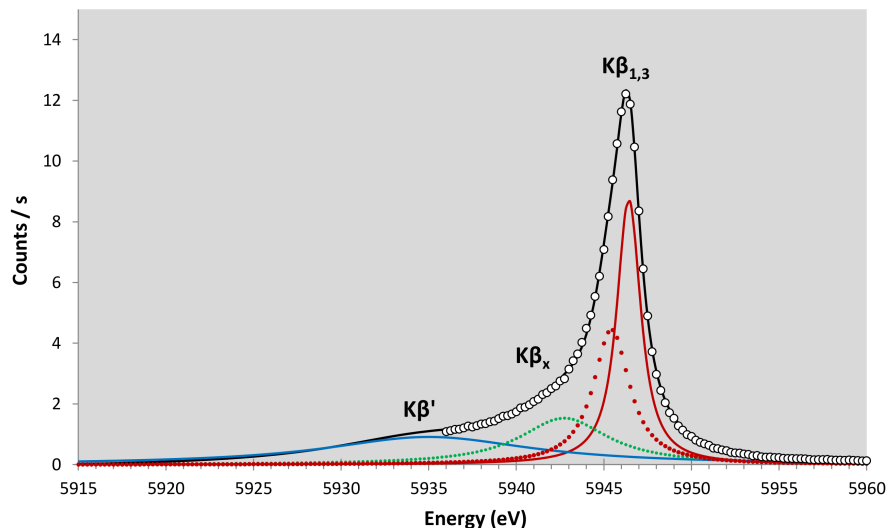


Figure IV.4 – Fit of the $K\beta_{1,3}$ spectrum of Cr metal (Cr^0) measured at SSRL. Shown are the background subtracted experimental spectrum (open circles), the total fit (black curve) together with the four individual Voigt components of the fit: the red solid and red dotted lines for the main $K\beta_{1,3}$ transition, the green dotted line for the $K\beta_x$ transition, and the blue line for the $K\beta'$ transition.

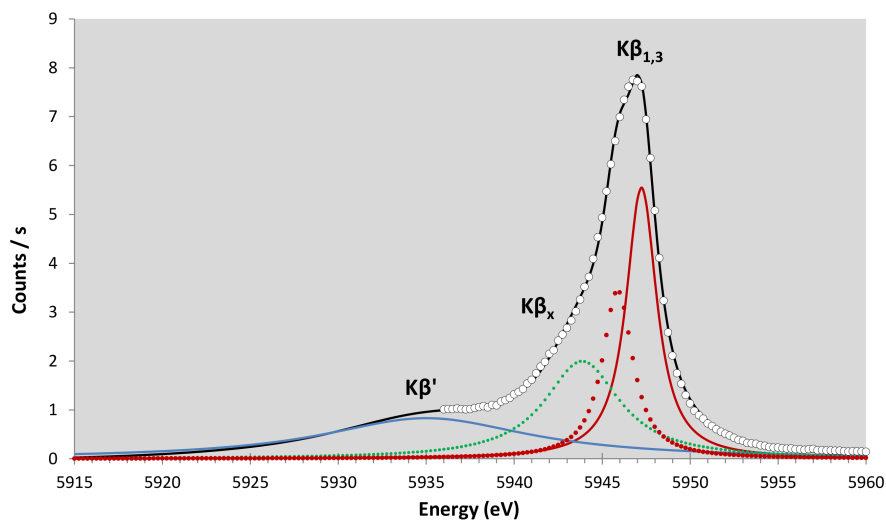


Figure IV.5 – Same as Fig. IV.4 but for Cr_2O_3 .

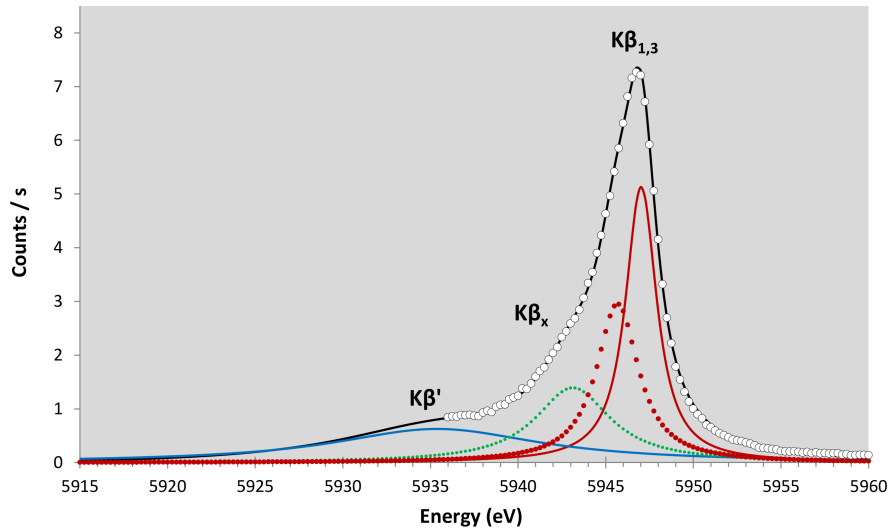


Figure IV.6 – Same as Fig. IV.4 but for CrO_2 .

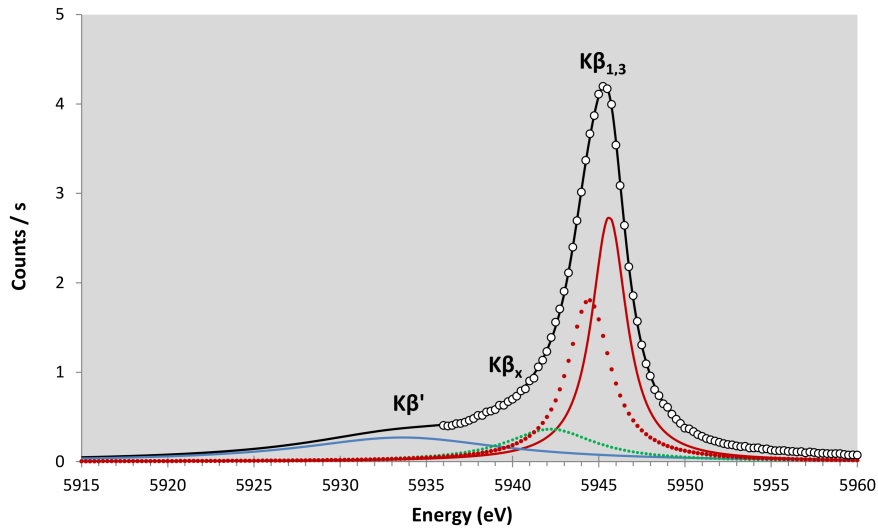


Figure IV.7 – Same as Fig. IV.4 but for $\text{K}_2\text{Cr}_2\text{O}_7$.

$K\beta_{2,5}$ and $K\beta''$ transitions

In Figs. IV.8, IV.9, IV.10 and IV.11 shown are the fitted VtC X-ray emission spectra of Cr-metal (Cr^0) and Cr compounds (Cr_2O_3 , CrO_2 and $\text{K}_2\text{Cr}_2\text{O}_7$). The $K\beta_{2,5}$ lines were fitted with several Voigtians, whereas for the fit of the the $K\beta''$ lines one Voigtian was used. The energies, intensities and Lorentzian widths were free fitting parameters, while the instrumental width was kept fixed. The fitted linear background was subtracted in the presented X-ray spectra.

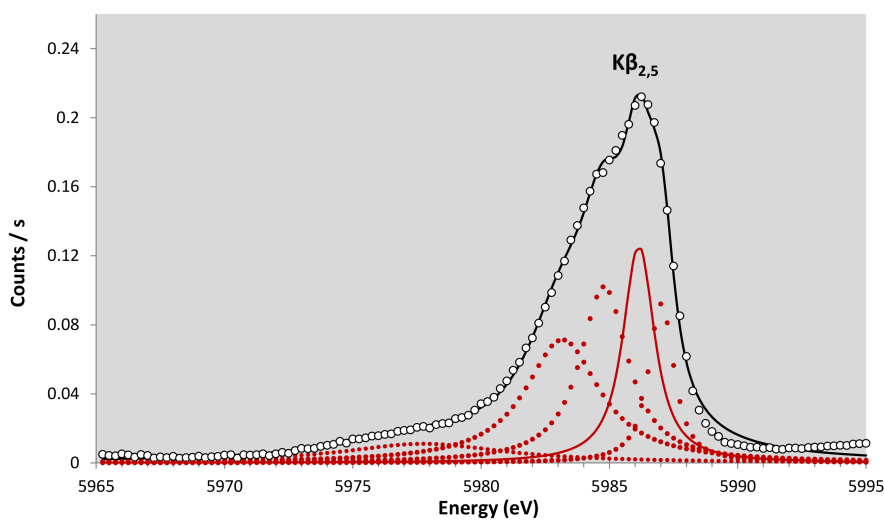


Figure IV.8 – Fit of the $K\beta_{2,5}$ spectrum of Cr metal. Shown are the measured spectrum (open circles) and the total fit (black curve). The red solid and dotted lines represent the individual Voigt components. The peak energy of the red solid Voigtian was assigned to the energy of the $K\beta_{2,5}$ transition.

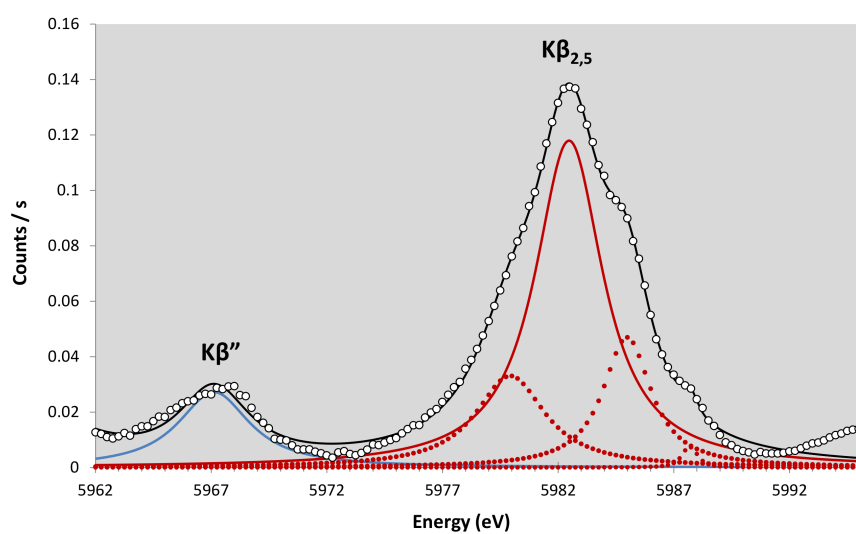


Figure IV.9 – Same as Fig. IV.8 but for Cr_2O_3 compound. The blue line represents the $K\beta''$ line.

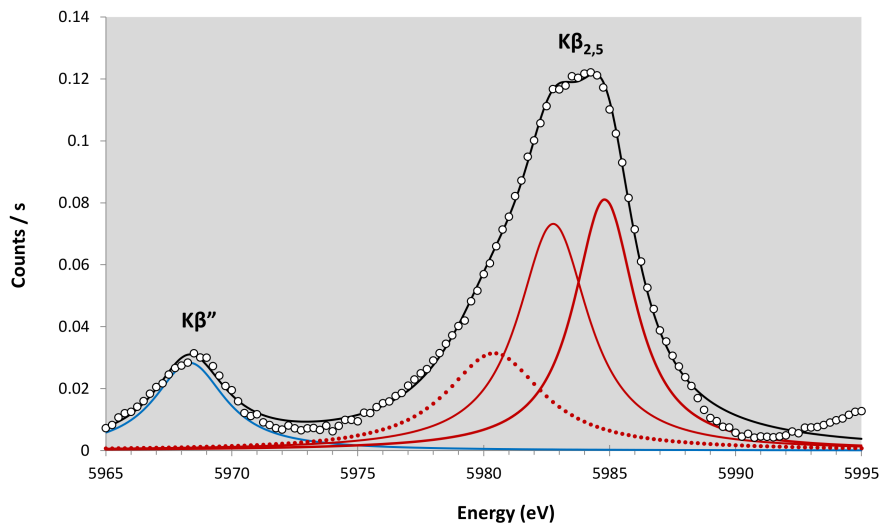


Figure IV.10 – Same as Fig. IV.8 but for CrO₂ compound. The weighted average energy of the two red solid Voigtians was assigned to the energy of the Kβ_{2,5} transition. The blue line represents the Kβ'' transition.

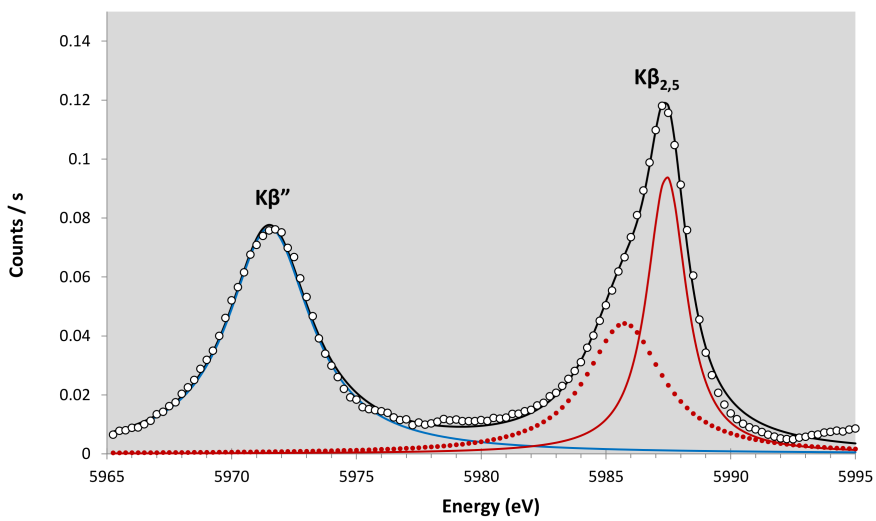


Figure IV.11 – Same as Fig. IV.8 but for K₂Cr₂O₇. The blue line represents the Kβ'' transition.

IV.2.2 $K^h\beta_{1,3}$ hypersatellite spectra

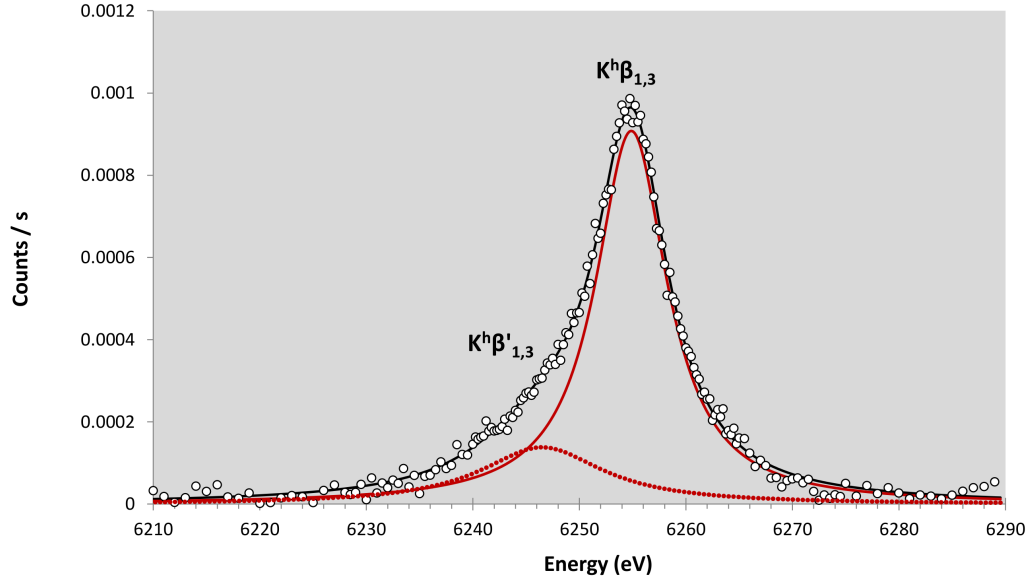


Figure IV.12 – Fit of the $K^h\beta_{1,3}$ hypersatellite spectrum of Cr metal (Cr^0) showing the measured spectrum (open circles) and the total fit (black curve). The fitted $K^h\beta_{1,3}$ component is depicted by the red solid line and the $K^h\beta'_{1,3}$ asymmetry by the red dotted line.

In Figs. IV.12, IV.13, IV.14 and IV.15 we present the $K^h\beta_{1,3}$ X-ray emission spectra of Cr metal, and Cr compounds Cr_2O_3 , CrO_2 and $K_2Cr_2O_7$, respectively. Each spectrum was fitted with two Voigtians, one corresponding to the highest peak assigned to $K^h\beta_{1,3}$ and the second to the low energy asymmetry denoted as $K^h\beta'_{1,3}$. Only one Voigtian was used for the main line because the $K^h\beta_1$ and $K^h\beta_3$ hypersatellite transitions are highly overlapping due to the small expected separation (≤ 1 eV) and large lifetime widths [112], and because the $K^h\beta_1$ ($1s^{-2} \rightarrow 1s^{-1}3p^{-1}_{3/2}$) intensity is only about 1.7 % of the $K^h\beta_3$ ($1s^{-2} \rightarrow 1s^{-1}3p^{-1}_{1/2}$) transition [178,188]. The intensities, energies and the Lorentzian widths of the Voigtians and the parameters of the linear background were used as free fitting parameters, whereas the instrumental response of the spectrometer was kept fixed in the fit.

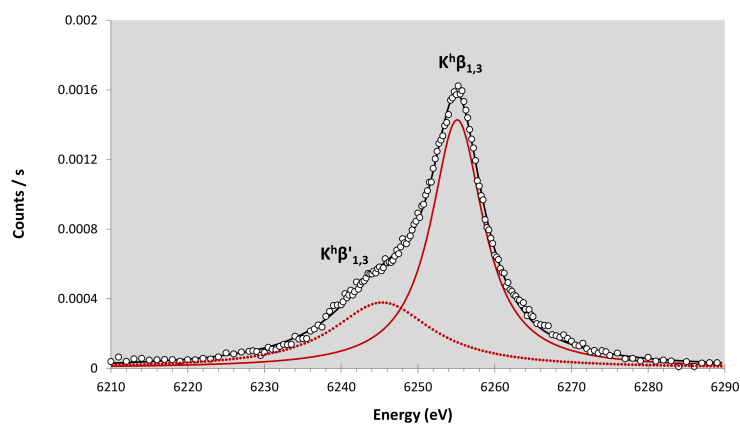


Figure IV.13 – Same as Fig. IV.12 but for Cr_2O_3 .

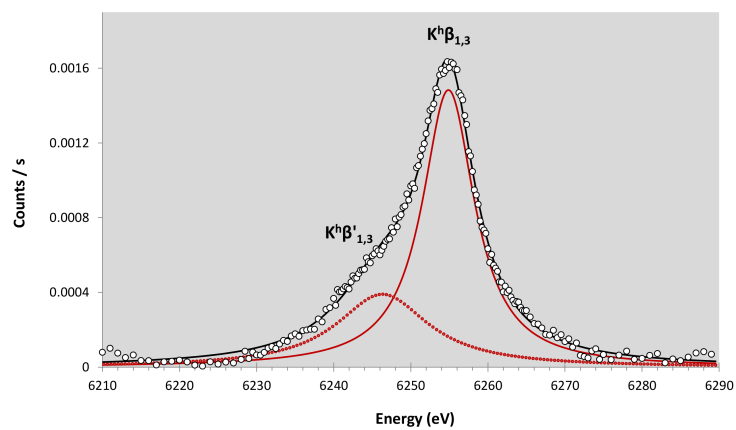


Figure IV.14 – Same as Fig. IV.12 but for CrO_2 .

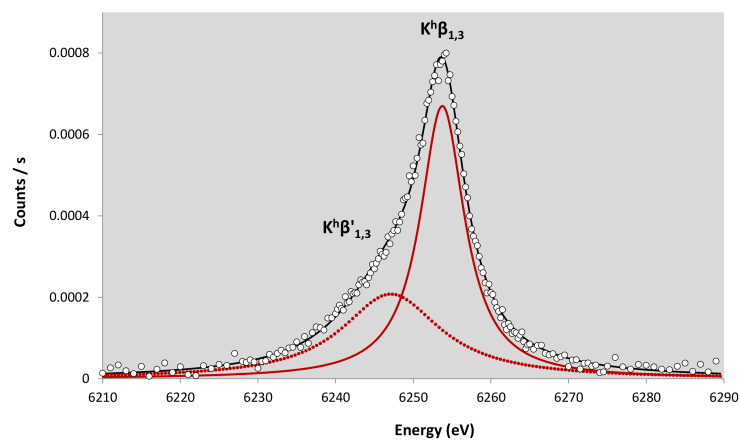


Figure IV.15 – Same as Fig. IV.12 but for $K_2Cr_2O_7$.

IV.3 Results and discussion

IV.3.1 $K\beta$ diagram and VtC transitions

A comparison of the $K\beta$ diagram emission spectra for Cr metal, Cr_2O_3 , CrO_2 and $K_2Cr_2O_7$ is represented in Fig. IV.16, while the comparison of the VtC transitions $K\beta'$ and $K\beta_{2,5}$ lines is depicted in Fig. IV.17. It can be clearly seen from the plots that the chemical effects on the Cr $K\beta$ transitions in oxide compounds are reflected in the relative energy shifts, and in the variation of spectral intensities, widths and shapes. In the following we present our experimental results on energies, energy shifts, line widths, and relative intensities for the $K\beta$ diagram and VtC emission spectra for Cr in different oxidation states, and compare our values to other published data.

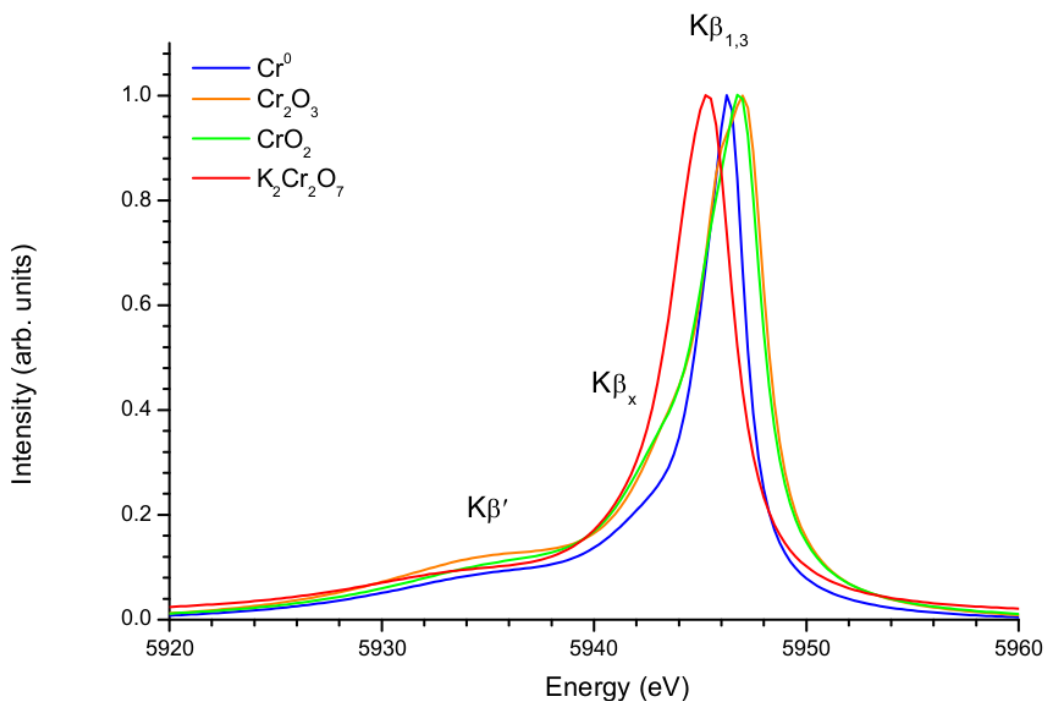


Figure IV.16 – Comparison of the $K\beta_{1,3}$ emission spectra for Cr metal (Cr^0) and different Cr compounds. All spectra were normalized to the same peak height.

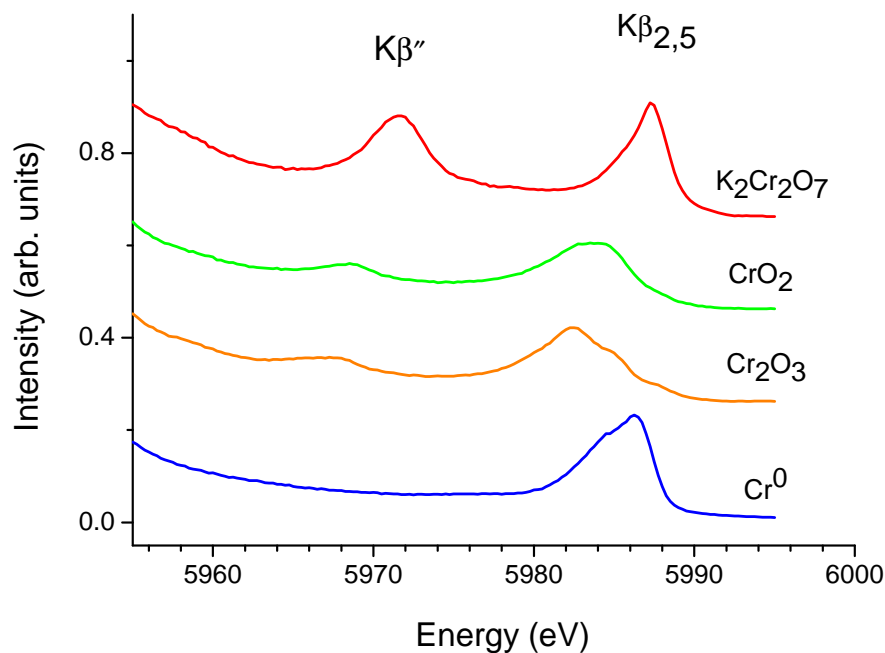


Figure IV.17 – Comparison of the $K\beta''$ and $K\beta_{2,5}$ lines measured for the Cr metal (Cr^0) and different Cr compounds. The Cr compound spectra were shifted up for clarity.

Energies

The energies of the $K\beta_{1,3}$ diagram transitions obtained in the present work are listed in Table IV.1, and those of the $K\beta_{2,5}$ and $K\beta''$ transitions in Table IV.2, where they are compared to other experimental values found in the literature. The latter were obtained by photon beam (XRF- X-ray Fluorescence), proton beam (PIXE - Particle Induced X-ray Emission) and Bremsstrahlung from X-ray tubes (BS) induced ionization mechanisms. Trends of the $K\beta_{1,3}$ and $K\beta_{2,5}$ energies with the formal oxidation number are illustrated in Fig.IV.18(a) and IV.18(b), respectively, and compared to other experimental values [100, 207–210].

A linear dependence of the $K\beta_{1,3}$ and $K\beta_{2,5}$ peak positions with the oxidation state is clearly observed for the three studied compounds. The $K\beta_{1,3}$ peak position shifts to lower energy with increasing formal oxidation number, whereas the $K\beta_{2,5}$ transitions shift to higher energies. The energy shift due to the oxidation state is more important for the $K\beta_{2,5}$ line as compared to the main $K\beta_{1,3}$ line. The position of the $K\beta''$ line follows that of $K\beta_{2,5}$.

Table IV.1 – Energies of the diagram $K\beta$ line in [eV]. The quoted values correspond to the energy of the highest peak in the fits (red solid curve). Present values are compared to other experimental values obtained by irradiating the targets with XRF, PIXE and BS excitation modes. The uncertainties correspond to statistical errors from the fits.

Compound	Oxidation state	X-ray line	Present data	Other Exp.
Cr^0	0	$K\beta_{1,3}$	5946.42(2)	5946.82(1) [104] 5946.70(1) ^a [100] 5946.5 ^a [211] 5947.29 ^c [208] 5946.62 ^a [207]
Cr_2O_3	3	$K\beta_{1,3}$	5947.20(1)	5947.84(5) ^a [100] 5946.9 ^a [211] 5948.20 ^c [208] 5945.80 ^a [207] 5947.15 ^b [102]
CrO_2	4	$K\beta_{1,3}$	5947.04(5)	5947.08 ^b [102] 5946.98 ^a [212] 5947.3 ^a [209] 5947.0 ^a [210]
$\text{K}_2\text{Cr}_2\text{O}_7$	6	$K\beta_{1,3}$	5945.62(4)	5946.26(5) ^a [100] 5946.27 ^c [208] 5944.30 ^a [207] 5946.21 ^b [102]

^a XRF; ^b PIXE; ^c BS;

Table IV.2 – Same as Table IV.1 but for the Cr $K\beta_{2,5}$ and $K\beta''$ energies.

Compound	Oxidation state	X-ray line	Present data	Other Exp.
Cr^0	0	$K\beta_{2,5}$	5986.15(7)	5986.80(1) ^a [100] 5986.20 ^a [211] 5985.17 ^c [208]
		$K\beta''$	-	-
Cr_2O_3	3	$K\beta_{2,5}$	5982.52(16)	5984.14 ^a [100] 5983.80 ^a [211] 5982.03 ^c [208] 5983.80 ^b [102]
		$K\beta''$	5967.43(19)	5966.74 ^a [100] 5969.90 ^a [211]
CrO_2	4	$K\beta_{2,5}$	5983.76(8)	5984.82 ^b [102] 5985.20 ^a [209]
		$K\beta''$	5968.33(7)	-
$\text{K}_2\text{Cr}_2\text{O}_7$	6	$K\beta_{2,5}$	5987.44(3)	5984.26 ^a [100] 5986.03 ^c [208] 5988.00 ^b [102]
		$K\beta''$	5971.51(2)	5965.86 ^a [100]

^a XRF; ^bPIXE; ^cBS;

Koster and Mendel [211] reported that the $K\beta_{1,3}$ energy shift should behave linearly if the bond character and the coordination number are approximately the same in the oxide compounds. According to Tyson *et al.* [213], the $3p \rightarrow 1s$ transition energy should decrease with increasing oxidation state because the 3d electron charge localized around the metal decreases. Although both the initial 3p and final 1s states shift to higher binding energies due to the reduced screening, the 3p shift is more important. In more recent works it is argued that the $K\beta_{1,3}$ shifts are less due to the change in the outer screening for different oxidation states, but principally to the variation of the 3p3d exchange interaction, i.e., to the change of the effective number of unpaired 3d electrons related with the oxidation state [55, 214, 215].

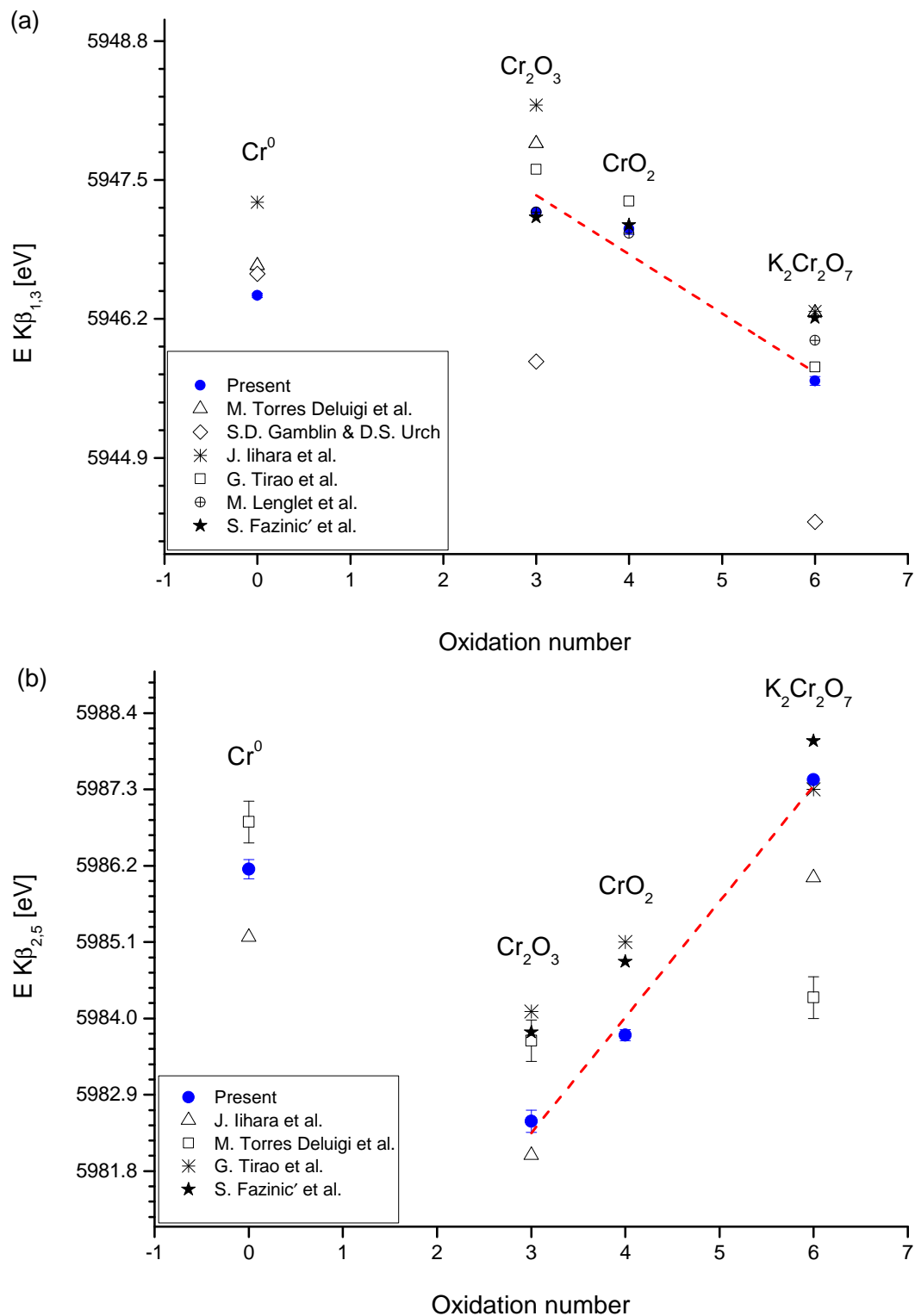


Figure IV.18 – Energies of the $K\beta_{1,3}$ main line (a) and the $K\beta_{2,5}$ VtC transition (b) as a function of the oxidation number, compared to other existing data. The dashed lines are linear fits to present data.

Data obtained in the present work confirm the linear dependence of the $K\beta_{1,3}$ and $K\beta_{2,5}$ energy positions with the oxidation states for the studied Cr compounds. Similar trends with the oxidation state for the $K\beta_{1,3}$ and $K\beta_{2,5}$ peak positions were reported in case of Mn-compounds [71,211]. The values for the $K\beta$ transition energies from different sources, however, show a noticeable dispersion. This spread is mainly due to the energy calibration procedures, the experimental energy resolution and spectra fitting methodology as pointed out by Fazinić *et al.* [102]. In this context, the relative energy differences seem more reliable for chemical speciation, and a comparison of different data sets more meaningful.

Energy shifts

Numerical values for the energy shifts of the $K\beta_{1,3}$ and $K\beta_{2,5}$ X-ray lines for Cr-compounds relative to the Cr-metal are listed in Table IV.3. One can observe an increase in the energy shift of the $K\beta_{1,3}$ X-ray line for Cr_2O_3 with respect to elemental Cr, and then a decrease with the oxidation number for CrO_2 and $\text{K}_2\text{Cr}_2\text{O}_7$. For the $K\beta_{2,5}$ transitions an inverse behavior is seen. The present energy shifts are in fair agreement with the values reported by J. Iihara *et al.* [208] and follow the general trends reported by other authors [100,207,208,210,211].

Table IV.3 – Energy shifts in [eV] for the Cr-compounds relative to the Cr-metal of the $K\beta_{1,3}$ and $K\beta_{2,5}$ X-ray lines. Present results are compared with the values reported by J. Iihara *et al.* [208].

Compound	$\Delta E(K\beta_{1,3})$		$\Delta E(K\beta_{2,5})$	
	Present	Exp. [208]	Present	Exp. [208]
Cr_2O_3	0.78(2)	0.91	-3.63(17)	-3.14
CrO_2	0.62(5)	-	-2.39(11)	-
$\text{K}_2\text{Cr}_2\text{O}_7$	-0.80(4)	-1.01	1.29(8)	1.23

The energy differences $\Delta E(K\beta_{2,5} - K\beta_{1,3})$ for the Cr^0 and the studied oxides together with other existing data are given in Table IV.4 and depicted as a function of the oxidation number in Fig. IV.19. For the Cr metal (Cr^0) the obtained value for the energy difference between the $K\beta_{2,5}$ and $K\beta_{1,3}$ lines is 39.73(7) eV which is very close to the value of 39.8 eV reported by Bearden [164]. For Cr oxides our values show a similar behavior as the one found by Tirao *et al.* [209], Iihara *et al.* [208] and by Fazinić *et al.* [102].

Table IV.4 – Energy separation in [eV] between the $K\beta_{2,5}$ and $K\beta_{1,3}$ lines for the Cr metal (Cr^0) and chromium compounds. Present results and available experimental data from the literature are listed.

Compound	Present data $\Delta E(K\beta_{2,5} - K\beta_{1,3})$	Other Exp.
Cr^0	39.73(7)	40.1(3) ^a [100] 37.88 ^c [208] 43.9(1.4) ^b [107] 39.5(3) ^a [209]
Cr_2O_3	35.32(2)	36.3(3) ^a [100] 33.83 ^c [208] 36.6(1.4) ^b [107] 36.4 ^a [209] 36.65 ^b [102]
CrO_2	36.72(9)	37.6 ^a [209] 37.72 ^b [102]
$K_2Cr_2O_7$	41.82(5)	38.0(3) ^a [100] 42.8 ^b [107] 39.76 ^c [208] 41.5 ^a [209] 42.1 ^b [102]

^a XRF; ^bPIXE; ^cBS;

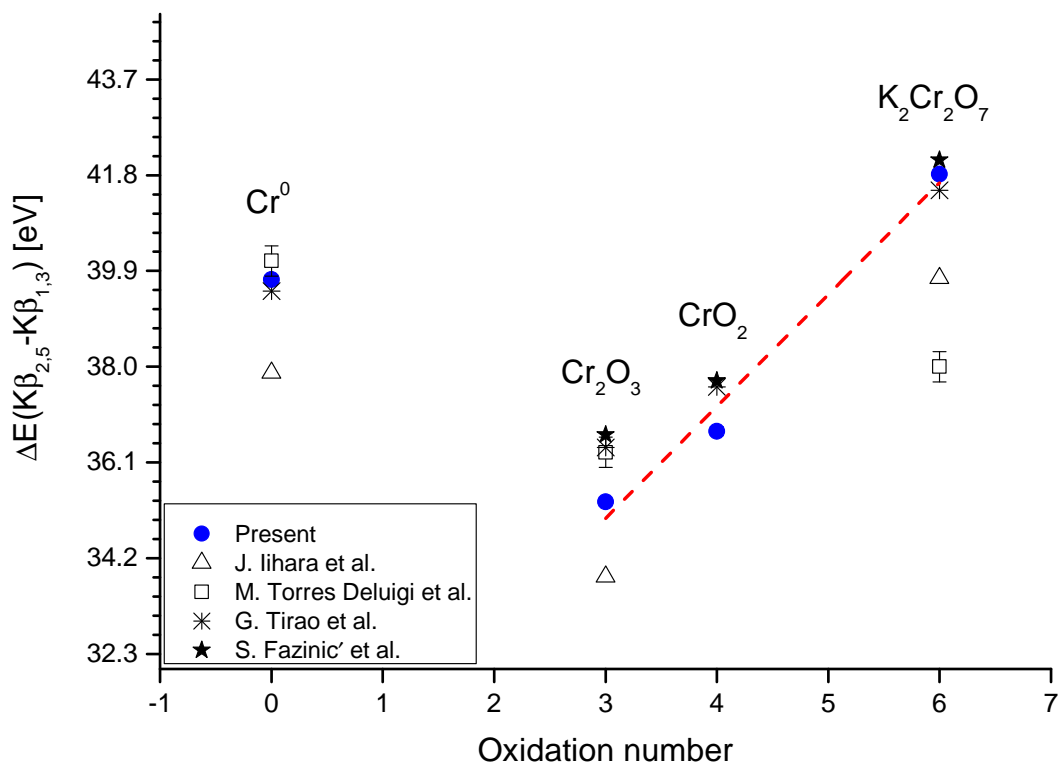


Figure IV.19 – $K\beta_{2,5}$ energy shift relative to the $K\beta_{1,3}$ line as a function of the oxidation number. The present data are compared with the results of other authors. The dashed line is a linear fit to the present data.

Table IV.5 – Energy separation in [eV] between the $K\beta''$ and $K\beta_{1,3}$ lines for chromium compounds. Present results and available experimental data from the literature are given.

Compound	Present data $\Delta E(K\beta'' - K\beta_{1,3})$	Other Exp.
Cr ₂ O ₃	20.23(19)	18.9(3) ^a [100] 23 ^a [211] 21.24 ^b [102]
CrO ₂	21.29(9)	22.2 ^a [209] 22.08 ^b [102]
K ₂ Cr ₂ O ₇	25.89(4)	19.6(3) ^a [100] 26.75 ^b [102]

^a XRF; ^b PIXE;

Table IV.6 – Energy separation in [eV] between the $K\beta_{2,5}$ and $K\beta''$ lines for the studied chromium compounds compared to available experimental data from the literature.

Compound	Present data $\Delta E(K\beta_{2,5} - K\beta'')$	Other Exp.
Cr_2O_3	15.09(25)	13.9 ^a [211]
		15.7 ^a [209]
		17.4 ^a [100]
		15.8 ^b [102]
		15.41 ^b [102]
CrO_2	15.43(11)	15.4 ^b [102]
		15.7 ^a [209]
		15.64 ^b [102]
$K_2Cr_2O_7$	15.93(4)	15.6 ^b [102]
		15.35 ^b [102]
		18.4 ^a [100]
		16 ^b [107]

^a XRF; ^bPIXE;

Results for the energy separation between the $K\beta''$ and $K\beta_{1,3}$ lines for the studied chromium compounds are presented in Table. IV.5 and for the $K\beta_{2,5}$ and $K\beta''$ lines in Table. IV.6. The relative energy differences between the $K\beta_{2,5}$ and $K\beta''$ lines are expected to behave in a similar way with the oxidation state because the difference in energies allows to identify the present ligand in the TM compound [211], [216]. The average energy separation between the $K\beta_{2,5}$ VtC and the crossover transition $K\beta''$ obtained in the present work is 15.48 ± 0.28 eV, which is consistent with the difference of the oxygen ligand 2s and 2p orbital energies of about 15 eV, and with the value of 15.6 eV reported by Fazinić *et al.* [102].

Relative intensities of the VtC transitions

As illustrated in Fig. IV.17, the line energies, spectral shapes and also the relative intensities of the VtC transitions are affected by the chemical environment of the metal ion. The $K\beta_{2,5}$ and $K\beta''$ transitions are indeed sensitive to the ligand s and p states, respectively, and to the local symmetry of the central metal ion (O_h vs

T_d). Furthermore, Bergmann *et al.* [71] have shown that for Mn compounds the $K\beta''$ relative intensities normalized by the number of oxygen ligands vary with the average bond lengths, and that the strength of the $K\beta''$ feature decreases exponentially with the metal-ligand distance. For Cr compounds similar observations were also reported [102, 209, 217].

Table IV.7 – Relative intensities of the $K\beta_{2,5}$ and $K\beta''$ lines to the total $K\beta$ intensity in percent. Values presented in columns 2 & 4 were obtained from the fitted intensities and compared with the other available experimental values given in columns 3 & 5.

Compound	$I(K\beta_{2,5})/I(K\beta)$		$I(K\beta'')/I(K\beta)$	
	Present	Other Exp.	Present	Other Exp.
Cr^0	1.77(62)	3.1 ^a [100] 4.12 ^a [208] 4.0(1.5) ^b [107]	-	-
Cr_2O_3	1.61(27)	3.5 ^a [100] 3.40 ^c [217] 3.91(23) ^a [208] 1.79(84) ^b [107]	0.25(5)	5.40 ^a [100] 0.66 ^c [217]
CrO_2	1.77(49)	4.04 ^c [217]	0.27(3)	0.98 ^c [217]
$K_2Cr_2O_7$	1.85(18)	4.3 ^a [100] 3.98 ^c [217] 2.70(13) ^a [208] 3.0(1.6) ^b [107]	1.68(6)	7.7 ^a [100] 2.58 ^c [217]

^a BS ^bPIXE ^cXRF

In Table IV.7 we present the relative intensities of the $K\beta_{2,5}$ and $K\beta''$ lines with respect to the total $K\beta$ intensity (sum of all components) together with other existing experimental values. The relative intensity of the $K\beta_{2,5}$ line to the sum of the $K\beta$ components shows an increasing behavior with the oxidation state as reported by Uršič *et al.* [107] and Torres Deluigi *et al.* [100, 217], whereas the relative intensity of the $K\beta''$ to the $K\beta$ increases as the valency increases. The reported relative intensities from different sources exhibit large variations, although the general trends for the intensity ratios are found to be similar. Since the VtC transitions are weak and are lying on the high energy tails of the intense diagram $K\beta$ lines, these im-

portant differences are mainly due to the difficulty of extracting accurately the VtC intensities from the measured X-ray emission spectra. In addition, present $K\beta_{2,5}$ -to- $K\beta$ intensity ratios are systematically smaller than those found in the literature because the $K\beta_{2,5}$ yields were not corrected for the target self absorption. As the employed samples were rather thick, the target self absorption is indeed not negligible and significantly bigger for the $K\beta_{2,5}$ line, which is partly overlapping with the Cr K absorption edge, than for the $K\beta$ transition.

IV.3.2 $K^h\beta_{1,3}$ hypersatellite transitions

The $K^h\beta$ hypersatellite transitions result from the radiative decay of double K-shell vacancy states through the M-shell. The $K^h\beta_1$ ($1s^{-2} \rightarrow 1s^{-1}3p^{-1}_{3/2}$) and $K^h\beta_3$ ($1s^{-2} \rightarrow 1s^{-1}3p^{-1}_{1/2}$) hypersatellite transitions are electric dipole transitions. The $K^h\beta_3$ hypersatellite is allowed in both the LS and jj coupling schemes, while the $K^h\beta_1$ hypersatellite is a spin-flip transition $^1S_0 - ^3P_1$ which is forbidden by the E1 selection rules in the LS coupling scheme. For low Z elements the $K^h\beta_1$ transition is not observable and the $I(K^h\beta_1)/I(K^h\beta_3)$ yield ratio reflects the degree of intermediacy of the coupling [178, 218]. Very few studies have been undertaken on photon induced $K^h\beta_{1,3}$ hypersatellite spectra. High energy resolution $K^h\beta_{1,3}$ hypersatellite spectra were reported for Fe by Diamant *et al.* [112] and for Ti by Huotari *et al.* [113]. To date, the influence of the chemical state on the $K^h\beta$ hypersatellite transitions is not known. This work is a first attempt in the investigation of the chemical sensitivity of $K^h\beta_{1,3}$ hypersatellite lines.

$K^h\beta_{1,3}$ spectral shapes and line widths

To illustrate the chemical effects on the spectral features, the measured $K^h\beta_{1,3}$ hypersatellite and $K\beta$ diagram spectra for elemental Cr and the three Cr compounds Cr_2O_3 , CrO_2 and $K_2Cr_2O_7$ are plotted together in Fig. IV.20. The plots clearly show that the spectral profiles of both the $K^h\beta_{1,3}$ hypersatellites and the $K\beta$ diagram transitions exhibit complex line shapes with characteristic low energy asymmetries. For the $K\beta$ diagram transitions, the 3p3d exchange interaction, that depends on the number of unpaired 3d electrons, gives rise to predominantly low-spin ($K\beta_{1,3}$ main line), high-spin ($K\beta'$) and spin-flip ($K\beta_x$) satellite transitions. In a simplified picture, the spin-orbit splitting, the change of the outer screening with the oxidation state and of the 3p3d exchange interaction are the main factors

determining the spectral shapes of the $K\beta$ diagram lines (see Sect. IV.3.1).

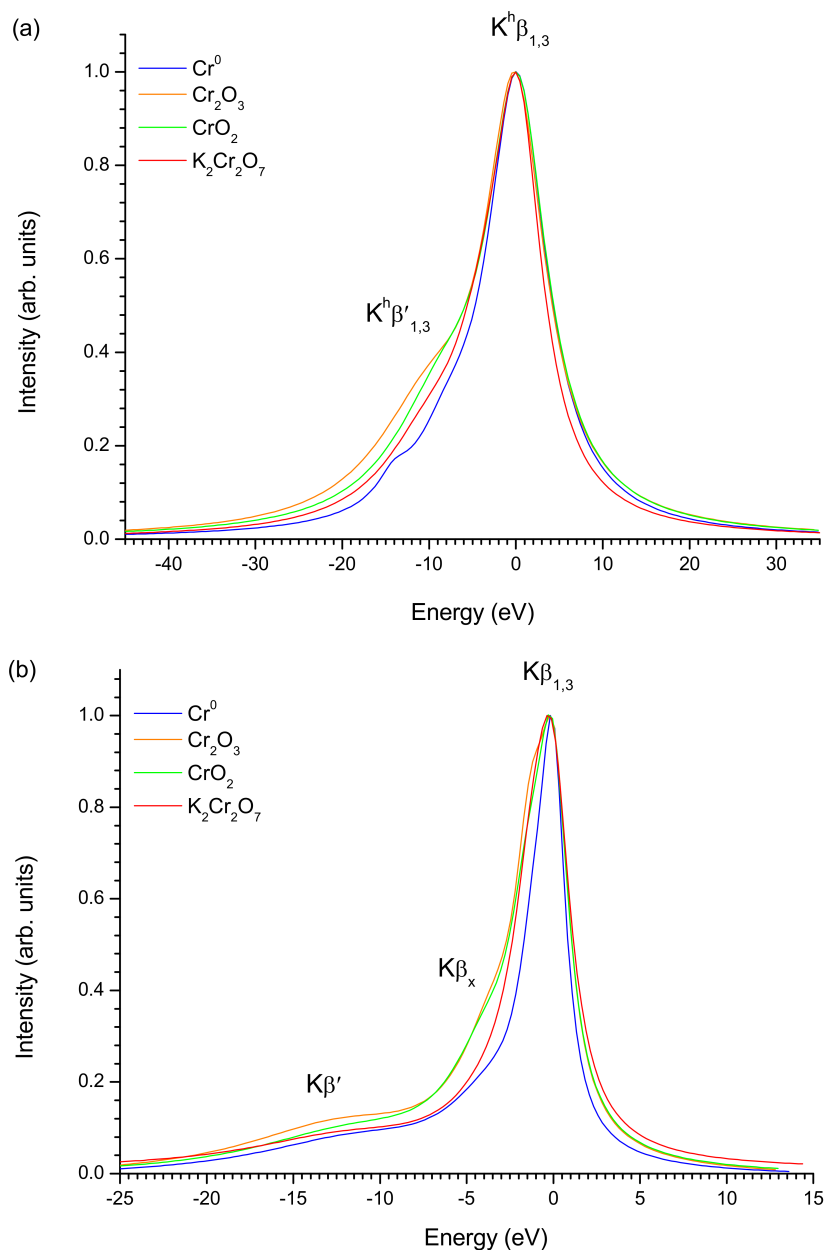


Figure IV.20 – (a) $K^h\beta_{1,3}$ and (b) $K\beta_{1,3}$ emission spectra for Cr metal and different Cr compounds. All spectra were normalized to the same height and aligned at the peak position of the $K^h\beta_{1,3}$ and $K\beta_{1,3}$ transitions of Cr^0 , respectively.

Regarding the $K^h\beta_{1,3}$ hypersatellite spectra plotted in Fig. IV.20(a), the overall shapes show a spread in the multiplet structure over a larger energy as compared to the $K\beta$ diagram transitions depicted in Fig. IV.20(b). The shorter lifetime of the initial double core-hole state results in a broadening of the spectral features

and merging of components into each other. This is reflected in the line widths of the $K^h\beta_{1,3}$ hypersatellite transitions.

Table IV.8 – The full widths at half maximum (FWHM) and the natural line widths of the Cr $K\beta_{1,3}$ main line for Cr metal and different Cr compounds. Present results and available experimental data from the literature are given.

Compounds	FWHM [eV]		Line width [eV]	
	Present	Other Exp.	Present	Other Exp.
Cr^0	2.7	2.53 [104] 2.68(5) [219]	1.47(7)	1.78(8) [100] 1.80 [219]
Cr_2O_3	3.8	-	1.98(6)	2.24(26) [100]
CrO_2	3.7	-	2.03(12)	-
$K_2Cr_2O_7$	3.7	-	2.36(13)	2.30(24) [100]

Table IV.9 – Full widths at half maximum (FWHM) and line widths of the Cr $K^h\beta_{1,3}$ and $K^h\beta'_{1,3}$ hypersatellite transitions for Cr metal and different Cr compounds.

Compounds	FWHM [eV]	Line width [eV]	
		$K^h\beta_{1,3}$	$K^h\beta'_{1,3}$
Cr^0	8.8	8.14(6)	14.0(5)
Cr_2O_3	10.0	8.28(4)	15.8(3)
CrO_2	10.2	8.23(6)	14.5(3)
$K_2Cr_2O_7$	9.1	6.92(5)	15.4(3)

The full width at half maximum (FWHM) and the Lorentzian widths of the Cr $K\beta_{1,3}$ main lines and the $K^h\beta_{1,3}$ hypersatellites obtained in the present experiment are presented in Tables IV.8 and IV.9 respectively, together with other existing experimental values. The obtained Lorentzian widths of the Cr $K\beta_{1,3}$ main line increase with the oxidation state. A similar behavior was reported by Torres Deluigi *et al.* [100]. For the Cr $K^h\beta_{1,3}$ hypersatellite lines the Lorentzian width increases for Cr_2O_3 and CrO_2 with respect to Cr^0 but then decreases for $K_2Cr_2O_7$. The values for the line widths of the low energy asymmetries $K^h\beta'_{1,3}$ were found to vary from 14 to 16 eV, with relative differences of few percent. The FWHM widths are larger for all Cr compounds relative to the Cr metal, and the FWHM

values of $K^h\beta_{1,3}$ hypersatellite and $K\beta$ diagram line follow similar trends with the nominal oxidation state.

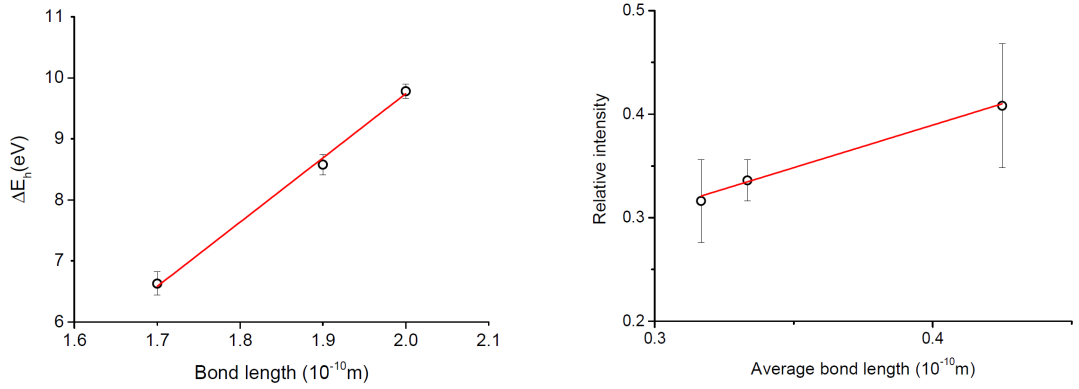


Figure IV.21 – Energy separation $\Delta E_h = E(K^h\beta_{1,3}) - E(K^h\beta'_{1,3})$ versus the Cr-O bond length (left panel) and relative intensities of the $K^h\beta'_{1,3}$ line to the sum of the $K^h\beta_{1,3}$ and $K^h\beta'_{1,3}$ transitions as a function of the average bond length (right panel). The solid lines represent linear fits to the data.

It is noteworthy that the $K^h\beta_{1,3}$ hypersatellite line width for Cr metal is larger than the value $\Gamma(K^h\beta_{1,3}) \cong 3 \cdot \Gamma_K + \Gamma_{M_{2,3}}$ expected from the sum of the initial state natural width $\Gamma_{KK} \cong 2 \cdot \Gamma_K$, where Γ_K stands for the 1s level width, and the natural width $\Gamma_K + \Gamma_{M_{2,3}}$ of the final states $1s^{-1}3p_{1/2,3/2}^{-1}$. Using for the atomic level widths the values recommended by Campbell and Papp [161] the line width derived from the above formula yields a value of 4.3 eV which is about a factor of two smaller than the measured line width. As already mentioned in Sect. III.3.2, the fact that this approximation underestimates the line widths is not really surprising. For the $K^h\alpha$ hypersatellite lines, in particular in the case of 3d transition metals, such discrepancies have been already observed (see, e.g., [32, 111]). From the reported $K^h\beta_{1,3}$ hypersatellite spectra plots for Ti [113] and Fe [112], one can derive the FWHM widths of about 7.8 eV and 6.4 eV, respectively. The latter are comparable to the FWHM of 8.8 eV obtained in this work for elemental Cr (see Table IV.9).

The low energy shoulder of the $K^h\beta_{1,3}$ hypersatellite transitions, denoted as $K^h\beta'_{1,3}$, varies with the compound and its intensity is stronger for Cr oxides compared to elemental Cr. The results for the energy separation and relative intensities of the

two transitions are presented in Table IV.10. To gain insight to the origin of the asymmetry, we plot the energy separation $\Delta E_h = E(K^h\beta_{1,3}) - E(K^h\beta'_{1,3})$ versus the Cr-O bond length and the relative intensity of the $K^h\beta'_{1,3}$ line to the total intensity of the $(K^h\beta_{1,3} + K^h\beta'_{1,3})$ transitions as a function of the average bond length (i.e., the bond length normalized by the number of bonds) in Fig. IV.21. Table IV.11 lists the different relevant parameters for the studied Cr compounds. The graph (left panel of Fig. IV.21) illustrates a linear dependence of the ΔE_h with the Cr-O bond length, and the fit yields a correlation coefficient of 0.994. For the relative intensities, a linear dependence (correlation coefficient 0.975) with the average bond length could be evinced (see right panel of Fig. IV.21).

Table IV.10 – Energy separation $\Delta E_h = E(K^h\beta_{1,3}) - E(K^h\beta'_{1,3})$ in [eV] and relative intensity of the $K^h\beta'_{1,3}$ line to the sum of the $K^h\beta_{1,3}$ and $K^h\beta'_{1,3}$ lines for Cr metal and Cr compounds.

Compound	ΔE_h	$\frac{I(K^h\beta'_{1,3})}{I(K^h\beta_{1,3})+I(K^h\beta'_{1,3})}$
Cr ⁰	8.39(28)	0.21(1)
Cr ₂ O ₃	9.78(12)	0.34(2)
CrO ₂	8.58(16)	0.32(4)
K ₂ Cr ₂ O ₇	6.63(13)	0.41(6)

As a general rule, the formal oxidation number applies well to purely ionic compounds. In the case of covalent bonding the effective charge on the central ion may be different due to charge-transfer effects, hybridization, and the nature of the ligand. The above observations suggest that the energy separation ΔE_h is indeed related to the strength of 3p3d exchange interaction which changes with inter-atomic ligand-metal p-d hybridization or charge-transfer. The relative intensity of the $K^h\beta'_{1,3}$ feature seems to reflect the degree of covalency as its intensity is higher for the Cr compounds compared to metallic Cr. It is difficult to draw definite conclusions for the Cr compounds, however, because the obtained relative intensities are almost consistent within the experimental uncertainties.

Table IV.11 – List of the studied Cr compounds and their characteristic parameters, the nominal oxidation state, symmetry (tetrahedral T_d and octahedral O_h), Cr-O bond lengths, average Cr-O bond lengths, coordination number (CN), and the nominal 3d spin state.

Compound	Oxidation	Symmetry	Bond length [Å]	<Bond length> [Å]	CN	Spin
Cr_2O_3	3	O_h	2.0 [220]	0.33	6	1.5
CrO_2	4	O_h	1.9 [221]	0.32	6	1.0
$K_2Cr_2O_7$	6	T_d	1.7 [222]	0.43	4	0.0

Energies and Energy shifts

The energies of the $K\beta$ hypersatellite and diagram transitions obtained in the present work are listed in Table IV.12. Energies of the $K^h\beta_{1,3}$, $K^h\beta'_{1,3}$ components, the center of gravity energies of the two hypersatellite transitions $K^h\beta$, and the center of gravity energies of the diagram main line $K\beta$ are listed. The numerical values for the energy shifts ΔE are presented in Table IV.13.

Table IV.12 – Energies of the $K^h\beta_{1,3}$, $K^h\beta'_{1,3}$ lines, and the center of gravity energies of the two hypersatellite transitions $K^h\beta$. The center of gravity energies of the diagram main lines denoted as $K\beta$ are also listed. All values are given in [eV]. The quoted uncertainties correspond to 1σ statistical errors from the fit.

Compound	$K^h\beta_{1,3}$	$K^h\beta'_{1,3}$	$K^h\beta$	$K\beta$
Cr^0	6254.88(3)	6246.49(28)	6253.14(6)	5945.09(2)
Cr_2O_3	6255.12(3)	6245.34(12)	6251.81(4)	5945.69(2)
CrO_2	6254.89(3)	6246.31(16)	6252.17(6)	5945.53(2)
$K_2Cr_2O_7$	6253.75(3)	6247.12(13)	6251.09(6)	5944.62(2)

Table IV.13 – Energy shifts $\Delta E = E(K^h\beta_{1,3}) - E(K\beta)$ in [eV] for Cr metal and Cr compounds. For Cr metal the second value for the shift corresponds to the difference of the center of gravity energies of all spectral components of the hypersatellite ($K^h\beta_{1,3}$ and $K^h\beta'_{1,3}$) and diagram ($K\beta$ and $K\beta'$) spectra. Experimental results are compared to theoretical predictions.

Compound	Present	Costa [178]	Santos [223]
Cr^0	309.79(6)	309.49	310.8
	310.85(7)		
Cr_2O_3	309.43(5)	-	-
CrO_2	309.36(6)	-	-
$K_2Cr_2O_7$	309.13(6)	-	-

In Fig. IV.22, we plot the energy shifts of the $K\beta$ hypersatellite to the diagram transitions as a function of the atomic number Z . The available experimental values are compared to theoretical predictions of Costa *et al.* [178] and Santos *et al.* [223]. The energy shift of 310.85(7) for elemental Cr obtained in this work is found to be in an excellent agreement with the theoretical value of 310.8 eV from Multi-configuration Dirac-Fock (MCDF) calculations of Santos *et al.* [223] (see Table IV.13).

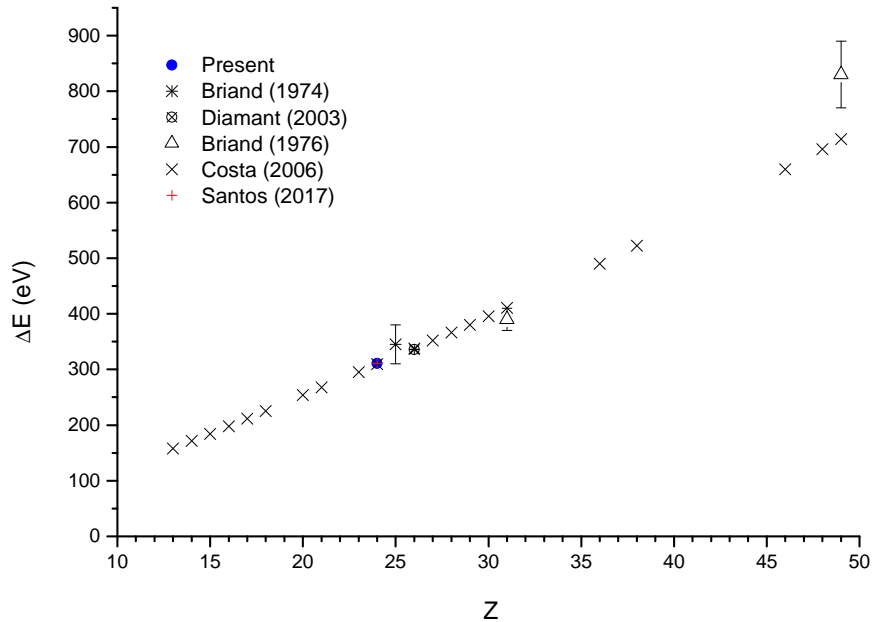


Figure IV.22 – Energy shift ΔE of the $K\beta$ hypersatellite to the diagram transition as a function of the atomic number Z . • present results, * [224], ⊗ [112], △ [44], × [178], + [223].

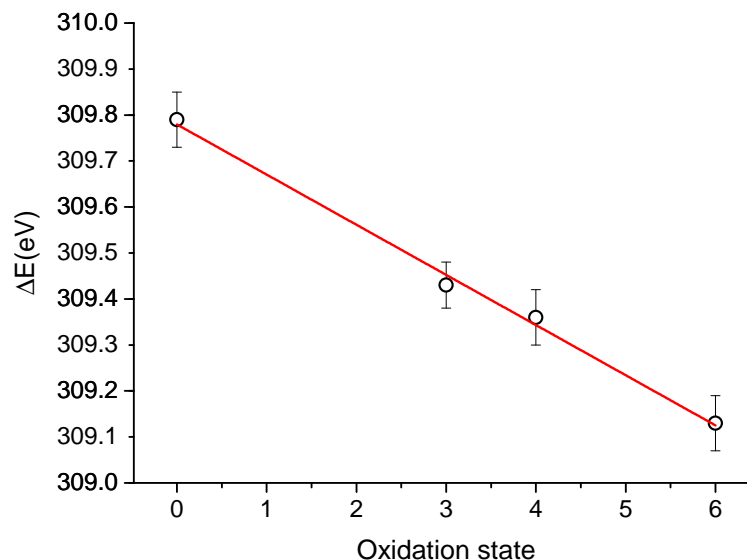


Figure IV.23 – Experimental shift ΔE of the hypersatellite main component $K^h\beta_{1,3}$ energy to the center of gravity energy of the diagram main line $K\beta$ as a function of the nominal oxidation state for elemental Cr and Cr compounds. The solid line represents a linear fit to the data.

In case of Cr compounds, a linear dependence with the oxidation state for the $K^h\beta$ and $K\beta$ energies is found, where the diagram $K\beta$ energy decreases per oxidation state increment by -0.37 eV, while the $K^h\beta$ by -0.47 eV. The shift ΔE as a function of the nominal oxidation state for elemental Cr and Cr compounds is illustrated in Fig. IV.23. The slope of the linear fit ΔE vs the oxidation state yields a value of $-0.109(6)$ eV and an intercept of $309.78(2)$ with a correlation coefficient of 0.992 . Note the excellent agreement of the intercept with the experimental value of $309.79(6)$ for Cr metal. One can surmise that this difference of $-0.109(6)$ eV per oxidation state increment is related to the change of the initial state potential of the single- and double-K-shell hole states that influences the outer electron screening, and thus the intra-electron and inter-atomic ligand-metal interactions. The effect of the $1s$ -vacancy creation on the effective $3d$ spin was put forward for classification of transition metal compounds by Suzuki *et al.* [116] using the method of spin unrestricted Hartree Fock Slater discrete-variational (DV- $X\alpha$). The observed linear dependence of ΔE on the oxidation state could be used as a diagnostic tool for the determination of effective oxidation states of complex compounds, and for comparison with theoretical calculations.

IV.4 Summary and concluding remarks

In this work we have investigated the influence of solid state and chemical effects on the shapes, line widths, energies and intensities of the $K^h\beta_{1,3}$ hypersatellite X-ray lines of metallic Cr and several Cr compounds (Cr_2O_3 , CrO_2 and $K_2Cr_2O_7$). For comparison, the $K\beta_{1,3}$ diagram lines and the $K\beta_{2,5}$ and $K\beta''$ valence-to-core (VtC) lines were also measured. The experiment was carried out at the Stanford Synchrotron Radiation Lightsource (SSRL), in Menlo Park, USA, using the 7-crystal Johann-type hard X-ray spectrometer installed at the beamline 6-2. For the measurements of the diagram and VtC lines, the beam energy was tuned to 6.1 keV, whereas for the hypersatellite measurements a beam energy of 13.7 keV close to the maximum of the double K-shell photoionization cross section for Cr was chosen. The high-energy resolution and high collection efficiency of the X-ray spectrometer combined with a photon beam intensity of about 10^{13} photons/s allowed to measure X-ray line energy shifts with high precision and to evince the variations in the X-ray line intensities and spectral shapes.

To the best of our knowledge, the $K^h\beta_{1,3}$ hypersatellite transitions of Cr compounds were measured for the first time. The main objective of the work was to explore the influence of the chemical environment on the $K^h\beta_{1,3}$ hypersatellite transitions and to derive any relevant dependencies of the energies, energy shifts, relative spectral intensities and line widths on the oxidation state, metal-ligand bond length or spin state. Further, the question of how these trends compare to the ones of the diagram and VtC transitions was also addressed.

To this end, the chemical sensitivity of the $K\beta_{1,3}$ diagram lines and the $K\beta_{2,5}$ and $K\beta''$ valence-to-core transitions to the oxidation state of Cr and Cr compounds was first investigated. The obtained results were compared to existing experimental data and theoretical predictions. Chemical speciation of 3d transition metal compounds based on the $K\beta$ X-ray emission spectra has been intensively studied. Numerous works have shown that the line energies, energy shifts, and relative intensities provide information on the oxidation state, ligand type and metal-ligand bond length, and the effective spin state. The present work, confirms the general expected trends reported in the literature despite a spread of the values from different sources. The peak energies of the $K\beta_{1,3}$ diagram lines for Cr compounds were found to decrease with the oxidation state with a negative slope of $-0.55(14)$ eV, whereas the for the $K\beta_{2,5}$ a positive slope of $1.67(15)$ eV per unit oxidation

state increment was obtained. The $\Delta E(K\beta_{2,5} - K\beta_{1,3})$ energy shift can be, indeed, considered as a good parameter for Cr compound characterization. The average energy separation of the $K\beta_{2,5}$ VtC and the cross-over $K\beta''$ transition of 15.48(28) eV was found to be consistent with the difference of the oxygen 2s and 2p orbital energies of about 15 eV, allowing thus to identify the ligand. The relative intensity of both the $K\beta_{2,5}$ and $K\beta''$ lines to the integrated intensity of the $K\beta$ diagram line showed an increasing behavior with the oxidation state. To summarize, the present results for the $K\beta_{1,3}$ diagram lines and the $K\beta_{2,5}$ and $K\beta''$ valence-to-core transitions agree with other experimental data and are in line with the previously determined trends of the different characteristic parameters with the oxidation state.

The principal findings of the work for the $K^h\beta_{1,3}$ hypersatellite transitions of elemental Cr and the three Cr compounds are the following. All the measured $K^h\beta_{1,3}$ hypersatellite spectra were found to exhibit complex spectral line shapes with a spread in the multiplet structure over a larger energy range compared to the diagram transitions. Two components, a main peak and a low energy shoulder whose relative positions and intensity ratios are sensitive to the chemical state, are characteristic of the $K^h\beta_{1,3}$ hypersatellite spectral shapes. A linear relationship for the energy separation between the two components and the Cr-O bond length was evinced suggesting that this value is related to the 3p-3d exchange interaction which is affected by the inter-atomic ligand-metal hybridization or charge-transfer. These spectral features are also reflected in the FWHM and line widths that were found to be larger for Cr compounds relative to elemental Cr. The FWHM values for the hypersatellite and diagram transitions follow similar trends with the oxidation state. For Cr metal, the line width of the $K^h\beta_{1,3}$ hypersatellite transition of 8.8 eV was found to be about a factor of two larger than the value expected from the sum of the widths of the initial and final states.

The energies of the hypersatellite transitions and the energy shifts to the diagram lines were determined. For Cr metal, the energy shift of 310.85(7) eV obtained in this work is in excellent agreement with the value of 310.8 eV from recent theoretical calculations of Santos *et al.* [223]. The energy differences of the main $K^h\beta_{1,3}$ hypersatellite line and the center of gravity of the main $K\beta_{1,3}$ diagram line for the Cr metal and Cr compounds follow a linear dependence with the nominal oxidation state with a slope of -0.109(6) eV per oxidation state increment. This finding suggests that the initial single- and double-K-shell potential influences intra- and

inter-atomic ligand-metal interactions through the influence of the outer electron screening. The observed linear dependence could be considered for chemical speciation and determination of effective oxidation states of complex compounds, and for comparison with theory.

LIST OF FIGURES

I.1.	Transmission of a collimated X-ray beam through a sample of thickness h	3
I.2.	K-edge XAFS spectrum of Fe	4
I.3.	Experimental setups of various XAS techniques	7
I.4.	Emission spectrum of a Cu X-ray tube	11
I.5.	Components of a 3rd generation SR facility	13
I.6.	Insertion device	14
I.7.	Brilliances of different X-ray sources	15
I.8.	Fe K X-ray spectrum induced by 179 MeV Ne ions	18
I.9.	Schematic illustration for the $K\alpha_{1,2}$ and $K^h\alpha_{1,2}$ transition lines	21
I.10.	Schematic illustration for the $K\beta_{1,3}$ and $K^h\beta_{1,3}$ transition lines	24
II.1.	Main components of the von Hamos curved crystal spectrometer	28
II.2.	Photograph of the interior of the von Hamos chamber	30
II.3.	Photograph of the target chamber of the von Hamos spectrometer	31
II.4.	Von Hamos setup for laboratory-based XAS measurements	32
II.5.	Angular alignment of the X-ray tube	33
II.6.	Definition of the X-ray tube angles φ and γ	34
II.7.	Incident and transmitted X-ray intensities for the Ti sample	35
II.8.	Cu K-edge spectrum as a function of the sample location	36
II.9.	Cu K-edge spectrum as a function of the sample thickness	38
II.10.	Cu K-edge spectrum as a function of the X-ray tube voltage	39
II.11.	Cu K-edge as a function of the chosen crystal	41
II.12.	K-edge XAS spectrum of Ti	45
II.13.	K-edge XAS spectrum of Fe	46

II.14.	K-edge XAS spectrum of Cu	46
II.15.	K-edge XAS spectrum of Ge	46
II.16.	L ₃ -edge XAS spectrum of Hf	47
II.17.	L ₃ -edge XAS spectrum of Ta	47
II.18.	L ₃ -edge XAS spectrum of Pt	48
II.19.	L ₁ , L ₂ and L ₃ absorption edges of Mo	49
II.20.	L ₁ , L ₂ and L ₃ absorption edges of Ag	50
II.21.	Mo L ₃ -edge spectrum and its first derivative	55
II.22.	Cu K-edge spectra measured at SLS and Fribourg	58
II.23.	Ta L ₃ -edge spectra measured at SLS and Fribourg	58
III.1.	Drawing of the collimator placed in front of the X-ray tube	69
III.2.	Cr K ^h α _{1,2} hypersatellite measured at 26.5 kV with the Si (220) crystal	72
III.3.	Exploratory scan of the Cr Kα hypersatellite region using a Si(220) crystal	73
III.4.	Exploratory scan of the Cr Kα hypersatellite region using a HAPG(004) crystal	74
III.5.	Fit of the Sc Kα hypersatellite spectrum	79
III.6.	Fit of the Sc Kβ hypersatellite spectrum	80
III.7.	Fit of the Cr K ^h α hypersatellite spectrum measured at 26.5 kV with a Si(220) crystal	81
III.8.	Fit of the Cr K ^h α hypersatellite spectrum measured at 60 kV with a Si(220) crystal	82
III.9.	Fit of the Cr K ^h α hypersatellite spectrum measured at 60 kV with a Ge(220) crystal	83
III.10.	Fit of the Cr K ^h α hypersatellite spectrum measured at 60 kV with a HAPG(004) crystal	84
III.11.	Fit of the Cu K ^h α hypersatellite spectrum	85
III.12.	Schematic drawing of the X-ray tube anode geometry	89
III.13.	Cr K-shell ionization cross section as the function of the electron energy	90
III.14.	Double-to-single K-shell ionization cross-section ratios versus atomic number	104

III.15. Double-to-single K-shell ionization cross-section ratios versus atomic number for photons, electrons and EC	105
IV.1. Schematic drawing of the overlapping Rowland circles	111
IV.2. The seven-crystal Johann-type hard X-ray spectrometer of SSRL .	112
IV.3. Fit of the $K\beta_{1,3}$ spectrum of Cr metal (Cr^0) measured at Fribourg	114
IV.4. Fit of the $K\beta_{1,3}$ spectrum of Cr metal (Cr^0) measured at SSRL .	115
IV.5. Fit of the $K\beta_{1,3}$ spectrum of Cr_2O_3 compound	115
IV.6. Fit of the $K\beta_{1,3}$ spectrum of CrO_2 compound	116
IV.7. Fit of the $K\beta_{1,3}$ spectrum of $K_2Cr_2O_7$ compound	116
IV.8. Fit of the $K\beta_{2,5}$ spectrum of Cr metal	117
IV.9. Fit of the $K\beta_{2,5}$ spectrum of Cr_2O_3 compound	117
IV.10. Fit of the $K\beta_{2,5}$ spectrum of CrO_2 compound	118
IV.11. Fit of the $K\beta_{2,5}$ spectrum of $K_2Cr_2O_7$ compound	118
IV.12. Fit of the $K^h\beta_{1,3}$ hypersatellite spectrum of Cr metal	119
IV.13. Fit of the $K^h\beta_{1,3}$ hypersatellite spectrum of Cr_2O_3	120
IV.14. Fit of the $K^h\beta_{1,3}$ hypersatellite spectrum of CrO_2	120
IV.15. Fit of the $K^h\beta_{1,3}$ hypersatellite spectrum of $K_2Cr_2O_7$	120
IV.16. $K\beta_{1,3}$ emission spectra for Cr metal and different Cr compounds .	121
IV.17. Shape comparison of the $K\beta''$ and $K\beta_{2,5}$ lines	122
IV.18. Energies of the $K\beta_{1,3}$ and the $K\beta_{2,5}$ lines as a function of the oxidation number	125
IV.19. $K\beta_{2,5}$ energy shift relative to the $K\beta_{1,3}$ line as a function of the oxidation number	128
IV.20. $K^h\beta_{1,3}$ (a) and $K\beta_{1,3}$ (b) emission spectra for Cr metal and different Cr compounds	132
IV.21. Energy separation and relative intensities of the hypersatellite components	134
IV.22. Hypersatellite energy shifts vs Z	137
IV.23. Energy shifts of the $K^h\beta_{1,3}$ hypersatellites	138

LIST OF TABLES

II.1. Characteristics of the measured samples	42
II.2. Crystals employed in the XAS measurements	43
II.3. Experimental setup parameters used in the XAS measurements	44
II.4. Edge energies	60
II.5. Absorption coefficients: comparison with theory	63
II.6. Absorption coefficients: comparison with experiment	65
III.1. Attenuation factors of the employed absorbers	71
III.2. Experimental parameters used for the hypersatellite measurements	76
III.3. Parameters for the target self absorption	92
III.4. Intensity correction factors	92
III.5. Energies of the hypersatellite lines	94
III.6. Energy shifts between diagram and hypersatellite lines	98
III.7. Natural line widths of the $K^h\alpha_2$ and $K^h\beta_{1,3}$ hypersatellites	100
III.8. Relative intensities of the $K\alpha$ hypersatellites	102
III.9. Relative intensities of the $K\beta$ hypersatellite of Sc	102
III.10. Partial fluorescence yields and source thickness correction factors	103
III.11. Ratios of double-to-single ionization cross sections	104
IV.1. Energies of the $K\beta$ diagram lines	123
IV.2. Cr $K\beta_{2,5}$ and $K\beta''$ energies	124
IV.3. $K\beta_{1,3}$ and $K\beta_{2,5}$ energy shifts of Cr-compounds relative to the Cr^0	126
IV.4. Energy separation between the $K\beta_{2,5}$ and $K\beta_{1,3}$ lines	127
IV.5. Energy separation between the $K\beta''$ and $K\beta_{1,3}$ lines	128
IV.6. Energy separation between the $K\beta_{2,5}$ and $K\beta''$ lines	129

IV.7. Relative intensities of the $K\beta_{2,5}$ and $K\beta''$ lines	130
IV.8. FWHM and line widths of the Cr $K\beta_{1,3}$ line	133
IV.9. FWHM and line widths of the Cr $K^h\beta_{1,3}$ line	133
IV.10. Energy separation $E(K^h\beta_{1,3})-E(K^h\beta'_{1,3})$ and relative intensity of the $K^h\beta'_{1,3}$ transition for Cr metal and Cr compounds.	135
IV.11. Characteristic parameters of the Cr compounds	136
IV.12. Energies of the hypersatellite and diagram lines	136
IV.13. Energy shifts for Cr metal and Cr compounds	137

REFERENCES

- [1] W. C. Röntgen, *On a new kind of rays. Science*, vol. 3, no. 59, p. 227, 1896.
- [2] W. C. Röntgen, *Nature*, vol. 53, no. 1369, p. 274, 1896.
- [3] F.W. Lytle, *J. Synchrotron Rad.*, vol. 6, no. 3, p. 123, 1999.
- [4] http://chemwiki.ucdavis.edu/Physical_Chemistry/Spectroscopy/X-ray_Spectroscopy/XANES%3A_Application#Soft_X-ray_Instrumentation.
- [5] R.D. Deslattes *et al.*, *Rev. Mod. Phys.*, vol. 75, p. 35, 2003.
- [6] L.G. Parratt, *Rev. Mod. Phys.*, vol. 31, p. 616, 1959.
- [7] J. Jaklevic *et al.*, *Solid State Commun.*, vol. 23, p. 679, 1977.
- [8] W. Gudat and C. Kunz, *Phys. Rev. Lett.*, vol. 29, p. 169, 1972.
- [9] L. G. Parratt, C. F. Hempstead and E. L. Jossem, *Phys. Rev.*, vol. 105, p. 1228, 1957.
- [10] M. Bianchini and P. Glatzel, *J. Synchrotron Rad.*, vol. 19, p. 911, 2012.
- [11] E.A. Stern and K. Kim, *Phys. Rev. B*, vol. 23, p. 3781, 1981.
- [12] P. Eisenberger, P. M. Platzman, and H. Winnick, *Phys. Rev. Lett.*, vol. 36, p. 623, 1976.
- [13] K. Hämäläinen, D.P. Siddons, J.B. Hastings and L.E. Berman, *Phys. Rev. Lett.*, vol. 67, p. 2850, 1991.
- [14] C.S. Schnorr and M.C. Ridgway, *Introduction to X-Ray Absorption Spectroscopy*. Springer Berlin Heidelberg, 2015, vol. 190.
- [15] G. Bunker, *Introduction to XAFS*. Cambridge University Press, Cambridge, 2010.
- [16] J. Szlachetko *et al.*, *Chem. Commun.*, vol. 48, p. 10898, 2012.
- [17] J. Szlachetko *et al.*, *Struct. Dyn.*, vol. 1, p. 021101, 2014.
- [18] J. Szlachetko *et al.*, *J. Phys. Chem. Lett.*, vol. 5, p. 80, 2014.
- [19] W. Błachucki *et al.*, *Spectrochim. Acta B*, vol. 136, p. 23, 2017.
- [20] W. Błachucki *et al.*, *Nucl. Instrum. Meth. Phys. Res. B*, vol. 411, p. 63, 2017.
- [21] W. Błachucki *et al.*, *Phys. Rev. Lett.*, vol. 112, p. 173003, 2014.
- [22] L.V. Azároff, *Elements of X-ray crystallography*. McGraw-Hill Book Company, New York, 1968.

- [23] H. Ebel, *X-ray tube spectra, X-ray spectrometry*. John Wiley and Sons, Ltd, 1999, vol. 28.
- [24] www-ssrl.slac.stanford.edu/sr-source.html.
- [25] P. Wilmott, *An Introduction to Synchrotron Radiation: Techniques and Applications*. West Sussex, Wiley, 2011.
- [26] G. Margaritondo, *Introduction to Synchrotron Radiation*. Oxford University Press, New York, Oxford, 1988.
- [27] P. Emma *et al.*, *Nature Photonics*, vol. 4, no. 9, p. 641, 2010.
- [28] P. Richard, W. Hodge and C.F. Moore, *Phys. Rev. Lett.*, vol. 29, p. 393, 1972.
- [29] B. Boschung *et al.*, *Phys. Rev. A*, vol. 51, p. 3650, 1995.
- [30] M. Kavčič, M. Kobal, M. Budnar, J.-Cl. Dousse and K. Tökesi, *Nucl. Instrum. Meth. Phys. Res. B*, vol. 233, p. 235, 2005.
- [31] K. Fennane *et al.*, *Phys. Rev. A*, vol. 79, p. 032708, 2009.
- [32] J. Hozzowska *et al.*, *Phys. Rev. A*, vol. 82, p. 063408, 2010.
- [33] L. Young *et al.*, *Nature*, vol. 466, p. 56, 2010.
- [34] G. Doumy *et al.*, *Phys. Rev. Lett.*, vol. 106, p. 0830002, 2011.
- [35] B. Rudek *et al.*, *Nat. Photon.*, vol. 6, p. 858, 2012.
- [36] K. Tamasaku *et al.*, *Phys. Rev. Lett.*, vol. 111, p. 0430001, 2013.
- [37] H. Yoneda *et al.*, *Nat. Commun.*, vol. 5, p. 5080, 2010.
- [38] J.D. Garcia, *Phys. Rev. A*, vol. 4, p. 955, 1971.
- [39] G. Basbas *et al.*, *Phys. Rev. A*, vol. 7, p. 983, 1973.
- [40] J.M. Hansteen *et al.*, *At. Data Nucl. Data Tables*, vol. 15, p. 305, 1975.
- [41] Y.-P. Maillard, *PhD thesis No 1995, Physics Department, University of Fribourg, Switzerland*, Dec. 2016.
- [42] E. Mikkola, O. Keski-Rahkonen and R. Kuoppala, *Phys. Scr.*, vol. 19, p. 29, 1979.
- [43] S.I. Salem, *Phys. Rev. A*, vol. 21, p. 858, 1980.
- [44] J.P. Briand *et al.*, *J. Phys. B*, vol. 9, p. 1055, 1976.
- [45] T. Åberg and J. Utriainen, *Phys. Rev. Lett.*, vol. 22, p. 1346, 1969.
- [46] J.A.R. Samson *et al.*, *Phys. Rev. A*, vol. 57, p. 1906, 1998.
- [47] T. Mukoyama and K. Taniguchi, *Phys. Rev. A*, vol. 36, p. 693, 1987.
- [48] J. Hozzowska *et al.*, *Phys. Rev. Lett.*, vol. 102, p. 073006, 2009.
- [49] G. Charpak, *C. R. Hebd. Séances Acad. Sci.*, vol. 237, p. 243, 1953.
- [50] W. Heisenberg, *Z. Phys.*, vol. 32, p. 841, 1925.
- [51] J.P. Briand, P. Chevallier, and M. Tavernier, *J. Phys. Colloq.*, vol. 32, pp. C4-165, 1971.

- [52] O. Keski-Rahkonen, J. Saijonmaa, M. Suvanen and A. Servomaa, *Phys. Scr.*, vol. 16, p. 105, 1977.
- [53] J. Saijonmaa and O. Keski-Rahkonen, *Phys. Scr.*, vol. 17, p. 451, 1978.
- [54] J. Lahtinen and O. Keski-Rahkonen, *Phys. Scr.*, vol. 27, p. 334, 1983.
- [55] P. Glatzel and U. Bergmann, *Coord. Chem. Rev.*, vol. 249, no. 1-2, p. 65, 2005.
- [56] G. Vankó *et al.*, *J. Phys. Chem. B*, vol. 110, p. 11647, 2006.
- [57] N. Lee, T. Petrenko, U. Bergmann, F. Neese and S. DeBeer, *J. Am. Chem. Soc.*, vol. 132(28), p. 9715, 2010.
- [58] K. O. Kvashnina and A. C. Scheinost, *J. Synchrotron Rad.*, vol. 23, p. 836, 2016.
- [59] V. A. Safonov *et al.*, *J. Phys. Chem. B*, vol. 110, p. 23192, 2006.
- [60] G. Smolentsev *et al.*, *J. Am. Chem. Soc.*, vol. 131, p. 13161, 2009.
- [61] A. Nilsson and L. G. M. Pettersson, *Surf. Sci. Rep.*, vol. 55(2-5), p. 49, 2004.
- [62] J. Nordgren *et al.*, *Rev. Sci. Instrum.*, vol. 60(7), p. 1690, 1989.
- [63] G. Ghiringhelli *et al.*, *Rev. Sci. Instrum.*, vol. 77, p. 113108, 2006.
- [64] U. Bergmann and P. Glatzel, *Photosynth. Res.*, vol. 102(2-3), p. 255, 2009.
- [65] J. Messinger *et al.*, *J. Am. Chem. Soc.*, vol. 123(32), p. 7804, 2001.
- [66] Y. Pushkar *et al.*, *Angew. Chem., Int. Ed.*, vol. 49(4), p. 800, 2010.
- [67] K.M. Lancaster *et al.*, *Science*, vol. 334(6058), p. 974, 2011.
- [68] U. Bergmann *et al.*, *J. Phys. Chem. B*, vol. 102(42), p. 8350, 1998.
- [69] H. Visser *et al.*, *J. Am. Chem. Soc.*, vol. 123(29), p. 7031, 2001.
- [70] M. A. Beckwith *et al.*, *Inorg. Chem.*, vol. 50(17), p. 8397, 2011.
- [71] U. Bergmann, C.R. Horne, T.J. Collins, J.M. Workman, and S.P. Cramer, *Chem. Phys. Lett.*, vol. 302(1-2), p. 119, 1999.
- [72] J.F. Lin *et al.*, *Nat. Geosci.*, vol. 1(10), p. 688, 2008.
- [73] R.A. Mori *et al.*, *Inorg. Chem.*, vol. 49(14), p. 6468, 2010.
- [74] R.A. Mori *et al.*, *Anal. Chem.*, vol. 81(15), p. 6516, 2009.
- [75] H. Johann, *Z. Phys.*, vol. 69, p. 185, 1931.
- [76] T. Johansson, *Z. Phys. A*, vol. 82, p. 507, 1933.
- [77] L. von Hamos, *Naturwiss.*, vol. 20, p. 705, 1932.
- [78] J.W.M. DuMond and H.A. Kirkpatrick, *Rev. Sci. Instrum.*, vol. 1, p. 88, 1930.
- [79] J.W.M. Dumond, *In beta and Gamma-ray Spectroscopy, 1st ed., Chapter IV: Crystal Diffraction Spectroscopy of Nuclear γ -Rays.* K. Siegbahn, ed., Amsterdam, North Holland, 1955.

- [80] J.W.C. Knowles, *In beta and Gamma-ray Spectroscopy, 2st ed., Chapter IV: Crystal Diffraction Spectroscopy of Nuclear γ -Rays.* K. Siegbahn, ed., Amsterdam, North Holland, 1965.
- [81] R. Alonso-Mori *et al.*, *Proc. Natl. Acad. Sci. U.S.A.*, vol. 109, p. 19103, 2012.
- [82] M. Kavčič *et al.*, *Rev. Sci. Instrum.*, vol. 83, p. 033113, 2012.
- [83] J. Hozzowska and J.-Cl. Dousse, *J. Electron Spectrosc. Relat. Phenom.*, vol. 137-140, p. 687, 2004.
- [84] H. Hayashi *et al.*, *J. Electron Spectrosc. Relat. Phenom.*, vol. 136(1-2), p. 191, 2004.
- [85] B. Dickinson *et al.*, *Rev. Sci. Instrum.*, vol. 79, p. 123112, 2008.
- [86] B. A. Mattern *et al.*, *Rev. Sci. Instrum.*, vol. 83, p. 023901, 2012.
- [87] J. Szlachetko *et al.*, *Rev. Sci. Instrum.*, vol. 83, p. 103105, 2012.
- [88] U. Bergmann and S.P. Cramer, *Proc. SPIE*, vol. 3448, p. 198, 1998.
- [89] S. Huotari *et al.*, *Rev. Sci. Instrum.*, vol. 77, p. 053102, 2006.
- [90] J.-L. Hazemann *et al.*, *J. Synchrotron Rad.*, vol. 16, p. 283, 2009.
- [91] E. Kleymenov *et al.*, *Rev. Sci. Instrum.*, vol. 82, p. 065107, 2011.
- [92] D. Sokaras *et al.*, *Rev. Sci. Instrum.*, vol. 84, p. 053102, 2013.
- [93] V. Stojanoff *et al.*, *Rev. Sci. Instrum.*, vol. 63(1), p. 1125, 1992.
- [94] W. Schulke, A. Kaprolat, T. Fischer, K. Hoppner and F. Wohlert, *Rev. Sci. Instrum.*, vol. 66, p. 2446, 1995.
- [95] U. Bergmann, P. Glatzel and S.P. Cramer, *Microchem. J.*, vol. 71, p. 221, 2002.
- [96] G. Tirao, G. Stutz and C. Cusatis, *J. Synchrotron Radiat.*, vol. 11, p. 335, 2004.
- [97] E. Kleimenov *et al.*, *J. Phys. Conf. Ser.*, vol. 190, p. 012035, 2009.
- [98] L. Journal *et al.*, *Rev. Sci. Instrum.*, vol. 80, p. 093105, 2009.
- [99] R. Verbeni *et al.*, *J. Synchrotron Radiat.*, vol. 16, p. 469, 2009.
- [100] M. T. Deluigi, G. Tirao, G. Stutz, C. Cusatis and J. Riveros, *Chem. Phys.*, vol. 325, p. 477, 2006.
- [101] S. Fazinić, M. Jakšić, L. Mandić and J. Dobrinić, *Phys. Rev. A*, vol. 74, p. 062501, 2006.
- [102] S. Fazinić, L. Mandić, M. Kavčič and I. Božičević, *Spectrochimica Acta Part B*, vol. 66, p. 461, 2011.
- [103] L. Mandić, S. Fazinić and M. Jakšić, *Phys. Rev. A*, vol. 80, p. 042519, 2009.
- [104] G. Hölzer, M. Fritsch, M. Deutsch, J. Härtwig and E. Förster, *Phys. Rev. A*, vol. 56, p. 4554, 1997.
- [105] T. Mukoyama, K. Taniguchi and H. Adachi, *Phys. Rev. A*, vol. 63, p. 042514, 2001.
- [106] M. Kavčič, M. Budnar, A. Mühleisen and I. Török, *Nucl. Instrum. Meth. B*, vol. 136-138, p. 173, 1998.

- [107] M. Uršič, M. Kavčič and M. Budnar, *Nucl. Instrum. Methods B*, vol. 211, p. 7, 2003.
- [108] U. Bergmann, J. Bendix, P. Glatzel, H.B. Gray and S.P. Cramer, *J. Chem. Phys.*, vol. 116, p. 2011, 2002.
- [109] E. Gallo, C. Lamberti, P. Glatzel, *Phys. Chem. Chem. Phys.*, vol. 13, p. 19409, 2011.
- [110] K. Tsutsumi, H. Nakamori and K. Ichikawa, *Phys. Rev. B*, vol. 13, p. 929, 1976.
- [111] R. Diamant *et al.*, *Phys. Rev. A*, vol. 79, p. 062511, 2009.
- [112] R. Diamant *et al.*, *Phys. Rev. Lett.*, vol. 91, no. 19, p. 193001, 2003.
- [113] S. Huotari *et al.*, *J. Electron Spectrosc. Relat. Phenom.*, vol. 137, p. 293, 2004.
- [114] B. L. Chamberland, *Crit. Rev. Solid State Mater. Sci.*, vol. 7, p. 1, 1977.
- [115] K. H. Schwarz, *J. Phys. F: Met. Phys.*, vol. 16, p. L211, 1986.
- [116] K. Suzuki and M. P. Tedrow, *Appl. Phys. Lett.*, vol. 74, p. 428, 1999.
- [117] P. G. Ivanov, S. M. Watts and D. M. Lind, *J. Appl. Phys.*, vol. 89, p. 1035, 2001.
- [118] J. Dai and J. Tang, *Phys. Rev. B: Condens. Matter. Phys.*, vol. 63, p. 1, 2001.
- [119] S.A. Chambers and Y.K. Yoo, *Mater. Res. Soc. Bull.*, vol. 28, p. 706, 2003.
- [120] G. P. Singh, B. Biswas, S. Ram and K. Biswas, *Mater. Sci. Eng. A*, vol. 498, p. 125, 2008.
- [121] L. A. Grunes, *Phys. Rev. B*, vol. 27, no. 4, p. 2111, 1983.
- [122] K.W. Nam, W.S. Yoon and K.B. Kim, *Electrochim. Acta.*, vol. 47, no. 19, p. 3201, 2002.
- [123] T. Matsushita and R.P. Phizackerley, *Jpn. J. Appl. Phys.*, vol. 20, p. 2223, 1981.
- [124] S. Kraft, J. Stümpel, P. Becker and U. Kuetsgens, *Rev. Sci. Instrum.*, vol. 67, no. 3, p. 681, 1996.
- [125] T.J. Regan *et al.*, *Phys. Rev. B*, vol. 64, p. 214422, 2001.
- [126] I.J. Pickering, R.C. Prince, T. Divers, G.N. George, *FEBS Lett.*, vol. 441, p. 11, 1998.
- [127] D.E. Salt, R.C. Prince, A.J.M. Baker, I. Raskin and I.J. Pickering, *Environ. Sci. Technol.*, vol. 33, no. 5, p. 713, 1999.
- [128] M.E. Fleet, C.T. Herzberg, G.S. Henderson, E.D. Crozier, M.D. Osborne, C.M. Scarfe, *Geochim. Cosmochim. Acta*, vol. 48, p. 1455, 1984.
- [129] M. G. Dowsett and A. Adriaens, *Anal. Chem.*, vol. 78, no. 10, p. 3360, 2006.
- [130] S. Reguer, P. Dillmann, F. Mirambet, J. Susini and P. Lagarde, *Appl. Phys. A*, vol. 83, p. 189, 2006.
- [131] L.M. Miller, Q. Wang, T.P. Pelivala, R.J. Smith, A. Lanzirrotti, J. Miklossy, *J. Struct. Biol.*, vol. 155, p. 30, 2006.
- [132] D. E. Sayers, E. A. Stern and F. W. Lytle, *Phys. Rev. Lett.*, vol. 27, p. 1204, 1971.
- [133] F. W. Lytle, D. E. Sayers and E. A. Stern, *Phys. Rev. B*, vol. 11, p. 4825, 1975.
- [134] E. A. Stern, D. E. Sayers and P. W. Lytle, *Phys. Rev. B*, vol. 11, p. 4836, 1975.

- [135] E.A. Stern, *Laboratory EXAFS Facilities*. American Institute of Physics, New York, 1980.
- [136] K. Nishihagi, A. Kawabata and K. Taniguchi, *Jpn. J. Appl. Phys. Part I*, vol. 32, p. 258, 1993.
- [137] Y. Inada, S. Funahashi and H. Ohtaki, *Rev. Sci. Instrum.*, vol. 65, no. 1, p. 18, 1994.
- [138] Y. Inada and S. Funahashi, *Z. Naturforsch.*, vol. 52, p. 711, 1997.
- [139] K. Sakurai and X. M. Guo, *Spectrochim. Acta, Part B*, vol. 54, no. 1, p. 99, 1999.
- [140] T. Taguchi, Q. F. Xiao and J. Harada, *J. Synchrotron Rad.*, vol. 6, p. 170, 1999.
- [141] T. Taguchi, J. Harada, A. Kiku, K. Tohji, and K. Shinoda, *J. Synchrotron Rad.*, vol. 8, p. 363, 2001.
- [142] H. Shigemura *et al.*, *J. Electrochem. Soc.*, vol. 148, no. 7, p. A730, 2001.
- [143] M. Tabuchi *et al.*, *J. Electrochem. Soc.*, vol. 149, no. 5, p. A509, 2002.
- [144] V. L. McLaren *et al.*, *J. Electrochem. Soc.*, vol. 151, no. 5, p. A672, 2004.
- [145] T. Taguchi, K. Shinoda, and K. Tohji, *Phys. Scr.*, vol. T115, p. 1017, 2005.
- [146] Y.N. Yuryev, H.-J. Lee, H.-M. Park, Y.-K. Cho, and M.-K. Lee, *Rev. Sci. Instrum.*, vol. 78, p. 025108, 2007.
- [147] G.T. Seidler *et al.*, *Rev. Sci. Instrum.*, vol. 85, p. 113906, 2014.
- [148] I. Mantouvalou *et al.*, *Appl. Phys. Lett.*, vol. 108, p. 201106, 2016.
- [149] J. Hozzowska and J.-Cl. Dousse, *J. Phys. B: At. Mol. Opt. Phys.*, vol. 29, p. 1641, 1996.
- [150] M. Szlachetko, M. Berset, J.-Cl. Dousse, J. Hozzowska, and J. Szlachetko, *Rev. Sci. Instrum.*, vol. 84, no. 9, p. 093104, 2013.
- [151] J. Hozzowska, J.-Cl. Dousse, J. Kern and C. Rhême, *Nucl. Instrum. Methods Phys. Res. sect. A*, vol. 376, no. 1, p. 129, 1996.
- [152] L. von Hamos, *Ann. Phys. (Leipzig)*, vol. 409, no. 6, p. 716, 1933.
- [153] W.H. Bragg and W.L. Bragg, *Proc. R. Soc. London, Ser. A*, vol. 88, p. 428, 1913.
- [154] J. Szlachetko *et al.*, *Rev. Sci. Instrum.*, vol. 78, p. 093102, 2007.
- [155] <http://www.goodfellow.com/home.aspx>.
- [156] <http://www.nist.gov/pml/data/xcom/>.
- [157] J. E. Müller, O. Jepsen and J.W. Wilkins, *Solid State Commun.*, vol. 42, no. 5, p. 365, 1982.
- [158] N. F. Mott, *Proc. R. Soc. London*, vol. 62, p. 416, 1949.
- [159] R. Sousa Jr, F. Colmati, E.G. Ciapina, and E.R. Gonzalez, *Solid State Electrochem.*, vol. 11, p. 1549, 2007.
- [160] D.H. Pearson, C.C. Ahn and B. Fultz, *Phys. Rev. B*, vol. 47, no. 14, p. 8471, 1993.
- [161] J. L. Campbell and T. Papp, *At. Data Nucl. Data Tables*, vol. 77, p. 1, 2001.

- [162] <http://www.esrf.eu/UsersAndScience/Experiments/TBS/SciSoft/xop2.3/>.
- [163] J.A. Bearden and A.F. Burr, *Rev. Mod. Phys.*, vol. 39, no. 1, p. 125, 1967.
- [164] J.A. Bearden, *Rev. Mod. Phys.*, vol. 39, no. 1, p. 78, 1967.
- [165] K.D. Sevier, *At. Data Nucl. Data Tables*, vol. 24, p. 323, 1979.
- [166] P.J. Mohr, B.N. Taylor and D.B. Newell, *J. Phys. Chem. Ref. Data*, vol. 37, p. 1187, 2008.
- [167] E. Storm and H.I. Israel, *Nucl. Data Tables*, vol. 7, p. 565, 1970.
- [168] B.L. Henke, E.M. Gullikson, and J.C. Davis, *At. Data Nucl. Data Tables*, vol. 54, p. 181, 1993.
- [169] Y. Ménesguen and M.-C. Lépy, *Metrologia*, vol. 53, p. 7, 2016.
- [170] Y. Ménesguen, *Private communication*, 2017.
- [171] Y. Ménesguen and M.-C. Lépy, *X-Ray Spectrom.*, vol. 40, p. 411, 2011.
- [172] C. Bonnelle *et al.*, *Nucl. Instrum. Meth. Phys. Res. A*, vol. 516, p. 594, 2004.
- [173] G.K. Wertheim, M.A. Butler, K.W. West and D.N.E. Buchanan, *Rev. Sci. Instrum.*, vol. 45, p. 11, 1974.
- [174] J.H. Scofield, *At. Data Nucl. Data Tables*, vol. 14, p. 121, 1974.
- [175] A. M. Costa, M. C. Martins, J. P. Santos, P. Indelicato and F. Parente, *J. Phys. B: At. Mol. Opt. Phys.*, vol. 40, p. 57, 2007.
- [176] F. Bloch, *Phys. Rev.*, vol. 48, p. 187, 1935.
- [177] C. Herren and J.-Cl. Dousse, *Phys. Rev. A*, vol. 53, p. 717, 1996.
- [178] A.M. Costa, M.C. Martins, J.P. Santos, F. Parente and P. Indelicato, *J. Phys. B: At. Mol. Opt. Phys.*, vol. 39, p. 2355, 2006.
- [179] F.P. Larkins, *At. Data Nucl. Data Tables*, vol. 20, p. 313, 1977.
- [180] <https://physics.nist.gov/PhysRefData/Star/Text/ESTAR.html>.
- [181] <http://xdb.lbl.gov/xdb-new.pdf>.
- [182] M. Liu *et al.*, *At. Data Nucl. Data Tables*, vol. 76, p. 213, 2000.
- [183] J.H. Paterson *et al.*, *J. Microscopy*, vol. 154, p. 1, 1989.
- [184] M.C. Martins *et al.*, *J. Phys. B*, vol. 37, p. 3785, 2004.
- [185] J. Ahopelto, E. Rentavuori and O. Keski-Rahkonen, *Phys. Scr.*, vol. 20, p. 71, 1979.
- [186] S. I. Salem, A. Kumar and B. L. Scott, *Phys. Rev. A*, vol. 29, p. 2634, 1984.
- [187] L. Natarajan, *Phys. Rev. A*, vol. 78, p. 052505, 2008.
- [188] M.H. Chen, B. Crasemann and H. Mark, *Phys. Rev. A*, vol. 25, p. 391, 1982.
- [189] T. Åberg and M. Suvanen, *Advances in X-Rays Spectroscopy*, C. Bonnelle and C. Mande, eds., Pergamon, New York, 1982.
- [190] R. Diamant *et al.*, *Phys. Rev. Lett.*, vol. 84, p. 3278, 2000.

- [191] D. Mitra, M. Sarkar, D. Bhattacharya and L. Natarajan, *X-Ray Spectrom.*, vol. 37, p. 585, 2008.
- [192] J.P. Mossé, P. Chevallier and J.P. Briand, *Z. Phys. A*, vol. 322, p. 207, 1985.
- [193] M. Polasik *et al.*, *Phys. Rev. Lett.*, vol. 107, p. 073001, 2011.
- [194] V.O. Kostroun, M.H. Chen and B. Crasemann, *Phys. Rev. A*, vol. 3, p. 533, 1971.
- [195] O. Keski-Rahkonen, E. Mikkola, K. Reinikainen, and M. Lehtonen, *J. Phys. C*, vol. 18, p. 2961, 1985.
- [196] M. Oura *et al.*, *J. Phys. B*, vol. 35, p. 3847, 2002.
- [197] S. Huotari *et al.*, *Phys. Rev. Lett.*, vol. 101, p. 043001, 2008.
- [198] E. P. Kanter *et al.*, *Phys. Rev. A*, vol. 73, p. 022708, 2006.
- [199] L. Spielberger *et al.*, *Phys. Rev. Lett.*, vol. 74, p. 4615, 1995.
- [200] A. Suzuki and J. Law, *Phys. Rev. C*, vol. 25, p. 2722, 1982.
- [201] R.C. Forrey, H.R. Sadeghpour, J.D. Baker, J.D. Morgan, and A. Dalgarno, *Phys. Rev. A*, vol. 51, p. 2112, 1995.
- [202] E.P. Kanter, R.W. Dunford, B. Krassig and S.H. Southworth, *Phys. Rev. Lett.*, vol. 83, p. 508, 1999.
- [203] L.H. Andersen *et al.*, *Phys. Rev. A*, vol. 36, p. 3612, 1987.
- [204] J.H. McGuire, *J. Phys. B*, vol. 17, p. L779, 1984.
- [205] L.H. Andersen *et al.*, *Phys. Rev. Lett.*, vol. 57, p. 2147, 1986.
- [206] G. Peng *et al.*, *J. Am. Chem. Soc.*, vol. 116, p. 2914, 1994.
- [207] S.D. Gamblin, D.S. Urch, *J. Electron Spectrosc. Relat. Phenom.*, vol. 113, p. 179, 2001.
- [208] J. Iihara, T. Omori, K. Yoshihara and K. Ishii, *Nucl. Instrum. Methods B*, vol. 75, p. 32, 1993.
- [209] G. Tirao, S. Ceppi, A. L. Cappelletti and E. P. Miner, *J. Phys. Chem. Solids*, vol. 71, p. 199, 2010.
- [210] M. Lenglet, M. Sakout, J. Dürr and G. Wrobel, *Spectrochim Acta, part A*, vol. 46, p. 1101, 1990.
- [211] A. S. Koster and H. Mendel, *J. Phys. Chem. Solids*, vol. 31, p. 2511, 1970.
- [212] Y. Gohshi and A. Ohtsuka, *Spectrochim. Acta Part B*, vol. 28, p. 179, 1973.
- [213] T.A. Tyson *et al.*, *Phys. Rev. B: Condens. Matter Mater. Phys.*, vol. 60, p. 4665, 1999.
- [214] P. Glatzel, U. Bergmann, F. M. F. de Groot and S. P. Cramer, *Phys. Rev. B*, vol. 64, p. 045109, 2001.
- [215] M. Rovezzi and P. Glatzel, *Semicond. Sci. Technol.*, vol. 29, p. 023002, 2014.
- [216] E.I. Esmail, C.J. Nicholls and D.S. Urch, *Analyst*, vol. 98, p. 725, 1973.
- [217] M. T. Deluigi *et al.*, *Phys. Chem. C*, vol. 118, p. 22202, 2014.

- [218] M.H. Chen, B. Crasemann, H. Mark and T. Papp, *Phys. Rev. A*, vol. 25, p. 1, 1982.
- [219] H. Sorum, O. Weng and J. Bremer, *Phys. Status Solidi B*, vol. 109, p. 335, 1982.
- [220] R.E. Newnham and Y.M.Z. Dehaan, *Kristallogr., Kristallgeom., Kristallphys., Kristallchem.*, vol. 117, p. 235, 1962.
- [221] W.H. Bauer, *Acta Crystallogr., Sect. B*, vol. 32, p. 2200, 1976.
- [222] R.W.G. Wyckoff, *Crystal Structures*. Interscience: New York, 1953.
- [223] J.P. Santos, *private communication*, 2017.
- [224] J.P. Briand *et al.*, *Phys. Lett. A*, vol. 49, p. 51, 1974.

ACKNOWLEDGEMENTS

This work would not have been possible without the help and support of many persons whom I would like to thank hereafter.

At first, I would like to express my special gratitude to my thesis supervisor Prof. Dr. Jean – Claude Dousse who gave me the opportunity to work in his Atomic and X-ray Physics (AXP) group and guided my work during my PhD years. I am deeply grateful to him for his unconditional support, active involvement in my research, suggestions, great supervision, patience and overall help for the completion of this work.

I would like to also warmly thank Dr. hab. Joanna Hoszowska for her continuous support during the measurements, data analysis, results interpretation and thesis writing. Her wide and solid expertise in X-ray spectroscopy was very helpful for me for a correct interpretation of the obtained results. She has spent a lot of time to discuss with me the problems I have encountered during my work and to answer competently and with patience my questions.

I would like to express my gratitude to Prof. Dr. José Paulo Santos from the Universidade Nova de Lisboa, Portugal, for having agreed to review my PhD thesis.

My gratitude goes also to my colleagues of the AXP group, in particular Dr. Wojciech Blachucki and Dr. Yves – Patrik Maillard for all the help and great company during the past 4 years.

The financial supports of the Swiss National Science Foundation and the University of Fribourg are acknowledged. Without them, the present work would not have been possible.

I wish also to thank the secretariat for the administrative support, especially Eliane Esseiva for her help in solving the administration problems related to my stay in Fribourg.

Many thanks also to the people working in the electronics and mechanical workshops, in particular Olivier Huot and Oswald Raetzo, for their technical support throughout my PhD thesis.

I would like to extend my sincerest thanks and appreciation to my lovely parents, brothers and sister for all their support, love and care. I want to pay special tribute to my late father Muhammad Younas who passed away during my PhD but I believe his support and prayers are always with me.

Finally above all of us, almighty Allah, for answering my prayers and for giving me the strength.

CURRICULUM VITAE

Personal details

First name & family name: **Faisal Zeeshan**

Date and place of birth: 05.07.1983, Sahiwal, Pakistan

Nationality: Pakistani

Marital status: Single

Current address: Rue de Rome 3
1700 Fribourg
Switzerland

Languages: Punjabi and Urdu (native)
English (fluent)
French (basic)

Education & research

2013 – present	<p>University of Fribourg PhD degree in Physics thesis title: <i>Laboratory based XAS measurements, Electron-induced double K-shell ionization of Sc, Cr and Cu and Chemical sensitivity of photoinduced Kβ hypersatellite transitions in Cr compounds</i> <u>other activities (not included in the PhD thesis):</u> participation to several experiments at the Swiss Light Source SLS (Paul Scherrer Institute, Villigen, Switzerland) and MAX III Laboratory (Lund, Sweden) as well as to in-house measurements. <u>other achievements:</u> certificate of completing 'hands-on Python' programming course</p>
2010 – 2012	<p>Lund University, Sweden MSc degree in Physics thesis title: <i>Test of a low Noise/low power preamplifier for the PANDA Electromagnetic Calorimeter.</i> The thesis was performed at the University of Basel, Switzerland, within an Erasmus scholarship (February 2012 - July 2012)</p>
2005 – 2007	<p>Federal Urdu University of Arts Science and Technology, Islamabad MSc degree in Applied Physics</p>
2002 – 2004	<p>University of the Punjab, Pakistan BSc degree in two majors: <i>Physics, Mathematics (A+B)</i></p>
2000 – 2002	<p>K.R.L Model College Kahuta, Pakistan Higher Secondary School Certificate</p>

Employment history

2013 – **present day** University of Fribourg
Graduate assistant
activities: assistant in physics laboratory experiments for first-year students.

06/2009 – **12/2009** K.R.L Model College Kahuta, Pakistan
Senior School Teacher
subjects: Physics and Mathematics

05/2008 – **05/2009** Bahria College Kahuta, Pakistan
Senior School Teacher
subjects: Physics and Mathematics

LIST OF PUBLICATIONS

Refereed articles

M. Guerra, J. M. Sampaio, T. I. Madeira, F. Parente, P. Indelicato, J. P. Marques, J. P. Santos, J. Hozzowska, J.-Cl. Dousse, L. Loperetti, F. Zeeshan, M. Müller, R. Unterumsberger, and B. Beckhoff

Theoretical and experimental determination of L-shell decay rates, line widths, and fluorescence yields in Ge.

Phys. Rev. A **92**, 022507 (2015).

Wojciech Blachucki, Jakub Szlachetko, Yves Kayser, Jean-Claude Dousse, Joanna Hozzowska, Faisal Zeeshan, Jacinto Sá,

In situ high energy resolution off-resonant spectroscopy applied to a time-resolved study of single site Ta catalyst during oxidation.

Nucl. Instrum. Methods B (2016) (in press).

Available online: <http://dx.doi.org/10.1016/j.nimb.2016.11.029>.

R. Bohinc, J. Hozzowska, J.-Cl. Dousse, J. Pérez-Pariente, A. B. Pinar, M. Nachtegaal, W. Blachucki, F. Zeeshan, Y. Kayser, and J. van Bokhoven,

Aluminum structure in ferrierite zeolites studied with valence to core X-ray emission spectroscopy.

Phys. Chem. Chem. Phys. **19** 29271 (2017).

Papers in preparation

F. Zeeshan, J.-Cl. Dousse, J. Hozzowska, and L. Loperetti,

In-house XAS measurements of 3d, 4d, and 5d transition metals using a von Hamos curved crystal spectrometer.

F. Zeeshan, J.-Cl. Dousse and J. Hozowska,
Double K-shell ionization of Sc, Cr and Cu induced by electron impact.

F. Zeeshan, J. Hozowska, J.-Cl. Dousse, D. Sokaras, D.-C. Weng, M. Kavcic and J.P. Santos,
Chemical sensitivity of photoinduced $K^h\beta$ hypersatellite transitions in metallic Cr and Cr compounds.

Conference abstracts

F. Zeeshan, J. Hozowska, L. Loperetti and J.-Cl. Dousse,
Laboratory-based XAS measurements with a von Hamos curved crystal spectrometer.
European Conference on X-Ray Spectrometry (EXRS), June 15-20, 2014, Bologna, Italy, booklet of abstr.

F. Zeeshan, J. Hozowska, L. Loperetti and J.-Cl. Dousse,
XAS measurements of 3d, 4d, and 5d transition metals using a laboratory-based set up.
Annual Meeting of the Swiss Physical Society (SPS), June 30 - July 2, 2014, Fribourg, Switzerland, booklet of abstr.

F. Zeeshan, J. Hozowska, L. Loperetti and J.-Cl. Dousse,
In-house XAS measurements using a von Hamos curved crystal spectrometer and an X-ray tube.
47th Conference of the European Group on Atomic Systems (EGAS), July 14-17, 2015, Riga, Latvia, booklet of abstr. p. 145.

